HARVARD UNIVERSITY

THE GRADUATE SCHOOL OF ARTS AND SCIENCES

THESIS ACCEPTANCE CERTIFICATE

The undersigned, appointed by the

Division

Department **Astronomy**

Committee

have examined a thesis entitled

"Exploding Stars, Near and Far"

presented by **Saurabh Jha**

candidate for the degree of Doctor of Philosophy and hereby certify that it is worthy of acceptance.

Signature .....

Typed name **John P. Huchra**

Signature Robert Kirshner

Typed name **Robert Kirshner**

Signature .....

Typed name **Dimitar D. Sasselov**

Signature R. Z. Stanek

Typed name **Krzysztof Z. Stanek**

Signature .....

Typed name **Nicholas B. Suntzeff**

Date **May 13, 2002**

Exploding Stars, Near and Far

A thesis presented

by

Saurabh Jha

to

the Department of Astronomy

in partial fulfillment of the requirements

for the degree of

Doctor of Philosophy

in the subject of

Astronomy

Harvard University

Cambridge, Massachusetts

May 2002

UMI Number: 3051196

ProQuest Information and Learning Company
300 North Zeeb Road
P.O. Box 1346
Ann Arbor, MI 48106-1346

Exploding Stars, Near and Far

advisor: Prof. Robert P. Kirshner

Saurabh Jha

Abstract

Type Ia supernovae (SNe Ia) play a key role in recent advances in our understanding of the Universe. We present cosmological applications of SNe Ia, including observational results as part of an ongoing campaign at the Harvard-Smithsonian Center for Astrophysics to monitor newly discovered SNe Ia at the F. L. Whipple Observatory (FLWO). We describe observations and analysis of SN 1998bu in M96, the only SN Ia yet to have appeared in a galaxy with a previously measured Hubble Space Telescope Cepheid distance. We show that SN 1998bu was a normal, reddened SN Ia and use it to constrain the Hubble constant, with attention to systematic uncertainties. We also present the largest set of SN Ia photometry published to date, consisting of 2190 *UBVRI* FLWO CCD observations of 44 SNe Ia discovered between 1997 and 2000. The large, homogeneous sample of U-band light curves is unique, with important applications to SN Ia at high redshift, and we present the first detailed description of SN Ia U-band properties. We also develop MLCS2k2, a new incarnation of the Multicolor Light Curve Shape method to measure SN Ia distances, incorporating the U-band and other improvements. Application of MLCS2k2 to a large sample of Hubble-flow and Cepheid-calibrated SNe Ia yields an estimate of $H_0 = 66 \pm 3$ (random) ± 7 (systematic) or $76 \pm 3 \pm 8$ km s^{-1} Mpc^{-1}, depending on which of two discrepant sets of Cepheid distances is used. With the High-Z SN Search Team, we present cosmological constraints on the dark energy equation of state, and combined constraints on $\Omega_{\rm M}$ and Ω_Λ from SNe Ia and the cosmic microwave background. Finally, via observations at FLWO, we measure the redshift of an extremely distant exploding star, GRB 010222, at $z = 1.477$.

Contents

The world goes round
Or we get thrown
Into the stars.

Stephin Merritt

For my family.

Acknowledgements

I have been extremely fortunate during my time at Harvard. The many exciting opportunities to learn, grow, and study the Universe that have been presented to me are a direct result of the wonderful, caring people I've encountered, and I'd like to thank them here. The research I present in this thesis certainly would not have been possible without them, but more importantly, they have made my life richer, and for that, I am immensely grateful.

First and foremost, I would like to thank my advisor, Bob Kirshner. Bob is an outstanding mentor, with the perfect combination of good humor and keen scientific insight, both of which I rely upon. His enthusiasm for astronomy and the study of supernovae makes you feel like you are working on something really important, and his unmatched wit ensures you never take it too seriously. Bob is also a wonderful teacher, and not only to the undergrads in Science A-35. He has taught me so many things, from the advantages of crisp prose to the importance of keeping sight of the big picture even when mired in details. Beyond the tremendous opportunities Bob has provided me, he has also allowed me to become more independent as a researcher, while always providing steadfast support and encouragement. I thank him for all this and much more.

I also want to acknowledge the stimulating (and fun!) supernova group at the Center for Astrophysics. Peter Garnavich is an amazing scientist, with an ability to see to the heart of diverse problems and understand and carry out whatever it takes to solve them. He is also an excellent observer and a warm, generous person. I feel privileged to have had him as a mentor, and more privileged to consider him a friend

(and I'd feel that way even without those prized Red Sox tickets!). Pete Challis is also a skilled observer and master of HST data, and I thank him for his help, advice, and that inevitable extra round. I admire Pete a lot, most of all for the fact that at the tennis net, he will volley back your shot that was probably going long — he has that rare quality of enjoying playing more than winning (of course, he still wins anyway!). Finally, thanks to Tom Matheson for all of his spectroscopic expertise, and other advice and help, not the least of which was letting me concentrate on my thesis rather than nightly requests to the telescopes.

I am also grateful to Adam Riess for helping me understand the intricacies of type Ia supernova light curves, as well as supporting and encouraging me through the process of writing this thesis. I further appreciate having the opportunity to work with the rest of the High-Z Supernova Search Team (and see the world!). In particular, I would like to thank our team leader Brian Schmidt, who showed such faith in me, and allowed me to be part of this incredibly exciting endeavor. Special thanks also to Alex Filippenko, whose support has been instrumental in enabling the next stage of my career; I very much look forward to working with him in Berkeley! Additionally I thank Nick Suntzeff, for instilling in me a sense of the importance of careful attention to detail in observations and data reduction (a large part of this thesis), as well as for making Chile such a hospitable place to visit, and for kindly agreeing to read my thesis and be part of the exam committee.

Thanks as well to the rest of my committee. I have immensely enjoyed working with Kris Stanek on GRB research, and I thank him for encouraging me in this exciting field; I treasure our collaboration and our conversations. I thank John Huchra for ever so gently prodding me to have that next TAC meeting, and for being

so supportive of my research, and so caring towards the graduate students in general. I am grateful as well to Dimitar Sasselov for his enthusiasm and many discussions on topics ranging from transiting planets to Cepheid metallicities. Thanks to Chris Kochanek for answering my statistical questions, inducting me into the Bayesian school, and never letting me forget about covariance. Finally, I am deeply indebted to Alyssa Goodman, who has continuously provided me with unwavering (and undeserved) support from the time I was an undergrad through today; I give her my heartfelt thanks.

Had it not been for an undergrad summer job offer that came in the nick of time, my research in astronomy would have been very different, and quite possibly non-existent. I thank Bob Noyes for giving me the wonderful opportunity to work with the AFOE spectrograph, and even be part of discovering an extrasolar planet! It was the first astronomical research I ever did, and my interest in this exciting new field has stayed with me to this day; I thank Bob for taking a chance on me. I would also like to thank the AFOE group, Pete Nisenson (and also for the weekly tennis) and Sylvain Korzennik (whose IDL scripts I still use everyday). Dave Latham supervised my undergraduate thesis, and I thank him for his support throughout the years, as well as for the triple stars, faraway summer jobs, planet seminars, wine tastings, and good cheer. On the same topic, thanks also to Willie Torres, whose dedication, thoroughness, and brilliance I admire greatly.

I thank all the graduate students here at CfA who have made graduate school such an enjoyable and educational experience. Whether at research forum, lunch at Lucky Garden, dinner at Boca Grande, or pub night at Grendel's, the discussions of astronomy (and everything else) with good friends have been an essential part of

grad school. I would especially like to thank Dave Charbonneau for his wonderful sense of humor, apparently adequate maritime navigation, and fulfilling scientific collaboration. Special thanks to "those who wish to remain relatively nameless" — I'll call them RB. Thanks also to my roommates, Aaron, Julia, and Cindy, for making Line Street so enjoyable, and of course, to Tybalt, whom I cherish.

I cannot adequately express my love and gratitude to my entire family. My parents have been incredibly supportive of all my choices, encouraging me to seek a fulfilling and happy life. They have cultivated my fascination with astronomy, and I thank them for their love and support. I would also like to thank Neeraj, Shalini, Smriti, Ashray, Pranay, as well as the rest of my extended family, whose closeness to me and love have been a source of great strength and joy.

Finally, I thank Frances Wall for her love, patience, and support. I am infinitely appreciative and grateful to have her in my life.

Chapter 1

Introduction

Aside from providing a cute near-rhyme, the title of this thesis really emphasizes its focus: measuring distances in the Universe. The linking of distance and time by the speed of light enables us to answer amazingly fundamental cosmological questions by measuring precise distances: how old is the Universe? how fast is it expanding? how did it evolve in the past and what does the future hold? what is the Universe made of? Nature has been kind to provide us with an excellent tool, exploding white dwarfs called type Ia supernovae, which can be used to measure distances to galaxies right next door as well as galaxies halfway across the observable Universe. Here we describe a number of observational projects involving SNe Ia, sharpening and applying these cosmological tools.

In **Chapter 2**, we present detailed spectroscopic and photometric optical and near-infrared observations of SN 1998bu in M96, published as Jha, Garnavich, Kirshner, Challis, et al. 1999, ApJS, 125, 73. This SN Ia is unique, as it occurred in a galaxy with an already measured HST Cepheid distance. Multicolor light curves of

SN 1998bu, from a large number of telescopes, showed it to be a normal SN Ia, but significantly extinguished by dust in its host galaxy. We used SN 1998bu and three other Cepheid-calibrated SNe Ia, along with a sample of 42 SNe Ia in the Hubble flow, to constrain the Hubble constant, paying particular attention to sources of systematic uncertainty, such as the metallicity-dependence of the Cepheid distance scale and the distance to the Large Magellanic Cloud (LMC).

A large fraction of the SN 1998bu observations were taken as part of our Harvard-Smithsonian Center for Astrophysics cooperative supernova monitoring campaign, with photometry using the F. L. Whipple Observatory (FLWO) 1.2m telescope, and spectroscopy from the FLWO 1.5m telescope. We present the recent SN Ia photometry from this campaign in **Chapter 3**, with 44 *UBVRI* light curves of SN Ia discovered (by others) during 1997 to 2000. This is the largest homogeneously observed and reduced set of SN Ia photometry to date. The U-band data are a new and timely development, with application to high-redshift SN Ia in which other bands redshift out of the optical passbands. We describe the properties of SN Ia U-band light curves and colors, and note an increased intrinsic dispersion in the U-band peak magnitude relative to other bands, that is not the result of reddening or variations in the reddening law. It is quite likely the photometric data tables presented will have the highest long-term value of anything in this thesis. Consequently, we take care to characterize the natural system of the photometric observations and our transformations of the data to standard passbands.

Turning SN Ia photometry in a number of passbands to a distance measurement requires tools to determine the intrinsic luminosity and extinction along the line of sight. In **Chapter 4** we develop a new incarnation of the Multicolor Light Curve

Shape method (Riess, Press, & Kirshner 1996, ApJ, 473, 88) dubbed MLCS2k2 (we hope the paper appears this year!) which simultaneously fits *UBVRI* light curves for model parameters of interest. We describe a number of improvements to the method, including incorporation of more precise K-corrections and a new framework for describing extinction. We also include the ability to impose prior constraints on any of the model parameters, making the method more versatile when the photometry is sparse but other data (such as spectroscopy) is available. We apply MLCS2k2 to a nearly doubled sample (compared to Chapter 2) of Hubble-flow SNe Ia and a doubled sample of Cepheid-calibrated SNe Ia and estimate $H_0 = 66 \pm 3$ (random) ± 7 (systematic) or $76 \pm 3 \pm 8$ km s^{-1} Mpc^{-1}, depending on which of two groups' Cepheid distances are used.

As part of the High-Z Supernova Search Team, we present analysis of high-redshift SN Ia data in **Chapter 5**, adapted from Garnavich, Jha, et al. 1998, ApJ, 509, 74 and Jha & the High-Z SN Search Team 2001 (astro-ph/0101521). We use observations of high-redshift SN Ia to constrain the equation of state of the dark energy responsible for acceleration of the cosmic expansion. We also refine the estimates Ω_M and Ω_Λ based on nearly orthogonal constraints from SNe Ia and the cosmic microwave background (CMB) power spectrum. We have also updated these constraints to reflect the most recent SN Ia and CMB results.

Our SN monitoring campaign at FLWO includes spectroscopy as well as photometry, through (dark-)nightly "combo" requests to the FLWO 1.5m telescope + FAST spectrograph. We provide the spectroscopic classification of a large fraction of newly discovered low-redshift supernovae, published in the form of IAU Circulars. The slightly self-indulgent Figure 1.1 shows my first IAU circular on supernovae

Circular No. 6641

Central Bureau for Astronomical Telegrams
INTERNATIONAL ASTRONOMICAL UNION

Mailstop 18, Smithsonian Astrophysical Observatory, Cambridge, MA 02138, U.S.A.
IAUSUBS@CFA.HARVARD.EDU or FAX 617-495-7231 (subscriptions)
BMARSDEN@CFA.HARVARD.EDU or DGREEN@CFA.HARVARD.EDU (science)
URL http://cfa-www.harvard.edu/cfa/ps/cbat.html
Phone 617-495-7244/7440/7444 (for emergency use only)

SUPERNOVA 1997bz IN ANONYMOUS GALAXY

The Mount Stromlo Abell Cluster Supernova Search Team (cf. *IAUC* 6418, 6639) reports the discovery of an apparent supernova ($V \sim 17.5$) on V and R CCD images taken on Apr. 27 by S. Chan on the Mount Stromlo 1.27-m telescope (+ Macho Camera). SN 1997bz is located near Abell 1238 at $\alpha = 11^h22^m25^s.46$, $\delta = +1°11'21''.5$ (equinox 2000.0). No star was detected at this position on frames taken on Apr. 11. SN 1997bz is also visible on CCD images taken with the Mount Stromlo 1.27-m telescope on Apr. 30. A nearby star has position end figures $22^s.56$, $13'24''.8$.

S. Jha, P. Challis, P. Garnavich, and R. Kirshner, Harvard-Smithsonian Center for Astrophysics, write: "Spectrograms were obtained by P. Berlind at the 1.5-m Tillinghast reflector on Apr. 30.18 UT and by P. Challis at the Multiple Mirror Telescope on May 2.15. The spectra are heavily contaminated by the host galaxy, but they indicate that SN 1997bz is of type Ia, slightly more than one week after maximum. The redshift derived from Hα emission in the host galaxy is 0.03, implying that it is in the foreground of the cluster (which is at redshift 0.072)."

COMET C/1995 O1 (HALE-BOPP)

R. Meier, University of Hawaii (UH); H. Matthews, Joint Astronomy Centre, Hilo, and National Research Council of Canada; T. Owen and D. Jewitt, UH; M. Senay, University of Massachusetts; and N. Biver, D. Gautier, D. Bockelée-Morvan, and J. Crovisier, Observatoire de Paris, Meudon, report the detection of DCN in comet C/1995 O1 with the James Clerk Maxwell Telescope at Mauna Kea on Apr. 27.9 UT: "The 10σ detection of the DCN 5–4 transition at 362.046 GHz was taken together with a quasi-simultaneous measurement of the HCN 4 3 line. Prior observations of HCN and $H_{13}CN$ 4-3 lines will allow an accurate, essentially model-independent determination of the D/H ratio in cometary HCN. Our preliminary analysis leads to an approximate DCN/HCN ratio on the order of 10^{-3}. At the time of the observations, the comet was passing in front of the Taurus dark clouds, and we have been careful to exclude the possibility of contamination by background sources. The detection of DCN is the first detection of cometary deuterium in a molecule other than water. The availability of a D/H ratio in both water (*IAUC* 6615) and a carbon-nitrogen-bearing molecule may provide fundamental information on the origin and evolution of comets."

1997 May 5 *Daniel W. E. Green*

Figure 1.1.— IAU Circular on spectroscopy of SN 1997bz, my first type-Ia supernova.

(with hundreds to follow); it is fitting that SN 1997bz was a type Ia! The daily coordination of observations of astronomical transients provided a clear path to research on gamma-ray bursts, not so very different than supernovae. In fact, we have shown that the cosmological GRB 011121 had SN 2001ke as its progenitor (Garnavich et al. 2002, astro-ph/0204234). In **Chapter 6**, we present rapid spectroscopic observations of GRB 010222 with the FLWO 1.5m telescope, and measure the distance to this exploding star, $z = 1.477$. We also provide quantitative estimates of the likelihood that the GRB really is associated with the presumed host galaxy, and constrain the host-galaxy extinction law.

Finally, in **Chapter 7**, we conclude and present future prospects for SN Ia research. In particular, we discuss three projects that are direct and natural extensions of work contained in this thesis. First, we describe tests of cosmological inferences based on high-redshift supernovae through observations covering the wide *UBVRI* wavelength range. Second, we detail our efforts soon to be underway, trying to measure SNe Ia at very high redshift in the epoch of deceleration, before dark energy dominated the expansion. These observations require HST, and the *U*-band light curve information developed here is an essential underpinning. Last, we describe a proposed project aimed at constraining the equation of state of the negative pressure component more strongly than the results in Chapter 5, hopefully leading us to understand what the dark energy really is.

Chapter 2

The Type Ia Supernova 1998bu in M96 and the Hubble Constant

Saurabh Jha, Peter M. Garnavich, Robert P. Kirshner, Peter Challis, Alicia M. Soderberg, Lucas M. Macri, John P. Huchra, Pauline Barmby, Elizabeth J. Barton, Perry Berlind, Warren R. Brown, Nelson Caldwell, Michael L. Calkins, Sheila J. Kannappan, Daniel M. Koranyi, Michael A. Pahre, Kenneth J. Rines, Krzysztof Z. Stanek, Robert P. Stefanik, Andrew H. Szentgyorgyi, Petri Väisänen, Zhong Wang, Joseph M. Zajac, Adam G. Riess, Alexei V. Filippenko, Weidong Li, Maryam Modjaz, Richard R. Treffers, Carl W. Hergenrother, Eva K. Grebel, Patrick Seitzer, George H. Jacoby, Priscilla J. Benson, Akbar Rizvi, Laurence A. Marschall, Jeffrey D. Goldader, Matthew Beasley, William D. Vacca, Bruno Leibundgut, Jason Spyromilio, Brian P. Schmidt, and Peter R. Wood 1999, *The Astrophysical Journal Supplement Series*, **125**, 73

Abstract

We present optical and near-infrared photometry and spectroscopy of the type Ia SN 1998bu in the Leo I Group galaxy M96 (NGC 3368). The data set consists of 356 photometric measurements and 29 spectra of SN 1998bu between UT 1998 May 11 and July 15. The well-sampled light curve indicates the supernova reached maximum light in B on UT 1998 May 19.3 (JD 2450952.8 $\pm$ 0.8) with $B = 12.22 \pm 0.03$ and $V = 11.88 \pm 0.02$. Application of a revised version of the Multicolor Light Curve Shape (MLCS) method yields an extinction toward the supernova of $A_V = 0.94 \pm 0.15$ mag, and indicates the supernova was of average luminosity compared to other normal type Ia supernovae. Using the *HST* Cepheid distance modulus to M96 (Tanvir et al. 1995) and the MLCS fit parameters for the supernova, we derive an extinction-corrected absolute magnitude for SN 1998bu at maximum, $M_V = -19.42 \pm 0.22$. Our independent results for this supernova are consistent with those of Suntzeff et al. (1999). Combining SN 1998bu with three other well-observed local calibrators and 42 supernovae in the Hubble flow yields a Hubble constant, $H_0 = 64^{+8}_{-6}$ km s^{-1} Mpc^{-1}, where the error estimate incorporates possible sources of systematic uncertainty including the calibration of the Cepheid period-luminosity relation, the metallicity dependence of the Cepheid distance scale, and the distance to the LMC.

2.1 Introduction

Type Ia supernovae (SNe Ia) have recently assumed an elite status at the top rung of the cosmic distance ladder. Comprehensive studies of SNe Ia have established their general spectroscopic and photometric homogeneity, along with quantifiable diversity. SNe Ia make reasonably good standard candles (Kowal 1968; Sandage & Tammann 1993; Branch & Miller 1993) and excellent calibrated candles (Phillips 1993; Hamuy et al. 1995, 1996b; Riess, Press, & Kirshner 1995a, 1996a; Tripp 1998; Phillips et al. 1999) which, combined with their high intrinsic luminosity, makes them superb indicators of very large distances and a powerful tool for cosmology (Branch 1998, and references therein).

The downside is that SNe Ia are rare and fleeting, making them more challenging to study than other astronomical distance indicators. Nevertheless, recent applications of these "standard bombs" have been numerous. Within a few hundred Mpc, they have been used to measure the expansion of the Universe: with recession velocities of their host galaxies and distances to individual SNe Ia, the Hubble law has been tested to redshifts $z \simeq 0.1$ at high precision (Hamuy et al. 1996b; Riess, Press, & Kirshner 1996a; Tammann 1998). SNe Ia have also been used to measure peculiar motions of galaxies and large scale flows (Tammann & Leibundgut 1990; Miller & Branch 1992; Jerjen & Tammann 1993; Riess, Press, & Kirshner 1995b; Riess et al. 1997a; Zehavi et al. 1998; Tammann 1998) as well as to provide constraints on the properties of extragalactic dust (Riess, Press, & Kirshner 1996b). At larger distances, SNe Ia serve as standard clocks: cosmological time dilation has been demonstrated by comparing light curves of distant supernovae

with light curves from those nearby (Leibundgut et al. 1996; Goldhaber et al. 1997), as well as from the relative rates of spectral evolution (Riess et al. 1997b). Most recently, SNe Ia have been used to measure luminosity distances at high redshift ($0.3 \lesssim z \lesssim 1.0$), from which the geometry and expansion history of the Universe can be determined (Nørgaard-Nielsen et al. 1989; Perlmutter et al. 1995; Schmidt et al. 1998). These measurements have likely tolled the death knell of standard ($\Omega_M = 1$) cold dark matter (CDM) cosmology, strongly disfavoring the possibility of enough gravitating matter to flatten the Universe (Perlmutter et al. 1998; Garnavich et al. 1998a). Even more surprisingly, preliminary indications show that the expansion is accelerating at the current epoch (Riess et al. 1998a; Perlmutter et al. 1999), inconsistent with the idea that ordinary matter is the dominant component of the Universe's energy density. Alternatives such as a cosmological constant, or other forms of energy density similar to it, seem to be favored (Garnavich et al. 1998b; Perlmutter et al. 1999). Combined with constraints from the cosmic microwave background anisotropy power spectrum, the supernovae have also given preliminary indications for a Universe with zero global curvature (Garnavich et al. 1998b; White 1998; Lineweaver 1998; Tegmark 1999; Efstathiou et al. 1999; Perlmutter, Turner, & White 1999; Roos & Harun-or-Rashid 1999).

These studies rely on SNe Ia only as bright, precise, *relative* distance indicators. However, the determination of the expansion rate of the Universe, the Hubble constant, and the age of the Universe require an accurate *absolute* distance scale. Measuring absolute distances to SNe Ia requires calibrating them through objects on lower rungs of the distance ladder. The best distance indicator for this remains what it has been since the days of Hubble himself: δ Cephei variable stars. Cepheids are

bright enough to be studied in nearby galaxies, including those which have hosted SNe Ia. In addition they can be found in significant numbers, which allows for a precise mean period-luminosity (PL) relation to be constructed and compared to nearby samples. In general Cepheids in external galaxies are compared to Cepheids in the Large Magellanic Cloud (LMC), whose distance is calibrated through a variety of means (not always with the same result, cf. Section 2.5.2.3). The importance of Cepheids to calibrate secondary distance indicators (including SNe Ia) prompted the creation of the *Hubble Space Telescope* (*HST*) Key Project on the Extragalactic Distance Scale, which has measured Cepheid distances to a number of nearby galaxies (Freedman et al. 1994, 1998 and references therein). Another *HST* effort has been underway to measure Cepheid distances to galaxies that have hosted SNe Ia, to calibrate them specifically (Sandage et al. 1992; Saha et al. 1997, and references therein). At present the use of SNe Ia to measure the Hubble constant is limited by the paucity of local calibrators, not by the number or precision of distances to objects in the Hubble flow.

Nature has been kind by providing us with SN 1998bu in the Leo I Group galaxy M96 (NGC 3368), for which a Cepheid distance had already been obtained with *HST* by a third group, Tanvir et al. (1995). In this paper we calibrate the absolute magnitude of SN 1998bu through extensive optical and near-infrared photometry and spectroscopy. In §2 we describe our observations and reduction procedure. In §3 we derive parameters of SN 1998bu, including the extinction along the line of sight as well as a quantitative estimate of the intrinsic luminosity of SN 1998bu compared to other SNe Ia. In §4 we combine the properties of SN 1998bu with other Cepheid-calibrated SNe Ia and SNe Ia in the Hubble flow to determine

the Hubble constant (H_0) and its statistical uncertainty. We discuss our results, sources of systematic error, and implications for the age of the Universe, t_0, in §5. Finally, we conclude and summarize in §6. Independent observations and analysis of SN 1998bu have been performed by Suntzeff et al. (1999), and we compare our analysis and results with theirs throughout the paper. Infrared and optical spectra and uncalibrated light curves of SN 1998bu have also been presented by Meikle & Hernandez (2000).

2.2 Observations and Analysis

2.2.1 Discovery

SN 1998bu was discovered by the amateur astronomer M. Villi on UT 1998 May 9.9 on CCD images of M96 (Villi 1998). The supernova was located at $\alpha = 10^{\rm h}46^{\rm m}46\overset{\rm s}{.}03$, $\delta = +11°50'07\overset{''}{.}1$ (equinox 2000.0), about one arcminute north of the host galaxy nucleus (Nakano & Aoki 1998). At the Center for Astrophysics we monitor new, bright supernovae spectroscopically with the Center for Astrophysics F. L. Whipple Observatory (FLWO) 1.5-m Tillinghast reflector and FAST spectrograph (Fabricant et al. 1998), and photometrically with the FLWO 1.2-m reflector in optical and near-infrared passbands. Our photometric observations of SN 1998bu with the 1.2-m began on May 11.1, with the new STELIRCAM near-infrared InSb array detector. The discovery of SN 1998bu ocurred during lunar bright time, and so the 1.5-m telescope was not equipped with the FAST instrument until May 15.

High resolution spectra taken by Munari et al. (1998) with the Asiago

Observatory 1.8-m telescope showed interstellar Na I D absorption from our Galaxy, as well as from M96 at a heliocentric radial velocity of 744.8 ± 0.3 km s^{-1}. Low-disperson spectra of SN 1998bu were taken by Meikle et al. (1998) on May 12.9 and Ayani, Nakatani & Yamaoka (1998) on May 14.5, which revealed the supernova to be of type Ia about a week before maximum light. Our first spectroscopic observations of SN 1998bu with the FLWO 1.5-m were taken on May 16.1.

A type Ia supernova in a galaxy whose Cepheid distance had already been measured by *HST* (Tanvir et al. 1995) provided a unique opportunity; it was the opposite of the usual case, in which an *HST* Cepheid distance to a galaxy is measured specifically because the galaxy was an SN Ia host. Well-measured light curves are the key to SN Ia distances, so we undertook extensive photometric observations in the $UBVRIJHK$ passbands.

2.2.2 Optical Photometry

The plurality of our optical photometric observations (29 nights) was obtained with the FLWO 1.2-m telescope + "4Shooter" CCD mosaic camera (Szentgyorgyi et al. 1999). The 4Shooter consists of a 2x2 array of thinned, back-side illuminated, anti-reflective coated Loral 2048^2 CCD detectors, situated at the f/8 Cassegrain focus. The pixel size is 15 μm, yielding a scale of $0\farcs335$ per pixel at the focal plane and a field of view of approximately $11\farcm4$ on a side for each chip, with total sky coverage of 0.15 deg^2. Our observations were taken in a 2x2 binned mode, so that the resulting images were sampled at $0\farcs67$ per pixel, well matched to the typical seeing ($1\farcs5$-$2''$ FWHM) achieved at this telescope. All observations of SN 1998bu with the

mosaic were made on the same CCD (chip 1), which has the best combination of cosmetic characteristics and quantum efficiency. Two nights of observations were obtained on this telescope with the "AndyCam" instrument, a CCD camera with a single CCD, very similar to those that make up the 4Shooter. Both instruments have good ultraviolet and near-infrared response, which enabled us to make observations in the Johnson UBV and Kron-Cousins RI bandpasses. Our optical filters are constructed from Schott glass components, as recommended by Bessell (1990) for coated CCDs. The FLWO $BVRI$ filter prescriptions are described by Riess et al. (1999); in general they match well the prescriptions of Bessell (1990), though the FLWO I filter extends to somewhat longer wavelengths. The FLWO U filter transmission is also a good match to the Bessell (1990) UX specification.

Our FLWO 1.2-m observations of SN 1998bu are part of an ongoing supernova monitoring program at CfA. Supernova observations are not well suited to the scheduled time allocation procedure that is typical at most telescopes. To follow supernovae, the time allocation committee authorizes us to enlist the generous aid of the scheduled observers, asking them to devote a small fraction of observing time (usually limited to $\sim$ 20 minutes per night) to the SN program. We complement the monitoring observations with scheduled nights (usually one night per month) to measure fainter objects and perform photometric calibrations. We have been quite successful observing in this mode; a set of 22 SNe Ia light curves garnered as a result of this program has been presented by Riess et al. (1999).

The FLWO 1.2-m is equipped with an infrared instrument during bright time, which provides useful IR supernova data (obtained in a similar observing mode), at the price of bright-time gaps in our optical light curves. For this object we made

a special effort to minimize these gaps by inviting observers at other institutions to participate. Six epochs of optical photometric observations in $UBVRI$ were taken at the Michigan-Dartmouth-MIT (MDM) Observatory 2.4-m Hiltner telescope and direct imager, with the thinned, back-illuminated, 1024^2 "Charlotte" CCD detector, located at the f/7.5 Cassegrain focus and providing a $4\farcm7 \times 4\farcm7$ field-of-view at $0\farcs28$ per pixel. Further observations on two nights were obtained at the Kitt Peak National Observatory (KPNO) 0.9-m telescope, with the T2KA (2048^2) CCD detector at the f/7.5 Cassegrain focus, yielding a $23' \times 23'$ field-of-view at $0\farcs68$ per pixel. Target of opportunity observations were also carried out on five nights during NOAO time at the WIYN Observatory 3.5-m telescope with the S2KB (2048^2) CCD Imager at f/6.3 with $0\farcs20$ per pixel and a $6\farcm8 \times 6\farcm8$ field-of-view.

Other sites also observed SN 1998bu and we report those data as well. We include CCD data from the Whitin Observatory 0.6-m telescope at Wellesley College (eight nights using a 1024^2 CCD at f/13.5, with a scale of $0\farcs91$ per pixel), the Gettysburg College Observatory 0.4-m (twelve nights using a 1024^2 CCD at f/11, $0\farcs84$ per pixel) and the 0.76-m Katzman Automatic Imaging Telescope (KAIT) at Lick Observatory run by the University of California, Berkeley (fifteen nights with a 512^2 CCD at f/8.2, $0\farcs63$ per pixel). The detectors used in these observations were not as blue-sensitive as the others, so only $BVRI$ images were taken. Our observations of SN 1998bu continued until July 2 when it was too close to the setting sun to provide good photometric data. In total our optical photometric data set consists of 327 measurements of SN 1998bu.

All CCD observations were reduced (uniformly, beginning with the raw data) in the standard fashion, with bias subtraction, dark current subtraction (not necessary

in most cases) and flat-field correction using the IRAF CCDPROC package. Most of the observations were taken in non-photometric conditions, so we have performed differential photometry with a sequence of six comparison stars in the supernova field, shown in Fig. 2.1. Comparison stars 1 and 2 were calibrated on four photometric nights (two from the FLWO 1.2-m, one each from the MDM 2.4-m and Kitt Peak 0.9-m). Stars 3, 4 and 5 were not in the MDM field of view, so these were calibrated from three nights. To calibrate the comparison stars into a local standard star sequence, Landolt (1992) standard fields providing stars in a wide range of color were observed in $UBVRI$ over a wide range in airmass. The supernova field was also observed in these filters at an airmass within the airmass range of the standard star observations. These data were reduced and stellar instrumental magnitudes were determined from aperture photometry using the APPHOT package in IRAF. We then derived zero points and transformation coefficients linear in airmass and color from the standard stars using the prescription of Harris, Fitzgerald, & Reed (1981). This transformation was then applied to the comparison star instrumental magnitudes to determine their standard magnitudes. We treated observations from each photometric night independently, and averaged the final standard magnitudes. Table 2.1 displays these mean standard magnitudes, along with the error in the mean determined from the scatter of repeat observations. We also list the comparison star identification numbers from Suntzeff et al. (1999). Our independent photometry of the comparison stars agrees well with their results.

To measure the brightness of SN 1998bu, we performed aperture photometry of the supernova and comparison stars on each image. We derived an aperture correction determined from one or a few isolated bright stars measured through

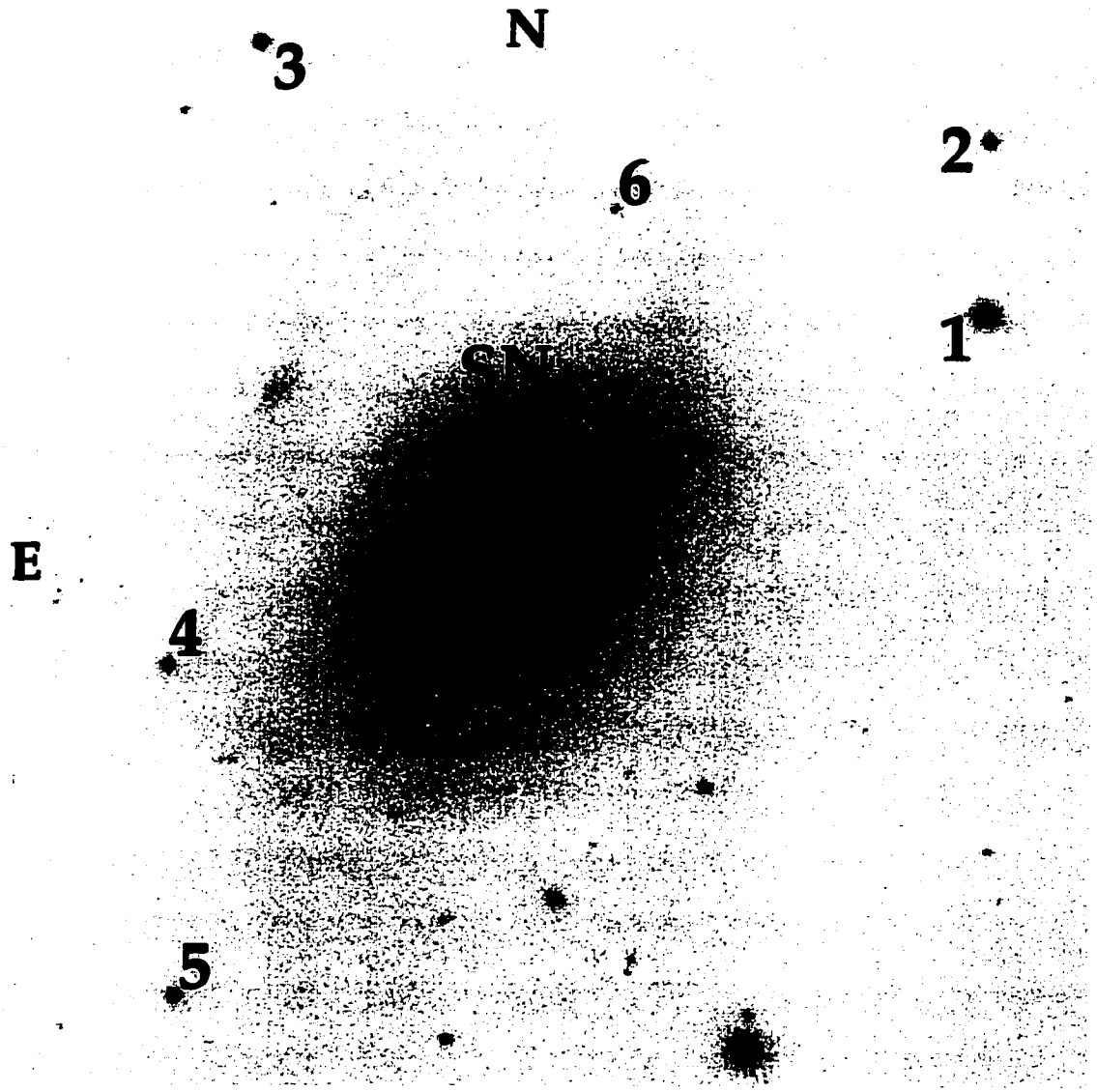

Figure 2.1.— SN 1998bu in M96 with local comparison stars. The field is 7.'6 × 7.'6; north is up and east is to the left. The image is a composite of several V-band observations of SN 1998bu taken with the F. L. Whipple Observatory 1.2-m telescope in May of 1998.

Table 2.1. Local standard star $UBVRIJHK$ magnitudes.

Star	U	B	V	R	I	J	H	K
1 (S6)	13.521(0.027)	13.594(0.012)	13.068(0.009)	12.774(0.012)	12.475(0.011)	12.02(0.05)	11.85(0.03)	11.77(0.03)
2 (S7)	15.437(0.029)	15.551(0.015)	15.016(0.013)	14.715(0.015)	14.403(0.015)	...	...	...
3 (S1)	15.523(0.035)	15.520(0.018)	14.895(0.017)	14.553(0.019)	14.199(0.019)	...	...	...
4 (S2)	16.501(0.040)	16.495(0.027)	15.789(0.024)	15.384(0.026)	14.971(0.025)	...	...	...
5 (S8)	16.778(0.039)	16.280(0.025)	15.441(0.024)	14.987(0.027)	14.573(0.025)	...	...	...
6 (S12)	...	19.210(0.042)	17.730(0.031)	16.805(0.040)	15.583(0.033)	14.36(0.05)	13.75(0.04)	13.54(0.03)

Note. — The S identifiers are from Suntzeff et al. (1999). Uncertainties in the magnitudes are listed in parentheses.

circular apertures of varying radii (with sky measurements in a surrounding annulus). We were thus able to measure the supernova light through a small aperture, so that noise from the background sky would be minimized. Due to the varying seeing and pixel scales at the sites, we did not impose a fixed angular size aperture for all the observations. In all cases, though, the aperture for the supernova instrumental magnitudes was the same size as the aperture for the comparison stars in the field. We chose aperture photometry over point-spread-function (PSF) fitting primarily out of convenience, but also because in many instances the fields were too small or the exposures too short to reliably determine the PSF from nearby stars.

We also determined the linear color transformation coefficients for each telescope/instrument/filter combination. At sites which had photometric conditions, these were the same as those used in determining comparison star magnitudes. For the other sites, color terms were determined from observations of either Landolt fields or other standard star fields but allowing for a varying zero point to account for the non-photometric conditions. The transformation coefficients were also checked with the local comparison stars. Color terms for each telescope/filter combination are listed in Table 2.2. Uncertainties in the transformation coefficients were propagated to the error estimate in the final photometry.

Since our observations of SN 1998bu used local standard stars at the same airmass as the supernova, no airmass correction was necessary for the differential photometry. By using the measured color terms, we only had to determine the zero point of each frame, by solving for the offset between the comparison star color-corrected instrumental magnitudes and their standard magnitudes. The zero point was determined from the flux-weighted combination of all available comparison

Table 2.2. Photometric Color Terms

Telescope	$U-B$	$B-V$	$V-R$	$V-I$	$V(B-V)$
CfA4	0.935	0.887	0.973	1.086	+0.041
CfA1	0.926	0.939	0.982	1.068	+0.027
MDM	0.782	1.061	0.981[a]	1.027	+0.019
KP09	0.907	0.912	1.005	1.027	+0.009
WIYN	1.140	0.974	1.060	1.100	+0.019
Gett	···	0.549[b]	0.894	1.006	+0.009
Well	···	0.658[b]	0.980	1.099	+0.030
KAIT	···	0.929	1.190	1.082	+0.001

Note. — The telescope designations are: CfA4, FLWO 1.2-m with 4Shooter; CfA1, FLWO 1.2-m with AndyCam; MDM, MDM Hiltner 2.4-m; KP09, KPNO 0.9-m; WIYN, WIYN 3.5-m; Gett, Gettysburg 0.4-m; Well, Wellesley 0.6-m; and KAIT, KAIT 0.76-m. The tabulated values for the color columns ($U-B$, $B-V$, $V-R$, $V-I$) are the transformation coeffiencents from the standard color to the instrumental color, e.g., CfA4: $(u-b) = 0.935(U-B) + \text{const}$. The tabulated values for the last column are transformation coefficients from $B-V$ to the instrumental v magnitude, e.g., CfA4: $v - V = +0.041(B-V) + \text{const}$.

[a]The MDM R-band photometry was not used; see text for details.

[b]As described in the text, we have not used a linear transformation to place Gettysburg and Wellesley B-band supernova photometry onto the standard system.

stars. The scatter in the comparison star magnitudes (typically ~ 0.02 mag) was used as an estimate of the internal error in determining the zero point. From the derived zero point and color transformation coefficient, we were then able to transform the supernova instrumental magnitude into a standard magnitude.

This procedure was quite effective in the majority of cases. However, supernova photometry requires special care. Where the color terms are large (due to a mismatch between the filter/detector response and a standard Landolt response), the use of a linear color correction can be insufficient. This problem is especially acute in supernova photometry because of deep, wide features in the spectra of supernovae. Even when a large color correction works well when applied to stars (i.e., yields very small differences with standard magnitudes), such large corrections may not be appropriate to supernovae. In most cases, filters were well-matched and the derived color corrections were small, so nothing more complicated was required. However, in two data sets (the Gettysburg and Wellesley B filters), the color-corrected supernova magnitudes were significantly discrepant with other data. In both of these cases the color terms were quite large. To combat this problem, we determined a correction based on the B filter transmission and detector sensitivity functions from these two sites. We used these response functions with spectrophotometric observations of a number of SNe Ia at varying ages, and determined magnitude corrections relative to the standard passband defined by Bessell (1990). This procedure mirrors the use of K-corrections for high-redshift supernovae (Kim, Goobar, & Perlmutter 1996; Schmidt et al. 1998). Combining these corrections (usually ~ 0.1 to 0.2 mag) with zero points determined from the comparison stars brought these two data sets into good accord with the others, though the photometry has signficantly higher

uncertainty (typically ~ 0.1 mag).

In addition, we encountered a puzzle in the MDM R-band data, which was discrepantly bright (by ~ 0.1 mag) compared to data from four other telescopes at nearly the same epoch. However, in this case, the derived R color term was not very large. We were unable to procure the filter and detector characteristics for this data set. Thus we cannot provide an adequate explanation for this anomaly; it is possible that the filter transmission is mismatched just such that a color term derived from stellar observations (which were somewhat limited in color) would be small (e.g., high transmission at some wavelengths compensated by low transmission at others), while the supernova spectrum at the epoch of the observations led to a discrepant magnitude. Since four other telescopes provided mutually consistent observations at the same epoch, we have disregarded the MDM R data. We were fortunate to possess contemporaneous observations so that we could discover this discrepancy, and it illustrates the need for a careful investigation of filter and detector characteristics when combining observations of supernovae made at various sites (Suntzeff et al. 1999; Wells et al. 1994).

A futher complication in supernova photometry is proper discrimination between light from the supernova and light from the underlying galaxy (Boisseau & Wheeler 1991). Accurate subtraction of the galaxy background is essential to measure correct magnitudes, and even more important in measuring light curves, as a constant unremoved galaxy background will cause a supernova light curve to look more shallow (i.e., mimic a slower decline rate). Though SN 1998bu is projected on a spiral arm of M96, the background from the galaxy is relatively faint. We were fortunate to possess $UBVRI$ images of M96 prior to the appearance of SN 1998bu,

taken with the FLWO 1.2-m for another program. Our original plan was to use this image as a template and apply the galaxy subtraction techniques described by Schmidt et al. (1998; see also Filippenko et al. 1986). This was very successful in a few cases, but it turned out that the template image quality was much poorer (due to seeing and the pixel scale) than many of our observations, and degrading the supernova observations to match the template added undesirable correlated noise. In additional cases the observed fields did not align well with the template image (because there were very few stars in some of the small-field observations). Instead we estimated the galaxy background flux directly from the template image (using an aperture and sky annulus appropriate to each observation) and subtracted this flux from that of the supernova. The correction to the supernova magnitude was initially negligibly small and grew larger as the supernova faded, but the maximum correction made was only 0.025 mag. Our prediscovery images justify the assumption of a small host-galaxy flux contribution made by Suntzeff et al. (1999). Our final photometry for SN 1998bu is listed in Table 2.3 and the optical light curves are shown in Figure 2.2.

Table 2.3. *UBVRI* Photometry of SN 1998bu.

Julian Day	*U*	*B*	*V*	*R*	*I*	Telescope
2450944.68	···	···	12.45(0.14)	12.23(0.10)	11.95(0.15)	KAIT
2450947.63	···	12.47(0.11)	12.15(0.02)	11.86(0.04)	11.72(0.04)	Gett
2450948.59	···	···	12.08(0.02)	11.80(0.04)	11.68(0.04)	Well
2450948.65	···	12.41(0.09)	12.09(0.02)	11.80(0.04)	11.70(0.04)	Gett
2450949.67	···	···	11.99(0.03)	11.74(0.05)	11.67(0.06)	Gett
2450949.67	11.96(0.04)	12.29(0.02)	11.98(0.01)	11.72(0.03)	11.63(0.03)	CfA4
2450951.58	···	12.28(0.07)	11.90(0.02)	11.71(0.04)	11.68(0.04)	Well
2450951.63	···	···	11.93(0.03)	11.72(0.04)	11.67(0.04)	Gett
2450951.67	···	···	11.91(0.03)	11.80(0.09)	···	KAIT
2450951.68	···	12.21(0.02)	11.90(0.01)	11.68(0.03)	11.66(0.03)	CfA4
2450952.62	···	12.29(0.07)	11.87(0.02)	11.70(0.04)	11.70(0.04)	Well
2450952.64	···	···	11.88(0.02)	11.71(0.05)	11.74(0.05)	Gett
2450952.66	12.00(0.05)	12.21(0.02)	11.86(0.01)	11.66(0.03)	11.71(0.03)	CfA4
2450952.67	···	···	11.85(0.03)	11.75(0.09)	11.69(0.06)	KAIT
2450953.63	···	12.34(0.11)	···	···	···	Gett
2450953.70	12.03(0.05)	12.24(0.02)	11.87(0.01)	11.66(0.03)	11.73(0.03)	CfA4
2450955.64	12.14(0.05)	12.28(0.02)	11.86(0.01)	11.65(0.03)	11.79(0.03)	CfA4
2450955.66	···	12.26(0.11)	11.88(0.02)	11.66(0.04)	11.80(0.05)	Gett
2450955.68	···	···	11.85(0.03)	···	11.82(0.06)	KAIT
2450956.59	···	12.35(0.07)	11.90(0.02)	11.71(0.04)	11.83(0.04)	Well
2450956.64	12.23(0.04)	12.32(0.02)	11.87(0.01)	11.67(0.03)	11.80(0.03)	CfA4
2450956.68	···	···	11.89(0.03)	11.79(0.09)	11.84(0.06)	KAIT
2450957.63	12.31(0.05)	12.36(0.02)	11.92(0.01)	11.72(0.03)	11.87(0.03)	CfA4
2450957.65	···	12.34(0.11)	11.96(0.03)	11.75(0.05)	11.88(0.05)	Gett
2450959.68	12.48(0.04)	12.50(0.02)	12.01(0.01)	11.82(0.03)	11.98(0.03)	CfA1
2450960.57	···	12.57(0.07)	12.02(0.02)	11.91(0.04)	12.04(0.04)	Well
2450960.69	12.61(0.05)	12.56(0.02)	12.04(0.01)	11.89(0.03)	12.05(0.03)	CfA1
2450961.57	···	12.74(0.11)	12.12(0.03)	12.02(0.05)	···	Gett
2450961.60	···	12.64(0.07)	12.07(0.02)	11.99(0.04)	12.10(0.04)	Well
2450962.66	12.76(0.05)	12.70(0.02)	12.12(0.01)	12.05(0.03)	12.21(0.03)	CfA4
2450963.64	12.86(0.05)	12.81(0.03)	12.21(0.02)	12.15(0.03)	12.26(0.04)	CfA4
2450963.68	···	12.88(0.05)	12.26(0.02)	12.28(0.06)	12.30(0.04)	KAIT
2450964.63	13.01(0.05)	12.94(0.03)	12.28(0.01)	12.21(0.03)	12.30(0.03)	CfA4
2450964.68	···	12.97(0.05)	12.34(0.02)	···	12.32(0.04)	KAIT
2450965.64	13.14(0.05)	13.03(0.02)	12.35(0.01)	12.29(0.03)	12.31(0.03)	CfA4
2450965.67	···	13.05(0.03)	12.42(0.02)	···	12.33(0.04)	WIYN
2450966.60	···	13.10(0.07)	12.42(0.02)	12.35(0.04)	12.29(0.04)	Well
2450967.65	13.45(0.05)	13.24(0.02)	12.48(0.01)	···	···	CfA4
2450967.66	13.35(0.05)	13.24(0.02)	12.50(0.01)	···	12.35(0.03)	MDM

Table 2.3—Continued

Julian Day	U	B	V	R	I	Telescope
2450968.67	13.53(0.04)	13.40(0.02)	12.59(0.01)	12.46(0.03)	12.33(0.03)	KP09
2450968.68	13.50(0.04)	13.36(0.02)	12.55(0.01)	···	12.33(0.03)	MDM
2450968.72	13.60(0.05)	13.43(0.03)	12.62(0.02)	12.48(0.03)	12.31(0.03)	WIYN
2450969.59	···	13.51(0.11)	12.62(0.02)	12.43(0.05)	12.26(0.04)	Gett
2450969.60	···	13.40(0.07)	12.61(0.02)	12.43(0.04)	12.25(0.04)	Well
2450969.65	13.68(0.04)	13.51(0.02)	12.64(0.01)	12.47(0.03)	12.31(0.03)	KP09
2450969.67	13.75(0.05)	13.52(0.03)	12.66(0.02)	12.50(0.03)	12.30(0.03)	WIYN
2450969.69	···	13.53(0.05)	12.66(0.02)	12.50(0.06)	12.32(0.06)	KAIT
2450969.69	13.66(0.04)	13.47(0.02)	12.59(0.01)	···	12.28(0.03)	MDM
2450970.69	13.82(0.05)	13.59(0.02)	12.64(0.01)	···	12.25(0.03)	MDM
2450971.71	13.97(0.05)	13.72(0.02)	12.69(0.01)	···	12.23(0.03)	MDM
2450972.65	14.12(0.04)	13.84(0.02)	12.74(0.01)	···	12.20(0.03)	MDM
2450972.68	14.16(0.04)	13.89(0.02)	12.80(0.01)	12.52(0.03)	12.22(0.03)	WIYN
2450973.58	···	13.95(0.11)	12.80(0.02)	12.45(0.05)	12.16(0.04)	Gett
2450973.68	···	14.01(0.05)	···	12.54(0.06)	12.22(0.04)	KAIT
2450974.67	14.45(0.05)	14.11(0.03)	12.87(0.02)	12.51(0.04)	12.19(0.04)	WIYN
2450978.69	···	14.51(0.06)	13.09(0.02)	12.61(0.06)	12.12(0.05)	KAIT
2450979.70	···	14.60(0.06)	13.14(0.03)	12.64(0.06)	12.14(0.05)	KAIT
2450980.65	15.15(0.04)	14.68(0.02)	13.16(0.01)	12.61(0.03)	12.08(0.03)	CfA4
2450981.66	15.22(0.04)	14.74(0.02)	13.25(0.01)	12.69(0.03)	12.12(0.03)	CfA4
2450981.69	···	14.74(0.06)	13.24(0.03)	12.71(0.07)	12.14(0.05)	KAIT
2450982.60	···	···	13.30(0.03)	12.79(0.06)	12.13(0.05)	Gett
2450982.65	15.29(0.05)	14.81(0.02)	13.30(0.02)	12.75(0.03)	12.16(0.03)	CfA4
2450982.70	···	14.84(0.06)	13.36(0.02)	12.83(0.06)	12.24(0.04)	KAIT
2450983.66	15.31(0.05)	14.89(0.02)	13.38(0.01)	12.83(0.03)	12.24(0.03)	CfA4
2450984.67	15.39(0.04)	14.94(0.02)	13.45(0.01)	12.92(0.03)	12.33(0.03)	CfA4
2450984.70	···	14.95(0.05)	13.51(0.02)	13.00(0.06)	···	KAIT
2450985.65	···	15.00(0.02)	13.53(0.01)	13.03(0.04)	12.42(0.03)	CfA4
2450986.66	15.48(0.05)	15.05(0.02)	13.56(0.01)	13.08(0.03)	12.47(0.03)	CfA4
2450986.69	···	15.09(0.05)	···	13.13(0.06)	···	KAIT
2450987.66	15.50(0.04)	15.09(0.02)	13.63(0.01)	13.12(0.03)	12.55(0.03)	CfA4
2450988.66	15.53(0.04)	15.12(0.02)	13.67(0.01)	13.18(0.03)	12.63(0.03)	CfA4
2450989.65	15.58(0.04)	15.18(0.02)	13.72(0.01)	13.24(0.03)	12.68(0.03)	CfA4
2450990.65	15.61(0.05)	15.21(0.02)	13.77(0.01)	13.28(0.03)	12.75(0.03)	CfA4
2450990.69	···	15.22(0.05)	13.82(0.02)	13.34(0.06)	12.80(0.05)	KAIT
2450991.65	15.62(0.05)	15.22(0.02)	13.82(0.01)	13.31(0.03)	12.81(0.03)	CfA4
2450992.64	15.64(0.04)	15.24(0.02)	13.84(0.01)	13.38(0.03)	12.86(0.03)	CfA4
2450993.64	15.62(0.06)	15.26(0.03)	13.88(0.02)	13.42(0.03)	12.91(0.03)	CfA4
2450994.64	15.69(0.05)	15.29(0.02)	13.92(0.01)	···	12.97(0.03)	CfA4

Table 2.3—Continued

Julian Day	U	B	V	R	I	Telescope
2450995.64	15.69(0.04)	15.31(0.02)	13.96(0.01)	13.49(0.03)	13.04(0.03)	CfA4
2450996.64	···	···	13.97(0.01)	···	13.09(0.03)	CfA4

Note. — The telescope designations are as in Table 2.2.

2.2.3 Infrared Photometry

Infrared photometry of SN 1998bu in the JHK passbands was obtained at the Fred L. Whipple Observatory (FLWO), the Mount Stromlo Observatory (MSO), the Infrared Telescope Facility (IRTF), and with the ESO New Technology Telescope (NTT). The FLWO data were obtained with the 1.2-m telescope and "STELIRCam" IR camera which consists of two 256^2 InSb detector arrays permitting simultaneous imaging in two filters (Tollestrup et al. 1999). The FLWO filters were manufactured by Barr Associates in 1987 for a number of institutions including NOAO. The MSO data was taken with the 2.3-m telescope and CASPIR Spectrograph/Imager which uses a 256^2 InSb detector. The IRTF data was obtained with the NASA 3-m telescope and NSFCAM IR camera which uses a 256^2 InSb detector. The NTT is a 3.5-m aperture telescope and observations were made using the SOFI imaging spectrograph which employs a 1024^2 HgCdTe array.

Flat fields and sky frames were created using offset field images staggered between the supernova exposures. The alternating offset field frames were subtracted from the corresponding data images and then divided by the normalized, average

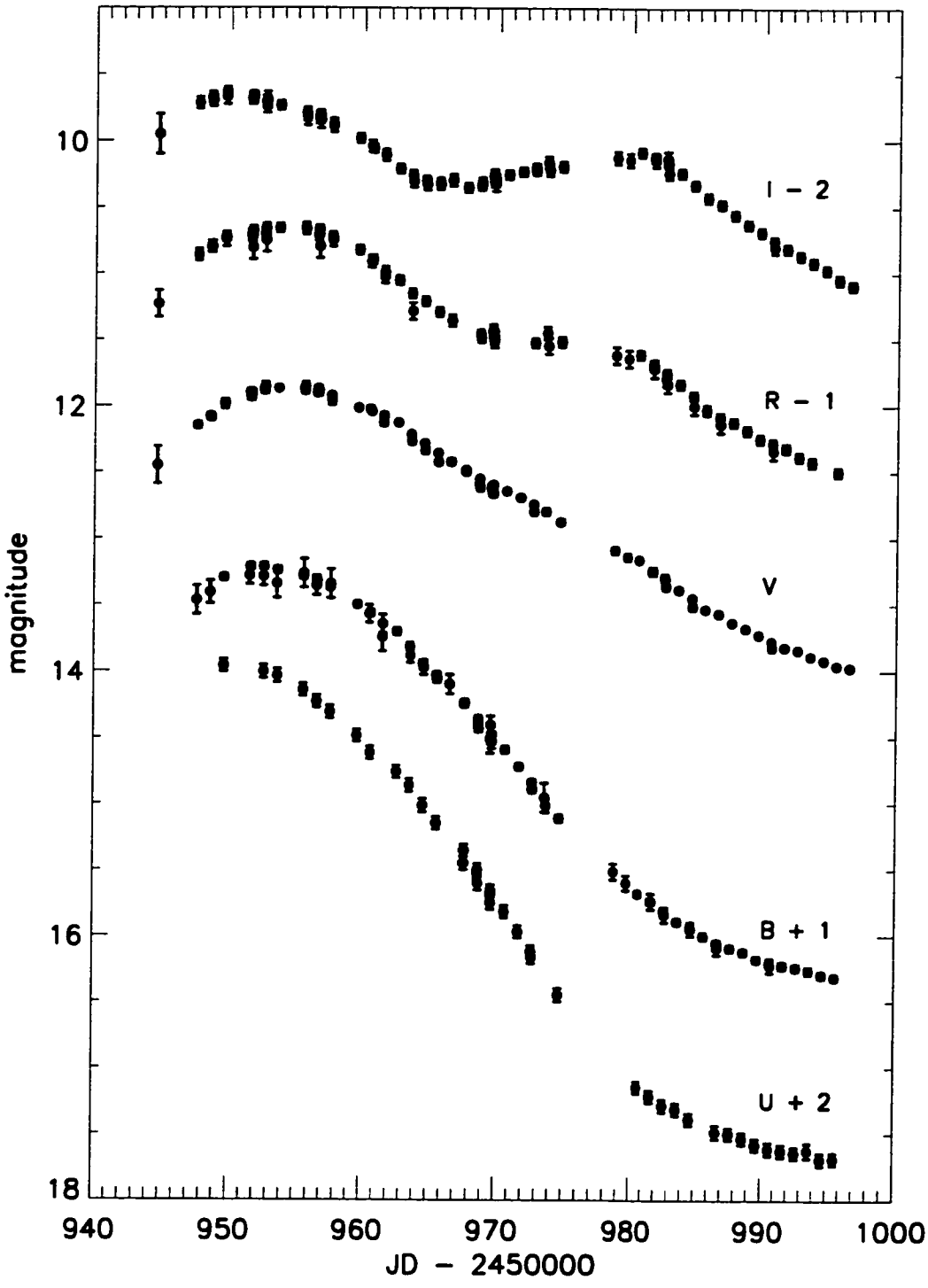

Figure 2.2.— *UBVRI* light curves of SN 1998bu.

flat field. Standard stars for the FLWO observations were taken from Elias et al. (1982), while the NTT used standards from Persson et al. (1998), and the IRTF used the UKIRT faint standards (Hunt et al. 1998). The MSO data was calibrated with standards from Carter & Meadows (1995). Where possible, the results were transformed to the Elias system, but the variety of detectors, filters and standards introduces systematic errors on the order of 0.05 mag. Two stars (stars 1 and 6) near the supernova were calibrated from the FLWO data and used as secondary standards on non-photometric nights; their magnitudes are listed in Table 2.1. The galaxy background at the position of the supernova is smooth and much fainter than the supernova light, so that aperture photometry was sufficient. The resulting supernova photometry is given in Table 2.4 and displayed in Figure 2.3.

Table 2.4. JHK Photometry of SN 1998bu.

Julian Day	J	H	K	Telescope
2450945.6	11.76(0.06)	11.88(0.06)	11.81(0.05)	FLWO
2450948.6	11.59(0.06)	11.77(0.06)	11.59(0.05)	FLWO
2450951.88	11.66(0.04)	11.84(0.04)	11.60(0.03)	IRTF
2450970.7	13.32(0.06)	11.94(0.05)	11.95(0.05)	FLWO
2450974.91	13.23(0.06)	11.68(0.06)	11.89(0.05)	MSO
2450975.97	13.12(0.04)	11.79(0.03)	11.77(0.03)	ESO
2450976.88	13.08(0.06)	11.65(0.06)	11.77(0.05)	MSO
2450978.65	12.81(0.06)	11.73(0.06)	11.74(0.05)	FLWO
2450978.87	...	11.67(0.10)	11.77(0.10)	MSO
2450984.76	12.68(0.05)	12.00(0.03)	12.05(0.04)	IRTF

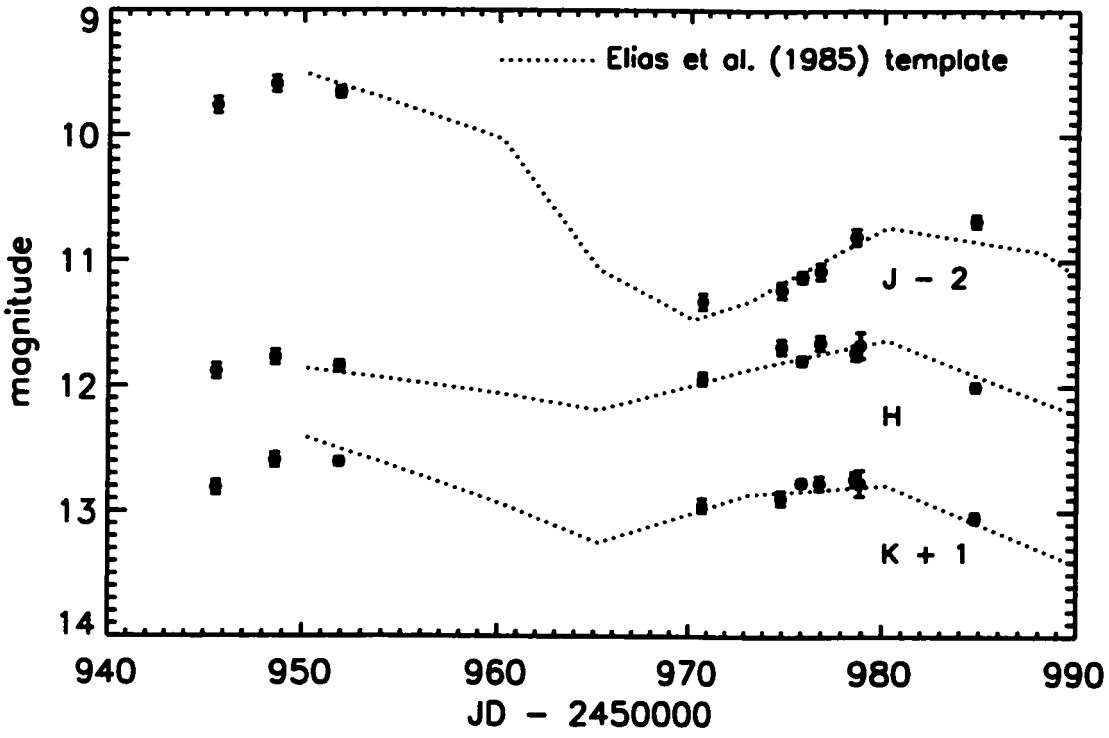

Figure 2.3.— JHK light curves of SN 1998bu.

2.2.4 Optical Spectroscopy

All of our optical spectroscopic observations were obtained at the FLWO 1.5-m telescope with the FAST spectrograph. This long-slit spectrograph has been designed for high throughput and features a thinned, back-side illuminated, anti-reflection coated CCD detector. The slit length is 180″ and can be adjusted to several widths; we have generally employed a 3″ slit for our observations. These were made using a 300 line/mm grating which results in a resolution of roughly 0.6 nm and a usable wavelength range from 360 to 720 nm. We began observations of SN 1998bu on May 16.1 and continued through July 15.1, on a total of 27 nights.

We have reduced the spectra in the standard manner with IRAF. The two-dimensional CCD exposures were corrected for bias and dark-current and were flat-fielded using CCDPROC. A 1D spectrum was extracted at the supernova position subtracting the neigboring sky using the APEXTRACT task. Wavelength calibration was performed by extracting the same aperture from an exposure of a HeNeAr lamp taken just after the supernova observation and identifying emission lines. We also performed flux calibration through the reduction of a spectrophotometric standard star each night (Massey et al. 1988). The conditions for the supernova observations were usually not photometric, so the absolute flux calibration is generally unreliable. The relative flux measurement may also suffer because of differential refraction (Filippenko 1982), as the slit was always oriented east-west (PA = 90°) rather than being optimally oriented at the parallactic angle. In general, then, our spectra likely underestimate the flux in the blue by 10 to 20%. In addition, since we have not used a blocking filter, second-order light

contaminates the red end of the spectra. The supernova flux in the blue is generally lower than in the red and the detector sensitivity to the blue photons is also low, so that the second-order contamination is on the order of only a few percent. Second order contamination in the standard star spectra is more significant (since the standard stars are typically quite blue), so that the flux calibration in the red is also somewhat uncertain. Uncertainties in the flux calibration in both the blue and the red thus make these spectra unsuitable for spectrophotometry. Contamination of the supernova spectra by underlying galaxy light (after subtracting the local sky) was small, as in the case of the optical photometry. In some cases, multiple observations on the same night were combined into one. Cosmic rays and telluric lines were removed by hand. Figure 2.4 shows a representative subset of our optical spectroscopy of SN 1998bu and the spectral evolution of the supernova covering 60 days, from approximately 3 days before maximum light in the B band. The complete spectroscopic data set is available upon request.

2.2.5 Infrared Spectroscopy

Infrared spectra of SN 1998bu were obtained with the KPNO 4-m telescope and OSU-NOAO Infrared Imager (ONIS) on 1998 June 14.2 UT. The ONIS covered the K-band range from 2.0 μm to 2.4 μm with a resolution of 1.6 nm (FWHM). A sequence of two-minute exposures was made, while stepping the target along the slit. These were combined for a total integration of 24 minutes. A spectrum of the F5V star BS 4281 was divided into the supernova spectrum to remove telluric absorption (except in the deep absorption bands at 1.4 and 1.9 μm). A smooth spectrum of

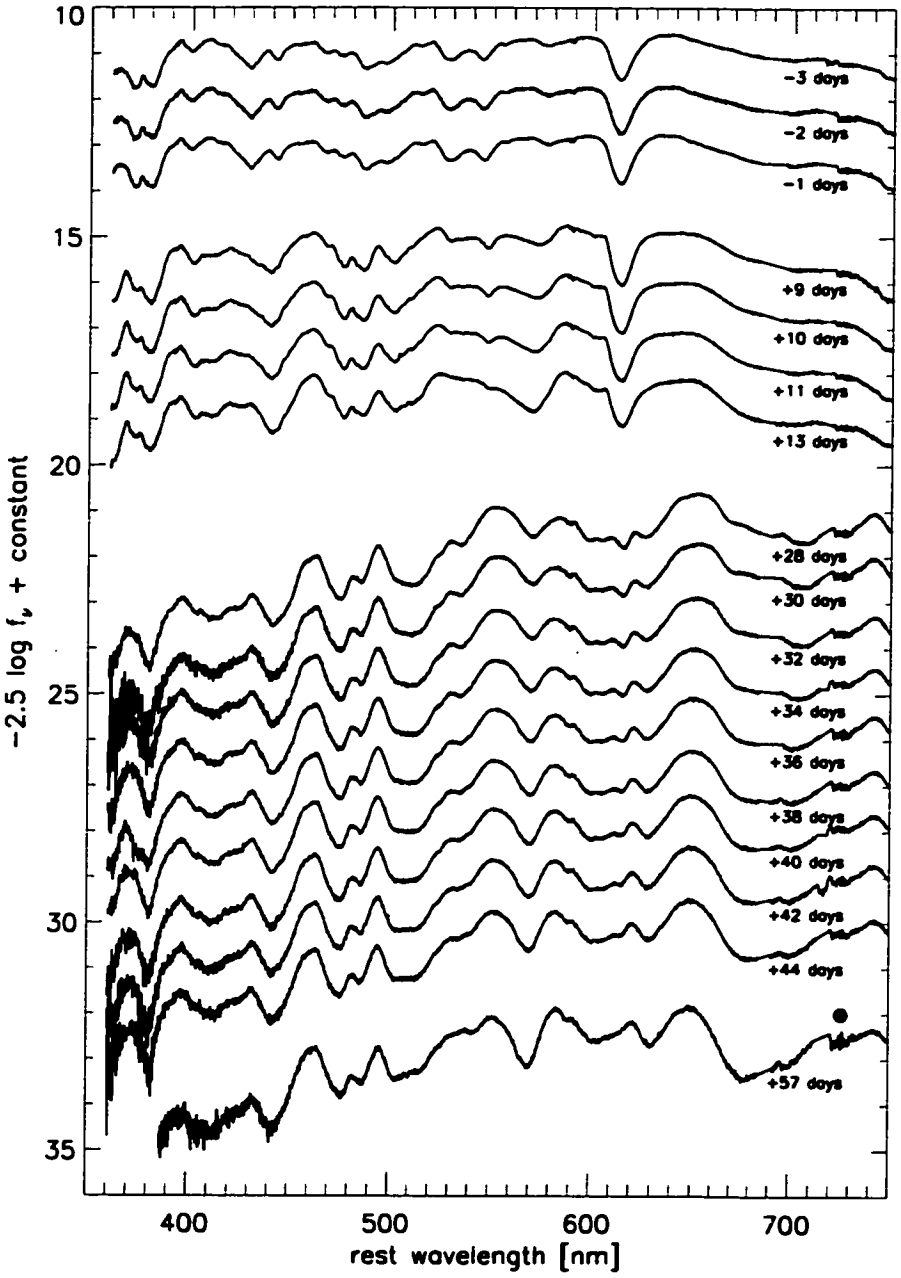

Figure 2.4.— Optical spectra of SN 1998bu labelled by epoch with respect to B maximum. For clarity the spectra have been shifted vertically by arbitrary amounts. Unremoved telluric features are marked.

an F5V star was created by interpolating the broad band colors (Johnson et al. 1968), with the zero point set by the catalog magnitude of BS 4281. Multiplying the supernova spectrum and the synthetic F5V star spectrum corrects for the detector sensitivity variations and roughly calibrates supernova flux. The spectral flux was then adjusted to match the observed K-band photometric magnitude of the supernova interpolated to the date of the spectrum.

A spectrum was also taken with the SOFI instrument on the ESO NTT on 1998 June 11.0 UT. SOFI covered 0.95 μm to 2.5 μm in two grating settings with significant overlap. Four 120-s exposures were obtained at each tilt at four slit positions allowing good sky subtraction. Spectra of HD177619 (an F7V star) were used to remove telluric bands and calibrate the relative sensitivity of the detector as described above. Absolute flux calibration was done using the H-band magnitude determined from SOFI imaging done on the same night.

The KPNO and ESO spectra were combined into a single high-quality spectrum of SN 1998bu at an age of about +25 days which is shown in Figure 2.5. There are few good infrared spectra of SNe Ia at the same epoch to compare with these data; however, a spectrum of SN 1995D taken with the MMT+FSPEC at an age of +24 days is also shown for comparison.

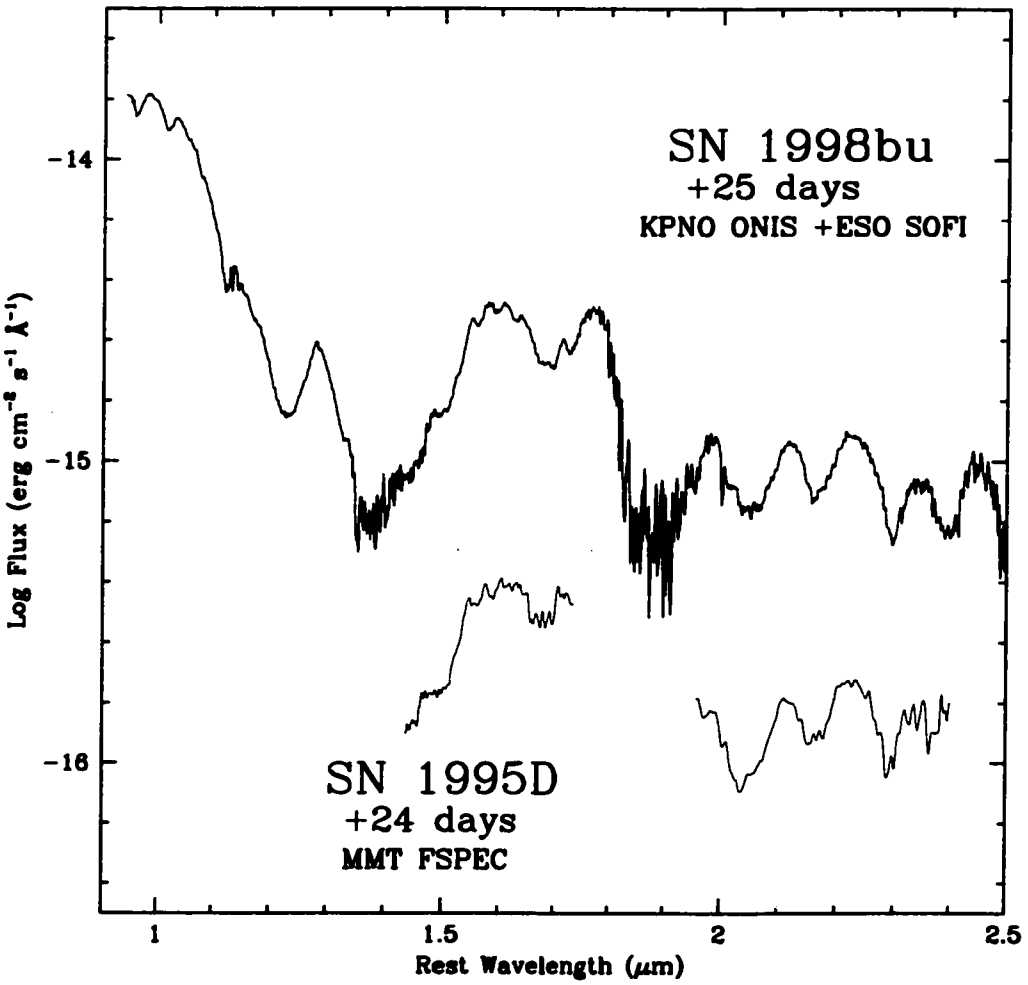

Figure 2.5.— Composite near-infrared spectrum of SN 1998bu at approximately 25 days past maximum light. A spectrum of the type Ia SN 1995D at roughly the same epoch is shown for comparison.

2.3 Results

2.3.1 Spectra

Type I supernovae are distinguished from those of type II by the absence of hydrogen in their spectra, and SNe Ia are further distinguished from SNe Ib and SNe Ic by the prominent Si II (λ635.5 nm) absorption at maximum light (for examples and a detailed discussion see Filippenko 1997). Other absorption features in the optical at maximum light are predominantly from intermediate mass elements (Si, Ca, S, O, Mg) at high velocity ($\sim 10,000$ km s^{-1}) in the outer layers of the supernova ejecta. Lines of Fe become prominent at about two weeks after maximum light as the effective photosphere recedes into the ejecta, and about a month after maximum light the supernova enters the optically-thin nebular phase where forbidden emission lines of iron-peak elements (Fe, Co) dominate (Kirshner & Oke 1975). The optical spectra of SN 1998bu shown in Figure 2.4 follow this typical evolution. A more detailed comparison is illustrated in Figure 2.6 where we show the optical spectra of SN 1998bu and other prototypical SNe Ia near maximum light. The spectra are remarkably similar, though there are some differences in the detailed shapes and velocities of the features.

A more quantitative comparison between SN 1998bu and other typical SNe Ia is illustrated in Figure 2.7. We show the velocities of Si II λ635.5 nm and Ca II H & K flux minima as a function of supernova phase for a number of prototypical SNe Ia: SN 1994D (Patat et al. 1996), SN 1992A (Kirshner et al. 1993), SN 1990N (Leibundgut et al. 1991a), SN 1989B (Barbon et al. 1990; Wells et al. 1994), and

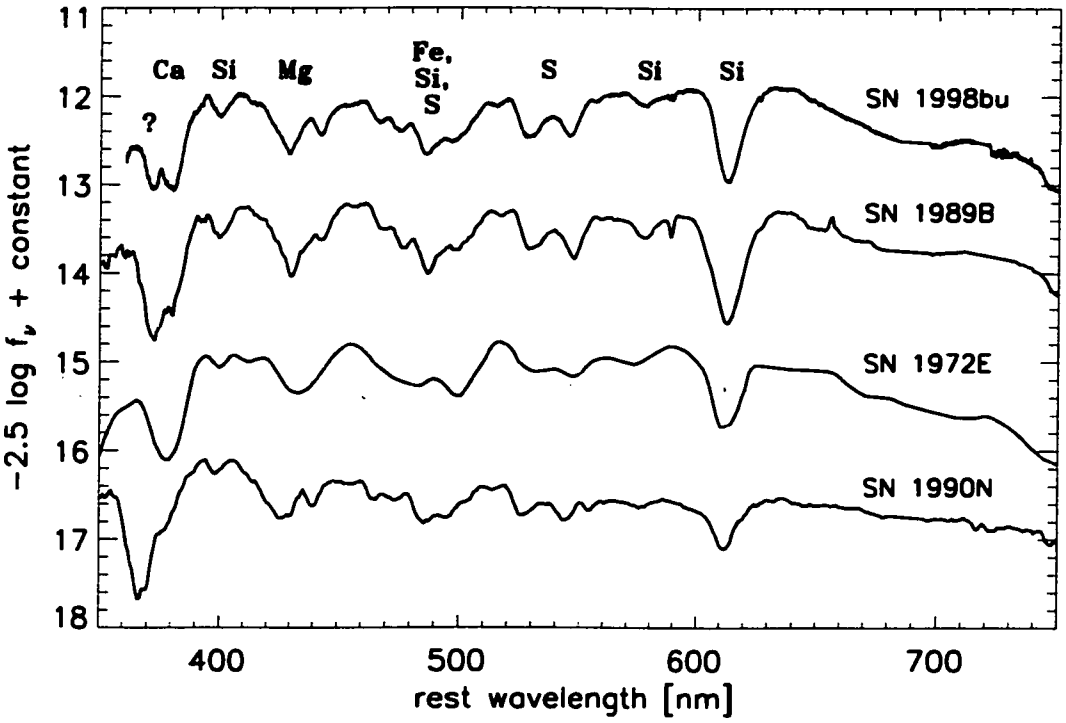

Figure 2.6.— Optical spectra near maximum light for SN 1998bu and prototypical SNe Ia: SN 1989B (Wells et al. 1994), SN 1972E (Kirshner et al. 1973; observed at significantly lower resolution than the others), and SN 1990N (Leibundgut et al. 1991a). The spectra show remarkable homogeneity and place SN 1998bu squarely among the typical SNe Ia.

SN 1981B (Branch et al. 1983). SN 1998bu falls well within the scatter defined by these other objects.

However, the measurement of Ca II H & K velocities is made more challenging by the presence of a feature blueward of the Ca feature (indicated in Figure 2.6 by a question mark), which may be due to either Si or possibly high-velocity Ca (Branch 1998, personal communication; Hatano et al. 1999). For SN 1998bu this unidentified feature was well separated from the normal Ca feature, as is seen in the early spectra of the sequence in Figure 2.4. The feature weakens with time such that by day +28 only the normal Ca feature remains. The sequence suggests that the Ca absorption velocity should be defined by the redder of the two troughs. For other SNe Ia, Figure 2.6 shows that the unidentified feature and the Ca feature are not always well separated, such as in the SN 1989B and SN 1990N spectra, where only a shoulder is visible rather than two distinct minima. The spectrum of SN 1972E was taken at significantly lower resolution, and there it looks like a single absorption feature. Thus comparing measured Ca II H & K velocities is tricky; our use of the red trough may lead to a systematically lower velocity measured at early times, as seems to be the case in Figure 2.7.

Supernovae with unusual luminosity also have unusual spectra. Both SN 1991T, one of the most luminous SNe Ia known, and SN 1991bg, one of the least luminous, showed spectral peculiarities in their maximum light spectra. SN 1991T lacked a well-defined Si II λ635.5 nm feature at maximum (Filippenko et al. 1992a; Phillips et al. 1992), though its subsequent evolution was similar to other SNe Ia. On the other hand, maximum light spectra of SN 1991bg showed a deep absorption trough attributed to Ti II centered at a wavelength of 420 nm (Filippenko et al. 1992b;

Leibundgut et al. 1993). The absence of spectroscopic peculiarities in SN 1998bu makes it a suitable calibrator of the SN Ia distance scale.

The infrared spectrum of SN 1998bu in Figure 2.5 is one of the best obtained for a type Ia supernova. It is strikingly similar to an IR spectrum of SN 1995D taken at the same phase. SN 1995D also showed no spectroscopic peculiarities in the optical and a typical light curve (Riess et al. 1999), bolstering the evidence that SN 1998bu is a fairly normal SN Ia. The IR spectra are qualitatively a good match to the model spectra of Wheeler et al. (1998), although the models do not extend to the observed age of SN 1998bu and are meant to fit the peculiar event SN 1986G. In the K-band (~ 2.2 μm), which consists of absorption features of Co, Ni, and Si, the spectra of SNe Ia 1998bu, 1995D and 1986G (Wheeler et al. 1998; Frogel et al. 1987) are nearly identical from 14 days past maximum onwards. The H-band (~ 1.6 μm) spectra of SN 1998bu and SN 1995D do not show as large a gap between the peaks at 1.6 μm and 1.8 μm as does SN 1986G. The deficit at 1.7 μm is not visible at all in the peculiar SN 1991T (Bowers et al. 1997), but that spectrum was taken at a more advanced age than the others. These observations suggest that the 1.7 μm gap depth may possibly be correlated with light curve decline rate (and therefore luminosity) and supports the idea of Wheeler et al. (1998) that the 1.7 μm gap is an indicator of the highest velocity of the Ni/Co region, though clearly more infrared spectra of SNe Ia are required to test this hypothesis. As in the optical spectra, the infrared spectra do not indicate that SN 1998bu was peculiar.

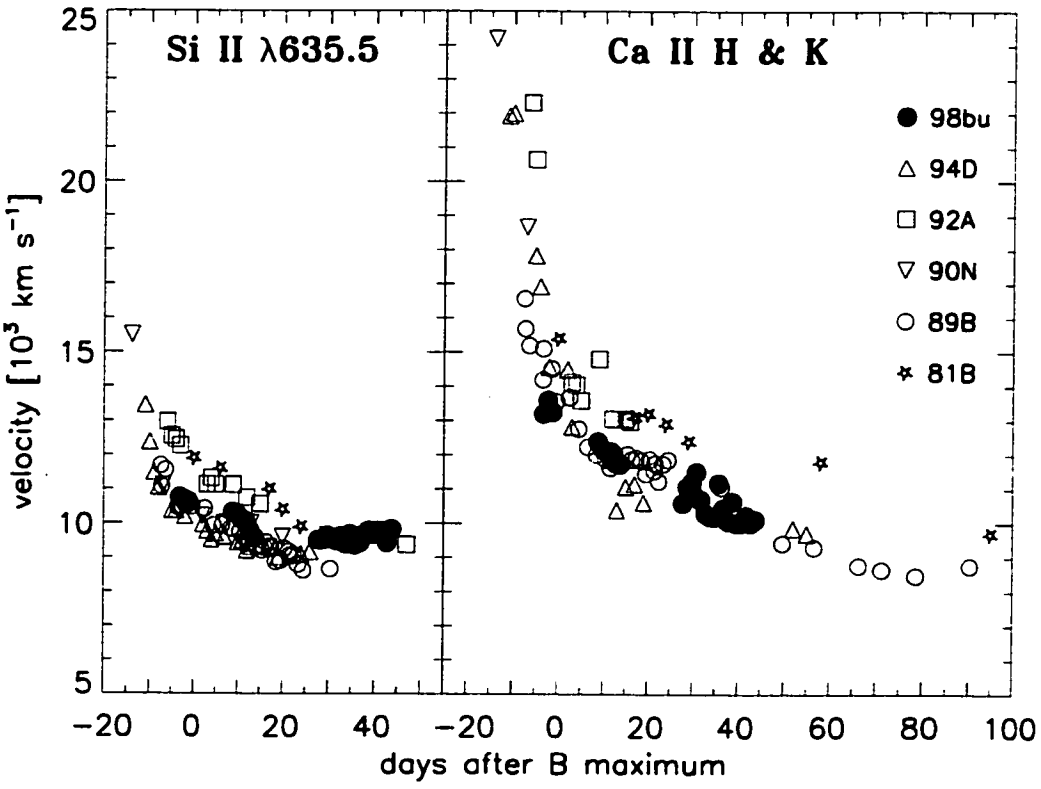

Figure 2.7.— Expansion velocities derived from the absorption minima of Si II λ635.5 nm and Ca II H & K for SN 1998bu (*filled circles*), SN 1994D (*triangles*), SN 1992A (*squares*), SN 1990N (*upside-down triangles*), SN 1989B (*open circles*), and SN 1981B (*stars*). The expansion velocities have been corrected for the recession velocity of the host galaxy. See text for references.

2.3.2 Light Curves and Peak Brightness

The optical light curves of SN 1998bu presented in Figure 2.2 are among the best sampled early-time light curves of any SN Ia. The U band observations are particularly valuable as SNe Ia have not often been observed in this passband. In addition, our observations began before maximum light (unless stated otherwise, we take maximum light to mean the time of maximum brightness in the B band). These light curves are typical of SNe Ia; the UBV curves are well fit by the templates of Leibundgut (1989). In section 2.3.3 we describe the detailed analysis of these light curve shapes, an essential part of using this SN Ia as a distance indicator.

Work on SNe Ia as standard or calibrated candles employs the maximum brightness in the B and V bands. We have determined the peak apparent magnitude and time of maximum in the B-band for SN 1998bu using a simple quadratic fit to the points within roughly five days of the light curve peak, weighted by their photometric uncertainties. The results are

$$\mathrm{JD}_{\mathrm{Bmax}} = 2450952.8 \pm 0.8, \tag{2.1}$$

$$B_{\mathrm{Bmax}} = 12.22 \pm 0.03. \tag{2.2}$$

(Throughout the paper, all apparent and absolute magnitudes are expressed in units of mag). The supernova apparent magnitude in V *at the time of* B *maximum given above* is

$$V_{\mathrm{Bmax}} = 11.88 \pm 0.02. \tag{2.3}$$

The time when the supernova was brightest in the V band was JD 2450954.4$\pm$1.0, at $V = 11.86 \pm 0.02$. These results are quite consistent with the finding of Leibundgut

(1989) that maximum light in V occurs about two days after maximum light in B and his result that the V magnitude at that time is 0.02 mag brighter than the V magnitude at the time of B maximum. The time of maximum brightness in the U band is not well determined because of the starting point of our data set, but our data are consistent with the Leibundgut (1989) result of U maximum occurring three days before maximum light in B. The U apparent magnitude at B maximum is $U_{\mathrm{Bmax}} = 12.01 \pm 0.05$. SNe Ia show increased variety in their R and I light curves as compared to the bluer passbands, illustrated clearly in the composite light curves presented by Riess et al. (1999). The R and I light curves of SN 1998bu are consistent with these composite curves both in their general shape and times of maximum in those bands.

In comparing our photometry with the independent data set of Suntzeff et al. (1999), we find excellent agreement. The times of maxima in the various passbands are quite consistent given the stated uncertainties, as are the light curves in general. In Figure 2.8, we compare the photometry directly by plotting the difference between our magnitudes and those of Suntzeff et al. (1999). To make this comparison we have spline-interpolated the Suntzeff et al. (1999) light curves to the times of our observations, and have only computed differences when observations were within two days of each other to ensure the accuracy of the interpolation. The uncertainty in the magnitude difference was taken as the quadrature sum of the stated photometric uncertainties. As in the case of the photometry itself, the difference uncertainties are significantly correlated (due to the uncertainty in the comparison stars, for instance). The largest differences occur, as expected, in the U-band, and in general the agreement between the two data sets is best near maximum light. Given

the difficulties particular to supernova photometry, the consistency in the light curves is reassuring. Because small systematic differences in photometry can have a magnified effect in distance determination (through the reddening, for example), proper accounting of the (correlated) photometric errors is vital in order to obtain consistent results.

One important result from the photometry is that the observed color of the supernova at maximum, $(B-V)_{\rm Bmax} = 0.34 \pm 0.04$ mag, is significantly redder than typical SNe Ia, which have $(B-V)_{\rm Bmax} \simeq 0.00 \pm 0.04$ mag (Schaefer 1995). Very underluminous supernovae such as SN 1991bg can have quite red intrinsic colors at maximum, but they also show distinct spectroscopic peculiarities. The absence of any such peculiarities in SN 1998bu suggests that this red color is not intrinsic to the supernova but rather a result of interstellar extinction along the line of sight. Supporting evidence for this extinction is presented in Section 2.3.3.

The optical color curves of SN 1998bu are also quite typical, as shown in Figure 2.9, where we present the color evolution of SN 1998bu compared to SN 1989B, also a spectroscopically normal SN Ia (Wells et al. 1994). Both of these supernovae had a similar $B-V$ color index at maximum light and the general shape of the color evolution of these two supernovae are in reasonable agreement. The slope of the $B-V$ rise is measurably different, resulting from the fact that SN 1989B was a faster-declining object. The other striking difference is the offset of the $U-B$ curves for the two supernovae. This could be a result of photometric uncertainties in calibrating the U band, where detector sensitivities and filter transmissions can differ substantially from one site to another and require careful calibration (see the discussion by Suntzeff et al. 1999). However, it may also point

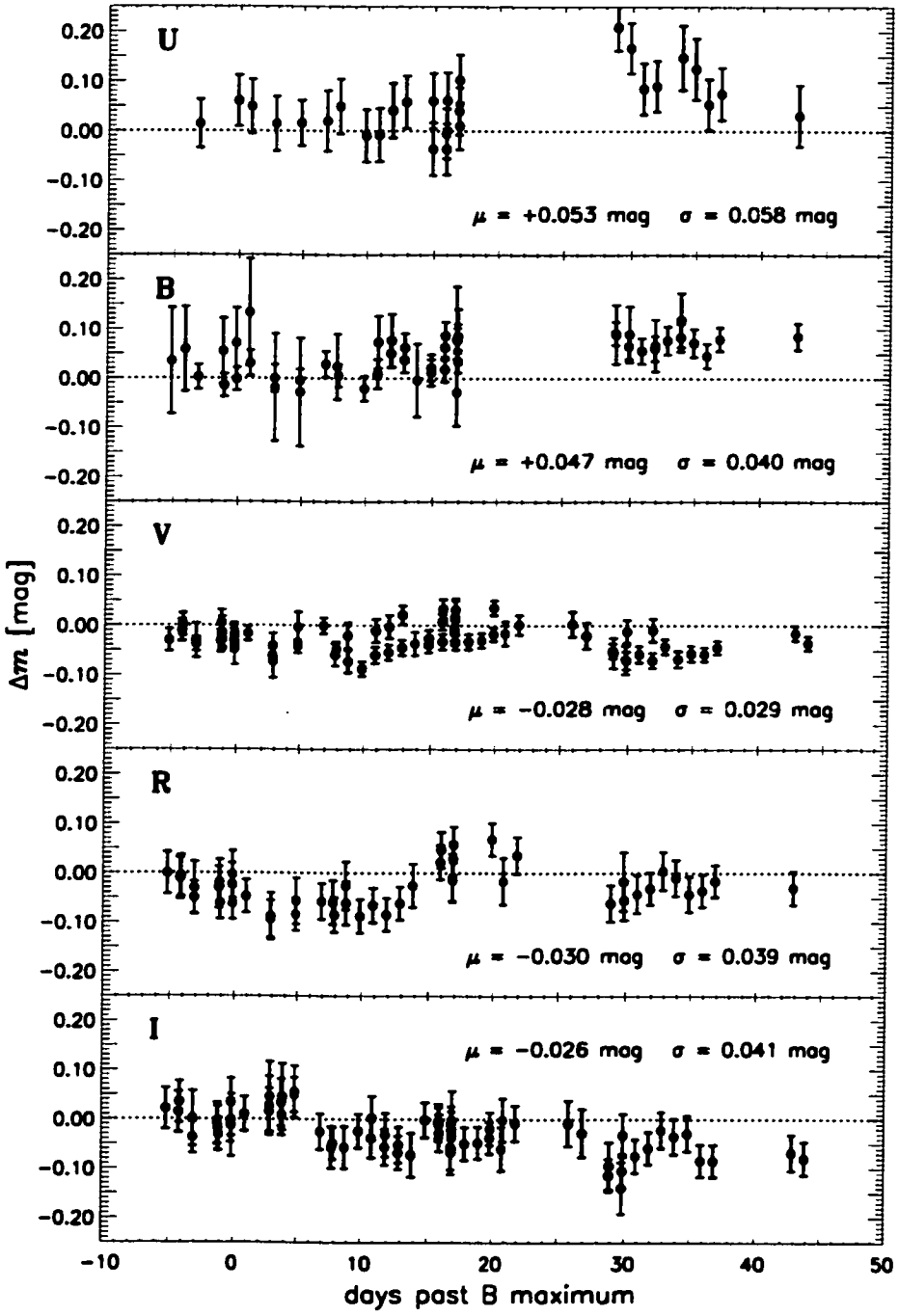

Figure 2.8.— Comparison of optical photometry with that of Suntzeff et al. (1999). Magnitude differences (this paper - Suntzeff et al.) in $UBVRI$ are plotted. The mean difference, μ, and the dispersion, σ, are also listed for each passband.

to interesting diversity in the U-band characteristics of SNe Ia, or diversity in the selective-to-total extinction properties of dust. A more detailed investigation of SNe Ia light curves in the near ultraviolet is warranted. This may be particularly important for observations of SNe Ia at high redshift where observations at optical wavelengths probe the rest-frame ultraviolet. Without a thorough understanding of SNe Ia U-band properties, cosmological inferences based on rest-frame U-band light curves are suspect.

In the infrared, the light curves of SN 1998bu match the JHK templates developed by Elias et al. (1985), as shown in Figure 2.3, where we have fit the templates to the data by adjusting them independently in magnitude and together in time. The bright second maximum typical of SNe Ia in the infrared passbands shown in the templates is clearly observed in SN 1998bu, as is the J-band deficit. The best-fit magnitude offsets to the templates are as follows: $J = 12.14 \pm 0.09$, $H = 11.99 \pm 0.05$, and $K = 12.04 \pm 0.05$. We find that the fiducial time t_0 as defined by Elias et al. (1985) is about 3 days before maximum light in B. This differs slightly from the Elias et al. result, which suggested t_0 was roughly 5 days before maximum light; however, only three supernovae were used in that determination, so it would not be surprising if there were some variance. A larger sample of infrared light curves, especially with observations near the first maximum, would be useful. We note that Meikle & Hernandez (2000) show a large amount of infrared photometry of SN 1998bu near optical maximum; combining these data with our light curve (which is dominated by later points) should yield one of the best infrared light curves of a type Ia supernova.

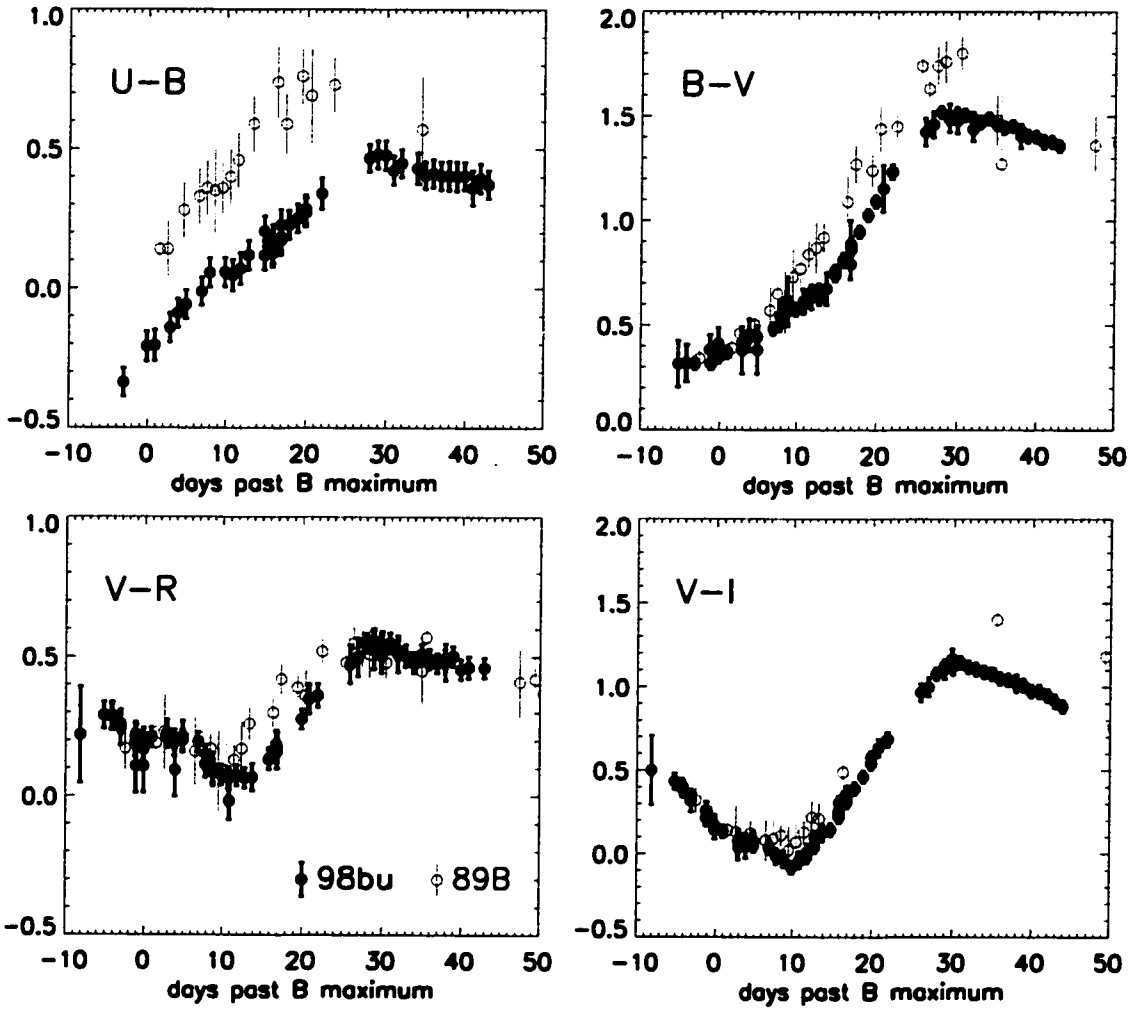

Figure 2.9.— Color curves for SN 1998bu (*filled circles*) compared with those of the reddened SN 1989B (*open circles*, Wells et al. 1994).

2.3.3 Multicolor Light Curve Shape Analysis

The relation between luminosity and light curve shapes for SNe Ia, as quantified by Phillips (1993), and subsequently Hamuy et al. (1996a), led to the development of techniques to measure distances to SNe Ia from multicolor light curves. Hamuy et al. (1996b) showed how BVI light curves and templates (Hamuy et al. 1996d) could be combined to derive accurate distances using a χ^2 analysis. In a similar vein, Riess, Press, & Kirshner (1996a) developed the Multicolor Light Curve Shape (MLCS) method, a statistical technique to measure distances to SNe Ia from their $BVRI$ light curves, allowing for reddening in the host galaxy. In this approach, the light curves of a "training set" of supernovae with estimated luminosities and extinctions are used to derive template light curves for a fiducial SN Ia, along with derived correction templates which detail the change in the light curve shapes as a function of luminosity and extinction. We focus on MLCS distances to SNe Ia in this paper; Phillips et al. (1999) present an extension to their template-fitting technique which also incorporates reddening, and the results of applying this method to SN 1998bu are reported by Suntzeff et al. (1999).

The orginal MLCS training set was based on nearby SNe Ia and relative distances measured to their host galaxies via the Tully-Fisher (TF), the surface brightness fluctuation (SBF), or the planetary nebula luminosity function (PNLF) methods. The only requirement was that these methods give accurate *relative* distances to the galaxies. Once trained, the method can be used on the light curves of a SN Ia, to determine the luminosity difference, Δ, between that supernova and the fiducial ($\Delta = 0$) supernova as well as a derived extinction to the supernova.

Application of MLCS to a sample of more distant supernovae indicated the effectiveness of this procedure. The dispersion in SN Ia distances about the Hubble line was reduced from $\sigma \simeq 0.4$ mag in the standard candle assumption to $\sigma \simeq 0.12$ mag with MLCS. The technique also demonstrated the Hubble law was applicable to large distances corresponding to velocities $cz \simeq 30,000$ km s^{-1}, as was also shown by Hamuy et al. (1996b).

However, uncertainties in these secondary distance determinations, inherent difficulties in estimating the extinction to some supernovae, and the small number of training set objects caused some problems in the derived MLCS SN Ia distance scale, as pointed out by Saha et al. (1997). To combat the major problems, Riess et al. (1998a) presented a new version of MLCS in which the relative distances for the training set objects were derived from their host galaxy recession velocities and the Hubble law for galaxies with redshifts $cz \geq 2500$ km s^{-1}. In addition, estimates of the extinction to the training set supernovae were refined, and effects of extinction on the *shape* of the light curve based on temporal variations in the effective selective-to-total extinction ratios from the evolving supernova spectrum (Nugent, Kim, & Perlmutter 2002) were also included. The procedure detailed in Riess et al. (1998a) was restricted to B and V light curves up to 40 days past maximum, to be applied to the high-redshift supernovae that are the focus of that paper, but a procedurally identical version (with one exception) using full $BVRI$ light curves is used in this paper. Here we have used a "wide" choice of the *a priori* extinction distribution, with $\sigma(A_V) \simeq 1$ mag rather than a distribution which overly simplified the models of Hatano, Branch, & Deaton (1998). We found that our distribution based on those models predicts many fewer significantly reddened supernovae than

are observed. Applying a Bayesian filter based on that particular distribution leads to underestimated extinctions in reddened supernovae and produces biased distances. We have reverted to the less restrictive prior distribution that was used by Riess, Press, & Kirshner (1996a), so that the posterior distribution is shaped primarily by the observations rather than by the prior (cf. Figure 2.12).

The MLCS analysis fits the light curves with templates that are a function of luminosity and extinction. To determine the peak brightness of the supernova (in the V band which is arbitrarily chosen as the default), rather than using just the points near maximum light, the whole light curve is used, through a weighted average of the difference between the light curve and the best-fit template. We designate this weighted average $\langle V_{\rm Bmax} \rangle$ to differentiate it from the estimate of maximum light brightness based on only the points near the time of maximum light, $V_{\rm Bmax}$. Again, we note that the *time* of maximum light is defined in the B band, such that both $V_{\rm Bmax}$ and $\langle V_{\rm Bmax} \rangle$ describe the V magnitude at the time of peak B luminosity. The difference between $V_{\rm Bmax}$ and $\langle V_{\rm Bmax} \rangle$ is quite small in all cases, but disregarding the distinction would make it appear as though there are discrepancies in derived distances at the level of ~ 0.02 mag.

The MLCS analysis of a set of supernova light curves results in three major parameters: $\langle V_{\rm Bmax} \rangle$, A_V, and Δ. Application of the MLCS method on the $BVRI$ light curves of SN 1998bu yields a maximum light brightness $\langle V_{\rm Bmax} \rangle = 11.89$, which is quite consistent with the result from just the points near maximum, $V_{\rm Bmax} = 11.88 \pm 0.02$. The derived extinction is $A_V = 0.94$ mag and the luminosity difference $\Delta = 0.02$ mag (i.e., the supernova was 2% less luminous than the fiducial). For the purposes of comparing supernovae and measuring distances, we

define $m_V \equiv \langle V_{\rm Bmax} \rangle - A_V$ as the extinction-corrected maximum light apparent magnitude of the supernova in the V band. We further define the quantity $m_V^0 \equiv \langle V_{\rm Bmax} \rangle - A_V - \Delta$, which would be the maximum light apparent V-band brightness of the supernova had it been free of absorption *and* of fiducial luminosity. For SN 1998bu, then, we have

$$m_V = 10.95 \pm 0.18 \quad \text{and} \tag{2.4}$$

$$m_V^0 = 10.93 \pm 0.18, \tag{2.5}$$

where the uncertainties are primarily due to the (correlated) uncertainties in the derived luminosity correction and extinction, with the uncertainty in the extinction (± 0.15 mag) being the dominant component.

The derived extinction can be compared directly with the supernova's red color at maximum light. Assuming that a typical unreddened SN Ia has $(B-V)_{\rm Bmax} \simeq 0.00 \pm 0.04$ (Schaefer 1995) implies a color excess for SN 1998bu of $E(B-V) = 0.34 \pm 0.06$ mag. Adopting (at maximum light) $R_V = 3.1$ yields $A_V = 1.05 \pm 0.19$ mag, fully consistent with the MLCS extinction derived from the full $BVRI$ light curves. We note that the expected extinction from our Galaxy along the line of sight to SN 1998bu is small, $E(B-V) = 0.025$ mag (Schlegel, Finkbeiner, & Davis 1998), so that the bulk of the reddening is from M96 itself[1]. The $B-V$ color of SNe Ia is also generally quite uniform at ~ 35 days past maximum light, with $B-V \simeq 1.1 \pm 0.1$ mag (Lira 1995; Riess et al. 1998a; Phillips et al. 1999). The

[1]Stanek (1998) and Arce & Goodman (1999) have recently concluded that the Galactic reddening maps of Schlegel, Finkbeiner, & Davis (1998) might overestimate the extinction in regions where $E(B-V) \gtrsim 0.15$ mag. The Galactic extinction towards M96 is well below this level, so this should not be a major concern.

observed color of SN 1998bu at that time, $B - V = 1.48 \pm 0.04$ mag, also implies a color excess consistent with the extinction derived from the full MLCS analysis. Suntzeff et al. (1999) derive a total reddening for SN 1998bu of $E(B - V) = 0.37$ mag based on the $B - V$ and $V - I$ color evolution (Phillips et al. 1999), which is consistent with our results.

Further evidence comes from the infrared light curves, where effects of dust are expected to be small. By comparing our IR observations with those of other well-observed type Ia events and assuming that the optical-IR colors are constant for normal SN Ia, we can derive another check on the inferred extinction. For example, the V maximum of SN 1981B was fainter by 0.08 mag than the V maximum of SN 1998bu, while in K-band the SN 1981B light curve was fainter than the SN 1998bu light curve by 0.87 mag (Elias et al. 1981). Using the extinction law of Cardelli, Clayton, & Mathis (1989) with $R_V = 3.1$, the difference in visual extinction between the two supernovae is given by $\Delta A_V = (\Delta K - \Delta V)/0.886$. Hence, the relative extinction between 1981B and 1998bu is $\Delta A_V = 0.89$ mag. Unfortunately, there are few type Ia supernovae with low extinctions and good IR light curves which can be used in this way. Combining infrared and optical data of SN 1980N and SN 1981D, both in NGC 1316 (Hamuy et al. 1991), gives a relative extinction of 0.81 mag and a rough lower limit consistent with our derived value. SN 1989B was highly extinguished as is SN 1998bu. The visual magnitude difference between these two is 0.11 mag (SN 1998bu is brighter) and the K difference is -0.07 mag (SN 1998bu is fainter), suggesting that there is 0.20 mag less visual extinction to SN 1998bu than SN 1989B. Wells et al. (1994) found a color excess to SN 1989B of $E(B - V) = 0.37$ mag, meaning the extinction to SN 1998bu would be $A_V = 0.95$ mag. All of the

estimates from the infrared photometry are consistent with a total visual extinction to SN 1998bu of $A_V = 0.9 \pm 0.2$ mag, supporting the value derived in the MLCS analysis.

These checks based on the color excesses at a number of wavelengths from B-band to K-band are consistent with the view that the shape of the extinction curve is likely close to the standard Galactic law (Riess, Press, & Kirshner 1996b), though the absolute normalization is not constrained. Spectrophotometric observations of SNe Ia have been used to determine the normalization, with $R_V \simeq 3.1$ at maximum light, as well as the temporal variation of the effective R_V due to the evolution of the supernova spectrum (Nugent, Kim, & Perlmutter 2002). The U-band photometry still provides some cause for concern: if the blue $U - B$ color is due to differences in the properties of the absorbing dust, the estimated extinction may be incorrect.

Independent checks of the MLCS-derived extinction are valuable. One such check is the presence of interstellar Na I D and Ca II H & K absorption in high-resolution spectra, which was reported by Munari et al. (1998) and Centurion et al. (1998). The equivalent width of the Na I D1 (λ589.0 nm) absorption lines reported by Munari et al. (1998) were 0.019 nm and 0.035 nm at velocities corresponding to our Galaxy and M96, respectively, and we confirm these measurements even with our low-dispersion spectra. Using the Munari & Zwitter (1997) calibration of the correlation between the equivalent width and reddening they derive color excesses of 0.06 and 0.15 mag, for a total reddening of $E(B - V) = 0.21$ mag. However, the relation between the absorption-line equivalent widths and the reddening has a large scatter, with a typical dispersion of 0.15 mag in $E(B - V)$ for multi-component lines (Munari & Zwitter 1997), so that these values do not contradict the extinction

inferred from the MLCS analysis (cf. discussion by Suntzeff et al. 1999).

We can also check our derived luminosity with other techniques. The relation between light curve shape and luminosity was pioneered by Phillips (1993) and Hamuy et al. (1995, 1996a) using the quantity $\Delta m_{15}(B)$, which parameterizes the BVI light curves in terms of the B magnitude decline of the supernova over the fifteen days after maximum light. From our light curve, we measure $\Delta m_{15}(B) = 1.02 \pm 0.04$, which agrees very with Suntzeff et al. (1999), who found $\Delta m_{15}(B) = 1.01 \pm 0.05$. Direct comparison of the luminosity correction is made difficult because of effects of extinction on the light curve shape, as well as differences in our respective fiducial templates. Nevertheless, we can measure $\Delta m_{15}(B)$ from the MLCS fiducial template ($\Delta = 0$, $A_V = 0$) which yields $\Delta m_{15}(B) = 1.08$. Thus the measured values of Δm_{15} and Δ, both of which imply SN 1998bu to be quite close to the MLCS fiducial template, indicate consistency in the two approaches. This is not surprising, since both methods use the shape of the observed light curve in a similar fashion.

An alternative approach was described by Nugent et al. (1995), who presented correlations between spectral features and intrinsic SNe Ia luminosity. In particular they define two indicators: $\mathcal{R}$(Si II), the ratio of the depths of Si II absorption lines observed at 580 and 615 nm; and $\mathcal{R}$(Ca II), the flux ratio of the continuum levels just blue and red of the Ca II H & K absorption. Our maximum-light spectra of SN 1998bu yield $\mathcal{R}$(Si II) $= 0.23 \pm 0.02$ and $\mathcal{R}$(Ca II) $= 1.47 \pm 0.04$. Riess et al. (1998b) present linear relations between Δ and both $\mathcal{R}$(Si II) and $\mathcal{R}$(Ca II), which yield a mean luminosity correction for SN 1998bu of $\Delta = -0.02 \pm 0.16$ and $\Delta = 0.06 \pm 0.22$, respectively. These agree well with the luminosity correction result derived in the

MLCS analysis.

All indications thus suggest that SN 1998bu was an intrinsically normal type Ia supernova, significantly extinguished by dust along the line of sight. With the MLCS analysis we determine the peak brightness ($\langle V_{\rm Bmax}\rangle = 11.89$), the luminosity correction ($\Delta = 0.02$ mag), and the extinction ($A_V = 0.94$ mag), so that SN 1998bu can be used to calibrate the SN Ia distance scale.

2.4 The Distance Scale

2.4.1 Hubble-Flow SNe Ia

Constructing the Hubble diagram requires a sample of well-observed SNe Ia in the Hubble flow where errors due to peculiar velocities are expected to be small, and which is analyzed in exactly the same way as the local calibrators. Our MLCS sample consists of 42 SNe Ia, 26 from the Calán/Tololo supernova search (Hamuy et al. 1993, 1996c) and 16 from the CfA supernova monitoring campaign (Riess et al. 1999). The only further selection criteria we have imposed (other than those inherent in the two data sets) is a cut in the host-galaxy recession velocity, which has been corrected to the cosmic microwave background (CMB) frame[2]. We have excluded supernovae in galaxies with $cz < 2500$ km s^{-1} where peculiar motions become

[2]Heliocentric redshifts for the host galaxies were first transformed to the Local Group rest frame by adding (-30, 297, -27) km s^{-1} in Galactic Cartesian coordinates (de Vaucouleurs et al. 1991; Lynden-Bell & Lahav 1988). The recession velocities in the Local Group frame were then transformed to the CMB rest frame by adding (10, -542, 300) km s^{-1} (Smoot et al. 1992).

increasingly important. Additionally, we have excluded supernovae in galaxies with $\log cz$ [km s^{-1}] > 4.5, where the relation between luminosity-distance and redshift begins to be non-linear at a level which could affect our results (Schmidt et al. 1998).

The Hubble-flow sample consists of the following SNe Ia: SN 1990O, SN 1990af, SN 1991U, SN 1991ag, SN 1992J, SN 1992K, SN 1992P, SN 1992ae, SN 1992ag, SN 1992al, SN 1992aq, SN 1992au, SN 1992bc, SN 1992bg, SN 1992bh, SN 1992bk, SN 1992bl, SN 1992bo, SN 1992bp, SN 1992br, SN 1992bs, SN 1993B, SN 1993H, SN 1993O, SN 1993ac, SN 1993ae, SN 1993ag, SN 1993ah, SN 1994M, SN 1994Q, SN 1994S, SN 1994T, SN 1995D, SN 1995E, SN 1995ac, SN 1995ak, SN 1995bd, SN 1996C, SN 1996Z, SN 1996bl, SN 1996bo, and SN 1996bv. We emphasize that all of these supernovae have well-sampled multicolor CCD light curves, with photometry obtained, reduced, and transformed to the standard system in a similar fashion, an essential feature which allows us to combine the data sets.

We use MLCS to turn these SNe Ia into standard candles, so that the extinction- and luminosity-corrected maximum light absolute magnitude, $M_V^0 = m_V^0 - \mu$, is a constant, where μ is the distance modulus. Using the definition of the distance modulus,

$$m_V^0 - M_V^0 = \mu = 5 \log d + 25 = 5 \log \frac{cz}{H_0} + 25, \tag{2.6}$$

where d is the distance in Mpc, cz is the recession velocity in km s^{-1}, and H_0 is the Hubble constant measured in its conventional units of km s^{-1} Mpc^{-1}, we get the result

$$\log cz - 0.2 m_V^0 = \log H_0 - 0.2 M_V^0 - 5. \tag{2.7}$$

Since the absolute magnitude of the fiducial SN Ia is taken to be constant, we can

determine that

$$\log cz = 0.2m_V^0 + a_V. \tag{2.8}$$

Here $a_V \equiv \log H_0 - 0.2M_V^0 - 5$ is "the intercept of the ridge line" and is a constant which can be determined from observations of Hubble-flow SNe Ia alone.

In Figure 2.10 we present this relation for our sample of 42 Hubble-flow SNe. The small scatter allows us to solve precisely for the intercept, a_V, as shown more clearly in Figure 2.11. The best-fit intercept (which is simply the mean of $\log cz - 0.2m_V^0$) using all the supernovae is $a_V = 0.6772 \pm 0.0049$, where the uncertainty is the formal standard error in the mean, and assumes the residuals from each supernova are normally distributed and independent. We assign a ± 300 km s^{-1} 1σ uncertainty to the redshift to account for the contribution of peculiar motions (Riess, Press, & Kirshner 1996a). The dispersion about the mean is $\sigma(a_V) = 0.0317$: this corresponds to a dispersion in magnitudes (obtained simply by multiplying by 5) of $\sigma = 0.16$ mag, implying only an 8% relative distance uncertainty per object[3]. Our derived intercept depends upon the choice for the fiducial luminosity ($\Delta = 0$) supernova. As long as the comparison with the local calibrators is made with the same choice, there is no problem. However, when comparing this set of Hubble-flow SNe with those analyzed by a different technique, such as the $\Delta m_{15}(B)$ method (Suntzeff et al. 1999; Phillips et al. 1999), there will likely be an offset in a_V due to the different choices of a fiducial luminosity. Such an offset will also be reflected as

[3]Some of this uncertainty arises from the uncertainty in the redshift due to peculiar velocities. Our sample has an error-weighted mean redshift of roughly 10,000 km s^{-1} so that the adopted 300 km s^{-1} uncertainty corresponds to a 3% distance uncertainty on average. This means the actual relative distance uncertainty intrinsic to the MLCS analysis of the supernovae is only 7% per object.

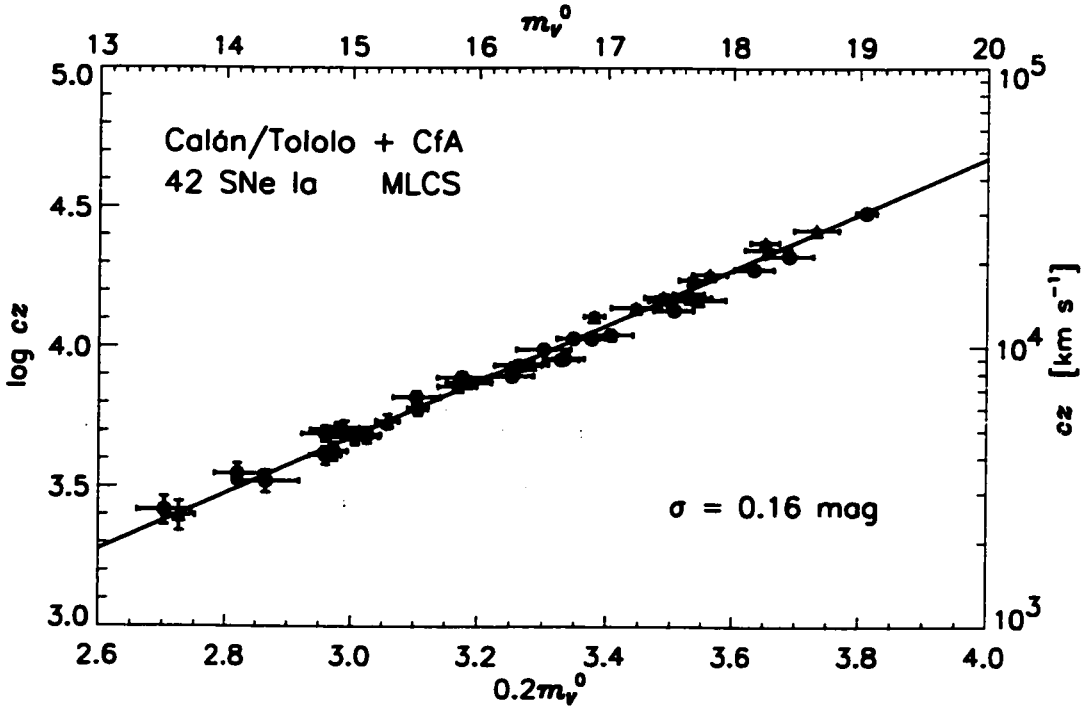

Figure 2.10.— Apparent magnitude-redshift relation for 42 Hubble-flow SNe Ia which were corrected for extinction and to a fiducial luminosity with a multicolor light curve shape (MLCS) analysis. The supernovae are from the Calán/Tololo (Hamuy et al. 1996c) and CfA (Riess et al. 1999) data sets. Supernovae in late-type ($\geq$Sa) galaxies are shown with circles, those in early-type (E/S0) galaxies are shown with triangles. The best-fit ridge line is shown, $\log cz = 0.2m_V^0 + 0.6772(\pm 0.0049)$. The dispersion about the best-fit line is $\sigma = 0.16$ mag.

the same offset for the fiducial absolute magnitude, M_V^0.

The quoted statistical uncertainty in the measurement of a_V is quite small, and it is surely underestimated. We assumed that each supernova distance is independent, whereas in reality there exists some covariance. Thus, the true uncertainty in the mean does not simply decrease as $\sigma/\sqrt{N}$, but rather levels off due to a floor caused by systematic uncertainties. It is thus important to estimate at what level this floor is reached. The formal uncertainty in a_V corresponds to ± 0.025 mag or just over one percent uncertainty in the Hubble constant arising just from the Hubble-flow supernovae.

Sample differences between the Hubble-flow and calibrating SNe Ia are one potential source of systematic uncertainty at this level. The present sample is necessarily imperfect; one difference occurs due to the host-galaxy type: our Hubble-flow sample includes supernovae in both early-type and late-type hosts, while hosts of the local calibrators have Cepheid distances, and thus are of late-type only. Hamuy et al. (1995) have shown that SNe Ia in E/S0 galaxies are systematically fainter than those in spirals or irregulars (we refer to galaxies classified Sa or later, including irregulars, as "spirals" in what follows). More accurately, the highest luminosity SNe Ia are found only in spirals (Riess et al. 1999), perhaps implying a relation between recent star formation and the brightest SNe Ia. Nevertheless, SNe Ia brightness in both early-type and late-type galaxies correlate similarly with light curve shape, so that an MLCS (or $\Delta m_{15}(B)$) analysis will still correct SNe Ia in spirals and ellipticals to the same fiducial luminosity without using any information on the galaxy morphology, as demonstrated by Schmidt et al. (1998). To further test this we have divided our sample into two subsets, early-type and late-type hosts,

solving independently for the intercept. The results are presented in Table 2.5. We see that after application of MLCS the offset between a_V in early-type and late-type galaxies is inconsistent with zero at only the 1.5σ level. Determining whether this difference is significant will require a larger sample. However, this offset would lead to a difference in the derived Hubble constant (for a fixed M_V^0) of $\sim 3\%$ (in the sense that early-type galaxies yield the slightly higher value).

Table 2.5. Intercepts of the Ridge Line for Hubble-Flow SNe Ia.

Sample	N	a_V	σ [mag]
All	42	0.6772 ± 0.0049	0.16
Late-type ($\geq$Sa)	25	0.6716 ± 0.0067	0.17
Early-type (E/S0)	17	0.6854 ± 0.0067	0.14
$cz \geq 7000$ km s^{-1}	28	0.6712 ± 0.0059	0.16
$cz < 7000$ km s^{-1}	14	0.6892 ± 0.0081	0.15

Another potential source of systematic uncertainty in the measurement of a_V is the effect of galaxy peculiar velocities and flows. We have transformed the measured host-galaxy recession velocity to the frame at rest with respect to the CMB frame, but distortions of the velocity field will result in errors in our derived intercept. Some peculiar velocity studies (e.g., Giovanelli et al. 1998) have indicated convergence of the flow field relative to the Local Group with the CMB dipole at redshifts $cz \simeq 4000$ km s^{-1}, though others do not (e.g., Lauer & Postman 1994). Our full sample is cut at $cz \geq 2500$ km s^{-1}, so flows may be important at the lowest redshifts. To check this we examined a subset of data with $cz \geq 7000$ km s^{-1} where such motions should have a much smaller effect. As Table 2.5 shows, there is no

signifcant difference in a_V between our full sample and the sample restricted to $cz \geq 7000$ km s^{-1}.

There is a larger difference in comparing the more distant sample with the remaining SNe Ia, i.e. those with $cz < 7000$ km s^{-1}. In this case the offset in a_V differs from zero at 1.8σ. Zehavi et al. (1998) have interpreted this result as the effect of a local void, whereby we live in a slightly underdense region compared to the average density of the universe, leading to a larger nearby expansion rate. For a fixed M_V^0 the difference in a_V would lead to a "local" Hubble constant larger than the global value by $\sim 4\%$. Again, more Hubble-flow SN Ia light curves will help determine whether this offset is real, a statistical fluke, or an artifact of the analysis technique. Since the large majority of our sample (28 of 42) have $cz \geq 7000$ km s^{-1}, the mean is more reflective of the global value.

We have performed an additional test of our derived intercept by employing a simple geometric flow model which includes the effects of nearby mass concentrations such as the Virgo Cluster, the Great Attractor, and the Shapley Supercluster on the velocities of the supernovae host galaxies (Mould et al. 2000). Using the position and redshifts of our galaxy sample, this model predicts that we underestimate the Hubble constant by $\sim 2\%$ in assuming that the Hubble-flow galaxies are at rest with respect to the CMB frame.

Additional sources of uncertainty may remain, for instance due to correlations in the MLCS analysis arising from the training set and construction of the templates, or uncertainties in the calibration of the photometric system. A larger sample of Hubble-flow SNe Ia would be helpful to determine what unidentified systematics

may remain and at what level they affect our conclusions.

Given that the identified systematic errors in the Hubble-flow SNe do not yet definitively suggest a bias in our derived intercept, we use these results only as a guide to the size of the systematic uncertainty. Based on these explorations, a reasonable estimate of the 1σ systematic uncertainty in the Hubble-flow supernovae would be $\pm 3\%$ in the Hubble constant. Our best estimate for the intercept of the ridge-line and its total uncertainty is then $a_V = 0.6772 \pm 0.0120$. As we discuss below, this uncertainty in the Hubble-flow SNe Ia is dwarfed by both statistical and systematic uncertainties in the Cepheid-calibrated supernovae and our measurement of M_V^0 (Hamuy et al. 1996b; Riess, Press, & Kirshner 1996a).

2.4.2 Cepheid-Calibrated SNe Ia

To measure the Hubble constant we need both the intercept of the ridge line, a_V, and the maximum light absolute magnitude of our fiducial SN Ia, M_V^0. We use a sample of SNe Ia in galaxies with distances measured via Cepheids. SN 1998bu in NGC 3368 is only the most recent example, others are listed by Saha et al. (1997) in their Table 6: SN 1895B and SN 1972E in NGC 5253, SN 1937C in IC 4182, SN 1960F in NGC 4496A, SN 1981B in NGC 4536, and SN 1990N in NGC 4639. Their table also includes SN 1989B in NGC 3627, but the distance to this galaxy is only inferred from distances to other galaxies in the Leo group (including NGC 3368). We restrict our sample to the best cases: supernovae in galaxies whose distances are directly measured by Cepheids rather than distances to groups or clusters. Schaefer (1998) has also recalibrated the light curve of SN 1974G in NGC 4414, for which the

host-galaxy Cepheid distance has been measured by the *HST* Distance Scale Key Project (Turner et al. 1998).

The supernovae we use as calibrators are only those which are measured and analyzed in the same way as our Hubble-flow sample, to avoid systematic errors. For this reason, we only consider SNe Ia which have photoelectrically measured multicolor light curves. As our observations of SN 1998bu have shown, even CCD data measured and calibrated similarly can yield discrepant photometry depending on the details of the telescope, detector, and filters. Such calibration problems, as well as problems of galaxy background subtraction and transformation to the Landolt system, make photographic photometry of supernovae subject to systematic differences in the peak brightness, colors, and the light curve shape. The last point is crucial; we must be certain that the observed light curve shape is an intrinsic property of the supernova, and not an artifact of systematic errors resulting from photographic photometry (Boisseau & Wheeler 1991; Pierce & Jacoby 1995). While heroic efforts (e.g., Schaefer 1998 and references therein) have been made in compiling and reanalyzing older photographic (and even visual) light curves, the best path to the Hubble constant lies along another route: precise distances to well-observed objects. The drawback to a high standard for the data is that our calibrating sample is small, consisting of four SNe Ia: SN 1998bu, SN 1990N, SN 1981B and SN 1972E. We pay in random error what we avoid in systematic bias and we believe this to be a good bargain.

The Cepheid distances to the host galaxies of these four supernovae have been measured by two *HST* programs, but the general approach among all the *HST* Cepheid programs is the same. From the derived mean magnitudes of the Cepheids

and a PL relation (Madore & Freedman 1991), distance moduli (relative to the LMC) can be determined. The two-color photometry allows for an estimate of the extinction, either on a Cepheid-by-Cepheid basis or in the mean, yielding an extinction-corrected distance modulus for the host galaxy.

It is important to use distance moduli for the host galaxies which are derived consistently (e.g., always using the same PL relation, the same LMC distance modulus, the same extinction prescription, etc.) so that each supernova is on an equal footing. Thus we have not simply used the final distance modulus quoted in the Cepheid papers, but rather have tried to extract as uniform a set of distance moduli as we can with limited information. This approach also allows us to more easily consider systematic effects in the Cepheid distances. For instance, in this section we use distance moduli with the LMC distance fixed at $\mu_{\rm LMC} \equiv 18.50$ mag (Hereafter, all distance moduli will have implied units of magnitudes). We *do not* yet include the uncertainty in this value because that uncertainty is implicit in each host galaxy distance, and moreover it is perfectly correlated, such that the derived mean absolute magnitudes will suffer the same uncertainty. We postpone discussion and quantification of such systematic ("external") uncertainties to the next section.

2.4.2.1 SN 1998bu in M96 (NGC 3368)

For SN 1998bu, Tanvir et al. (1995) discovered seven Cepheids with well-determined light curves in M96. They derived an extinction-corrected distance modulus of $\mu = 30.32 \pm 0.12$ with the uncertainty coming from the photometric errors and the uncertainty (in the mean) of the fit to the PL relation. However, their photometry

was not corrected for the WFPC2 "long/short" exposure effect (Hill et al. 1998) which leads to V and I magnitudes systematically too bright by 0.05 mag in long exposures such as those for Cepheid programs. We have corrected the distance modulus of M96 for this effect, yielding $\mu = 30.37 \pm 0.12$, with the quoted uncertainty being only the "internal" error. Combined with the extinction-corrected maximum light apparent magnitude from Equation 2.4, we derive an extinction-corrected maximum light absolute magnitude for SN 1998bu, $M_V = -19.42 \pm 0.22$. To determine the absolute magnitude of our fiducial SN Ia, M_V^0, we also include the derived luminosity difference $\Delta = 0.02$ mag for SN 1998bu, which leads to $M_V^0 = -19.44 \pm 0.22$.

Our absolute magnitude for SN 1998bu is fainter than that reported by Suntzeff et al. (1999) who found $M_V = -19.63 \pm 0.19$. This offset arises from different estimates of the extinction. We have employed $A_V = 0.94$ mag derived from the MLCS analysis of the $BVRI$ light curves, whereas Suntzeff et al. (1999) derive a total $E(B-V) = 0.37$ mag, yielding $A_V = 1.15$ mag. This difference is, for better or worse, within the uncertainties, and may arise partly from an offset in the intrinsic colors in the light curve fitting methods, but some more careful comparisons between the two methods may be necessary. Nevertheless, it turns out that the derived Hubble constant is not very different in the two methods.

2.4.2.2 SN 1990N in NGC 4639

For SN 1990N we have performed an MLCS analysis on $BVRI$ light curves from Lira et al. (1998), with the results presented in Table 2.6. We have used the

extinction corrected Cepheid distance modulus to NGC 4639 determined by Saha et al. (1997), $\mu = 32.03 \pm 0.22$, based on 15 high-quality Cepheids. From this we derive an absolute magnitude for SN 1990N of $M_V = -19.78 \pm 0.33$ and an estimate of the fiducial absolute magnitude $M_V^0 = -19.46 \pm 0.33$.

2.4.2.3 SN 1981B in NGC 4536

Our MLCS analysis of SN 1981B was based on the BVR light curves of Buta & Turner (1983). Saha et al. (1996) found a total of 73 Cepheids in NGC 4536 and determined an extinction corrected distance modulus, $\mu = 31.10 \pm 0.13$. This leads to an absolute magnitude for SN 1981B of $M_V = -19.46 \pm 0.23$ and $M_V^0 = -19.12 \pm 0.23$.

2.4.2.4 SN 1972E in NGC 5253

Finally, for SN 1972E, we have BVI light curves from Ardeberg & de Groot (1973) and Leibundgut et al. (1991b). Saha et al. (1995) have presented their final analysis of Cepheids in NGC 5253, with their result $\mu = 28.08 \pm 0.10$. However, some cautions are in order. These observations were made with the original WFPC instrument (with spherical aberration) rather than WFPC2; also, the I-band light curves were transformed from the *HST* F785LP filter rather than F814W. These differences may possibly lead to a small systematic difference in the derived distance modulus compared to the other host galaxies. Furthermore, the Cepheid sample is small, as there are only 5 Cepheids with high-confidence mean magnitudes in both V and I. Using the derived apparent moduli in V and I, and estimating the

Cepheid extinction in the same manner as for the other three host galaxies, we have rederived the same distance modulus as Saha et al. (1995) but with a significantly larger uncertainty, $\mu = 28.08 \pm 0.26$. Our MLCS analysis of SN 1972E then leads to $M_V = -19.80 \pm 0.29$ and $M_V^0 = -19.42 \pm 0.29$.

We present the MLCS results, Cepheid distances, and absolute magnitudes for SN 1998bu and the three other calibrating SNe Ia in Table 2.6. We note that the estimates for M_V^0 are consistent given their uncertainties, though SN 1981B seems to give a measurably fainter value. Since the estimates are mutually consistent and there is no *a priori* reason to distrust any of them, we take the data at face value. The error-weighted mean gives the maximum light absolute magnitude of our fiducial SN Ia, $M_V^0 = -19.34 \pm 0.13$. As with the ridge-line intercept, here again we must be wary of the uncertainty estimate since it ignores the covariance in the Cepheid distances. Kochanek (1997) has shown there is significant statistical covariance in the Cepheid distance moduli, even beyond the common zero-point set by the LMC distance, which arises from a number of sources including the Cepheid photometry, the determination of mean magnitudes, and the fit to the PL relation. If we include an estimate of this statistical covariance to determine how to combine the Cepheid distances (usually incorrectly assumed to be independent) by using the Pearson correlation coefficient, $r \simeq 0.5$ (C. Kochanek, personal communication), our best estimate of the fiducial absolute magnitude and its statistical uncertainty becomes $M_V^0 = -19.34 \pm 0.17$. This estimate still does not incorporate some sources of systematic uncertainty, including the LMC distance, which we dicuss in detail in Section 2.5.2.

Table 2.6. Cepheid-Calibrated SNe Ia

SN Ia	Galaxy	$\langle V_{\rm Bmax}\rangle$	A_V	Δ	$\sigma_{\rm MLCS}$	$\mu_{\rm Cepheid}$	M_V	M_V^0
1998bu	NGC 3368	11.89	0.94	+0.02	±0.18	30.37 ± 0.12	-19.42 ± 0.22	-19.44 ± 0.22
1990N	NGC 4639	12.68	0.43	−0.32	±0.25	32.03 ± 0.22	-19.78 ± 0.33	-19.46 ± 0.33
1981B	NGC 4536	11.99	0.35	−0.34	±0.18	31.10 ± 0.13	-19.46 ± 0.23	-19.12 ± 0.23
1972E	NGC 5253	8.43	0.15	−0.38	±0.13	28.08 ± 0.26	-19.80 ± 0.29	-19.42 ± 0.29
Mean	...	...	...	...	...	...	...	-19.34 ± 0.17

2.4.3 The Hubble Constant

With estimates of the ridge-line intercept and the maximum-light absolute magnitude of our fiducial SN Ia, we derive the Hubble constant, from

$$\log H_0 = 0.2M_V^0 + 5 + a_V. \tag{2.9}$$

The mean of the four calibrating SNe Ia gives $M_V^0 = -19.34 \pm 0.17$, and using all 42 Hubble-flow SNe Ia gives $a_V = 0.6772 \pm 0.0120$, which results in our best estimate of the Hubble constant,

$$H_0 = 64.4^{+5.6}_{-5.1}\ \mathrm{km\ s^{-1}\ Mpc^{-1}}, \tag{2.10}$$

where the uncertainty *does not* include systematic uncertainties in the Cepheid distance scale to be discussed below. Even so, it is important to note that the total uncertainty in $a_V(\pm 0.0120)$ is about three times smaller than the statistical uncertainty in $0.2M_V^0(\pm 0.034)$. The statistical error in this small sample of calibrating SNe Ia, arising from both the uncertainty in the luminosity- and extinction-corrected supernova brightness and the uncertainty in the Cepheid distance moduli, dominates the statistical uncertainty in H_0 (Hamuy et al. 1996b; Riess, Press, & Kirshner 1996a). Reducing this statistical error can best be accomplished by observations of additional nearby SNe Ia and Cepheids in their host galaxies. SN 1998bu is the first example where a new supernova has been studied in a galaxy where the Cepheid work is already in the literature, but more will follow in the years ahead. The systematic uncertainty in the calibrating SNe and their Cepheid distances is still an important consideration, discussed in the next section.

2.5 Discussion

2.5.1 Comparison with other work

Suntzeff et al. (1999) used SN 1998bu and four other local calibrators (they included SN 1937C in IC 4182 in their local sample), combined with distant SNe Ia from the Calán/Tololo sample to derive a Hubble constant, $H_0 = 64.0 \pm 2.2$ km s^{-1} Mpc^{-1} (this uncertainty ignores covariances in the Cepheid distances). Their result, using a different method to convert light curves to luminosities and extinction (Phillips et al. 1999), is quite consistent with ours. There are slight differences in measurements of individual objects, but the overall agreement is reassuring and indicates that SNe Ia are excellent distance indicators whose intrinsic diversity can be understood and quantified.

The calibration of the peak absolute magnitude of SNe Ia has been driven by the great efforts of the *HST* program to measure Cepheid distances to the supernova host galaxies (Sandage et al. 1992). That group's latest published determination of the Hubble constant and statistical uncertainty (also ignoring Cepheid covariances) is $H_0 = 58 \pm 3$ km s^{-1} Mpc^{-1} (Saha et al. 1997). This is consistent with our result – agreement to $\sim 10\%$ is good given the long history of measurements of the Hubble constant. Nonetheless, it is instructive to pinpoint where the differences arise. The Saha et al. (1997) analysis uses a "fiducial sample" of 56 Hubble-flow SNe Ia with B and V peak magnitudes, typically determined from photographic plates. Enforced upon the sample is a velocity constraint, $3 < \log cz[\mathrm{km\ s^{-1}}] < 4.5$, and a color constraint $-0.25 \leq B_{\max} - V_{\max} \leq 0.20$ mag (after correction for Galactic

extinction) to avoid peculiar SNe Ia and those with large amounts of extinction. As local calibrators, they use seven SNe Ia in six galaxies with five Cepheid distances (the distance to SN 1989B was estimated by association to other Leo Group galaxies with measured Cepheid distances; see their Table 6). Their local calibrator sample is *not* selected by the same criteria as their fiducial sample, as no color constraint was applied to the local calibrators. So SN 1895B was used with an estimated $B_{\rm max}$ but no color information, and SN 1989B was used though it was too red, with $B_{\rm max} - V_{\rm max} = 0.35 \pm 0.07$ mag (Wells et al. 1994). (SN 1998bu would also be too red to meet the color requirement of their fiducial sample.) Nevertheless, excluding SN 1895B and 1989B from their analysis would only have a small effect and would increase their derived H_0 by about 1 km s^{-1} Mpc^{-1}.

Though we have not used SN 1895B and SN 1989B in our local sample for reasons adduced earlier, there are additional differences between the two analyses. Saha et al. (1997) include no correction for variation in intrinsic SN Ia luminosity based on light curve shape. This is particularly significant for the calibrator sample where 3 out of the 4 objects are slow decliners; including this correction makes the estimated fiducial absolute peak magnitude slightly fainter and explains about half our disagreement in H_0. Most of the balance of the difference likely arises from the treatment of extinction. While Saha et al. (1997) correct some of their local calibrator peak magnitudes for extinction individually, they do not apply an extinction correction to their fiducial sample SNe. If the mean color excess of their fiducial sample were as little as $E(B-V) \simeq 0.03$ mag, correcting for extinction would increase the mean m_V by ~ 0.1 mag, and raise a_V by ~ 0.02, which is the other half of the difference in H_0. Saha et al. (1997) argue that selection effects against

the discovery of extinguished distant supernovae preclude a significant amount of extinction in the fiducial sample. While this *could be* true, there is no demonstration that it *is* true for the sample they use. The selection effects in the several searches that led to the SNe Ia of their fiducial sample are quite complicated (see, e.g. Hamuy & Pinto 1999), and *a priori* statements about the possible extinction distribution of the distant supernovae are not, by themselves, evidence. In particular, discovery of SNe Ia with $A_V \simeq 0.1$ mag does not seem to be strongly suppressed. In Figure 2.12 we show the extinction distribution for our Hubble-flow and calibrating samples and it is clear that a some of the supernovae found this way are, in fact, signifcantly extinguished.

The MLCS analysis was designed to address these concerns; the supernova peak magnitude, extinction and luminosity correction are quantitatively estimated for each object, with a careful attention to correlations and the final distance modulus uncertainty. This obviates the need to make arbitrary sample cuts. We have taken particular care to analyze the local calibrators and the Hubble-flow SNe Ia by the same methods. While these technical differences are significant, the difference in the derived Hubble constant between our approach and others is small. Uncertainty in the true Hubble constant still arises principally from the small size of the calibrator sample and from uncertainties in the lower rungs of the distance ladder.

2.5.2 External uncertainties

We examine three sources of systematic uncertainty in the distances of the galaxies that host the calibrating SNe Ia: the effect of metallicity on *HST* Cepheid distance

moduli, recalibration of the Cepheid PL relation, and the distance to the LMC, which are likely to be the most important sources of systematic error.

2.5.2.1 Metallicity dependence of the Cepheid scale

The remarkably tight PL relation of Cepheids in the LMC is quite a boon to distance measurement, but also calls for understanding variation in the PL (and therefore derived distance moduli) with environment. Metallicity, in particular, may play an important role. Theoretical studies of Cepheid pulsation (e.g., Chiosi, Wood, & Capitanio 1993) indicate metallicity can have an effect on the brightness and colors of Cepheids, though the size of this effect is uncertain. If the brightness and colors of Cepheids vary with metallicity, their distances will be misestimated, both because of an incorrect estimate of their intrinsic brightness as well as an incorrect estimate of the extinction based on the color excess. Systematic errors in distances would occur in Cepheid populations with significantly different mean abundances than the LMC.

While it is important to understand the effects of metallicity on Cepheid luminosities and colors in many wavebands (see, e.g., Freedman & Madore 1990; Gould 1994; Stift 1995), our particular concern is the effect on the *HST* Cepheid distances. Recently great efforts have been made to determine empirically the relation between metallicity and distance moduli measured in V and I with the standard procedure of extinction correction. The "metallicity" dependence of extragalactic Cepheids is usually parameterized in terms of [O/H], the logarithmic number abundance of oxygen to hydrogen, relative to solar composition and

measured via H II region spectra. We adopt the notation

$$\gamma_{VI} = \frac{\Delta\mu}{\Delta[\mathrm{O/H}]}, \tag{2.11}$$

which gives the change in the distance modulus per factor of ten in metallicity, measured in mag/dex. Then the true distance modulus of a galaxy is given by $\mu_{\mathrm{true}} = \mu_{VI} - \gamma_{VI}([\mathrm{O/H}] - [\mathrm{O/H}]_{\mathrm{LMC}})$, where μ_{VI} is the measured extinction-corrected distance modulus. Recently, Kennicutt et al. (1998) used *HST* observations of three fields in M101 over which a large abundance gradient has been observed from measurements of H II regions. Their analysis showed a slight correlation of distance modulus with metallicity, with $\gamma_{VI} = -0.24 \pm 0.16$. Beaulieu et al. (1997) and Sasselov et al. (1997) analyzed the effects of metallicity on the *PL* relation from observations of LMC and SMC Cepheids from the EROS microlensing project. Their conclusion was for a slightly stronger dependence[4], $\gamma_{VI} = -0.48^{+0.1}_{-0.2}$. A global analysis of many Galactic and extragalactic Cepheids by Kochanek (1997) yielded a similar metallicity dependence; we consider this analysis in more detail in the next section.

To assess the possible impact of metal abundance on the Hubble Constant from SNe Ia, we have recalculated the distance moduli to the calibrating galaxies with these empirically determined metallicity corrections. We adopt $[\mathrm{O/H}] - [\mathrm{O/H}]_{\mathrm{LMC}}$ measurements for NGC 3368 and NGC 5253 as compiled by Kennicutt et al. (1998) in their Table 4. The abundances for NGC 4639 and NGC 4536 are from Kochanek (1997), who estimated these based on metallicity-magnitude and metallicity-galaxy

[4]The value of $\gamma_{VI} = -0.44$ quoted in their papers is for abundances measured in terms of [Fe/H]; $\gamma_{VI} = -0.48$ is correct for [O/H] (D. Sasselov, personal communication).

type relations; we have adopted an uncertainty of ± 0.20 on these estimates, though the results are not particularly sensitive to this choice. The effect of the recalculated distance moduli is shown in Table 2.7, where we have derived M_V^0 estimates for three cases: $\gamma_{VI} \equiv 0$, i.e., no metallicity dependence, $\gamma_{VI} = -0.24 \pm 0.16$ from Kennicutt et al. (1998), and $\gamma_{VI} = -0.48^{+0.1}_{-0.2}$ from Beaulieu et al. (1997) and Sasselov et al. (1997).

The results are interesting; the corrections for metallicity yield little change in the inferred Hubble constant. Low H_0 values from SNe Ia are not due to metallicity effects on the Cepheid distances to this sample of galaxies. This is primarily due to our inclusion of SN 1998bu in NGC 3368, which is the only metal-rich calibrator, by a factor of 0.7 dex compared to the LMC. If metallicity were the culprit causing a low SNe Ia H_0, we would expect our inferred M_V^0 for SN 1998bu to be very faint without a metallicity correction. However, the distance modulus of Tanvir et al. (1995) and our observations do not require a faint value. More strikingly, comparing SN 1998bu and SN 1972E we see that the estimates of M_V^0 are almost exactly the same without a metallicity correction, even though the metal abundance is higher in NGC 3368 than in NGC 5253 by more than a factor 10.

As a result, including a metallicity correction increases the dispersion in the estimates of M_V^0 from the four calibrating SNe Ia, from $\sigma(M_V^0) = 0.16$ mag with no metallicity correction, to $\sigma(M_V^0) = 0.21$ mag for the Kennicutt et al. (1998) value, to $\sigma(M_V^0) = 0.29$ mag for the Sasselov et al. (1997) value. The sample size of four is probably too small to place much confidence in this result, but if it were borne out by a larger sample, it would have interesting implications. Assuming that the intrinsic dispersion in the MLCS-corrected luminosity for the calibrating supernovae

Table 2.7. Effects of Metallicity

SN Ia	Galaxy	$[O/H]-[O/H]_{\rm LMC}$	M_V^0		
			$\gamma_{VI}\equiv 0$	$\gamma_{VI}=-0.24\pm0.16$	$\gamma_{VI}=-0.48^{+0.1}_{-0.2}$
1998bu	NGC 3368	$+0.70\pm0.20$	-19.44 ± 0.22	-19.61 ± 0.25	$-19.78^{+0.25}_{-0.27}$
1990N	NGC 4639	$+0.10\pm0.20$	-19.46 ± 0.33	-19.48 ± 0.33	$-19.51^{+0.34}_{-0.34}$
1981B	NGC 4536	0.00 ± 0.20	-19.12 ± 0.23	-19.12 ± 0.23	$-19.12^{+0.24}_{-0.24}$
1972E	NGC 5253	-0.35 ± 0.15	-19.42 ± 0.29	-19.34 ± 0.30	$-19.25^{+0.30}_{-0.30}$
Mean	...	...	-19.34 ± 0.17	-19.36 ± 0.17	-19.40 ± 0.18
H_0	...	...	$64.4^{+5.6}_{-5.1}$	$63.8^{+5.6}_{-5.1}$	$62.7^{+5.7}_{-5.2}$

is the same as that for the Hubble-flow SNe Ia ($\sigma \simeq 0.16$ mag), any increase in the dispersion would arise from the Cepheid distance moduli. A significant increase in dispersion with a metallicity correction would imply either that the association between H II region metallicity and Cepheid metallicity is not straightforward, that the metallicity correction was incorrect, or that some other systematic uncertainty (perhaps in the properties of SNe in regions of different metallicity) was colluding with the metallicity to counter its effect in the uncorrected distance moduli. Increasing the sample of SNe Ia in galaxies with Cepheid distances (particularly covering a wide range of metallicity) would be a very desirable path to understanding this important uncertainty in the distance scale. We note that Nevalainen & Roos (1998) used this idea of "statistical consistency" between Cepheid-calibrated distance indicators (including SNe Ia) to derive a metallicity dependence which brought the estimates of H_0 into the best concordance, $\gamma_{VI} = -0.31^{+0.15}_{-0.14}$. Because of the high metallicity of NGC 3368, including SN 1998bu in their analysis would likely affect this result.

In principle the supernovae themselves can provide an estimate of the metallicity correction, but minimizing the dispersion in our four calibrating supernovae yields $\gamma_{VI} = +0.11 \pm 0.37$, which is only a weak constraint given the very small sample size. In addition, such a procedure ignores a possibly significant metallicity dependence in the brightness of the supernovae themselves. Thus the current supernova data do not provide strong evidence either for or against the incorporation of a metallicity dependence in the Cepheid distance moduli. We take the results at face value, and combined with the current best estimates of γ_{VI} we conclude that the systematic 1σ error in H_0 from metallicity considerations for this sample is small,

$^{+0.0}_{-1.7}$ km s^{-1} Mpc^{-1}.

2.5.2.2 The Cepheid PL relation

We (and most authors) have adopted the V-band and I-band PL relations derived from LMC Cepheids by Madore & Freedman (1991). The relations are consistent with earlier estimates (e.g., Sandage & Tammann 1968; Feast & Walker 1987), but are based on a relatively small sample of objects compared to the number now known in more distant galaxies. An error in the PL slope or zero-point could be an important source of systematic uncertainty. In this section, by the zero-point we do not mean to include the uncertainty in the distance to the LMC (still adopted as $\mu_{\rm LMC} \equiv 18.50$, and discussed extensively in the next section), but only uncertainty in the zero-point that arises from a small sample of LMC Cepheids, even after assuming the LMC distance is perfectly known.

The Madore & Freedman (1991) PL relations have statistical zero-point uncertainties of 0.05 and 0.03 mag in V and I respectively. Unfortunately, residuals for the fit to the PL relations are correlated, and the PL slope is also slightly correlated to the zero point, so that the real uncertainty in the application of the PL relations is not just a straightforward quadrature combination of these uncertainties. Tanvir (1996) analyzed an augmented sample of LMC Cepheids with particular attention to correlated residuals and found a slightly tighter relation. However, his result indicated bias in the Madore & Freedman (1991) calibration such that for typical period distributions, *HST* Cepheid distance moduli are overestimated by ~ 0.1 mag, which would imply an increase in our estimate of M_V^0 (to fainter intrinsic

luminosity) by the same amount and a $\sim$ 5% increase in H_0 for any given LMC distance.

The global analysis of Kochanek (1997) carefully and consistently treats the Cepheid data to allow for distance estimates including the systematic uncertainties we have discussed so far. Again, the distance to the LMC is fixed at $\mu \equiv 18.5$. In Table 2.8 we present our estimates of M_V^0 given the distance moduli derived by Kochanek (1997) and presented in his Table 3. We have added 0.05 mag to the NGC 3368 distance modului presented there to correct for the WFPC2 "long/short" exposure effect, which was not included in his analysis of the Cepheids in that galaxy (this is just a first approximation; the correct method would be to repeat his analysis with the fainter NGC 3368 Cepheid magnitudes). With that caveat, we have considered two of his models, the first being Model 0 which derives distances in the "standard" method, with a global solution for the PL relation and correct treatment of correlated errors. As Table 2.8 shows, the M_V^0 estimates are generally fainter in this model, in line with the suggestion of Tanvir (1996), leading to a modest increase in H_0. The second model we consider is Model 3-15, which also derives a global solution, but further allows for effects of metallicity and positive extinction. The result is again generally to decrease the host galaxy distances, and lead to a fainter M_V^0 and higher H_0. However, we note that the estimates of M_V^0 are not consistent with their uncertainties (which are derived from the quadrature sum of the uncertainty in m_V^0 from MLCS and the uncertainty in the Cepheid distance modulus). Furthermore, the dispersion is much larger than the $\sim$ 0.16 mag expected from the SNe Ia alone; this implies that either the local calibrating SNe Ia are very different from the Hubble-flow SNe Ia (a possibility we feel is unlikely based on their

spectra and light curves), or that systematic errors remain in the Cepheid distances derived from this particular model. Further analysis is required.

Table 2.8. Results Based on the Global Analysis of Kochanek (1997)

SN Ia	Galaxy	M_V^0		
		Published[a]	Model 0[b]	Model 3-15[b]
1998bu	NGC 3368	-19.44 ± 0.22	-19.40 ± 0.33	-19.54 ± 0.23
1990N	NGC 4639	-19.46 ± 0.33	-19.54 ± 0.41	-19.21 ± 0.28
1981B	NGC 4536	-19.12 ± 0.23	-18.99 ± 0.28	-18.63 ± 0.22
1972E	NGC 5253	-19.42 ± 0.29	-19.04 ± 0.35	-18.74 ± 0.20
Mean	...	-19.34 ± 0.17	-19.20 ± 0.22	-19.03 ± 0.27[c]
H_0	...	$64.4^{+5.6}_{-5.1}$	$68.7^{+7.6}_{-6.8}$	$74.3^{+10.1}_{-8.9}$

[a]Published refers to M_V^0 estimates based on published distance moduli as described and modified in section 2.4.2.

[b]These two columns are from Kochanek (1997). See text for details regarding the models.

[c]Since the values in this column seem to be inconsistent with their derived uncertainties, we have calculated an unweighted mean.

These results suggest a 1σ systematic uncertainty in the calibrating SNe Ia host galaxy Cepheid distance moduli of $^{+0.05}_{-0.10}$ mag due to the combined effects of metallicity, extinction and the calibration of the PL relation. (The resulting uncertainty in M_V^0 is in the opposite sense, $^{+0.10}_{-0.05}$ mag.) Since definitive results regarding the exact magnitude of these effects are lacking, we just include these effects in our uncertainty, with $M_V^0 = -19.34^{+0.20}_{-0.18}$. Our estimate of the Hubble constant then becomes

$$H_0 = 64.4^{+6.6}_{-5.4} \text{ km s}^{-1} \text{ Mpc}^{-1}. \tag{2.12}$$

2.5.2.3 Distance to the LMC

The final source of systematic error in the Hubble constant that we consider is the distance to the LMC. All methods to measure H_0 which are based on *HST* Cepheid distances share this systematic uncertainty, so that comparisons in the resulting H_0 values between these methods should not include an error component from the LMC distance (i.e., comparisons of *HST* Cepheid-calibrated H_0 measurements should be to the analog of equation 2.12; if two such measurements disagree, they will disagree regardless of the LMC distance). Formally, our best estimate of the Hubble constant, including the systematic uncertainties discussed above, is given by

$$\log H_0 = 1.809^{+0.042}_{-0.038} - 0.2\,(\mu_{\rm LMC} - 18.50)\,. \qquad (2.13)$$

Of course, if we wish to compare our value of H_0 with those derived from techniques which are independent of the LMC distance (e.g., SNe II expanding photospheres, gravitational lens time delays, Sunyaev-Zel'dovich effect, etc.), we have to provide a best estimate for μ_{LMC} and perhaps more importantly, its uncertainty. Measurement of quantities derived from the "true" Hubble constant, such as the dynamical age of the Universe, also requires such an estimate.

However, measurements of the LMC distance modulus are notoriously inconsistent, ranging for the most part from $\sim$ 18.2 to $\sim$ 18.7. The value of $\mu_{\rm LMC} = 18.5$ that we have adopted has recently faced a strong challenge from a "short" LMC distance based on Hipparcos-calibrated red clump stars (Stanek, Zaritsky, & Harris 1998; Udalski 1998) and the study of detached eclipsing binaries such as HV2274 (Guinan et al. 1998), which give $\mu_{\rm LMC} = 18.18 \pm 0.06$ and 18.30 ± 0.07, respectively. However, recent applications of other methods, including

Cepheids, RR Lyrae stars, Mira variables, and the SN 1987A ring still yield a wide range of distance moduli, many with inconsistent error bars. As an exercise, we compiled a representative (though not exhaustive) sample of 19 LMC distance moduli published in the last two years (Alcock et al. 1997; Di Benedetto 1997; Feast & Catchpole 1997; Gratton et al. 1997; Panagia et al. 1997; van Leeuwen et al. 1997; Whitelock, van Leeuwen, & Feast 1997; Bergeat, Knapik, & Rutily 1998; Cole 1998; Fernley et al. 1998; Gieren, Fouqué, & Gómez 1998; Gould & Uza 1998; Guinan et al. 1998; Luri et al. 1998a; Luri et al. 1998b; Madore & Freedman 1998; Oudmaijer, Groenewegen, & Schrijver 1998; Reid 1998; Udalski 1998). Naively assuming each measurement to be independent, a Bayesian analysis of these distance estimates in the spirit of Press (1997) yields a narrow probability density function (PDF) for the mean, with $\mu_{\rm LMC} = 18.55^{+0.02}_{-0.04}$, as shown in Figure 2.13. If we modify the analysis so that each distance method only gets one "vote" to reduce correlated errors, the PDF becomes quite asymmetric with $\mu_{\rm LMC} = 18.50^{+0.05}_{-0.15}$, where the stated value is the peak of the PDF and the upper and lower uncertainties are derived from the points at which the cumulative probability is 0.841 and 0.159. This analysis does not provide a reason for the discrepant values, and is subject to additional correlated errors that may still be lurking. Nevertheless, given the incompatible data, the method provides a reasonable and statistically defensible way to estimate $\mu_{\rm LMC}$, and its uncertainty.

As the current best estimate of the LMC distance modulus, we adopt $\mu_{\rm LMC} = 18.50^{+0.10}_{-0.15}$ mag. Others will undoubtedly have differing estimates, and can use equation 2.13 to determine the resulting Hubble constant. With our choice, we have as the estimate of the fiducial absolute magnitude, including all identified

systematic uncertainties, $M_V^0 = -19.34^{+0.25}_{-0.21}$. Thus, our final estimate of the Hubble constant incorporating this total systematic uncertainty is

$$H_0 = 64.4^{+8.1}_{-6.2} \text{ km s}^{-1} \text{ Mpc}^{-1}. \tag{2.14}$$

2.5.3 Implications

One direct implication of our derived Hubble constant is an estimate of the dynamical age of the universe, t_0, assuming a Friedmann-Robertson-Walker cosmology. In an $\Omega_M = 1$, Einstein-de Sitter universe, $H_0 t_0 = 2/3$. However, evidence from SNe Ia at high redshifts provides a strong observational constraint on this product, with Riess et al. (1998a) deriving $H_0 t_0 = 0.93 \pm 0.06$ and Perlmutter et al. (1999) obtaining $H_0 t_0 = 0.93 \pm 0.05$. Assuming that systematic errors in these estimates are small (discussed extensively in both papers), we have

$$t_0 = 14.1 \pm 1.6 \text{ Gyr}. \tag{2.15}$$

This estimate is very nearly the same as that presented by Riess et al. (1998), and is in good accord with measurements of the ages of the oldest objects in the Universe (see Chaboyer 1998 for a review). The solution to the cosmological "age crisis" is not to be found in alternative estimates of H_0, but rather in discarding the $\Omega_M = 1$ cosmology (which would require $t_0 = 10.1 \pm 1.1$ Gyr).

The supernovae can also tell us about the structure of groups and clusters. For instance, Graham et al. (1997) obtained a Cepheid distance to NGC 3351 which is also a member of the Leo I group along with NGC 3368. However, the distance modulus they derive, $\mu_{\text{NGC3351}} = 30.01 \pm 0.19$, is almost 0.4 mag closer

than the Tanvir et al. (1995) distance for NGC 3368, $\mu_{\rm NGC3368} = 30.37 \pm 0.12$. This corresponds to a 2 Mpc difference in the line of sight distance to these galaxies, even though their projected separation is 41 arcmin, or about 120 kpc at the inferred distance. Graham et al. (1997) suggest one alternative explanation is that the I-band NGC 3368 Cepheid photometry of Tanvir et al. (1995) is systematically faint, which would lead to an underestimated extinction and an overestimated distance. Metallicity corrections to the Cepheid distances do not change this conclusion, as both NGC 3368 and NGC 3351 are similarly metal rich (Kennicutt et al. 1998). If we adopt the mean M_V^0 from the three other calibrators, SN 1998bu can in principle be used to test the Tanvir et al. (1995) distance. However, this procedure yields $\mu_{\rm NGC3368} = 30.26 \pm 0.27$, and the uncertainty is too large to provide a definitive test.

This discussion does point out an important attribute of our analysis. We have assumed that the internal errors in the Cepheid distances (i.e., excluding those factors we discuss in Section 2.5.2) are accurately estimated. While we have tried to create a uniform set of distance moduli from the published values, a better procedure would be to reanalyze all the Cepheid data from the different groups in a completely consistent manner, beginning with the raw *HST* images. The Key Project team is doing this (Gibson et al. 2000); if needed, revised distance moduli for the SN calibrators can then be used in Table 2.6 to determine a new estimate for M_V^0 and H_0.

More information about the structure of the Leo I group can be determined by relying on the supernovae themselves. For instance, the galaxy NGC 3389, host of the SN Ia 1967C, is sometimes considered a member of the Leo I group, though various group-finding algorithms disagree about its inclusion (Schneider

1989). We have used MLCS to analyze the photoelectric light curve of SN 1967C (de Vaucouleurs 1968), and conclude that NGC 3389 is at $\mu \simeq 32.6$, placing it significantly farther away than the other Leo I group galaxies.

We can also compare the distance of NGC 3368 with that of NGC 3627, in the Leo triplet, located on the sky roughly 8 degrees from the Leo I group. NGC 3627 was the host of the SN Ia 1989B, which had a light curve similar to that of SN 1998bu. From our MLCS analysis of the SN 1989B we derive $\langle V_{\rm Bmax} \rangle = 12.01$, $A_V = 0.99$ mag, and $\Delta = 0.19$ mag, yielding $m_V^0 = 10.83 \pm 0.19$. Combined with our result for SN 1998bu, $m_V^0 = 10.93 \pm 0.18$, we see that NGC 3627 is most likely ~ 0.1 mag closer than NGC 3368, though there is a bit of uncertainty (arising from the correlated uncertainties in the MLCS analysis of each supernova). Since the supernovae only tell us the distances of their hosts, without further information we cannot determine the relationship between the Leo I Group and the Leo triplet as a whole. *HST* data has been taken to measure a Cepheid distance to NGC 3627 directly; with our analysis of SN 1989B and taking $M_V^0 = -19.34 \pm 0.17$ derived from all four calibrators, we predict the distance modulus for NGC 3627, $\mu = 30.17 \pm 0.25$. In a very recent preprint, Saha et al. (1999) report their Cepheid distance to NGC 3627, with the result $\mu = 30.22 \pm 0.12$, in excellent agreement with our expectation. With this new Cepheid distance, we will be able to use SN 1989B as a calibrator in the future; including it in the analysis presented here would decrease our estimate H_0 by merely 0.3 km s^{-1} Mpc^{-1}.

This discussion strengthens our opinion that the sample of calibrating SNe Ia should be restricted to those for which Cepheid distances have been directly determined, rather than relying on indirect association with other members of a

group or cluster. Suntzeff et al. (1999) make this point with two SNe Ia in the Fornax cluster, SN 1980N in NGC 1316 and SN 1992A in NGC 1380. Adopting the Cepheid distance to NGC 1365 (Silbermann et al. 1999; Madore et al. 1999) as the distance to the cluster and these two galaxies in particular leads to a correlated systematic effect on the SN Ia calibration. The analysis of Suntzeff et al. (1999) indicates that NGC 1365 is probably foreground to both NGC 1316 and NGC 1380 by ~ 0.3 mag. We have analyzed the SN Ia in both of these galaxies with MLCS and concur that NGC 1365 is closer than NGC 1316 by ~ 0.3 mag. Our result for NGC 1380 is slightly different, with the MLCS analysis suggesting NGC 1365 is closer than NGC 1380 by only ~ 0.05 mag. Nevertheless, this is exactly the sort of systematic error we wish to avoid, since the number of calibrators is small and systematic errors in any of them can significantly affect the mean.

2.6 Conclusion

We have presented extensive photometric and spectroscopic observations of SN 1998bu as well as an MLCS analysis to determine the intrinsic luminosity (relative to the fiducial) of the supernova and the extinction along the line of sight. Using the Cepheid distance to NGC 3368 and three other SN Ia host galaxies, we have calibrated the absolute magnitude of our fiducial SN Ia, and applied this calibration to a set of 42 distant SNe Ia to derive a Hubble constant, $H_0 = 64^{+8}_{-6}$ km s^{-1} Mpc^{-1}, including systematic uncertainties such as in the distance to the LMC. The statistical uncertainty in our estimate (~ 0.17 mag) arises from the fact that we have only 4 local calibrators; this uncertainty will be reduced by more SNe Ia occurring in

galaxies with *HST* Cepheid distances, or more controllably by measuring more Cepheid distances to the host galaxies of well-observed SNe Ia (SN 1998aq in NGC 3982 is an excellent target, for example). Reducing the systematic uncertainty in the Hubble constant ($\sim$ 0.15 mag) will be more difficult as it will entail a better understanding of the Cepheid distance scale and most importantly, a definitive distance modulus for the LMC. Nevertheless, we are optimistic that these reductions are possible, and eagerly await the day in the not-too-distant future when the Hubble constant is known to better than 10%.

We gratefully acknowledge the efforts of the staff maintaining the many telescopes we have utilized. We also thank those engaged in searching the skies for new supernovae, and particularly the amateur astronomers who dedicate themselves to the task. Thanks also to Dan Green and Brian Marsden of the IAU Central Bureau for Astronomical Telegrams, who play a pivotal role in disseminating information about new supernova discoveries and enable quick follow-up. We are grateful to Di Harmer and Richard Green for accomodating our WIYN Target of Opportunity observations, as well as Bob Joseph for allowing us IRTF observations during engineering time. We thank F. Patat for providing absorption-line velocities for several SNe Ia in electronic format, and M. Hanson for advice on reducing infrared spectra. We are grateful to Chris Kochanek, Dimitar Sasselov and Alyssa Goodman for helpful discussions, and to the referee, Nick Suntzeff, for suggesting many improvements to the manuscript. P.J.B. thanks the W. M. Keck Foundation for its support of astronomy at Wellesley College through the Keck Northeast Astronomy Consortium and the Wellesley College Brachman Hoffman Research

Grant. E.K.G. gratefully acknowledges support by Dennis Zaritsky through NASA LTSA grant NAG-5-3501 and by NASA through grant HF-01108.01-98A from the Space Telescope Science Institute, which is operated by the Association of Universities for Research in Astronomy, Inc., under NASA contract NAS5-26555. This work was also supported by NSF grants AST-9528899 (R.P.K.), AST-9417213 (A.V.F.), and AST-9417359 (P.J.B.), as well as through an NSF Graduate Research Fellowship (S.J.).

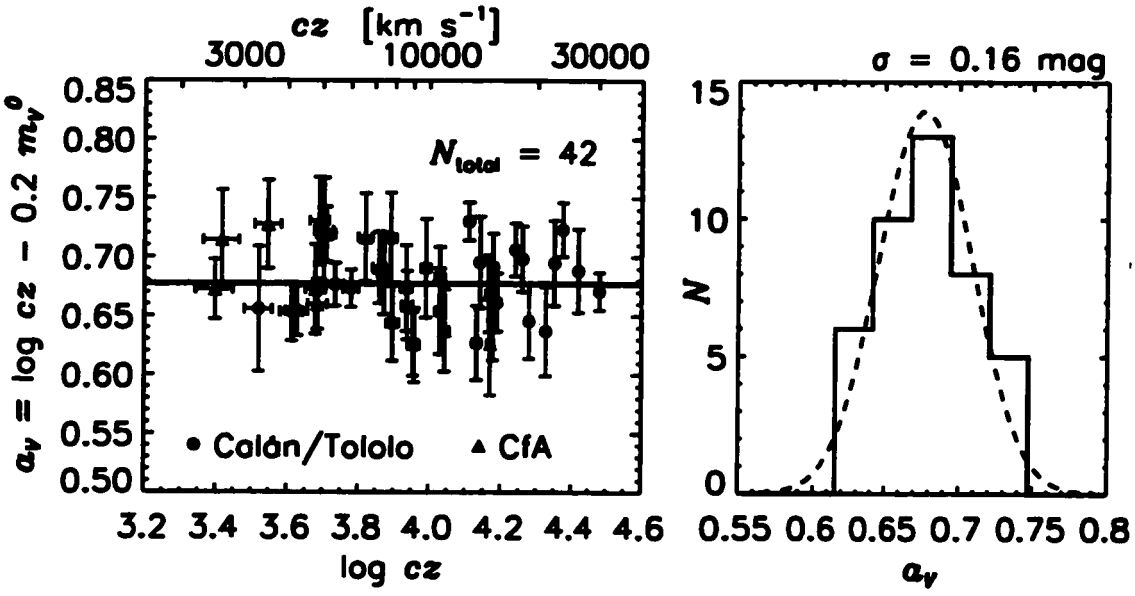

Figure 2.11.— Ridge-line intercept versus recession velocity for the Hubble-flow sample (*left*) and ridge-line intercept histogram (*right*). The best-fit mean intercept and its formal uncertainty are $a_V = 0.6772 \pm 0.0049$.

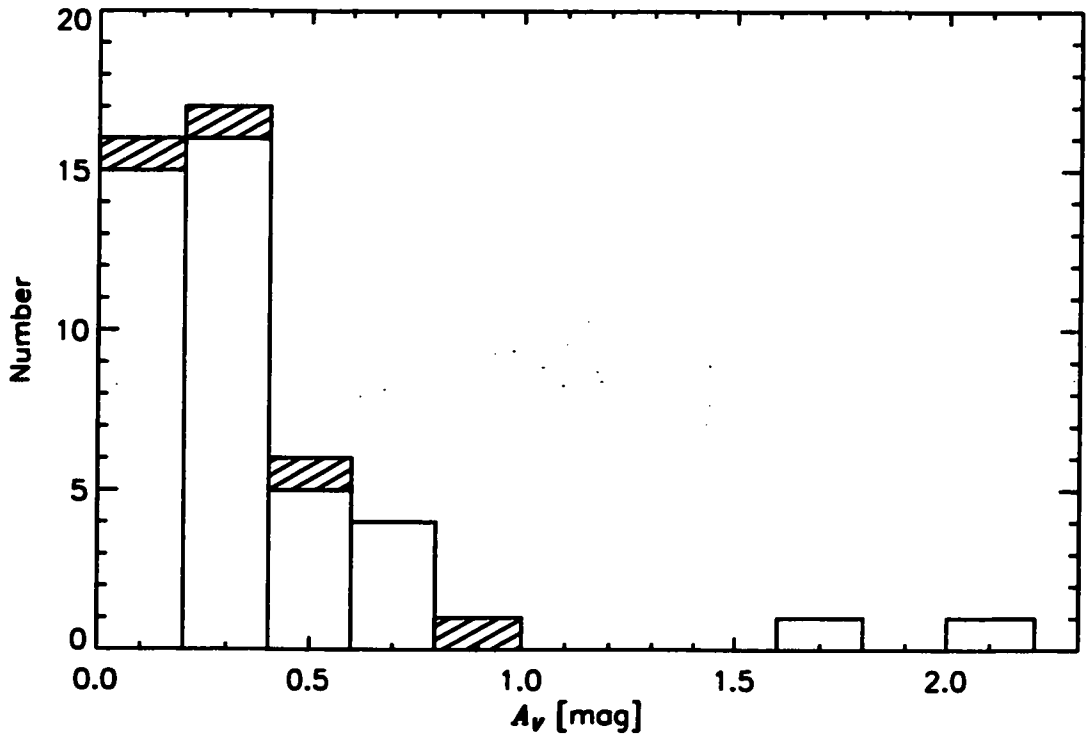

Figure 2.12.— Distribution of the total visual extinction, A_V, along the lines-of-sight to the 42 Hubble-flow SNe Ia (*clear*) and the 4 calibrators (*shaded*). The extinction estimates are derived from the MLCS analysis of the $BVRI$ light curves.

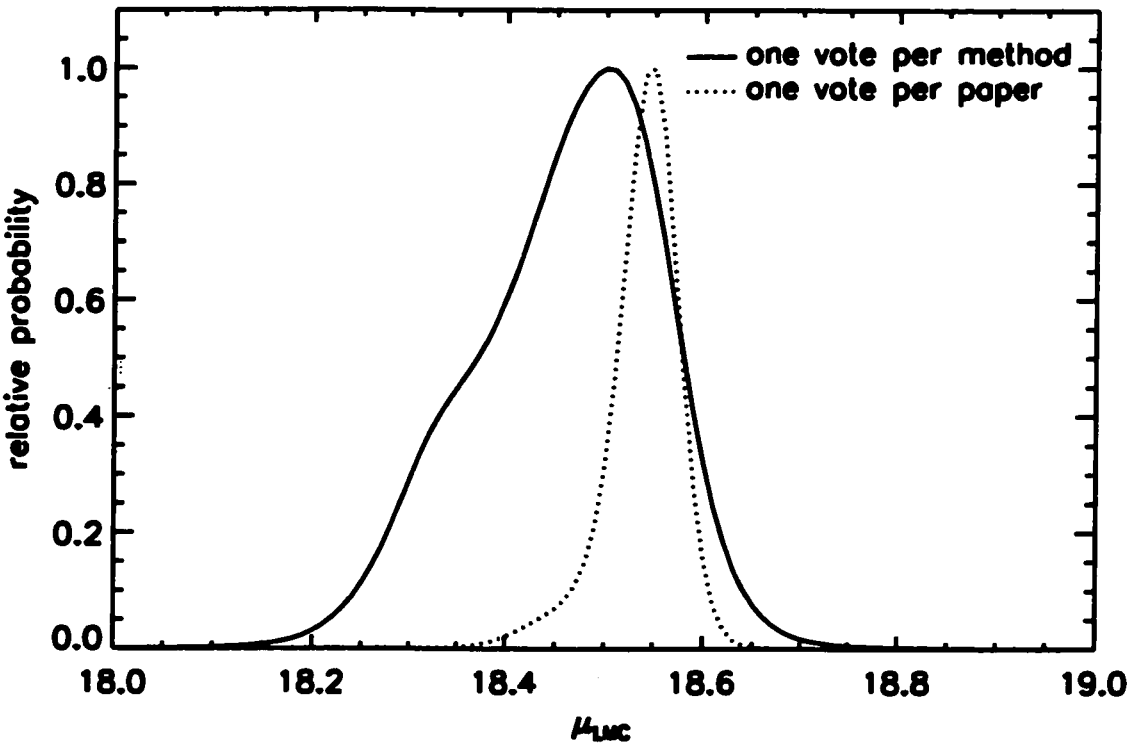

Figure 2.13.— Probability density functions for the mean LMC distance modulus based on a Bayesian analysis of 19 recent measurements. The dotted curve shows the pdf if each measurement is treated independently, while the solid curve shows the PDF when each distance measuring *technique* is given equal weight. For clarity, both distributions have been rescaled to peak at unity.

2.7 References

Alcock, C., et al. 1997, ApJ, 482, 89

Ardeberg, A., & de Groot, M. 1973, A&A, 28, 295

Ayani, K., Nakatani, H., & Yamaoka, H. 1998, IAU Circ., 6905

Barbon, R., Benetti, S., Cappellaro, E., Rosino, L., & Turatto, M. 1990, A&A, 237, 79

Beaulieu, J. P., et al. 1997, A&A, 318, L47

Bergeat, T. J., Knapik, A., & Rutily, B. 1998, A&A, 332, L53

Bessell, M. S. 1990, PASP, 102, 1181

Boisseau, J. R., & Wheeler, J. C. 1991, AJ, 101, 1281

Bowers, E. J. C., Meikle, W. P. S., Geballe, T. R., Walton, N. A., Pinto, P. A., Dhillon, V. S., Howell, S. B., & Harrop-Allin, M. K. 1997, MNRAS, 290, 663

Branch, D., Lacy, C. H., McCall, M. L., Uomoto, A., Wheeler, J. C., Wills, B. J., & Sutherland, P. G. 1983, ApJ, 270, 123

Branch, D. 1998, ARA&A, 36, 17

Branch, D., & Miller, D. L. 1993, ApJ, 405, L5

Buta, R. J., & Turner, A. 1983, PASP, 95, 72

Cardelli, J. A., Clayton, G. C., & Mathis, J. S. 1989, ApJ, 345, 245

Carter, B. S., & Meadows, V. S. 1995, MNRAS, 276, 734

Centurion, M., Bonifacio, P., Walton, N., & King, D. 1998, IAU Circ., 6918

Chaboyer, B. 1998, Physics Reports, 307, 23

Chiosi, C., Wood, P. R., & Capitanio, N. 1993, ApJS, 86, 541

Cole, A. A. 1998, ApJ, 500, L137

de Vaucouleurs, G. 1968, Contrib. McDonald Obs., 426

de Vaucouleurs, G., et al. 1991, in Third Reference Catalogue of Bright Galaxies, New York: Springer-Verlag

Di Benedetto, G. P. 1997, ApJ, 486, 60

Efstathiou, G., Bridle, S. L., Lasenby, A. N., Hobson, M. P., & Ellis, R. S. 1999, MNRAS, 303, L47

Elias, J. H., Frogel, J. A., Hackwell, J. A., & Persson, S. E. 1981, ApJ, 251, L13

Elias, J. H., Frogel, J. A., Matthews, K., & Neugebauer, G. 1982, AJ, 87, 1029

Elias, J. H., Matthews, K., Neugebauer, G., & Persson, S. E. 1985, ApJ, 296, 379

Fabricant, D., Cheimets, P., Caldwell, N., & Geary, J. 1998, PASP, 110, 79

Feast, M. W., & Catchpole, R. M. 1997, MNRAS, 286, L1

Fernley, J., Barnes, T. G., Skillen, I., Hawley, S. L., Hanley, C. J., Evans, D. W., Solano, E., & Garrido, R. 1998, A&A, 330, 515

Filippenko, A. V. 1982, PASP, 94, 715

Filippenko, A. V. 1997, ARA&A, 35, 309

Filippenko, A. V., Porter, A. C., Sargent, W. L. W., & Schneider, D. P. 1986, AJ, 92, 1341

Filippenko, A. V., et al. 1992a, ApJ, 384, L15

Filippenko, A. V., Richmond, M. W., Branch, D., Gaskell, M., Herbst, W., Ford,

C. H., Treffers, R. R., Matheson, T., Ho, L. C., Dey, A., Sargent, W. L. W., Small, T. A., & Van Breugel, W. J. M. 1992b, AJ, 104, 1543

Freedman, W. L., & Madore, B. F. 1990, ApJ, 365, 186

Freedman, W. L., et al. 1994, Nature, 371, 757

Freedman, W. L., Mould, J. R., Kennicutt, R. C., & Madore, B. F. 1998, to appear in "Cosmological Parameters and the Evolution of the Universe", IAU Symposium 183 (astro-ph/9801080)

Frogel, J. A., Gregory, B., Kawara, K., Laney, D., Phillips, M. M., Terndrup, D., Vrba, F., & Whitford, A. E. 1987, ApJ, 315, L129

Garnavich, P. M., et al. 1998a, ApJ, 493, L53

Garnavich, P. M., et al. 1998b, ApJ, 509, 74

Gibson, B. K., et al. 2000, ApJ, 529, 73

Gieren, W. P., Fouqué, P., & Gómez, M. 1998, ApJ, 496, 17

Giovanelli, R., Haynes, M. P., Freudling, W., da Costa, L. N., Salzer, J. J., & Wegner, G. 1998, ApJ, 505, L91

Goldhaber, G., et al. 1997, in Thermonuclear Supernovae, eds. Ruiz-Lapuente, P., Canal, R., & Isern, J., Netherlands: Kluwer Academic Publishers, 777

Gould, A. 1994, ApJ, 426, 542

Gould, A., & Uza, O. 1998, ApJ, 494, 118

Graham, J. A., et al. 1997, ApJ, 477, 535

Gratton, R. G., Fusi Pecci, F., Carretta, F., Clementini, G., Corsi, C. E., & Lattanzi, M. 1997, ApJ, 491, 749

Guinan, E. F., Fitzpatrick, E. L., DeWarf, L. E., Maloney, F. P., & Maurone, P. A. 1998, ApJ, 509, L21

Hamuy, M., Phillips, M. M., Maza, J., Wischnjewsky, M., Uomoto, A., Landolt, A. U., & Khatwani, R. 1991, AJ, 102, 208

Hamuy, M., et al. 1993, AJ, 106, 2392

Hamuy, M., Phillips, M. M., Maza, J., Suntzeff, N. B., Schommer, R. A., & Avilés, R. 1995, AJ, 109, 1

Hamuy, M., Phillips, M. M., Suntzeff, N. B., Schommer, R. A., Maza, J., & Avilés, R. 1996a, AJ, 112, 2391

Hamuy, M., Phillips, M. M., Suntzeff, N. B., Schommer, R. A., Maza, J., & Avilés, R. 1996b, AJ, 112, 2398

Hamuy, M., et al. 1996c, AJ, 112, 2408

Hamuy, M., Phillips, M. M., Suntzeff, N. B., Schommer, R. A., Maza, J., Smith, R. C., Lira, P., & Avilés, R. 1996d, AJ, 112, 2438

Hamuy, M., & Pinto, P. 1999, AJ, in Harmonizing Cosmic Distance Scales in a Post-Hipparcos Era (astro-ph/9812084)

Harris, W. E., Fitzgerald, M. P., & Reed, B. C. 1981, PASP, 93, 507

Hatano, K., Branch, D., & Deaton, J. 1998, ApJ, 502, 177

Hatano, K., Branch, D., Fisher, A., Baron, E., & Filippenko, A. V. 1999, ApJ, 525, 881

Hill, R. J., et al. 1998, ApJ, 496, 648

Hunt, L. K., Mannucci, F., Testi, L., Migliorini, S., Stanga, R. M., Baffa, C., Lisi, F., & Vanzi, L. 1998, AJ, 115, 2594

Jerjen, H., & Tammann, G. A. 1993, A&A, 276, 1

Johnson, H. L., MacArthur, J. W., & Mitchell, R. I. 1968, ApJ, 152, 465

Kennicutt, R. C., et al. 1998, ApJ, 498, 181

Kim, A., Goobar, A., & Perlmutter, S. 1996, PASP, 108, 190

Kirshner, R. P., Oke, J. B., Penston, M. V., & Searle, L. 1973, ApJ, 185, 303

Kirshner, R. P., & Oke, J. B. 1975, ApJ, 200, 574

Kirshner, R. P., et al. 1993, ApJ, 415, 589

Kochanek, C. S. 1997, ApJ, 491, 13

Kowal, C. T. 1968, AJ, 73, 1021

Landolt, A. U. 1992, AJ, 104, 340

Lauer, T. R., & Postman, M. 1994, ApJ, 425, 418

Leibundgut, B. 1989, PhD thesis, University of Basel

Leibundgut, B., Kirshner, R. P, Filippenko, A. V., Shields, J. C., Foltz, C. B., Phillips, M. M., & Sonneborn, G. 1991a, ApJ, 371, L23

Leibundgut, B., Tammann, G. A., Cadonau, R., & Cerrito, D. 1991b, A&AS, 89, 537

Leibundgut, B., et al. 1993, AJ, 105, 301

Leibundgut, B., et al. 1996, ApJ, 466, L21

Lineweaver, C. H. 1998, ApJ, 505, L69

Lira, P. 1995, Master's Thesis, University of Chile

Lira, P., et al. 1998, AJ, 115, 234

Luri, X., Gómez, A. E., Torra, J., Figueras, F., & Mennessier, M. O. 1998, A&A, 335, L81

Luri, X., Torra, J., Figueras, F., Gómez, A. E., Goupil, M. J., & Beaulieu, J. P. 1998, Ap&SS, 263, 215

Lynden-Bell, D., & Lahav, O. 1988, in Large-Scale Motions in the Universe, eds. V. C. Rubin, & G. V. Coyle, Princeton: Princeton University Press

Madore, B. F., & Freedman, W. L. 1991, PASP, 103, 933

Madore, B. F., & Freedman, W. L. 1998, ApJ, 492, 110

Madore, B. F., et al. 1999, ApJ, 515, 29

Massey, P., Strobel, K., Barnes, J. V., & Anderson, E. 1988, ApJ, 328, 315

Meikle, P., Hernandez, M., Fassia, A., & Iglesias, J. 1998, IAU Circ., 6905

Meikle, P., & Hernandez, M. 2000, Mem. Soc. Astron. Ital., 71, 299 (astro-ph/9902056)

Miller, D. L., & Branch, D. 1992, AJ, 103, 379

Mould, J. R., et al. 2000, ApJ, 529, 786

Munari, U., & Zwitter, T. 1997, A&A, 318, 269

Munari, U., Barbon, R., Tomasella, L., & Rejkuba, M. 1998, IAU Circ., 6902

Nakano, S., & Aoki, M. 1998, IAU Circ., 6899

Nevalainen, J., & Roos, M. 1998, A&A, 339, 7

Nørgaard-Nielsen, H. U., Hansen, L., Jørgensen, H. E., Aragón Salamanca, A., Ellis, R. S., & Couch, W. J. 1989, Nature, 339, 523

Nugent, P., Phillips, M., Baron, E., Branch, D., & Hauschildt, P. 1995, ApJ, 455, L147

Nugent, P., Kim, A., & Perlmutter, S. 2002, PASP, in press

Oudmaijer, R. D., Groenewegen, M. A. T., & Schrijver, H. 1998, MNRAS, 294, L41

Panagia, N., et al. 1997, BAAS, 191, 1909

Patat, F., Benetti, S., Cappellaro, E., Danziger, I. J., Della Valle, M., Mazzali, P. A., & Turatto, M. 1996, MNRAS, 278, 111

Perlmutter, S., et al. 1995, ApJ, 440, L41

Perlmutter, S., et al. 1998, Nature, 391, 51

Perlmutter, S., et al. 1999, ApJ, 517, 565

Perlmutter, S., Turner, M. S., & White, M. 1999, Phys. Rev. Lett., 83, 670

Persson, S. E., Murphy, D. C., Krzeminski, W., Roth, M., & Rieke, M. J. 1998, AJ, 116, 2475

Phillips, M. M., Wells, L. A., Suntzeff, N. B., Hamuy, M., Leibundgut, B., Kirshner, R. P., & Foltz, C. B. 1992, AJ, 103, 1632

Phillips, M. M. 1993, ApJ, 413, L105

Phillips, M. M., Lira, P., Suntzeff, N. B., Schommer, R. A., Hamuy, M., & Maza, J. 1999, AJ, 118, 1766

Pierce, M. J., & Jacoby, G. H. 1995, AJ, 110, 2885

Press, W. H. 1997, in Unsolved Problems in Astrophysics, eds. J. N. Bahcall and J. P. Ostriker, Princeton: Princeton University Press, 49

Reid, I. N. 1998, AJ, 115, 204

Riess, A. G., Davis, M., Baker, J., & Kirshner, R. P. 1997a, ApJ, 488, L1

Riess, A. G., et al. 1997b, AJ, 114, 722

Riess, A. G., Press, W. H., & Kirshner, R. P. 1995a, ApJ, 438, L17

Riess, A. G., Press, W. H., & Kirshner, R. P. 1995b, ApJ, 445, L91

Riess, A. G., Press, W. H., & Kirshner, R. P. 1996a, ApJ, 473, 88

Riess, A. G., Press, W. H., & Kirshner, R. P. 1996b, ApJ, 473, 588

Riess, A. G., et al. 1998a, AJ, 116, 1009

Riess, A. G., Nugent, P., Filippenko, A. V., Kirshner, R. P., & Perlmutter, S. 1998b, ApJ, 504, 935

Riess, A. G., et al. 1999, AJ, 117, 707

Roos, M., & Harun-or-Rashid, S. M. 1998, A&A, 329, L17

Saha, A., Sandage, A., Labhardt, L., Schwengeler, H., Tammann, G. A., Panagia, N., & Macchetto, F. D. 1995, ApJ, 438, 8

Saha, A., Sandage, A., Labhardt, L., Tammann, G. A., Macchetto, F. D., & Panagia, N. 1996, ApJ, 466, 55

Saha, A., Sandage, A., Labhardt, L., Tammann, G. A., Macchetto, F. D., & Panagia, N. 1997, ApJ, 486, 1

Saha, A., Sandage, A., Tammann, G. A., Labhardt, L., Macchetto, F. D., & Panagia, N. 1999, ApJ, 522, 802

Sandage, A., & Tammann, G. A. 1993, ApJ, 415, 1

Sandage, A., Saha, A., Tammann, G. A., Panagia, N., & Macchetto, F. D. 1992, ApJ, 401, L7

Sasselov, D. D., et al. 1997, A&A, 324, 471

Savage, B., & Mathis, J. 1979, ARA&A, 17, 73

Schaefer, B. 1995, ApJ, 450, L5

Schaefer, B. E. 1998, ApJ, 509, 80

Schlegel, D. J., Finkbeiner, D. P., & Davis, M. 1998, ApJ, 500, 525

Schmidt, B. P., et al. 1998, ApJ, 507, 46

Silbermann, N. A., et al. 1999, ApJ, 515, 1

Smoot, G. F., et al. 1992, ApJ, 396, L1

Stanek, K. Z. 1998, ApJ, submitted (astro-ph/9802307)

Stanek, K. Z., Zaritsky, D., & Harris, J. 1998, ApJ, 500, L41

Stift, M. J. 1995, A&A, 301, 776

Suntzeff, N. B., et al. 1999, AJ, 117, 1175

Szentgyorgyi, A. H., et al. 1999, in preparation

Tammann, G. A. 1998, in "General Relativity", 8th Marcel Grossmann Symposium, ed. T. Piran, Singapore: World Scientific (astro-ph/9805013)

Tammann, G. A., & Leibundgut, B. 1990, A&A, 236, 9

Tanvir, N. R., Shanks, T., Ferguson, H. C., & Robinson, D. R. T. 1995, Nature, 377, 27

Tanvir, N. R. 1996, in The Extragalactic Distance Scale, eds. Livio, M., Donahue, M., & Panagia, N., United Kingdom: Cambridge University Press, 91 (astro-ph/9611027)

Tegmark, M. 1999, ApJ, 514, L69

Tollestrup, E., et al. 1999, in preparation

Tripp, R. 1998, A&A, 331, 815

Turner, A., et al. 1998, ApJ, 505, 207

Udalski, A. 1998, Acta Astronomia, 48, 383

van Leeuwen, F., Feast, M. W., Whitelock, P. A., & Yudin, B. 1997, MNRAS, 287, 955

Villi, M. 1998, IAU Circ., 6899

Wells, L. A., et al. 1994, AJ, 108, 2233

Wheeler, J. C., Höflich, P., Harkness, R. P., & Spyromilio, J. 1998, ApJ, 496, 908

Whitelock, P. A., van Leeuwen, F., & Feast, M. W. 1997, in Hipparcos Venice '97, ed. Battrick, B., Netherlands: ESA Publications Division, 213 (astro-ph/9706096)

White, M. 1998, ApJ, 506, 495

Zehavi, I., Riess, A. G., Kirshner, R. P, & Dekel, A. 1998, ApJ, 503, 483

Chapter 3

UBVRI Light Curves of 44 Type Ia Supernovae

Saurabh Jha, Robert P. Kirshner, Peter Challis, Peter M. Garnavich, Thomas Matheson, et al. 2002, to be submitted to *The Astronomical Journal*

Abstract

We present *UBVRI* photometry of 44 recent type-Ia supernovae (SNe Ia) observed as part of a continuing monitoring campaign at the Fred Lawrence Whipple Observatory of the Harvard-Smithsonian Center for Astrophysics. This is the largest homogeneously observed and reduced sample of SNe Ia to date, nearly doubling the sample of well-observed, nearby SNe Ia with published multicolor CCD light curves. The large sample of U-band photometry is a unique addition, with important connections to SNe Ia observed at high-redshift. The decline rate of SN Ia U-band

light curves correlates well with the decline rate in other bands, as does the $U-B$ color at maximum light. However, the U-band peak magnitudes show an increased dispersion relative to other bands, even after accounting for extinction and decline rate.

3.1 Introduction

Over the last decade, type Ia supernovae (SNe Ia) have become increasingly sharpened tools for precision cosmology, with applications of these exquisite distance indicators ranging from our galactic neighbors to halfway across the observable Universe (see, e.g., §2.1). These cosmological applications of SNe Ia rely on accurate, high-precision measurements of their light curves in multiple passbands over a period of weeks, presenting a challenge to would-be observers.

The project of collecting a large sample of nearby SNe Ia with high-quality, multicolor CCD photometry to be used in cosmological studies began in earnest in 1990, with the Calán/Tololo survey (Hamuy et al. 1993), which combined a photographic search for SNe in the southern sky with a program of CCD followup photometry obtained with the help of visiting astronomers. Hamuy et al. (1996) present Johnson/Cousins *BVI* photometry of 29 SNe Ia from this project (27 of which were discovered as part of the survey itself) out to redshifts $z \simeq 0.1$.

In 1993, astronomers at the Harvard-Smithsonian Center for Astrophysics (CfA) began a campaign of CCD photometric and spectroscopic monitoring of newly-discovered supernovae at the Fred L. Whipple Observatory (FLWO) on

Mt. Hopkins in southern Arizona, and this program has been ongoing ever since. We employ a similar cooperative observing strategy for the follow-up photometry, whereby the SN monitoring program is allocated a small amount of time each night ($\sim$ 20 minutes), with the observations being carried out by the scheduled observer. Our SN program is also allocated approximately one dedicated night per month, which is used for photometry of the fainter objects, photometric calibration of the SN fields, and template observations after the SN have faded.

Our cooperative observing strategy has been very successful so far. FLWO *BVRI* observations of 22 type Ia supernovae discovered between 1993 and 1996 have been published by Riess et al. (1999) and we have also undertaken *UBVRI* photometry and in-depth analysis of a number of individual SNe Ia observed as part of this program: SN 1998bu (Jha et al. 1999), SN 1999by (Garnavich et al. 2002), SN 1998aq (Boffi et al. 2002, in preparation) and SN 2001V (Mandel et al. 2002, in preparation).

Here we report our *UBVRI* photometry for 44 SNe Ia discovered between 1997 and 2000. The full data set presented here consists of 2190 observations on 338 nights, and is the largest set of homogeneously observed and reduced SN Ia data published to date.

Table 3.1. SNe Ia Discovery and Classification Data

SN Ia	Galaxy	Discovery Date	Discoverer	IAUC	Spectroscopic ID	IAUC
1997E	NGC 2258	1997-01-14.5	R. Kushida	6538	P. Garnavich & R. Kirshner (CfA)	6538
1997Y	NGC 4675	1997-02-02	W. Li et al. (BAO)	6556	A. Filippenko et al., P. Garnavich et al. (CfA)	6557
1997bp	NGC 4680	1997-04-06.5	R. Evans	6613	M. Phillips et al.	6613
1997bq	NGC 3147	1997-04-08.0	S. Laurie (UK)	6616	P. Challis (CfA)	6616
1997br	ESO 576-40	1997-04-10.6	Q. Qiao et al. (BAO)	6623	Q. Qiao et al.	6623
1997cn	NGC 5490	1997-05-14.6	W. Li et al. (BAO)	6661	M. Turatto et al.	6667
1997cw	NGC 105	1997-07-10.8	Q. Qiao et al. (BAO)	6699	Q. Qiao et al.	6699
1997dg	anonymous	1997-09-27.7	Q. Qiao et al. (BAO)	6749	S. Jha et al. (CfA)	6749
1997do	UGC 3845	1997-10-31	Y. Qiu et al. (BAO)	6766	Y. Qiu et al.	6766
1997dt	NGC 7448	1997-11-22.4	Q. Qiao et al. (BAO)	6775	Q. Qiao et al.	6775
1998D	NGC 5440	1998-01-28.9	Y. Qiu et al. (BAO)	6815	Y. Qiu et al.	6815
1998V	NGC 6627	1998-03-12.1	M. Armstrong (UK)	6841	S. Jha et al. (CfA)	6844
1998ab	NGC 4704	1998-04-01.7	J. Wei et al. (BAO)	6858	P. Garnavich et al. (CfA)	6858
1998bp	NGC 6495	1998-04-29.1	M. Armstrong (UK)	6890	F. Patat & M. Maia	6890
1998co	NGC 7131	1998-06-21	W. Johnson	6950	P. Garnavich et al. (CfA)	6950
1998de	NGC 252	1998-07-23	M. Modjaz et al. (LOSS)	6977	P. Garnavich et al. (CfA)	6980
1998dh	NGC 7541	1998-07-20.5	W. Li et al. (LOSS)	6978	P. Garnavich et al. (CfA)	6980
1998dk	UGC 139	1998-08-19.4	J. King et al. (LOSS)	6991	A. Filippenko	6997
1998dm	MCG-01-4-44	1998-08-22.5	M. Modjaz et al. (LOSS)	6993	A. Filippenko	6997
1998dx	UGC 11149	1998-09-10.2	M. Modjaz et al. (LOSS)	7011	S. Jha et al. (CfA)	7011
1998ec	UGC 3576	1998-09-26.8	Y. Qiu et al. (BAO)	7022	S. Jha et al. (CfA)	7024
1998ef	UGC 646	1998-10-18.3	W. Li et al. (LOSS)	7032	A. Filippenko	7032
1998eg	UGC 12133	1998-10-19.9	T. Boles (UK)	7033	M. Salvo et al., S. Jha et al. (CfA)	7037
1998es	NGC 632	1998-11-13.3	E. Halderson et al. (LOSS)	7050	S. Jha et al. (CfA)	7054

Table 3.1. Continued

SN Ia	Galaxy	Discovery Date	Discoverer	IAUC	Spectroscopic ID	IAUC
1999X	CGCG 180-22	1999-01-23.2	M. Schwartz (TO)	7105	P. Garnavich et al. (CfA)	7105
1999aa	NGC 2595	1999-02-11.0	R. Arbour (UK)	7108	A. Filippenko et al.	7108
1999ac	NGC 6063	1999-02-26.5	M. Modjaz et al. (LOSS)	7114	M. Phillips, A. Filippenko	7122
1999cc	NGC 6038	1999-05-08.3	M. Schwartz (TO)	7163	P. Garnavich et al. (CfA)	7169
1999cl	NGC 4501 (M88)	1999-05-29	M. Papenkova et al. (LOSS)	7185	P. Garnavich et al. (CfA)	7190
1999cw	MCG-01-02-001	1999-06-28.5	R. Johnson & W. Li (LOSS)	7211	L. Rizzi et al.	7216
1999dq	NGC 976	1999-09-02.5	W. Li (LOSS)	7247	S. Jha et al. (CfA)	7250
1999ef	UGC 607	1999-10-09	J. Mueller	7275	M. Kuchner & D. Branch	7275
1999ej	NGC 495	1999-10-18.3	A. Friedman et al. (LOSS)	7286	S. Jha et al. (CfA)	7298
1999ek	UGC 3329	1999-10-20.5	R. Johnson & W. Li (LOSS)	7286	L. Strolger et al., S. Jha et al. (CfA)	7300
1999gd	NGC 2623	1999-11-24.5	W. Li (LOSS)	7319	A. Filippenko & P. Garnavich	7328
1999gh	NGC 2986	1999-12-03.8	K. Takamizawa	7328	A. Filippenko & P. Garnavich	7328
1999gp	UGC 1993	1999-12-23.2	M. Papenkova & W. Li (LOSS)	7337	S. Jha et al. (CfA)	7341
2000B	NGC 2320	2000-01-11.0	P. Antonini et al.	7347	F. Colas et al.	7351
2000ce	UGC 4195	2000-05-08.1	T. Puckett (POSS)	7417	S. Jha et al. (CfA)	7422
2000cf	MCG+11-19-25	2000-05-09.2	T. Puckett & A. Sehgal (POSS)	7421	S. Jha et al. (CfA)	7423
2000cn	UGC 11064	2000-06-02.5	M. Papenkova & W. Li (LOSS)	7436	S. Jha et al. (CfA), M. Turatto et al.	7437
2000cx	NGC 524	2000-07-17.5	C. Yu et al. (LOSS)	7458	R. Chornock et al.	7463
2000dk	NGC 382	2000-09-18.3	S. Beckmann & W. Li (LOSS)	7493	S. Jha et al. (CfA)	7494
2000fa	UGC 3770	2000-11-30.5	A. Friedman & W. Li (LOSS)	7533	T. Matheson et al. (CfA)	7535

3.2 Data and Reduction

3.2.1 Discovery

Our program of supernova photometry consists solely of follow-up; we search only our email, not the sky, to find new supernovae. A number of observers, both amateur and professional, are engaged in searching for supernovae. We rely on these searches, as well as prompt notification of candidates, coordinated by Dan Green and Brian Marsden of the IAU's Central Bureau for Astronomical Telegrams (CBAT), with confirmed SNe reported in the IAU Circulars. In some cases the SN discoverers provide spectroscopic classification of the new objects, but generally spectroscopy is obtained by others, and reported separately in the IAU Circulars. With our spectroscopic SN follow-up program at the F. L. Whipple Observatory 1.5m telescope and FAST spectrograph (Fabricant et al. 1998), we have classified a large fraction of the new, nearby supernovae reported over the last several years.

Given a newly discovered and classified supernova, several factors help determine whether or not we include it in our monitoring program. Because of their importance, SNe Ia are often given higher priority, but factors such as ease of observability (southern targets and those discovered far to the west are less appealing), supernova phase (objects whose spectra indicate they are after maximum light are given lower priority), redshift (more nearby objects are favored), as well as the number of objects we are already monitoring are significant. Our final sample of well-observed SNe Ia, then, is not one obtained from a single well-defined set of criteria, and selection effects in both the searches and follow-up may make the sample unsuitable for

some applications (such as determining the intrinsic luminosity function of SNe Ia, for example). A thorough discussion of the selection biases in the Calán/Tololo supernova search and follow-up campaign can be found in Hamuy & Pinto (1999).

The discovery data for the sample of SNe Ia presented here are given in Table 3.1. All of the SNe Ia listed were discovered with CCD images, except for SN 1997bp which was discovered visually, and SN 1999ef and SN 1999gh which were discovered photographically. We make special note of new, systematic CCD supernova searches that have provided the great majority of our sample: the Beijing Astronomical Observatory Supernova Survey (Li et al. 1996; designated as BAO in Table 3.1), the UK Nova/Supernova Patrol (Armstrong & Hurst 1996; UK), the Puckett Observatory Supernova Search (Puckett 1998; POSS), the Tenagra Observatories supernova patrol (Schwartz 1997; TO), and the Lick Observatory Supernova Search (Treffers et al. 1997; LOSS), which is now part of the Lick Observatory and Tenagra Observatory Supernova Searches (Schwartz et al. 2000; LOTOSS). In addition, we note in Table 3.1 supernovae whose classification as SNe Ia is from our spectroscopic monitoring program described above (designated as "CfA").

3.2.2 Observations

All the photometry presented here was obtained with the F. L. Whipple Observatory (FLWO) 1.2m telescope, with either the "AndyCam" CCD camera or the "4Shooter" 2x2 CCD mosaic (Szentgyorgyi et al. 2002, in preparation). Both instruments use thinned, backside illuminated, anti-reflective coated Loral 2048^2 CCD detectors, situated at the f/8 Cassegrain focus. The pixel scale is approximately $0\farcs33$ per pixel,

yielding a field of view of over 11′ on a side for each chip. All the data were taken in a 2x2 binned mode, resulting in a sampling of 0.″66 per pixel, which is well matched to the typical image quality (1.″5 to 2″ FWHM). Observations using the 4Shooter taken before October 1998 were made with the "chip 1" CCD detector, while those taken afterwards were made on "chip 3", trading off slightly improved quantum efficiency for slightly inferior cosmetic characteristics.

Both instruments have good near-ultraviolet and near-infrared response, and our observations have been in the Johnson *UBV* and Kron-Cousins *RI* bandpasses. The data were taken with two *UBVRI* filtersets, the "SAO" set and the newer "Harris" set. Observations before December 1998 were taken with the SAO filterset (the same described by Riess et al. 1999 and Jha et al. 1999), while those taken after May 1999 were taken with the Harris set. Between December 1998 and May 1999 only the Harris *UBVR* filters were available, and the *I* filter used was from the SAO filterset. Because of the importance of knowing precisely the bandpasses used for a given observation (particularly for supernova photometry), we discuss these in greater detail in §3.2.4.

Our observing approach, combining nightly requests for one or two objects with monthly dedicated nights, allows us to sample the light curves with the appropriate cadence. Generally observations are more frequent when the SNe Ia are near maximum light, and less frequent (but deeper) as each SN Ia fades. During the period of these observations, the FLWO 1.2m was equipped with the 4Shooter or AndyCam usually only during dark time, with an infrared imager on the telescope when the moon was near full. This unfortunately leads to $\sim$1 to 2 week gaps in our light curves, but in most cases the light curves are still well-defined and suitable for

distance analyses.

3.2.3 Differential Photometry

To measure the brightness of the supernova in any image, we perform the photometry differentially with respect to stars in the field of view, allowing for useful measurements even in non-photometric conditions. In general we use as many of these comparison stars (or "field standards") as feasible, choosing stars that are bright enough to be precisely measured but faint enough to not saturate the detector in the late-time, deeper images. In addition, we try to choose comparison stars that cover a range of color comparable to those exhibited by SNe Ia over their evolution, though it is often not possible to find stars in the field that are as blue as SNe Ia at or before maximum light. Figure 3.1 shows R-band finder charts for all of the supernovae and their associated comparison stars.

All of the CCD observations were reduced uniformly, with bad pixel masking, bias subtraction and flat-field correction using the NOAO Image Reduction and Analysis Facility (IRAF) CCDPROC package. In addition, we remove, to the extent possible, the small, but non-negligible, amount of fringing for observations in the I-band.

A major complication in supernova photometry arises in separating light from the SN itself from light from the underlying galaxy at the SN position. Poor subtraction of the background light can have significant effects on the supernova light curve shapes and colors (cf. discussion in Riess et al. 1999; Boisseau & Wheeler 1991). For this reason, we take observations of the supernova fields the following

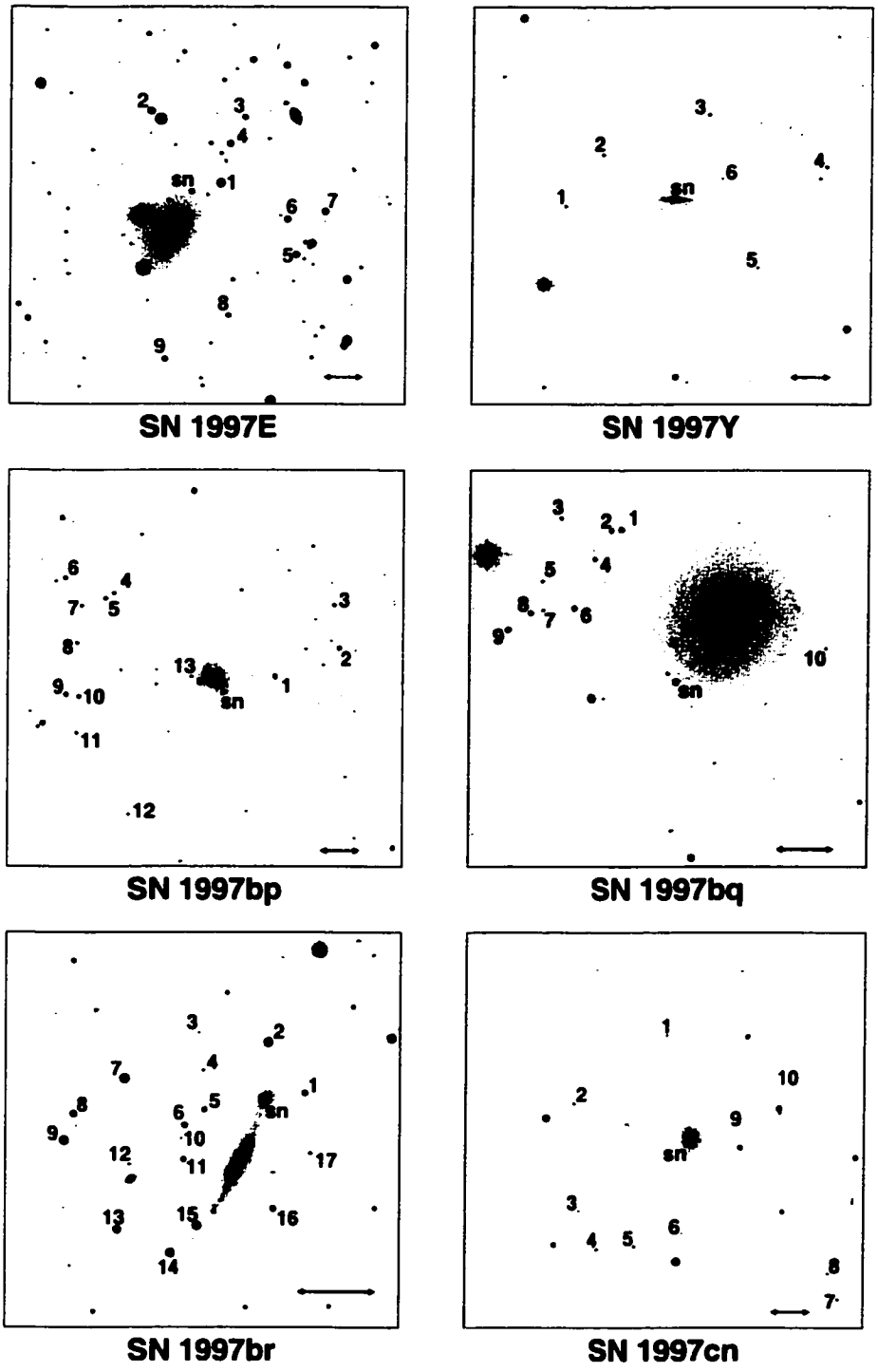

Figure 3.1.— Finder charts for the 44 SNe Ia presented here and associated comparison stars. The images are a combination of all the R-band SN images. North is up and east is to the left. The horizontal double-arrow in the lower right delineates 1′.

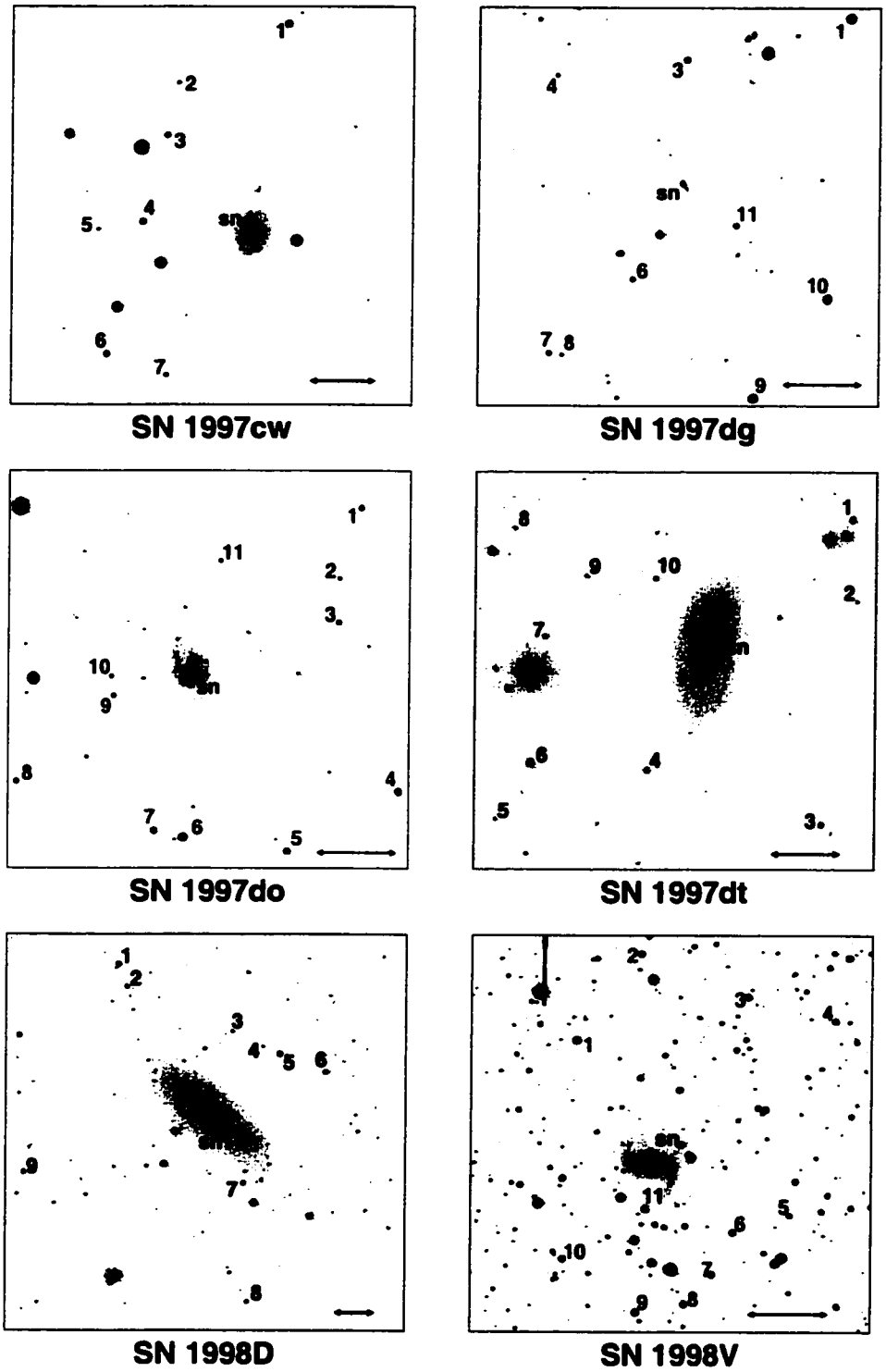

Figure 3.1.— Continued

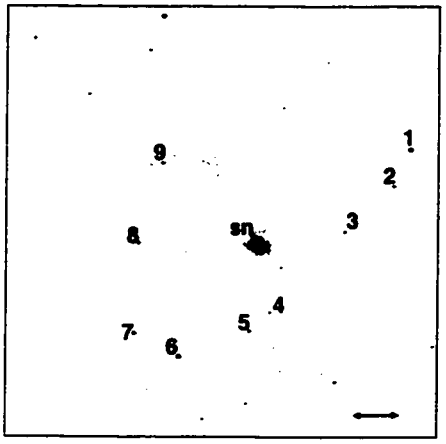

SN 1998ab

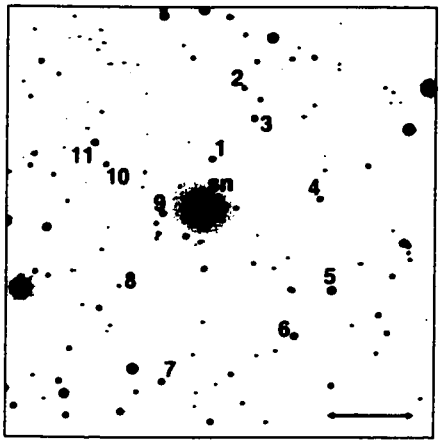

SN 1998bp

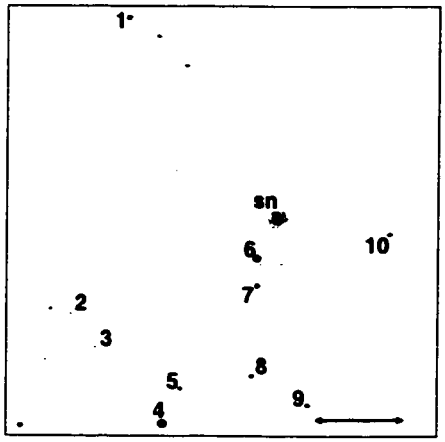

SN 1998co

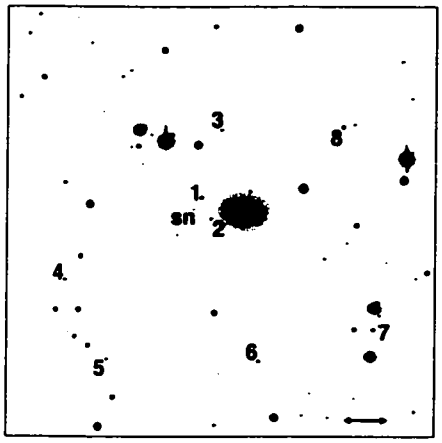

SN 1998de

SN 1998dh

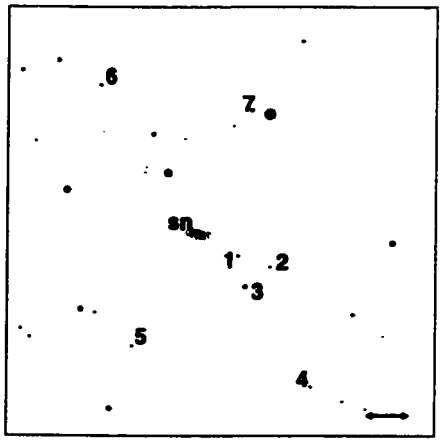

SN 1998dk

Figure 3.1.— Continued

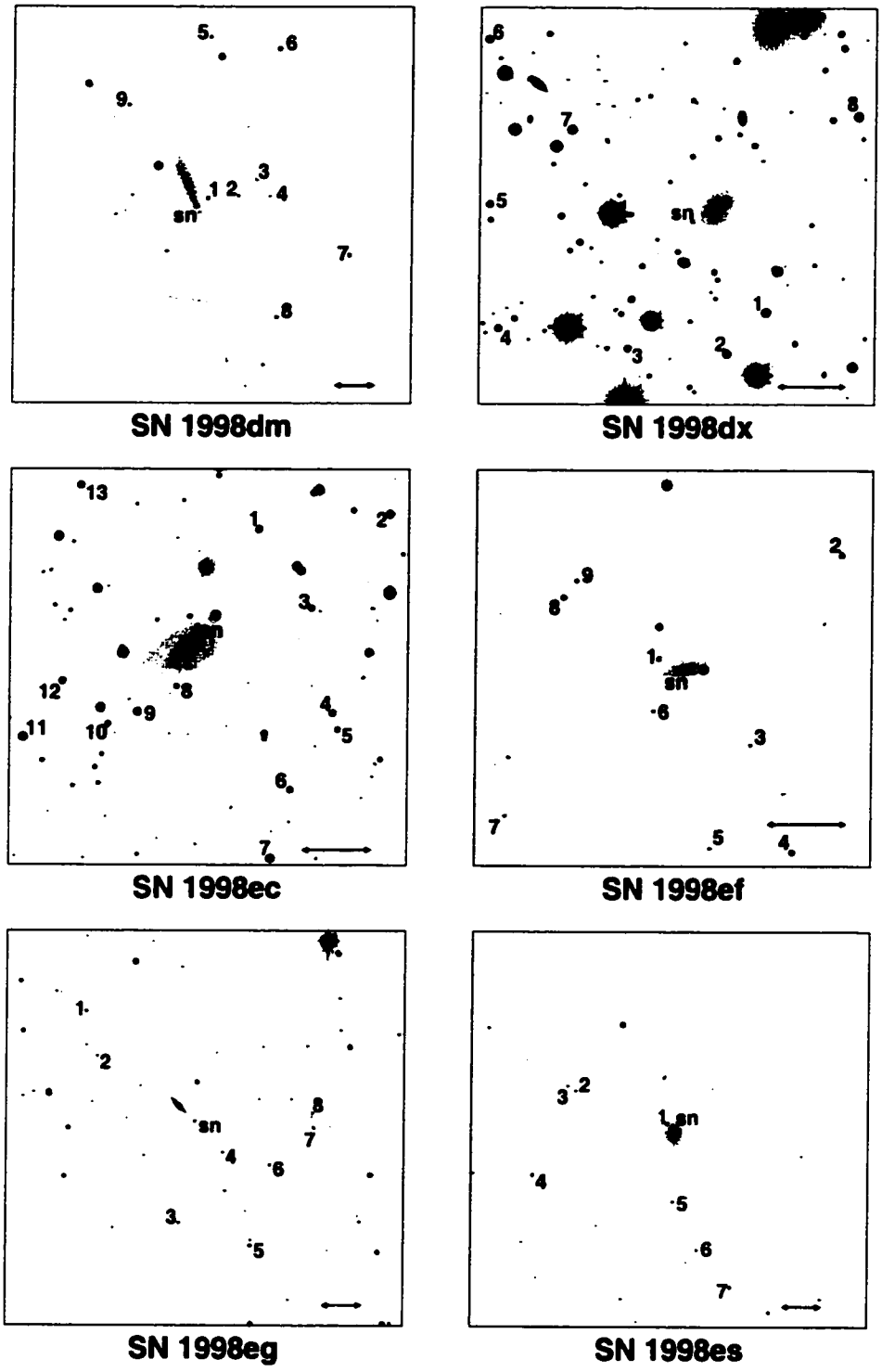

Figure 3.1.— Continued

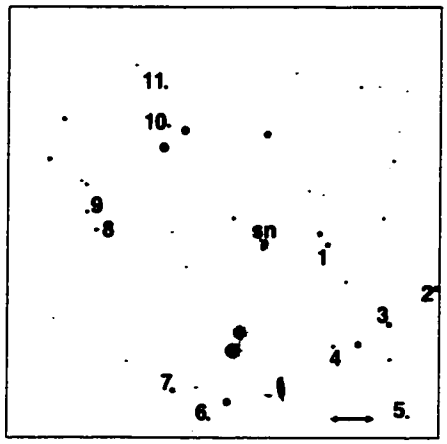

SN 1999X

SN 1999aa

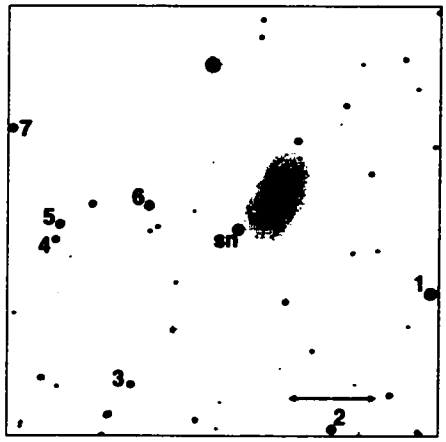

SN 1999ac

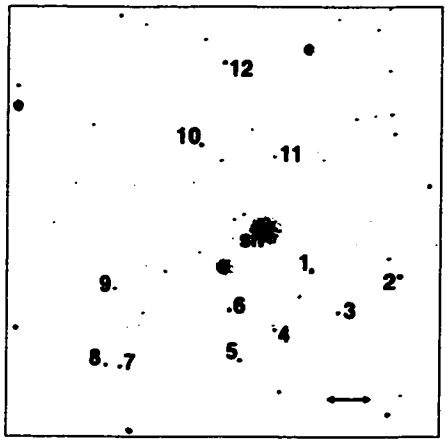

SN 1999cc

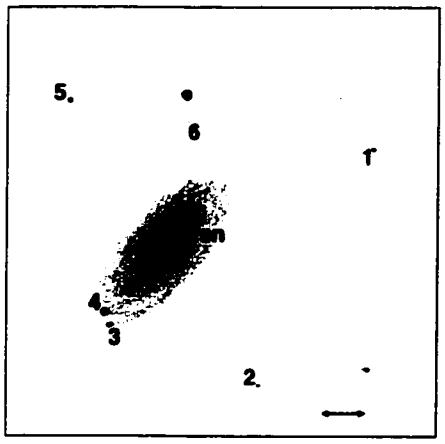

SN 1999cl

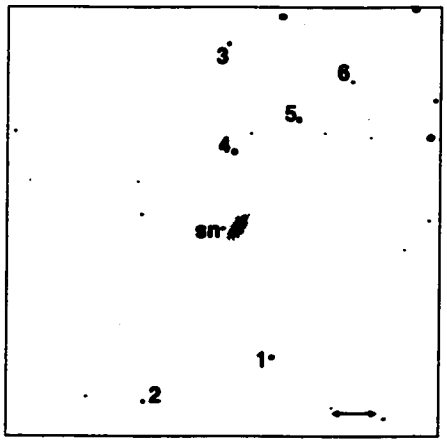

SN 1999cw

Figure 3.1.— Continued

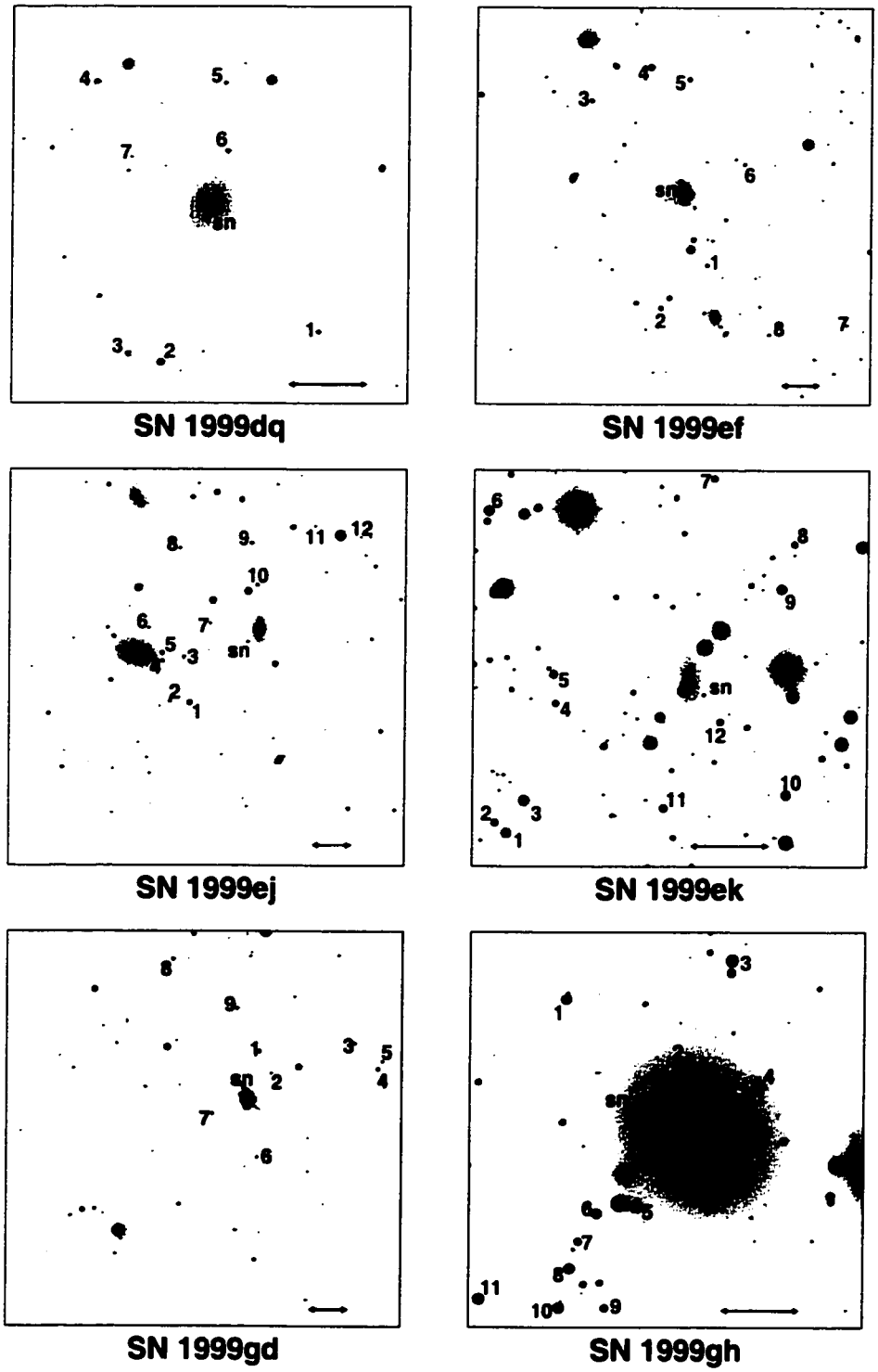

Figure 3.1.— Continued

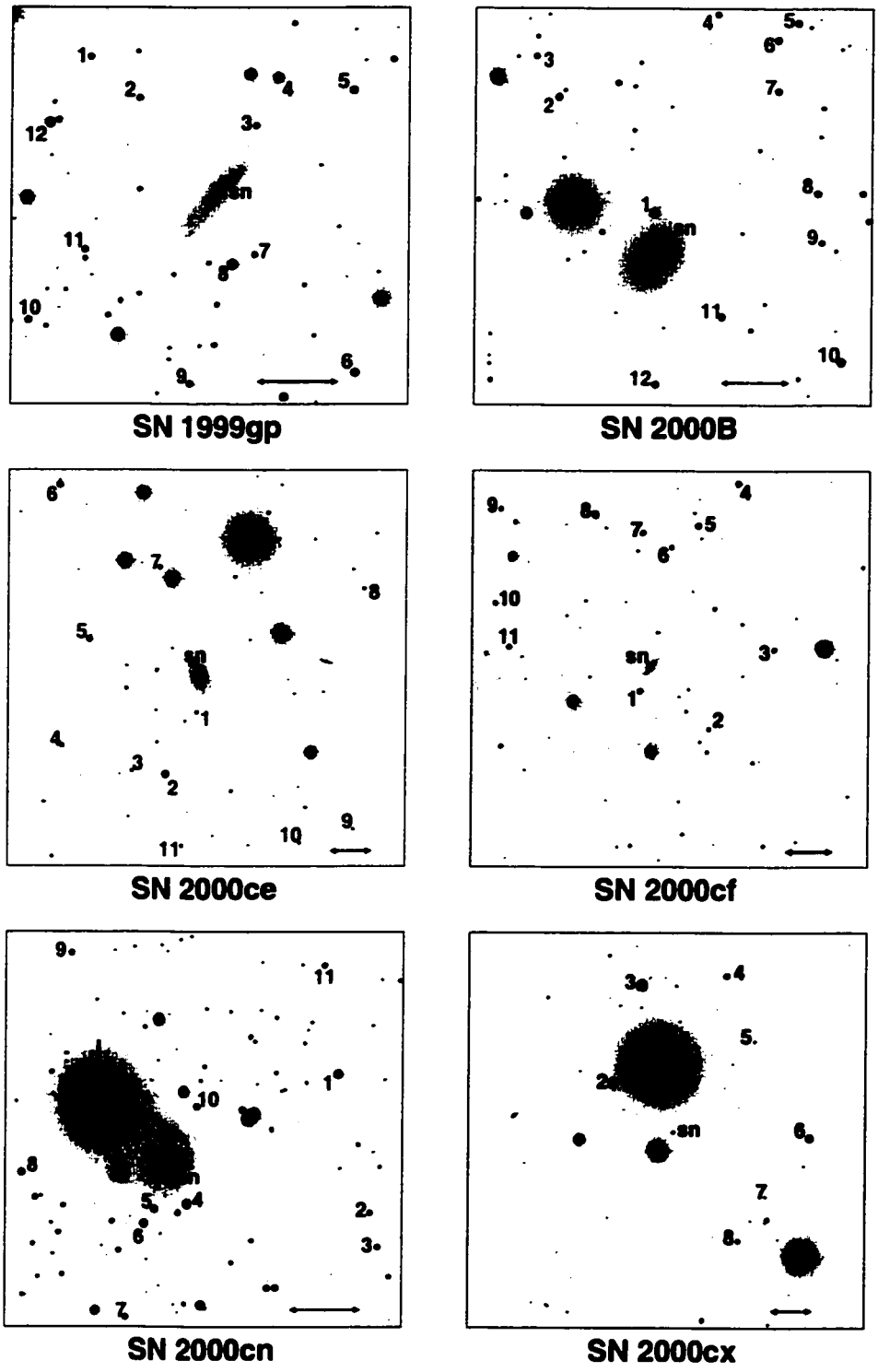

Figure 3.1.— Continued

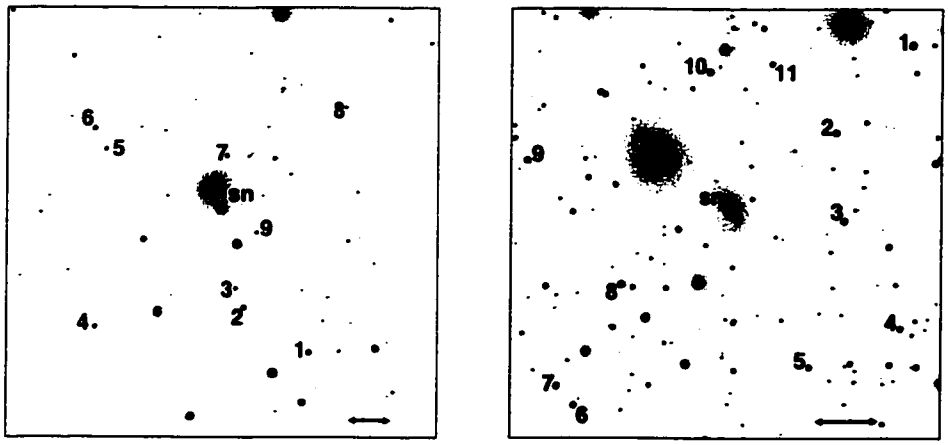

Figure 3.1.— Continued

year, after the SN has faded, to use as templates that are subtracted from all of the previous images. We have used galaxy subtraction to perform the differential photometry of all the SNe Ia except for SN 2000cx, which was located very far from the nucleus of its (elliptical) host galaxy, where the galaxy background was negligible and template subtraction only added undesirable correlated noise. For SN 2000cx, we performed point-spread function (PSF) fitting photometry on the SN and comparison stars, using the DAOPHOT/ALLSTAR (Stetson 1987, 1994) package in IRAF.

For the other 43 objects, we employed template subtraction as follows. Generally a number of late-time images were taken in each passband with exposure times comparable to or slightly longer than the deepest images with the SN present, and we chose the set of images with the best seeing to serve as the templates. For each passband, all of the images were registered to the template, and the image subtraction was performed using the ISIS subtraction package (Alard & Lupton 1998) as modified by B. Schmidt, to allow for more robust selection of regions in the two images suitable for determination of the convolution kernel (avoiding saturated stars, cosmic rays, and cosmetic defects). We subtracted the template from each SN image, and replaced a small region around the SN with the template-subtracted version. We took care to ensure that the SN PSF matched that of the comparison stars in the final image, i.e. we replaced the subtracted version into the original SN image if the template was convolved to the SN image (the usual case), otherwise we replaced the subtracted version into the convolved SN image (in the rare cases where the SN image had better seeing than the template). We also added artificial stars of known brightness into the SN images, mimicking the SN subtraction procedure

on these stars. Finally, we performed aperture photometry as well as PSF fitting photometry on the SN, comparison stars and artificial stars in the galaxy-subtracted images using DoPHOT (Schechter, Mateo, & Saha 1993). We have checked that the recovered magnitudes of the added stars match their input magnitudes, and that the aperture photometry and PSF photometry gave consistent results. We have also verified that this photometry derived via galaxy subtraction is consistent with direct PSF photometry for SNe where the galaxy background is exceptionally smooth.

This general strategy is identical to that used by the High-Z Supernova Search Team (Schmidt et al. 1998) in analysis of high-redshift SNe Ia; while the actual software is in a state of constant evolution, we have used one incarnation for all the light curves presented here. The result of this process is homogeneous and reliable differential *UBVRI* photometry of each supernova and its associated comparison stars on the natural system of the observations (i.e., instrumental magnitudes).

3.2.4 Calibration

We calibrate each of the supernova fields following the precepts of Harris, Fitzgerald & Reed (1981), using the all-sky *UBVRI* standard stars of Landolt (1992). On photometric nights, we typically observe on the order of 10 to 15 Landolt fields over a wide range of airmass (generally from 1.1 to $\sim$2). We perform aperture photometry on the reduced Landolt fields using the APPHOT package in IRAF, using a 6 pixel aperture ($\sim$4″), which is then corrected to a 15 pixel aperture ($\sim$10″) via a curve of growth defined by a few isolated, bright stars in each image. We then determine the zeropoints and transformation coefficients linear in airmass and color from the

instrumental magnitudes *ubvri* to the standard Landolt *UBVRI* magnitudes and $U-B$, $B-V$, $V-R$, and $V-I$ colors. For nights when many standard stars were observed, we check the linear solution by also fitting a quadratic term in color and as well as a color times airmass term; in all cases the coefficients for the higher order terms are negligible, and so we use only the linear solutions. Because of the different detector and filterset combinations we have used, we take care to keep track of the transformation coefficients separately. As expected, for a given detector/filterset combination, the variations in the zeropoints and airmass terms are small but significant, while the color terms are always consistent.

Once we have the standard solution for a photometric night, we apply this solution to the instrumental aperture magnitudes of the comparison stars in each SN field, measured in exactly the same way as the Landolt standard stars. This yields the standard *UBVRI* magnitudes of the comparison stars in each SN field. For most of the fields, we have several calibrations, enabling us to average the results and identify and eliminate outliers. For a handful of SN, however, we have only one night of photometric calibration, a somewhat perilous situation. Nevertheless, for every one of these objects we have checked that other SN fields taken on the same night have consistent photometry on other nights, bolstering our confidence that the photometry of objects with only one night of calibration is not significantly in error. In Table 3.2, we present the final comparison star V magnitudes and colors with their uncertainties (in the mean), as well as the number of photometric nights averaged to yield the results. We also give positions of the supernovae and comparison stars, as measured using the USNO-A2.0 catalogue (Monet et al. 1998), with a typical root-mean-square (RMS) uncertainty of $\pm 0\farcs3$.

Table 3.2. Comparison Star Photometry

Star	α (J2000)	δ (J2000)	V	$U-B$	$B-V$	$V-R$	$V-I$	N
			SN 1997E					
SN	06:47:38.16	+74:29:51.0						
1	06:47:27.41	+74:30:02.6	14.402(014)	0.086(041)	0.675(011)	0.427(007)	0.846(010)	3
2	06:47:52.40	+74:31:52.6	15.139(015)	0.123(040)	0.715(011)	0.436(007)	0.863(010)	3
3	06:47:18.41	+74:31:40.7	15.895(017)	0.018(040)	0.584(013)	0.365(008)	0.747(009)	3
4	06:47:23.92	+74:31:01.6	15.410(022)	0.580(045)	0.946(019)	0.539(007)	1.021(014)	3
5	06:47:00.39	+74:28:13.5	15.358(014)	0.594(041)	0.907(012)	0.511(009)	0.968(009)	3
6	06:47:03.36	+74:29:06.4	15.152(013)	0.143(040)	0.733(012)	0.439(008)	0.877(010)	3
7	06:46:49.48	+74:29:17.2	15.181(014)	0.390(042)	0.833(012)	0.481(009)	0.930(013)	3
8	06:47:25.35	+74:26:43.6	16.150(015)	0.231(045)	0.812(011)	0.476(009)	0.926(012)	3
9	06:47:48.60	+74:25:39.1	15.718(014)	0.055(040)	0.657(011)	0.399(007)	0.800(009)	3
			SN 1997Y					
SN	12:45:31.46	+54:44:17.4						
1	12:45:50.75	+54:44:06.0	16.576(011)	0.563(061)	0.911(015)	0.544(010)	1.042(011)	2
2	12:45:44.09	+54:45:22.3	16.029(014)	0.428(040)	0.823(013)	0.470(010)	0.946(011)	2
3	12:45:26.06	+54:46:22.0	16.174(061)	0.177(042)	0.766(019)	0.425(008)	0.870(037)	2
4	12:45:05.99	+54:45:01.8	16.562(016)	1.209(119)	1.499(010)	0.941(025)	1.949(009)	2
5	12:45:18.05	+54:42:31.9	17.846(010)	1.081(195)	1.493(029)	1.025(057)	2.370(020)	2
6	12:45:23.93	+54:44:45.6	18.317(040)	0.216(238)	0.830(056)	0.449(013)	0.908(032)	2
			SN 1997bp					
SN	12:46:53.78	−11:38:33.2						
1	12:46:48.63	−11:38:09.3	14.525(012)	−0.001(042)	0.610(014)	0.360(007)	0.717(014)	3
2	12:46:42.03	−11:37:27.5	14.840(014)	−0.036(043)	0.590(011)	0.353(009)	0.698(014)	3
3	12:46:42.53	−11:36:22.2	15.953(012)	0.234(041)	0.731(012)	0.436(007)	0.832(015)	3
4	12:47:04.62	−11:36:00.8	16.150(013)	0.090(043)	0.750(016)	0.447(014)	0.899(013)	3
5	12:47:05.48	−11:36:08.6	15.462(011)	0.789(044)	0.951(016)	0.552(008)	1.022(015)	3
6	12:47:09.57	−11:35:37.1	15.227(014)	0.003(048)	0.630(014)	0.408(012)	0.832(016)	3
7	12:47:07.87	−11:36:19.4	16.201(014)	0.106(042)	0.634(010)	0.379(012)	0.737(019)	3
8	12:47:08.39	−11:37:15.4	16.309(013)	−0.007(042)	0.604(015)	0.366(015)	0.723(024)	3
9	12:47:09.58	−11:38:32.9	14.889(011)	0.124(042)	0.688(011)	0.414(008)	0.799(011)	3
10	12:47:08.24	−11:38:36.4	15.463(011)	0.385(042)	0.821(013)	0.493(009)	0.963(011)	3
11	12:47:08.53	−11:39:31.1	16.236(013)	−0.278(042)	0.481(014)	0.331(016)	0.666(012)	3
12	12:47:03.38	−11:41:35.2	16.879(012)	0.099(041)	0.657(019)	0.375(021)	0.755(017)	3
13	12:46:57.05	−11:38:08.0	16.722(053)	−0.052(054)	0.585(034)	0.356(015)	0.691(036)	3
			SN 1997bq					
SN	10:17:05.48	+73:23:01.5						
1	10:17:18.23	+73:25:38.3	15.948(032)	−0.108(041)	0.531(026)	0.344(007)	0.687(022)	2
2	10:17:20.64	+73:25:37.4	16.633(026)	0.861(041)	1.015(021)	0.620(011)	1.141(024)	2
3	10:17:33.01	+73:25:50.8	17.225(042)	−0.136(078)	0.506(017)	0.349(013)	0.724(032)	2
4	10:17:24.78	+73:25:08.2	16.621(023)	0.186(093)	0.740(023)	0.431(013)	0.827(021)	2
5	10:17:37.69	+73:24:46.0	17.991(056)	0.361(207)	0.590(233)	0.479(010)	...	2
6	10:17:29.91	+73:24:18.0	15.928(031)	0.197(040)	0.744(029)	0.445(007)	0.877(014)	2
7	10:17:37.52	+73:24:16.0	17.971(010)	...	0.968(042)	0.541(022)	1.050(011)	2
8	10:17:40.47	+73:24:13.5	16.432(014)	0.299(046)	0.746(018)	0.459(010)	0.890(014)	2
9	10:17:45.85	+73:23:56.5	16.004(039)	0.303(041)	0.816(013)	0.462(016)	0.912(014)	2
10	10:16:29.63	+73:23:33.6	18.017(027)	0.780(209)	0.875(028)	0.488(019)	0.987(044)	2

Table 3.2—Continued

Star	α (J2000)	δ (J2000)	V	$U-B$	$B-V$	$V-R$	$V-I$	N
				SN 1997br				
SN	13:20:42.38	−22:02:12.7						
1	13:20:40.15	−22:02:07.0	17.570(021)	···	0.900(017)	0.507(021)	0.914(090)	3
2	13:20:42.28	−22:01:27.6	16.014(017)	1.172(100)	1.187(010)	0.736(010)	1.362(010)	3
3	13:20:46.13	−22:01:21.4	19.816(078)	···	0.832(205)	0.638(154)	1.099(168)	2
4	13:20:45.81	−22:01:51.1	19.227(038)	···	0.873(016)	0.432(065)	0.898(257)	3
5	13:20:45.67	−22:02:22.2	18.330(011)	···	1.552(028)	1.191(007)	2.613(014)	3
6	13:20:46.75	−22:02:34.9	17.407(023)	0.423(163)	0.860(011)	0.508(029)	0.974(012)	3
7	13:20:50.08	−22:01:59.1	15.483(016)	0.655(051)	0.956(015)	0.544(007)	1.022(009)	3
8	13:20:52.84	−22:02:27.9	16.966(011)	···	1.168(016)	0.713(013)	1.315(023)	3
9	13:20:53.35	−22:02:49.2	15.608(015)	0.371(059)	0.903(012)	0.521(011)	1.013(019)	3
10	13:20:46.92	−22:02:45.2	···	···	0.775(197)	0.441(043)	1.086(102)	3
11	13:20:46.75	−22:03:01.9	17.709(014)	···	1.111(014)	0.702(028)	1.316(012)	3
12	13:20:49.68	−22:03:06.7	19.166(035)	···	1.062(027)	0.587(046)	1.249(073)	3
13	13:20:50.22	−22:03:58.2	16.404(018)	0.006(043)	0.734(013)	0.402(008)	0.776(018)	3
14	13:20:47.32	−22:04:15.8	15.600(021)	−0.053(046)	0.634(012)	0.380(008)	0.755(009)	3
15	13:20:45.89	−22:03:53.5	15.908(019)	0.031(083)	0.697(012)	0.427(007)	0.844(011)	3
16	13:20:41.71	−22:03:38.8	17.519(023)	···	0.879(017)	0.514(007)	0.983(018)	3
17	13:20:39.75	−22:02:54.3	19.337(197)	···	1.283(165)	0.884(014)	1.784(072)	3
				SN 1997cn				
SN	14:09:57.74	+17:32:32.2						
1	14:09:59.56	+17:35:18.1	17.456(014)	1.269(166)	1.322(024)	0.817(012)	1.562(013)	3
2	14:10:09.47	+17:33:38.0	16.137(011)	0.153(049)	0.726(015)	0.407(009)	0.813(013)	3
3	14:10:09.00	+17:30:57.3	17.694(012)	0.622(105)	0.876(013)	0.512(009)	0.988(017)	3
4	14:10:07.12	+17:30:00.0	16.150(011)	0.128(058)	0.677(013)	0.375(008)	0.753(016)	3
5	14:10:03.12	+17:30:03.5	15.966(011)	0.059(045)	0.653(013)	0.377(008)	0.753(011)	3
6	14:09:58.30	+17:30:22.4	17.694(018)	0.436(088)	0.798(014)	0.447(019)	0.885(010)	3
7	14:09:42.17	+17:28:41.7	16.683(016)	1.135(124)	1.111(011)	0.664(015)	1.230(033)	3
8	14:09:43.14	+17:29:19.9	16.975(012)	1.080(138)	1.448(017)	0.915(009)	1.804(023)	3
9	14:09:52.00	+17:33:02.7	18.516(015)	0.050(260)	0.622(032)	0.380(015)	0.696(069)	3
10	14:09:46.13	+17:33:59.5	17.894(025)	0.169(199)	0.719(029)	0.393(009)	0.831(022)	3
				SN 1997cw				
SN	00:25:17.26	+12:53:06.4						
1	00:25:14.51	+12:56:11.1	15.147(029)	0.294(080)	0.797(031)	0.447(027)	0.877(028)	1
2	00:25:21.21	+12:55:18.5	17.368(063)	0.161(160)	0.721(069)	0.451(053)	0.874(058)	1
3	00:25:21.89	+12:54:31.0	16.035(038)	−0.018(100)	0.651(041)	0.385(033)	0.765(035)	1
4	00:25:23.36	+12:53:12.6	15.813(035)	0.085(094)	0.708(038)	0.406(031)	0.807(033)	1
5	00:25:26.06	+12:53:06.2	17.994(082)	1.684(207)	1.361(090)	0.846(069)	1.577(075)	1
6	00:25:25.54	+12:51:12.5	15.801(035)	0.160(094)	0.723(038)	0.420(031)	0.814(033)	1
7	00:25:21.96	+12:50:52.9	16.990(054)	0.091(139)	0.716(059)	0.405(046)	0.793(050)	1

Table 3.2—Continued

Star	α (J2000)	δ (J2000)	V	$U-B$	$B-V$	$V-R$	$V-I$	N
				SN 1997dg				
SN	23:40:14.28	+26:12:11.2						
1	23:40:05.02	+26:14:16.0	15.777(035)	0.001(093)	0.637(038)	0.383(031)	0.766(033)	1
3	23:40:14.02	+26:13:45.1	17.499(066)	0.820(169)	1.061(073)	0.653(056)	1.219(061)	1
4	23:40:20.99	+26:13:33.7	18.674(110)	0.205(278)	0.927(122)	0.508(093)	1.006(101)	1
6	23:40:16.90	+26:10:58.6	17.974(081)	0.605(206)	0.954(090)	0.540(069)	1.017(074)	1
7	23:40:21.45	+26:10:02.8	18.347(096)	...	1.406(106)	0.936(080)	1.782(087)	1
8	23:40:20.75	+26:10:01.4	18.857(120)	...	0.930(133)	0.533(100)	0.976(109)	1
9	23:40:10.41	+26:09:27.4	15.969(037)	0.083(098)	0.699(040)	0.416(033)	0.816(035)	1
10	23:40:06.33	+26:10:43.1	15.959(037)	−0.054(098)	0.558(040)	0.343(033)	0.698(035)	1
11	23:40:11.33	+26:11:39.0	17.698(072)	0.802(183)	1.018(080)	0.616(061)	1.121(066)	1
				SN 1997do				
SN	07:26:42.59	+47:05:34.6						
1	07:26:30.31	+47:07:44.1	16.999(054)	0.206(139)	0.795(059)	0.448(046)	0.885(050)	1
2	07:26:31.90	+47:06:49.9	17.761(074)	−0.048(188)	0.616(082)	0.391(063)	0.738(068)	1
3	07:26:31.95	+47:06:16.2	17.294(061)	0.590(156)	0.893(067)	0.528(052)	1.016(056)	1
4	07:26:27.49	+47:04:06.3	16.194(040)	0.736(105)	1.011(043)	0.591(035)	1.151(037)	1
5	07:26:35.73	+47:03:20.7	16.362(042)	0.251(111)	0.774(046)	0.432(037)	0.858(039)	1
6	07:26:43.33	+47:03:31.7	15.545(033)	−0.008(088)	0.675(035)	0.361(029)	0.718(031)	1
7	07:26:45.40	+47:03:37.2	16.352(042)	0.072(111)	0.694(046)	0.388(037)	0.772(039)	1
8	07:26:55.57	+47:04:15.6	17.046(055)	0.454(142)	0.881(060)	0.506(047)	0.946(051)	1
9	07:26:48.30	+47:05:20.9	17.250(060)	0.431(153)	0.860(066)	0.464(051)	0.885(055)	1
10	07:26:48.46	+47:05:35.9	17.955(080)	1.550(204)	1.340(089)	0.897(068)	1.705(074)	1
11	07:26:40.59	+47:07:03.9	17.893(078)	0.607(199)	0.948(087)	0.547(066)	1.016(072)	1
				SN 1997dt				
SN	23:00:02.97	+15:58:50.4						
1	22:59:55.18	+16:00:31.0	15.940(037)	−0.004(098)	0.581(040)	0.347(033)	0.682(034)	1
2	22:59:54.90	+15:59:23.2	18.007(082)	−0.213(208)	0.547(091)	0.332(069)	0.728(075)	1
3	22:59:57.02	+15:56:18.8	16.646(047)	0.167(122)	0.767(051)	0.434(041)	0.911(044)	1
4	23:00:07.16	+15:57:04.8	16.520(045)	0.894(117)	1.051(049)	0.639(039)	1.209(042)	1
5	23:00:15.93	+15:56:24.4	18.056(084)	−0.086(213)	0.543(093)	0.346(071)	0.734(077)	1
6	23:00:13.88	+15:57:11.1	15.256(030)	0.143(082)	0.790(032)	0.464(027)	0.951(029)	1
7	23:00:13.03	+15:58:55.3	16.807(050)	−0.182(130)	0.547(055)	0.338(043)	0.708(046)	1
8	23:00:14.85	+16:00:25.1	17.785(075)	−0.077(190)	0.573(083)	0.362(063)	0.711(069)	1
9	23:00:10.63	+15:59:45.5	17.496(066)	0.247(169)	0.785(073)	0.463(056)	0.883(061)	1
10	23:00:06.65	+15:59:43.2	17.146(057)	0.019(147)	0.659(063)	0.381(049)	0.808(053)	1
				SN 1998D				
SN	14:02:59.33	+34:44:54.6						
1	14:03:11.93	+34:49:23.6	15.350(013)	0.082(049)	0.672(014)	0.370(007)	0.755(029)	3
2	14:03:10.88	+34:48:48.1	16.041(012)	−0.059(042)	0.584(012)	0.354(010)	0.725(027)	4
3	14:02:57.85	+34:47:36.6	16.896(014)	0.037(067)	0.724(013)	0.427(009)	0.900(015)	4
4	14:02:53.98	+34:47:12.0	17.567(012)	−0.016(063)	0.038(015)	0.015(014)	0.123(045)	4
5	14:02:51.94	+34:47:00.5	15.281(014)	0.336(053)	0.780(016)	0.445(007)	0.878(029)	3
6	14:02:46.22	+34:46:31.8	15.687(013)	0.608(048)	0.904(016)	0.559(011)	1.057(032)	4
7	14:02:56.40	+34:43:34.8	15.889(015)	−0.054(041)	0.587(012)	0.348(008)	0.707(034)	4
8	14:02:55.85	+34:40:26.0	16.586(013)	−0.075(044)	0.587(010)	0.344(008)	0.703(019)	4
9	14:03:23.77	+34:43:51.6	15.522(013)	0.032(040)	0.600(011)	0.341(010)	0.707(031)	4

Table 3.2—Continued

Star	α (J2000)	δ (J2000)	V	$U-B$	$B-V$	$V-R$	$V-I$	N
				SN 1998V				
SN	18:22:37.40	+15:42:08.0						
1	18:22:42.93	+15:43:30.7	15.705(011)	0.434(050)	0.894(013)	0.516(007)	1.007(012)	5
2	18:22:39.60	+15:44:39.8	16.421(014)	0.169(051)	0.653(016)	0.409(008)	0.813(012)	5
3	18:22:33.94	+15:44:06.1	16.029(012)	0.156(053)	0.732(024)	0.425(013)	0.864(011)	5
4	18:22:29.21	+15:43:47.4	16.437(010)	0.194(048)	0.810(013)	0.480(007)	0.978(013)	5
5	18:22:31.58	+15:41:12.9	17.034(011)	0.246(045)	0.848(010)	0.524(009)	1.070(019)	5
6	18:22:34.57	+15:40:59.2	16.513(011)	0.616(058)	1.074(036)	0.639(009)	1.291(013)	5
7	18:22:35.69	+15:40:25.7	16.180(011)	0.381(042)	0.890(011)	0.529(007)	1.040(011)	5
8	18:22:37.15	+15:40:02.0	16.120(011)	0.208(043)	0.784(016)	0.479(008)	0.968(012)	5
9	18:22:39.65	+15:39:55.5	16.129(012)	0.746(044)	1.113(012)	0.642(007)	1.263(014)	5
10	18:22:43.56	+15:40:37.2	16.653(012)	0.678(041)	1.141(013)	0.664(008)	1.339(013)	5
11	18:22:39.20	+15:41:17.4	16.101(012)	0.957(042)	1.117(013)	0.670(008)	1.258(014)	5
				SN 1998ab				
SN	12:48:47.28	+41:55:29.0						
1	12:48:27.54	+41:57:37.0	15.196(013)	0.306(044)	0.754(011)	0.420(009)	0.814(023)	4
2	12:48:29.50	+41:56:43.4	17.322(012)	0.612(043)	0.890(012)	0.538(009)	1.041(020)	5
3	12:48:35.46	+41:55:35.9	17.430(013)	−0.044(042)	0.671(016)	0.431(010)	0.899(034)	5
4	12:48:44.97	+41:53:37.3	18.253(013)	...	1.426(031)	0.894(013)	1.746(014)	5
5	12:48:47.63	+41:53:09.1	16.361(011)	−0.552(042)	0.135(011)	−0.038(013)	−0.055(028)	5
6	12:48:56.78	+41:52:30.7	15.648(010)	−0.055(041)	0.587(013)	0.337(009)	0.676(020)	5
7	12:49:02.45	+41:53:04.5	16.189(011)	0.408(042)	0.816(014)	0.449(008)	0.876(018)	5
8	12:49:02.01	+41:55:17.6	17.318(014)	1.194(095)	1.377(020)	0.879(010)	1.729(019)	5
9	12:48:59.07	+41:57:15.3	17.300(011)	1.311(272)	1.569(013)	1.010(013)	2.201(011)	5
				SN 1998bp				
SN	17:54:50.73	+18:19:50.2						
1	17:54:50.25	+18:20:13.9	17.290(014)	1.276(117)	1.330(020)	0.814(014)	1.515(017)	6
2	17:54:48.77	+18:21:05.7	16.960(013)	0.062(049)	0.658(019)	0.378(008)	0.750(011)	6
3	17:54:48.24	+18:20:43.5	16.565(014)	0.094(044)	0.662(014)	0.387(009)	0.768(016)	6
4	17:54:44.94	+18:19:44.9	16.987(014)	0.597(044)	0.881(015)	0.508(010)	0.977(015)	6
5	17:54:44.30	+18:18:37.9	15.575(015)	0.389(044)	0.812(014)	0.466(008)	0.906(012)	6
6	17:54:46.13	+18:18:04.0	16.122(015)	0.285(042)	0.771(015)	0.443(008)	0.884(011)	6
7	17:54:52.68	+18:17:30.1	16.492(014)	0.142(045)	0.712(014)	0.408(007)	0.816(012)	6
8	17:54:54.92	+18:18:40.0	18.093(012)	0.052(041)	0.658(022)	0.381(011)	0.766(020)	6
9	17:54:52.72	+18:19:33.9	16.783(015)	0.275(047)	0.735(013)	0.411(009)	0.813(020)	6
10	17:54:55.65	+18:20:09.3	17.219(013)	0.105(045)	0.678(018)	0.411(008)	0.821(022)	6
11	17:54:56.27	+18:20:25.0	15.992(015)	−0.077(045)	0.500(013)	0.315(008)	0.653(013)	6
				SN 1998co				
SN	21:47:36.27	−13:10:52.7						
1	21:47:44.17	−13:08:23.1	16.237(012)	0.539(042)	0.894(012)	0.535(012)	1.016(009)	3
2	21:47:47.13	−13:12:11.7	17.779(018)	0.053(059)	0.681(028)	0.416(012)	0.811(031)	3
3	21:47:45.79	−13:12:37.3	17.968(018)	1.240(247)	1.208(017)	0.751(007)	1.396(024)	3
4	21:47:42.14	−13:13:36.0	14.245(024)	−0.045(042)	0.568(025)	0.338(023)	0.667(024)	3
5	21:47:41.21	−13:13:08.7	16.837(011)	0.591(063)	0.815(069)	0.508(007)	0.944(012)	3
6	21:47:37.19	−13:11:27.8	14.691(011)	0.157(041)	0.715(011)	0.409(009)	0.797(025)	3
7	21:47:37.15	−13:11:48.8	16.011(012)	0.153(045)	0.705(013)	0.404(008)	0.777(020)	3
8	21:47:37.39	−13:12:58.6	16.248(011)	0.068(042)	0.659(011)	0.392(009)	0.768(019)	3
9	21:47:34.34	−13:13:20.7	16.371(012)	0.315(045)	0.801(011)	0.467(007)	0.912(013)	3
10	21:47:30.18	−13:11:08.3	16.583(014)	0.092(048)	0.655(010)	0.375(007)	0.747(017)	2

Table 3.2—Continued

Star	α (J2000)	δ (J2000)	V	$U-B$	$B-V$	$V-R$	$V-I$	N
				SN 1998de				
SN	00:48:06.88	+27:37:29.9						
1	00:48:06.02	+27:37:47.0	17.247(017)	0.991(050)	1.059(013)	0.605(011)	1.140(014)	5
2	00:48:05.00	+27:37:16.0	17.968(015)	0.072(047)	0.622(012)	0.382(012)	0.794(015)	5
3	00:48:03.80	+27:39:24.4	17.898(012)	1.096(119)	1.490(017)	0.942(012)	1.870(013)	5
4	00:48:21.44	+27:35:50.6	17.620(012)	0.620(059)	0.962(012)	0.577(009)	1.110(011)	5
5	00:48:16.70	+27:33:55.2	17.795(015)	0.762(065)	0.992(012)	0.595(009)	1.136(020)	5
6	00:48:00.04	+27:33:48.7	16.941(013)	−0.058(048)	0.557(010)	0.340(008)	0.711(012)	5
7	00:47:47.53	+27:34:32.6	17.079(019)	1.217(227)	1.556(013)	0.992(026)	2.113(026)	3
8	00:47:50.70	+27:39:26.1	16.543(011)	0.543(068)	0.895(011)	0.522(009)	1.012(010)	5
				SN 1998dh				
SN	23:14:40.31	+04:32:13.4						
1	23:14:27.33	+04:30:10.4	16.180(014)	1.228(044)	1.240(011)	0.775(008)	1.462(016)	5
2	23:14:39.10	+04:29:59.2	16.065(013)	0.557(085)	0.965(013)	0.543(008)	1.073(012)	5
3	23:14:43.25	+04:28:31.4	16.942(013)	0.165(042)	0.747(013)	0.428(008)	0.863(018)	5
4	23:14:50.84	+04:29:37.6	16.454(012)	0.560(073)	0.930(013)	0.556(009)	1.099(014)	5
5	23:14:49.56	+04:30:46.0	17.268(011)	0.375(043)	0.875(013)	0.533(008)	1.054(011)	5
6	23:14:57.13	+04:30:24.6	16.636(011)	−0.216(041)	0.604(010)	0.398(008)	0.831(013)	5
7	23:14:55.76	+04:30:56.2	16.036(011)	0.533(041)	0.917(011)	0.537(007)	1.036(012)	5
8	23:14:50.34	+04:33:22.8	17.539(011)	0.185(048)	0.768(011)	0.470(010)	0.927(016)	5
				SN 1998dk				
SN	00:14:32.26	−00:44:12.6						
1	00:14:27.99	−00:44:47.9	17.367(012)	1.141(072)	1.186(012)	0.745(010)	1.401(010)	4
2	00:14:25.04	−00:45:04.2	17.751(011)	0.014(041)	0.671(012)	0.393(009)	0.804(014)	4
3	00:14:27.39	−00:45:32.6	16.248(020)	1.153(052)	1.478(015)	0.983(018)	2.124(015)	4
4	00:14:21.31	−00:47:59.2	17.197(014)	0.395(051)	0.806(015)	0.445(009)	0.875(019)	4
5	00:14:38.33	−00:46:56.6	17.374(018)	0.125(042)	0.717(011)	0.410(010)	0.809(010)	4
6	00:14:41.27	−00:40:36.5	17.349(019)	1.232(154)	1.537(024)	1.064(031)	2.425(014)	4
7	00:14:26.63	−00:41:15.9	16.705(014)	1.354(057)	1.307(014)	0.829(010)	1.581(013)	4
				SN 1998dm				
SN	01:26:13.64	−06:06:13.7						
1	01:26:12.33	−06:06:01.0	16.125(011)	0.933(048)	1.036(010)	0.618(007)	1.146(012)	4
2	01:26:09.10	−06:05:58.2	16.953(012)	0.876(045)	1.046(011)	0.629(008)	1.181(013)	4
3	01:26:07.15	−06:05:32.7	17.633(013)	1.310(083)	1.460(017)	0.930(012)	1.875(010)	4
4	01:26:05.77	−06:05:58.9	17.742(012)	0.406(046)	0.826(011)	0.457(008)	0.910(014)	4
5	01:26:11.93	−06:01:46.8	17.304(017)	0.974(120)	1.525(015)	1.026(023)	2.239(016)	4
6	01:26:04.64	−06:02:06.3	15.238(011)	0.156(041)	0.674(012)	0.381(008)	0.753(011)	4
7	01:25:57.54	−06:07:33.3	16.063(015)	1.192(042)	1.359(012)	0.865(009)	1.656(010)	4
8	01:26:05.16	−06:09:10.3	16.170(013)	0.713(044)	0.937(012)	0.542(008)	1.048(010)	4
9	01:26:20.60	−06:03:32.5	16.699(018)	1.146(049)	1.471(011)	0.982(020)	2.117(011)	4

Table 3.2—Continued

Star	α (J2000)	δ (J2000)	V	$U-B$	$B-V$	$V-R$	$V-I$	N
				SN 1998dx				
SN	18:11:11.95	+49:51:40.9						
1	18:11:05.17	+49:50:20.8	15.413(010)	0.021(043)	0.625(014)	0.368(008)	0.734(021)	3
2	18:11:08.65	+49:49:43.8	15.808(011)	0.094(046)	0.680(014)	0.398(008)	0.781(014)	3
3	18:11:17.65	+49:49:47.6	16.869(011)	0.544(040)	0.844(014)	0.480(009)	0.891(025)	3
4	18:11:29.28	+49:50:03.9	16.360(010)	0.220(042)	0.740(017)	0.421(008)	0.800(011)	3
5	18:11:30.26	+49:51:53.9	16.429(012)	−0.068(046)	0.602(015)	0.364(010)	0.720(016)	3
6	18:11:30.58	+49:54:19.4	16.009(011)	−0.067(040)	0.616(014)	0.376(012)	0.748(014)	3
7	18:11:22.96	+49:53:00.6	15.312(010)	0.037(044)	0.650(014)	0.388(011)	0.751(017)	3
8	18:10:56.96	+49:53:15.1	15.152(012)	0.013(042)	0.566(014)	0.340(010)	0.663(022)	3
				SN 1998ec				
SN	06:53:06.10	+50:02:22.8						
1	06:53:00.72	+50:03:50.2	16.886(011)	0.582(050)	0.937(012)	0.543(007)	1.045(010)	4
2	06:52:48.81	+50:04:05.6	16.139(011)	0.156(041)	0.716(013)	0.411(007)	0.821(011)	4
3	06:52:55.76	+50:02:40.8	17.628(010)	1.171(178)	1.483(016)	0.953(015)	1.903(010)	4
4	06:52:53.61	+50:01:07.9	16.845(011)	0.132(044)	0.712(015)	0.410(009)	0.804(016)	4
5	06:52:53.13	+50:00:53.5	18.101(010)	1.112(217)	1.238(025)	0.786(010)	1.454(020)	4
6	06:52:57.30	+49:59:59.4	17.243(014)	0.932(040)	1.105(013)	0.669(009)	1.270(014)	4
7	06:52:58.94	+49:58:57.6	16.018(012)	0.127(042)	0.713(012)	0.410(007)	0.804(016)	4
8	06:53:07.87	+50:01:29.3	17.788(014)	0.258(044)	0.779(019)	0.449(013)	0.912(011)	4
9	06:53:11.40	+50:01:06.1	16.161(012)	0.075(041)	0.711(013)	0.409(007)	0.818(010)	4
10	06:53:14.07	+50:00:54.6	17.367(013)	0.890(040)	1.055(014)	0.634(009)	1.199(013)	4
11	06:53:21.78	+50:00:41.7	16.206(012)	0.444(050)	0.867(014)	0.489(007)	0.950(012)	4
12	06:53:18.34	+50:01:32.1	16.723(013)	0.078(042)	0.660(016)	0.385(009)	0.764(015)	4
13	06:53:17.10	+50:04:26.3	16.563(011)	0.128(040)	0.712(013)	0.431(007)	0.879(012)	4
				SN 1998ef				
SN	01:03:26.80	+32:14:12.8						
1	01:03:28.07	+32:14:23.8	16.428(011)	0.394(060)	0.849(030)	0.498(020)	0.976(019)	2
2	01:03:15.87	+32:15:51.4	15.622(011)	0.003(042)	0.619(019)	0.378(016)	0.758(020)	2
3	01:03:21.89	+32:13:11.1	17.391(042)	0.636(162)	0.878(024)	0.450(008)	0.865(017)	2
4	01:03:19.05	+32:11:40.5	15.695(011)	0.373(040)	0.816(017)	0.463(014)	0.899(013)	2
5	01:03:24.54	+32:11:43.8	17.316(010)	0.123(059)	0.695(014)	0.430(007)	0.842(019)	2
6	01:03:28.39	+32:13:39.4	17.036(010)	0.312(041)	0.785(028)	0.447(020)	0.869(010)	2
7	01:03:38.20	+32:12:10.5	17.424(012)	0.747(164)	1.004(048)	0.608(013)	1.140(009)	2
8	01:03:34.44	+32:15:15.0	16.021(010)	0.166(048)	0.781(014)	0.459(015)	0.913(011)	2
9	01:03:33.59	+32:15:28.9	17.498(011)	0.973(169)	1.535(034)	1.067(057)	2.421(012)	2
				SN 1998eg				
SN	22:39:30.34	+08:36:20.8						
1	22:39:42.06	+08:39:15.3	16.067(038)	0.153(101)	0.757(041)	0.425(034)	0.856(036)	1
2	22:39:40.85	+08:38:03.9	16.985(054)	0.174(138)	0.874(059)	0.516(046)	1.039(050)	1
3	22:39:31.99	+08:33:39.8	16.504(045)	0.103(117)	0.818(049)	0.471(039)	0.949(041)	1
4	22:39:27.33	+08:35:31.9	17.143(057)	1.151(147)	1.206(063)	0.715(049)	1.308(053)	1
5	22:39:24.30	+08:33:04.1	15.762(035)	0.698(093)	1.073(037)	0.590(031)	1.174(033)	1
6	22:39:22.24	+08:35:12.0	16.749(049)	0.488(127)	0.893(054)	0.540(042)	1.052(045)	1
7	22:39:17.61	+08:36:11.0	16.640(047)	0.819(122)	1.111(051)	0.604(041)	1.212(044)	1
8	22:39:17.74	+08:36:34.8	16.566(046)	0.400(119)	0.894(050)	0.500(040)	1.021(042)	1

Table 3.2—Continued

Star	α (J2000)	δ (J2000)	V	$U-B$	$B-V$	$V-R$	$V-I$	N
				SN 1998es				
SN	01:37:17.52	+05:52:50.2						
1	01:37:18.27	+05:52:55.6	15.423(011)	−0.023(041)	0.589(014)	0.367(009)	0.742(014)	4
2	01:37:27.84	+05:53:48.7	16.633(011)	−0.032(050)	0.635(012)	0.391(007)	0.783(012)	4
3	01:37:28.69	+05:53:56.3	17.006(011)	0.663(050)	0.937(022)	0.565(008)	1.088(014)	4
4	01:37:32.42	+05:51:35.6	15.932(010)	0.617(057)	0.921(017)	0.547(009)	1.041(015)	4
5	01:37:17.72	+05:50:51.4	16.745(011)	1.361(076)	1.385(025)	0.897(011)	1.755(014)	4
6	01:37:15.25	+05:49:34.3	16.841(010)	0.654(045)	0.899(018)	0.536(007)	1.005(013)	4
7	01:37:11.74	+05:48:35.2	16.162(015)	1.217(045)	1.445(020)	0.973(015)	1.996(019)	4
				SN 1999X				
SN	08:54:32.28	+36:30:41.7						
1	08:54:24.12	+36:30:35.4	15.229(012)	0.478(040)	0.871(011)	0.539(010)	1.071(013)	3
2	08:54:11.00	+36:29:33.0	15.137(013)	0.184(041)	0.717(010)	0.416(010)	0.821(017)	3
3	08:54:16.57	+36:28:39.9	15.524(015)	0.119(053)	0.673(030)	0.399(013)	0.806(014)	2
4	08:54:23.31	+36:28:07.6	16.596(011)	0.496(042)	0.843(011)	0.488(007)	0.953(020)	3
5	08:54:14.21	+36:26:25.3	17.534(012)	···	1.448(013)	0.958(007)	1.971(016)	3
6	08:54:38.42	+36:26:20.2	16.801(013)	0.016(043)	0.575(011)	0.347(007)	0.700(031)	3
7	08:54:42.96	+36:27:01.3	16.026(013)	1.173(055)	1.463(017)	0.953(008)	1.930(018)	3
8	08:54:52.59	+36:30:54.5	16.711(012)	1.140(073)	1.122(011)	0.668(007)	1.236(018)	3
9	08:54:53.73	+36:31:21.1	16.884(014)	0.595(042)	0.892(011)	0.538(009)	1.050(012)	3
10	08:54:43.86	+36:33:26.8	16.979(014)	0.416(047)	0.820(012)	0.458(008)	0.903(012)	3
11	08:54:44.30	+36:34:22.8	17.323(011)	0.934(158)	1.424(014)	0.921(007)	1.826(020)	3
12	08:54:35.63	+36:31:13.4	17.068(011)	1.259(143)	1.256(011)	0.798(007)	1.496(018)	3
				SN 1999aa				
SN	08:27:42.15	+21:29:15.6						
1	08:27:37.96	+21:26:48.5	15.595(028)	0.376(054)	0.758(019)	0.417(012)	0.805(014)	4
2	08:27:40.83	+21:27:21.3	15.835(015)	0.436(045)	0.828(011)	0.465(011)	0.908(011)	4
3	08:27:53.81	+21:28:15.8	16.854(015)	0.238(051)	0.754(011)	0.408(013)	0.817(012)	4
4	08:27:52.63	+21:28:57.1	16.543(014)	0.008(041)	0.599(012)	0.354(008)	0.705(010)	4
5	08:27:53.95	+21:29:17.4	16.876(013)	0.009(043)	0.631(013)	0.354(015)	0.731(025)	4
6	08:27:52.41	+21:29:34.1	14.572(010)	0.038(041)	0.578(011)	0.336(024)	0.667(019)	4
7	08:27:43.33	+21:29:52.2	16.764(024)	0.609(048)	0.834(016)	0.456(012)	0.859(016)	4
8	08:27:44.66	+21:31:11.8	15.380(014)	0.173(057)	0.727(013)	0.393(010)	0.781(012)	4
9	08:27:37.39	+21:31:19.2	14.492(011)	−0.062(041)	0.506(011)	0.304(024)	0.619(012)	4
10	08:27:37.33	+21:30:58.2	16.659(023)	0.937(059)	1.049(011)	0.622(008)	1.153(011)	4
11	08:27:38.22	+21:29:54.9	15.104(014)	0.119(041)	0.666(011)	0.393(009)	0.770(011)	4
				SN 1999ac				
SN	16:07:15.05	+07:58:20.1						
1	16:07:05.51	+07:57:33.2	14.776(010)	0.178(042)	0.673(010)	0.394(019)	0.743(011)	3
2	16:07:10.32	+07:55:53.8	15.728(011)	0.052(044)	0.653(012)	0.387(015)	0.748(011)	3
3	16:07:20.41	+07:56:26.2	16.888(013)	0.032(053)	0.775(013)	0.485(012)	0.973(024)	3
4	16:07:24.10	+07:58:12.3	16.869(011)	0.031(045)	0.688(016)	0.399(010)	0.770(013)	3
5	16:07:23.90	+07:58:23.6	16.192(010)	0.272(042)	0.742(011)	0.418(015)	0.785(011)	3
6	16:07:19.55	+07:58:37.3	15.839(010)	0.764(061)	1.104(014)	0.609(014)	1.179(011)	3
7	16:07:26.19	+07:59:33.9	16.286(011)	0.141(042)	0.696(010)	0.417(016)	0.803(010)	3

Table 3.2—Continued

Star	α (J2000)	δ (J2000)	V	$U-B$	$B-V$	$V-R$	$V-I$	N
				SN 1999cc				
SN	16:02:42.04	+37:21:33.7						
1	16:02:34.48	+37:20:34.6	15.663(011)	−0.155(044)	0.531(013)	0.362(009)	0.734(009)	2
2	16:02:23.86	+37:20:25.5	16.054(012)	1.276(056)	1.359(011)	0.867(009)	1.656(012)	2
3	16:02:31.18	+37:19:33.0	16.728(013)	0.329(040)	0.767(011)	0.450(014)	0.856(020)	2
4	16:02:39.12	+37:19:08.0	16.866(014)	0.141(044)	0.699(016)	0.412(010)	0.838(015)	2
5	16:02:43.52	+37:18:23.8	16.439(027)	0.285(041)	0.755(011)	0.427(008)	0.834(028)	2
6	16:02:44.80	+37:19:37.3	16.425(019)	0.531(067)	0.902(021)	0.538(011)	1.056(013)	2
7	16:02:58.15	+37:18:15.1	16.743(011)	0.054(040)	0.624(015)	0.363(013)	0.685(020)	2
8	16:02:59.90	+37:18:17.9	16.668(048)	...	0.851(052)	0.539(041)	1.097(044)	1
9	16:02:58.78	+37:20:09.8	17.185(016)	0.085(046)	0.666(012)	0.376(019)	0.708(025)	2
10	16:02:48.32	+37:23:39.2	16.545(010)	0.944(068)	1.181(016)	0.733(010)	1.392(011)	2
11	16:02:39.21	+37:23:21.6	17.160(013)	−0.213(148)	0.518(014)	0.347(007)	0.716(017)	2
12	16:02:45.46	+37:25:39.5	16.001(016)	−0.068(041)	0.560(010)	0.357(010)	0.710(010)	2
				SN 1999cl				
SN	12:31:56.03	+14:25:35.1						
1	12:31:37.92	+14:27:33.1	15.374(028)	−0.095(043)	0.570(014)	0.341(011)	0.693(025)	3
2	12:31:49.45	+14:21:48.0	16.320(018)	0.470(058)	0.842(020)	0.473(010)	0.908(014)	3
3	12:32:04.75	+14:23:15.6	14.991(025)	0.257(045)	0.765(022)	0.438(009)	0.848(023)	3
4	12:32:05.24	+14:23:34.5	13.655(033)	0.490(053)	0.883(031)	0.509(022)	0.969(029)	3
5	12:32:08.80	+14:28:44.1	14.712(026)	−0.087(047)	0.577(014)	0.348(008)	0.695(019)	3
6	12:31:56.80	+14:28:12.9	17.561(016)	−0.026(043)	0.622(021)	0.347(016)	0.703(013)	3
				SN 1999cw				
SN	00:20:01.46	−06:20:02.5						
1	00:19:56.46	−06:23:10.7	14.926(011)	−0.022(041)	0.596(010)	0.366(007)	0.730(011)	5
2	00:20:09.05	−06:24:15.6	16.608(016)	1.163(062)	1.501(023)	1.031(010)	2.224(014)	4
3	00:20:01.04	−06:15:31.5	15.696(011)	0.146(040)	0.712(010)	0.425(008)	0.837(012)	5
4	00:20:00.40	−06:18:09.9	14.719(013)	1.096(040)	1.107(011)	0.667(010)	1.226(018)	5
5	00:19:53.92	−06:17:22.2	14.723(011)	0.025(041)	0.611(011)	0.370(008)	0.734(011)	5
6	00:19:48.63	−06:16:26.0	16.742(011)	0.595(043)	1.015(011)	0.556(008)	1.093(014)	5
				SN 1999dq				
SN	02:33:59.71	+20:58:30.2						
1	02:33:53.71	+20:56:54.5	16.537(011)	0.225(043)	0.745(012)	0.438(007)	0.849(011)	6
2	02:34:02.63	+20:56:29.0	14.976(011)	0.096(041)	0.695(011)	0.414(007)	0.829(012)	6
3	02:34:04.45	+20:56:35.5	15.791(011)	0.237(041)	0.761(012)	0.443(007)	0.865(011)	6
4	02:34:06.45	+21:00:12.9	15.497(010)	0.149(041)	0.716(011)	0.423(007)	0.833(011)	6
5	02:33:59.23	+21:00:12.8	17.540(011)	0.341(045)	0.966(013)	0.692(008)	1.527(015)	6
6	02:33:59.03	+20:59:18.6	16.780(011)	1.549(119)	1.429(016)	0.905(008)	1.743(014)	6
7	02:34:04.42	+20:59:13.1	17.802(012)	−0.152(044)	0.540(014)	0.369(010)	0.747(023)	6

Table 3.2—Continued

Star	α (J2000)	δ (J2000)	V	$U-B$	$B-V$	$V-R$	$V-I$	N
				SN 1999ef				
SN	00:58:46.39	+12:44:45.2						
1	00:58:42.23	+12:42:58.1	16.797(011)	0.047(041)	0.670(010)	0.405(008)	0.814(010)	6
2	00:58:47.26	+12:41:49.0	15.961(011)	−0.122(043)	0.588(011)	0.389(007)	0.792(011)	6
3	00:58:54.80	+12:47:21.6	16.871(011)	1.121(107)	1.210(014)	0.756(009)	1.433(013)	6
4	00:58:48.58	+12:48:15.4	15.142(010)	0.399(041)	0.851(012)	0.487(007)	0.943(010)	6
5	00:58:44.35	+12:47:56.1	16.254(010)	0.270(045)	0.793(012)	0.466(007)	0.914(011)	6
6	00:58:38.25	+12:45:40.7	17.183(014)	0.475(043)	0.921(015)	0.570(009)	1.093(012)	6
7	00:58:26.88	+12:41:22.7	17.775(011)	−0.158(045)	0.538(024)	0.356(013)	0.685(081)	5
8	00:58:35.40	+12:41:07.0	17.778(013)	0.787(189)	1.063(015)	0.658(012)	1.243(030)	6
				SN 1999ej				
SN	01:22:57.38	+33:27:57.4						
1	01:23:04.61	+33:26:18.9	14.843(010)	0.013(042)	0.654(011)	0.390(007)	0.779(014)	5
2	01:23:07.11	+33:26:21.4	16.608(011)	1.161(051)	1.154(015)	0.681(008)	1.250(012)	5
3	01:23:05.42	+33:27:32.0	16.368(011)	0.424(041)	0.842(011)	0.468(008)	0.912(013)	4
4	01:23:08.12	+33:27:25.2	16.588(013)	0.131(044)	0.698(011)	0.409(008)	0.808(015)	5
5	01:23:08.12	+33:27:38.1	16.292(012)	0.828(047)	1.001(017)	0.573(008)	1.086(012)	5
6	01:23:09.86	+33:28:18.0	17.134(014)	0.401(043)	0.890(013)	0.517(010)	0.999(013)	5
7	01:23:02.20	+33:28:26.4	16.865(011)	0.222(042)	0.810(012)	0.480(007)	0.933(013)	5
8	01:23:06.16	+33:30:26.1	16.537(012)	0.106(041)	0.724(013)	0.418(010)	0.839(011)	5
9	01:22:57.10	+33:30:35.6	16.634(011)	1.075(070)	1.580(017)	1.012(008)	2.110(020)	5
10	01:22:56.29	+33:29:28.9	15.959(011)	0.237(042)	0.719(012)	0.408(007)	0.797(011)	5
11	01:22:48.92	+33:31:04.0	17.435(014)	0.449(049)	0.896(023)	0.509(013)	0.992(015)	5
12	01:22:43.02	+33:30:46.9	17.501(017)	−0.011(053)	0.619(017)	0.364(009)	0.736(017)	5
				SN 1999ek				
SN	05:36:31.55	+16:38:17.1						
1	05:36:42.31	+16:36:24.5	15.152(012)	0.281(046)	0.840(022)	0.543(007)	1.089(009)	4
2	05:36:42.94	+16:36:32.7	16.480(011)	1.159(078)	1.422(027)	0.850(008)	1.663(013)	4
3	05:36:41.35	+16:36:50.9	15.130(012)	1.720(072)	1.627(029)	0.926(027)	1.778(015)	4
4	05:36:39.67	+16:38:09.1	16.485(011)	0.394(044)	0.983(024)	0.607(008)	1.202(011)	4
5	05:36:39.79	+16:38:32.5	15.681(012)	0.276(045)	0.690(022)	0.440(008)	0.909(013)	4
6	05:36:43.52	+16:40:43.4	15.095(011)	0.520(047)	1.016(023)	0.609(008)	1.205(010)	4
7	05:36:31.16	+16:41:10.8	16.302(011)	0.267(052)	0.873(022)	0.564(007)	1.140(009)	4
8	05:36:26.63	+16:40:18.5	16.368(012)	0.294(060)	0.914(024)	0.590(008)	1.164(011)	4
9	05:36:27.33	+16:39:42.6	15.165(011)	0.431(048)	0.996(021)	0.614(008)	1.209(010)	4
10	05:36:26.91	+16:36:57.4	15.330(012)	0.344(046)	0.924(024)	0.598(008)	1.195(011)	4
11	05:36:33.73	+16:36:45.6	15.737(012)	0.461(041)	0.784(022)	0.493(007)	0.993(011)	4
12	05:36:30.63	+16:37:55.4	16.282(012)	0.266(049)	0.847(018)	0.561(007)	1.116(011)	4
				SN 1999gd				
SN	08:38:24.57	+25:45:33.8						
1	08:38:22.74	+25:46:32.3	16.157(011)	0.291(043)	0.775(011)	0.443(008)	0.867(010)	7
2	08:38:21.31	+25:45:57.2	17.472(011)	0.273(053)	0.797(012)	0.457(009)	0.894(012)	7
3	08:38:11.48	+25:46:46.9	16.574(011)	0.206(043)	0.751(011)	0.433(007)	0.848(011)	7
4	08:38:08.68	+25:46:06.2	15.832(011)	−0.095(040)	0.559(011)	0.346(009)	0.684(010)	7
5	08:38:08.13	+25:46:18.4	16.904(011)	0.013(043)	0.629(011)	0.384(007)	0.754(012)	7
6	08:38:22.88	+25:43:42.2	17.581(012)	...	1.582(020)	1.125(010)	2.500(014)	7
7	08:38:28.18	+25:44:51.6	17.577(011)	0.371(050)	0.841(012)	0.497(008)	0.943(018)	7
8	08:38:33.00	+25:49:00.2	16.343(011)	−0.051(042)	0.603(011)	0.361(007)	0.717(010)	7
9	08:38:25.52	+25:47:41.7	17.077(011)	−0.040(043)	0.587(012)	0.350(007)	0.699(009)	7

Table 3.2—Continued

Star	α (J2000)	δ (J2000)	V	$U-B$	$B-V$	$V-R$	$V-I$	N
				SN 1999gh				
SN	09:44:19.73	−21:16:25.3						
1	09:44:23.52	−21:14:57.1	16.305(011)	1.183(042)	1.268(014)	0.832(008)	1.597(010)	5
2	09:44:16.73	−21:15:46.6	16.766(022)	1.125(069)	1.150(016)	0.712(010)	1.376(017)	5
3	09:44:14.27	−21:14:21.9	15.283(012)	1.029(041)	1.052(012)	0.596(008)	1.090(010)	5
4	09:44:12.53	−21:16:01.8	15.470(012)	0.257(040)	0.730(012)	0.412(008)	0.791(011)	5
5	09:44:19.24	−21:17:43.0	15.683(011)	−0.073(040)	0.571(011)	0.349(008)	0.700(009)	5
6	09:44:21.44	−21:17:49.4	16.504(013)	1.082(105)	1.076(013)	0.647(008)	1.194(011)	5
7	09:44:22.40	−21:18:12.3	17.084(015)	0.375(055)	0.795(013)	0.449(009)	0.846(018)	5
8	09:44:22.84	−21:18:34.5	15.635(011)	0.055(041)	0.638(011)	0.367(009)	0.725(012)	5
9	09:44:20.84	−21:19:05.5	17.120(012)	0.910(081)	1.049(012)	0.636(010)	1.182(020)	5
10	09:44:23.39	−21:19:06.2	15.611(012)	0.243(041)	0.733(012)	0.419(008)	0.807(009)	5
11	09:44:27.93	−21:19:01.0	15.681(011)	0.963(049)	1.065(011)	0.673(009)	1.288(009)	5
				SN 1999gp				
SN	02:31:39.08	+39:22:52.4						
1	02:31:48.99	+39:24:30.0	16.469(011)	0.077(041)	0.682(010)	0.403(009)	0.790(014)	5
2	02:31:45.65	+39:23:57.6	16.547(011)	1.124(076)	1.156(012)	0.697(009)	1.272(013)	5
3	02:31:37.46	+39:23:36.8	16.838(011)	0.686(050)	0.960(010)	0.549(008)	1.021(016)	5
4	02:31:36.00	+39:24:14.8	14.364(011)	0.330(041)	0.794(010)	0.440(007)	0.852(011)	4
5	02:31:30.97	+39:24:05.8	15.836(011)	−0.019(041)	0.577(011)	0.361(008)	0.712(013)	5
6	02:31:30.61	+39:20:21.3	15.800(011)	0.410(042)	0.880(011)	0.496(007)	0.957(012)	5
7	02:31:37.44	+39:21:54.3	16.846(012)	0.526(045)	0.869(011)	0.510(008)	0.984(015)	5
8	02:31:38.95	+39:21:46.6	14.481(010)	0.024(040)	0.571(011)	0.334(007)	0.658(015)	5
9	02:31:41.78	+39:20:10.8	16.214(011)	0.822(042)	1.025(011)	0.614(007)	1.137(011)	5
10	02:31:52.97	+39:21:00.5	16.280(011)	0.599(051)	0.932(013)	0.532(008)	0.996(013)	5
11	02:31:49.18	+39:21:56.9	16.272(014)	−0.015(041)	0.461(011)	0.318(008)	0.666(015)	5
12	02:31:51.74	+39:23:37.5	14.874(010)	0.571(042)	0.893(011)	0.500(007)	0.941(012)	5
				SN 2000B				
SN	07:05:40.49	+50:35:12.3						
1	07:05:42.01	+50:35:32.5	14.637(012)	0.037(040)	0.623(011)	0.366(009)	0.743(009)	6
2	07:05:51.38	+50:37:15.6	15.252(012)	−0.087(040)	0.511(010)	0.315(008)	0.641(009)	6
3	07:05:53.69	+50:37:52.2	16.087(012)	0.202(040)	0.757(011)	0.427(007)	0.836(010)	6
4	07:05:36.09	+50:38:31.8	16.073(013)	0.364(042)	0.849(011)	0.499(008)	0.968(010)	6
5	07:05:28.49	+50:38:24.7	15.394(012)	0.056(040)	0.646(011)	0.372(007)	0.739(011)	6
6	07:05:30.35	+50:38:09.1	15.330(013)	−0.090(040)	0.530(011)	0.326(008)	0.659(010)	6
7	07:05:30.27	+50:37:23.1	15.521(012)	0.039(040)	0.606(011)	0.347(007)	0.689(010)	6
8	07:05:26.45	+50:35:51.4	15.855(012)	0.725(045)	0.979(012)	0.570(007)	1.088(011)	6
9	07:05:26.01	+50:35:06.8	16.517(011)	0.116(040)	0.658(011)	0.378(007)	0.731(010)	6
10	07:05:24.05	+50:33:18.8	14.606(011)	−0.074(040)	0.487(011)	0.292(012)	0.585(009)	6
11	07:05:35.32	+50:33:58.8	15.636(012)	−0.039(042)	0.540(011)	0.322(008)	0.647(011)	6
12	07:05:41.67	+50:32:56.9	15.592(012)	0.609(042)	0.945(011)	0.517(007)	0.998(010)	6

Table 3.2—Continued

Star	α (J2000)	δ (J2000)	V	$U-B$	$B-V$	$V-R$	$V-I$	N
				SN 2000ce				
SN	08:05:09.40	+66:47:16.2						
1	08:05:07.45	+66:46:00.0	15.821(035)	−0.008(094)	0.699(038)	0.416(031)	0.805(033)	1
2	08:05:15.94	+66:44:21.3	13.455(022)	0.134(065)	0.703(023)	...	...	1
3	08:05:25.21	+66:44:26.3	15.782(035)	−0.023(093)	0.609(038)	0.355(031)	0.704(033)	1
4	08:05:43.87	+66:45:05.1	15.031(028)	0.118(079)	0.700(030)	0.399(026)	0.776(027)	1
5	08:05:37.00	+66:47:54.7	13.955(024)	−0.087(067)	0.526(024)	0.328(022)	0.651(023)	1
6	08:05:45.57	+66:51:58.7	14.093(024)	0.692(068)	1.005(025)	0.549(023)	1.060(023)	1
7	08:05:18.27	+66:49:49.7	15.277(030)	0.195(083)	0.721(032)	0.401(028)	0.777(029)	1
8	08:04:23.74	+66:49:18.3	14.314(025)	0.059(070)	0.676(026)	0.376(023)	0.743(024)	1
9	08:04:25.82	+66:42:56.3	15.480(032)	0.404(087)	0.936(034)	0.525(029)	1.031(030)	1
10	08:04:39.59	+66:42:33.8	15.416(031)	−0.028(085)	0.599(034)	0.350(028)	0.672(030)	1
11	08:05:11.23	+66:42:26.9	14.942(028)	0.285(077)	0.743(029)	0.432(026)	0.820(027)	1
				SN 2000cf				
SN	15:52:56.33	+65:56:13.2						
1	15:52:58.02	+65:55:36.0	15.914(016)	0.174(062)	0.704(012)	0.419(014)	0.789(028)	2
2	15:52:42.68	+65:54:45.7	17.080(015)	...	1.342(010)	0.869(016)	1.620(012)	2
3	15:52:28.84	+65:56:33.7	15.848(012)	0.990(095)	1.138(014)	0.728(008)	1.333(010)	2
4	15:52:37.02	+66:00:18.0	15.353(014)	0.056(042)	0.669(014)	0.411(010)	0.773(009)	2
5	15:52:45.76	+65:59:20.4	15.490(012)	0.625(248)	0.926(014)	0.551(008)	0.991(010)	2
6	15:52:51.53	+65:58:51.0	16.598(023)	0.638(120)	0.923(010)	0.529(015)	0.957(024)	2
7	15:52:57.95	+65:59:10.2	16.015(024)	0.546(040)	0.874(016)	0.526(021)	0.975(020)	2
8	15:53:08.27	+65:59:34.1	14.739(018)	−0.022(045)	0.568(011)	0.344(008)	0.650(017)	2
9	15:53:29.51	+65:59:40.1	16.130(013)	0.225(054)	0.754(011)	0.435(008)	0.805(018)	2
10	15:53:30.37	+65:57:32.5	16.378(013)	0.739(112)	1.000(024)	0.585(009)	1.059(012)	2
11	15:53:27.12	+65:56:33.5	15.797(020)	0.284(055)	0.746(017)	0.428(014)	0.793(018)	2
				SN 2000cn				
SN	17:57:40.47	+27:49:58.0						
1	17:57:29.79	+27:51:24.1	14.643(018)	0.337(041)	0.734(010)	0.403(024)	0.781(012)	2
2	17:57:27.62	+27:49:22.8	16.512(021)	0.886(046)	0.989(010)	0.619(015)	1.158(016)	2
3	17:57:27.11	+27:48:52.9	16.289(018)	0.514(065)	0.848(010)	0.488(016)	0.921(011)	2
4	17:57:39.73	+27:49:28.5	14.873(018)	−0.005(041)	0.592(011)	0.365(014)	0.720(010)	2
5	17:57:42.03	+27:49:23.8	15.624(019)	0.336(040)	0.732(013)	0.418(008)	0.793(011)	2
6	17:57:42.73	+27:49:10.8	15.068(021)	0.816(040)	0.990(010)	0.560(015)	1.071(010)	2
7	17:57:43.88	+27:47:49.1	15.905(012)	−0.120(042)	0.570(012)	0.387(012)	0.779(012)	2
8	17:57:50.93	+27:49:54.5	15.441(018)	0.097(044)	0.629(012)	0.383(012)	0.742(011)	2
9	17:57:47.87	+27:53:07.8	16.096(017)	0.099(055)	0.748(014)	0.461(016)	0.920(011)	2
10	17:57:39.15	+27:50:54.1	15.960(020)	−0.007(042)	0.603(017)	0.360(010)	0.720(010)	2
11	17:57:30.79	+27:52:59.8	16.328(020)	−0.005(045)	0.606(010)	0.368(017)	0.719(011)	2

Table 3.2—Continued

Star	α (J2000)	δ (J2000)	V	$U-B$	$B-V$	$V-R$	$V-I$	N
				SN 2000cx				
SN	01:24:46.15	+09:30:31.1						
2	01:24:52.67	+09:31:48.9	13.490(022)	0.303(045)	0.804(023)	...	...	3
3	01:24:49.71	+09:34:24.1	...	0.051(040)	...	...	...	2
4	01:24:40.49	+09:34:39.8	14.538(010)	0.334(043)	0.818(011)	0.470(007)	0.920(010)	3
5	01:24:37.44	+09:32:55.8	17.199(011)	0.285(118)	0.754(014)	0.432(013)	0.854(015)	3
6	01:24:31.62	+09:30:23.1	13.746(010)	0.340(045)	0.763(010)	...	0.798(012)	3
7	01:24:36.20	+09:28:50.3	17.147(010)	0.010(042)	0.699(010)	0.422(013)	0.949(141)	3
8	01:24:39.00	+09:27:40.2	15.636(010)	1.129(078)	1.170(013)	0.709(009)	1.299(010)	3
				SN 2000dk				
SN	01:07:23.53	+32:24:23.4						
1	01:07:13.76	+32:20:46.7	14.312(010)	0.212(041)	0.719(013)	0.409(023)	0.785(011)	2
2	01:07:21.20	+32:21:51.0	14.582(010)	0.448(044)	0.831(011)	0.457(008)	0.868(013)	2
3	01:07:22.16	+32:22:18.6	15.972(011)	0.121(042)	0.673(017)	0.395(010)	0.775(009)	2
4	01:07:38.60	+32:21:20.3	15.382(011)	0.022(040)	0.621(015)	0.373(007)	0.737(009)	2
5	01:07:37.54	+32:25:39.0	16.083(010)	1.211(106)	1.522(012)	0.994(015)	2.066(017)	2
6	01:07:38.92	+32:26:08.6	14.805(011)	0.600(047)	0.942(012)	0.525(007)	1.007(011)	2
7	01:07:23.40	+32:25:31.2	15.991(010)	1.085(045)	1.116(013)	0.681(007)	1.239(009)	2
8	01:07:09.84	+32:26:43.6	16.059(010)	0.593(041)	0.861(063)	0.495(007)	0.939(010)	2
9	01:07:19.88	+32:23:39.9	15.794(011)	−0.037(040)	0.544(012)	0.331(012)	0.669(012)	2
				SN 2000fa				
SN	07:15:29.87	+23:25:42.4						
1	07:15:15.98	+23:28:24.3	15.206(013)	0.108(041)	0.687(010)	0.394(008)	0.771(011)	4
2	07:15:21.55	+23:26:54.6	15.511(012)	0.007(041)	0.647(010)	0.389(007)	0.778(010)	4
3	07:15:21.01	+23:25:23.5	15.444(013)	0.178(041)	0.713(011)	0.403(008)	0.781(011)	4
4	07:15:16.94	+23:23:32.5	15.736(012)	0.029(041)	0.580(010)	0.345(007)	0.674(010)	4
5	07:15:23.53	+23:22:53.6	15.890(013)	0.001(041)	0.533(011)	0.327(007)	0.643(014)	4
6	07:15:41.39	+23:22:15.8	15.395(010)	−0.010(048)	0.563(010)	0.349(008)	0.694(012)	3
7	07:15:42.66	+23:22:35.8	15.497(012)	0.007(043)	0.644(011)	0.391(007)	0.775(013)	4
8	07:15:37.82	+23:24:19.5	15.317(011)	0.795(043)	0.978(011)	0.577(008)	1.076(010)	4
9	07:15:44.77	+23:26:28.0	15.686(013)	0.301(044)	0.749(015)	0.435(008)	0.849(010)	4
10	07:15:30.96	+23:27:58.0	15.801(012)	1.235(041)	1.222(012)	0.762(008)	1.448(010)	4
11	07:15:26.26	+23:28:05.9	16.169(014)	−0.082(043)	0.553(013)	0.364(016)	0.708(013)	4

We present the average color terms for each detector/filterset combination in Table 3.3, along with the internal uncertainties in the mean. We do not have data on any photometric nights when the AndyCam and the Harris filters were on the telescope, and thus we could not use observations of standard stars to determine the color terms for this detector/filterset combination. Instead we used the color

terms based on the calibrated comparison stars themselves (allowing for a variable zeropoint for each frame, given the non-photometric conditions). For the other detector/filterset combinations, we successfully used this method to check the color terms for consistency.

Armed with the comparison star standard magnitudes and the color terms for each detector/filterset combination, we determined the zeropoint for each SN image by transforming the comparison star standard magnitudes to instrumental magnitudes (using the appropriate color term) and comparing to them to the observed comparison star magnitudes. Because the SN is observed at the same time (and thus, airmass) as the comparison stars, the airmass term is consumed into the zeropoint, which is robustly determined from the flux-weighted average of the comparison stars. We then use this zeropoint to determine calibrated instrumental magnitudes for the SN, and use the linear color term transformation to arrive at the final standard magnitudes for the supernova. We keep track of and propagate the uncertainties throughout this procedure, including photon noise in the instrumental magnitudes, dispersion in the photometric solution, uncertainties in the transformation coefficients, and internal uncertainty in the zeropoint for each image. The final standard system *UBVRI* magnitudes of the supernovae, along with the uncertainties and the detector/filterset combination are given in Tables 3.4 to 3.47.

Table 3.3. Photometric Color Terms

Detector/Filterset	Color Term	Value	Nights
AndyCam/SAO	$(v-V)/(B-V)$	$+0.0340 \pm 0.0016$	7
AndyCam/SAO	$(u-b)/(U-B)$	0.9312 ± 0.0016	6
AndyCam/SAO	$(b-v)/(B-V)$	0.9293 ± 0.0011	7
AndyCam/SAO	$(v-r)/(V-R)$	0.9824 ± 0.0020	7
AndyCam/SAO	$(v-i)/(V-I)$	1.0739 ± 0.0015	7
AndyCam/Harris+I_{SAO}[a]	$(v-i)/(V-I)$	1.0639 ± 0.0088	2[b]
AndyCam/Harris	$(v-V)/(B-V)$	$+0.0441 \pm 0.0035$	3[b]
AndyCam/Harris	$(u-b)/(U-B)$	0.9617 ± 0.0075	3[b]
AndyCam/Harris	$(b-v)/(B-V)$	0.9631 ± 0.0086	3[b]
AndyCam/Harris	$(v-r)/(V-R)$	1.0947 ± 0.0117	3[b]
AndyCam/Harris	$(v-i)/(V-I)$	0.9899 ± 0.0224	1[b]
4Sh-chip1/SAO	$(v-V)/(B-V)$	$+0.0423 \pm 0.0025$	3
4Sh-chip1/SAO	$(u-b)/(U-B)$	0.9433 ± 0.0064	3
4Sh-chip1/SAO	$(b-v)/(B-V)$	0.8937 ± 0.0099	3
4Sh-chip1/SAO	$(v-r)/(V-R)$	0.9873 ± 0.0073	3
4Sh-chip1/SAO	$(v-i)/(V-I)$	1.0837 ± 0.0119	3
4Sh-chip3/SAO	$(v-V)/(B-V)$	$+0.0398 \pm 0.0026$	4
4Sh-chip3/SAO	$(u-b)/(U-B)$	0.9650 ± 0.0156	1
4Sh-chip3/SAO	$(b-v)/(B-V)$	0.8830 ± 0.0050	4
4Sh-chip3/SAO	$(v-r)/(V-R)$	0.9685 ± 0.0134	2
4Sh-chip3/SAO	$(v-i)/(V-I)$	1.0725 ± 0.0012	4
4Sh-chip3/Harris+I_{SAO}[a]	$(v-i)/(V-I)$	1.0900 ± 0.0149	1
4Sh-chip3/Harris	$(v-V)/(B-V)$	$+0.0447 \pm 0.0002$	19
4Sh-chip3/Harris	$(u-b)/(U-B)$	0.9638 ± 0.0019	18
4Sh-chip3/Harris	$(b-v)/(B-V)$	0.9155 ± 0.0008	19
4Sh-chip3/Harris	$(v-r)/(V-R)$	1.0812 ± 0.0006	19
4Sh-chip3/Harris	$(v-i)/(V-I)$	1.0284 ± 0.0004	17

Note. — Lowercase/uppercase letters in the color terms refer to instrumental/standard magnitudes. All color terms implicitly contain an additive constant. For example, for the AndyCam/SAO combination: $(v-V) = +0.0340(B-V) + \text{const}$, and $(u-b) = 0.9312(U-B) + \text{const}$.

[a]This filterset consists of the Harris *UBVR* filters and the SAO *I* filter.

[b]These nights were not photometric; the color terms were derived from the calibrated comparison stars. See text for details.

Table 3.4. Photometry of SN 1997E

HJD	*U*	*B*	*V*	*R*	*I*	Detector/Filterset
2450464.92	···	15.694(017)	15.598(011)	15.377(015)	···	AndyCam/SAO
2450465.69	15.441(038)	15.667(015)	15.544(010)	15.357(013)	15.423(014)	AndyCam/SAO
2450466.78	15.414(036)	15.656(013)	15.502(008)	15.323(011)	15.468(011)	AndyCam/SAO
2450468.66	15.500(037)	15.620(014)	15.492(010)	15.322(012)	15.480(013)	AndyCam/SAO
2450472.66	15.789(037)	15.779(013)	15.491(008)	15.323(013)	15.638(012)	AndyCam/SAO
2450476.89	16.330(061)	16.166(032)	15.741(023)	15.716(030)	15.940(032)	AndyCam/SAO
2450479.87	16.802(037)	16.547(013)	15.933(008)	15.906(011)	16.006(011)	AndyCam/SAO
2450485.62	17.725(041)	17.381(015)	16.301(009)	16.003(013)	15.847(018)	AndyCam/SAO
2450489.77	···	17.891(022)	16.627(014)	16.131(019)	15.823(019)	AndyCam/SAO
2450512.65	19.247(060)	18.929(025)	17.829(016)	17.448(026)	17.296(023)	AndyCam/SAO
2450521.62	19.383(186)	19.147(028)	18.101(016)	17.811(023)	17.736(024)	AndyCam/SAO
2450523.66	19.668(114)	19.147(051)	18.113(034)	17.933(048)	17.831(074)	AndyCam/SAO
2450545.65	20.159(120)	19.495(070)	18.783(046)	18.622(066)	18.717(129)	AndyCam/SAO

Table 3.5. Photometry of SN 1997Y

HJD	*U*	*B*	*V*	*R*	*I*	Detector/Filterset
2450488.96	15.073(037)	15.379(015)	15.368(010)	15.278(015)	15.592(014)	AndyCam/SAO
2450489.91	15.157(038)	15.421(016)	15.384(011)	15.284(016)	15.600(015)	AndyCam/SAO
2450515.94	···	18.000(025)	16.852(013)	16.332(019)	15.928(018)	AndyCam/SAO
2450518.84	18.429(056)	18.225(022)	17.012(010)	16.563(015)	16.168(014)	AndyCam/SAO
2450520.86	18.549(056)	18.256(024)	17.141(012)	16.681(023)	16.339(017)	AndyCam/SAO
2450536.84	18.827(069)	18.707(030)	17.690(011)	17.396(018)	17.174(020)	AndyCam/SAO
2450545.87	18.989(099)	18.821(046)	17.944(024)	17.672(037)	17.530(032)	AndyCam/SAO

Table 3.6. Photometry of SN 1997bp

HJD	*U*	*B*	*V*	*R*	*I*	Detector/Filterset
2450546.79	14.077(036)	14.122(012)	14.018(007)	13.921(010)	14.144(011)	AndyCam/SAO
2450547.80	14.079(038)	14.097(014)	13.980(009)	13.894(012)	14.133(014)	AndyCam/SAO
2450548.79	14.110(036)	14.085(012)	13.934(007)	13.838(009)	14.105(011)	AndyCam/SAO
2450549.80	14.175(037)	14.109(014)	13.902(009)	13.812(015)	14.119(013)	AndyCam/SAO
2450550.76	14.229(035)	14.124(013)	13.879(008)	13.792(013)	14.150(018)	AndyCam/SAO
2450552.82	14.340(037)	14.179(015)	13.875(009)	13.762(012)	14.169(013)	AndyCam/SAO
2450567.77	15.914(039)	15.680(017)	14.594(010)	14.494(015)	14.564(024)	AndyCam/SAO
2450569.71	16.114(037)	15.866(016)	14.648(011)	14.483(014)	14.523(014)	AndyCam/SAO
2450573.79	16.494(037)	16.200(012)	14.822(007)	14.461(009)	14.412(010)	AndyCam/SAO
2450575.73	16.689(039)	16.311(015)	14.890(008)	14.475(013)	14.366(012)	AndyCam/SAO
2450579.74	16.983(046)	16.655(016)	15.135(010)	14.655(013)	14.417(015)	AndyCam/SAO
2450597.73	17.733(041)	17.118(016)	15.962(009)	15.540(013)	15.482(012)	AndyCam/SAO
2450610.69	17.859(040)	17.226(020)	16.284(013)	16.025(017)	16.058(018)	AndyCam/SAO

Table 3.7. Photometry of SN 1997bq

HJD	*U*	*B*	*V*	*R*	*I*	Detector/Filterset
2450547.62	···	15.676(020)	15.641(012)	15.493(016)	15.522(017)	AndyCam/SAO
2450548.81	14.971(042)	15.350(023)	15.401(017)	15.234(022)	15.270(021)	AndyCam/SAO
2450549.82	14.735(043)	15.135(023)	15.168(017)	15.054(023)	15.080(023)	AndyCam/SAO
2450550.70	14.551(070)	14.994(042)	15.013(020)	14.902(028)	14.914(027)	AndyCam/SAO
2450551.83	14.451(044)	14.824(021)	14.865(009)	14.740(012)	14.807(014)	AndyCam/SAO
2450568.66	15.323(046)	15.255(018)	14.675(011)	14.711(015)	15.032(017)	AndyCam/SAO
2450570.76	15.650(039)	15.501(012)	14.819(007)	14.827(010)	15.052(011)	AndyCam/SAO
2450573.70	16.078(041)	15.860(016)	15.009(011)	14.918(014)	15.000(016)	AndyCam/SAO
2450575.68	16.380(038)	16.114(014)	15.102(008)	14.951(012)	14.954(013)	AndyCam/SAO
2450578.66	···	16.429(020)	15.259(011)	15.027(019)	14.908(014)	AndyCam/SAO
2450582.78	17.162(089)	16.824(022)	15.473(013)	15.068(017)	14.853(018)	AndyCam/SAO
2450600.72	17.968(045)	17.575(017)	16.422(011)	16.030(015)	15.834(015)	AndyCam/SAO
2450609.66	18.047(054)	17.679(021)	16.636(011)	16.355(016)	16.237(016)	AndyCam/SAO

Table 3.8. Photometry of SN 1997br

HJD	*U*	*B*	*V*	*R*	*I*	Detector/Filterset
2450551.84	13.713(045)	14.397(016)	14.154(008)	13.983(011)	13.922(011)	AndyCam/SAO
2450552.83	13.695(053)	14.317(028)	14.078(016)	13.847(023)	13.811(021)	AndyCam/SAO
2450567.79	14.278(043)	14.371(015)	13.800(009)	13.637(013)	13.759(012)	AndyCam/SAO
2450569.79	14.537(042)	14.574(014)	13.855(008)	13.717(012)	13.825(012)	AndyCam/SAO
2450571.81	14.826(037)	14.811(016)	13.936(010)	13.849(013)	13.833(015)	AndyCam/SAO
2450573.75	15.205(039)	15.060(015)	14.080(009)	13.890(012)	13.838(014)	AndyCam/SAO
2450575.76	15.532(041)	15.315(014)	14.208(008)	13.985(012)	13.828(014)	AndyCam/SAO
2450578.73	15.988(040)	15.672(019)	14.416(013)	14.048(017)	13.789(017)	AndyCam/SAO
2450582.80	16.381(056)	16.002(021)	14.609(012)	14.162(017)	13.875(017)	AndyCam/SAO
2450597.75	17.156(046)	16.810(017)	15.331(009)	14.825(012)	14.350(014)	AndyCam/SAO
2450607.75	17.334(046)	17.009(017)	15.701(009)	15.262(013)	14.915(013)	AndyCam/SAO

Table 3.9. Photometry of SN 1997cn

HJD	*U*	*B*	*V*	*R*	*I*	Detector/Filterset
2450597.76	18.897(068)	18.523(027)	17.216(014)	16.708(019)	16.465(019)	AndyCam/SAO
2450598.83	18.915(068)	18.653(029)	17.291(012)	16.761(016)	16.428(016)	AndyCam/SAO
2450599.71	...	18.780(048)	...	...	...	AndyCam/SAO
2450600.75	19.119(060)	18.858(026)	17.497(014)	16.948(019)	16.563(021)	AndyCam/SAO
2450602.73	19.471(099)	19.081(038)	17.694(016)	17.160(022)	16.724(022)	AndyCam/SAO
2450604.82	19.440(076)	19.290(037)	17.911(020)	17.402(028)	16.941(031)	AndyCam/SAO
2450605.88	19.422(099)	...	...	17.487(041)	17.078(039)	AndyCam/SAO
2450607.77	19.559(080)	...	18.062(014)	17.623(018)	17.191(021)	AndyCam/SAO
2450608.70	19.493(072)	19.421(045)	...	17.710(039)	17.265(039)	AndyCam/SAO
2450609.67	19.643(065)	19.454(030)	18.189(020)	17.746(026)	17.286(027)	AndyCam/SAO
2450610.79	19.679(106)	19.595(053)	18.238(023)	17.810(030)	17.391(031)	AndyCam/SAO
2450611.82	19.632(101)	...	18.301(019)	17.837(025)	17.447(029)	AndyCam/SAO
2450627.67	...	20.076(051)	18.911(020)	18.616(031)	18.345(029)	AndyCam/SAO
2450640.75	...	...	19.238(034)	19.135(052)	18.932(063)	AndyCam/SAO

Table 3.10. Photometry of SN 1997cw

HJD	*U*	*B*	*V*	*R*	*I*	Detector/Filterset
2450642.94	17.041(039)	16.892(016)	16.146(008)	15.948(011)	16.109(014)	AndyCam/SAO
2450643.88	17.227(038)	17.024(015)	16.184(009)	16.002(012)	16.155(013)	AndyCam/SAO
2450644.85	17.319(056)	17.096(027)	16.222(015)	16.079(020)	16.189(024)	AndyCam/SAO
2450645.98	17.469(048)	17.213(020)	16.341(010)	16.132(014)	16.197(020)	AndyCam/SAO
2450646.98	17.594(059)	17.282(019)	16.359(009)	16.199(012)	16.182(013)	AndyCam/SAO
2450647.98	17.804(076)	17.424(045)	16.429(008)	16.215(014)	16.167(013)	AndyCam/SAO
2450652.92	18.453(119)	17.971(046)	16.643(018)	16.268(024)	16.113(027)	AndyCam/SAO
2450653.94	18.484(079)	18.145(028)	16.707(018)	16.290(025)	16.038(025)	AndyCam/SAO
2450665.99	19.368(116)	18.808(033)	17.227(013)	16.619(019)	16.196(018)	AndyCam/SAO
2450673.99	19.612(187)	19.229(050)	17.612(021)	17.044(027)	16.627(027)	AndyCam/SAO
2450680.99	...	19.258(097)	17.920(058)	17.427(075)	16.956(073)	AndyCam/SAO
2450682.97	...	19.293(094)	17.983(057)	17.469(072)	17.194(070)	AndyCam/SAO
2450685.97	...	19.379(051)	18.075(030)	17.545(042)	17.299(040)	AndyCam/SAO
2450688.00	...	19.329(051)	18.138(037)	17.655(047)	17.444(047)	AndyCam/SAO
2450693.79	...	19.499(036)	18.260(021)	17.828(028)	17.769(040)	AndyCam/SAO
2450783.74	...	21.126(092)	20.068(051)	20.421(093)	...	AndyCam/SAO
2450810.62	...	...	20.472(086)	20.690(160)	...	AndyCam/SAO

Table 3.11. Photometry of SN 1997dg

HJD	*U*	*B*	*V*	*R*	*I*	Detector/Filterset
2450720.90	16.806(047)	17.186(027)	17.095(018)	16.921(024)	17.141(026)	AndyCam/SAO
2450722.74	16.919(044)	17.178(021)	17.098(014)	16.927(019)	17.231(023)	AndyCam/SAO
2450726.83	17.405(044)	17.364(022)	17.230(013)	17.078(019)	17.392(022)	AndyCam/SAO
2450730.65	17.958(049)	17.745(022)	17.387(012)	17.344(017)	17.714(024)	AndyCam/SAO
2450747.71	···	19.612(132)	18.416(029)	17.910(038)	17.587(039)	AndyCam/SAO
2450761.79	19.311(275)	20.406(191)	19.205(047)	18.668(066)	18.406(063)	AndyCam/SAO
2450783.72	20.664(144)	···	19.786(034)	19.420(046)	19.424(111)	AndyCam/SAO
2450810.60	···	21.392(192)	20.383(116)	20.227(183)	···	AndyCam/SAO
2450842.61	···	22.062(176)	21.224(127)	21.404(222)	···	4Sh-chip1/SAO

Table 3.12. Photometry of SN 1997do

HJD	*U*	*B*	*V*	*R*	*I*	Detector/Filterset
2450760.01	···	14.849(029)	14.880(022)	14.716(028)	14.873(027)	AndyCam/SAO
2450762.84	14.455(038)	14.626(014)	14.635(008)	14.454(011)	14.691(013)	AndyCam/SAO
2450778.02	···	···	14.807(009)	14.773(012)	···	AndyCam/SAO
2450780.90	15.959(037)	15.607(013)	15.003(007)	15.021(009)	15.288(010)	AndyCam/SAO
2450783.81	16.190(038)	15.960(013)	15.131(008)	15.096(011)	15.203(011)	AndyCam/SAO
2450810.78	17.991(065)	17.722(039)	16.480(008)	16.063(012)	15.833(013)	AndyCam/SAO
2450842.74	18.458(059)	18.116(024)	17.329(009)	17.093(014)	17.223(019)	4Sh-chip1/SAO

Table 3.13. Photometry of SN 1997dt

HJD	*U*	*B*	*V*	*R*	*I*	Detector/Filterset
2450777.60	···	···	15.919(007)	15.402(010)	···	AndyCam/SAO
2450781.68	15.863(038)	15.801(014)	15.369(009)	14.928(011)	14.636(013)	AndyCam/SAO
2450810.58	18.539(051)	17.847(015)	16.242(008)	15.570(011)	14.986(012)	AndyCam/SAO
2450842.59	···	18.915(044)	17.510(019)	16.945(027)	16.474(035)	4Sh-chip1/SAO

Table 3.14. Photometry of SN 1998D

HJD	*U*	*B*	*V*	*R*	*I*	Detector/Filterset
2450874.04	18.902(057)	18.588(028)	17.433(013)	16.971(020)	16.571(024)	4Sh-chip1/SAO
2450893.93	19.445(079)	19.094(032)	18.156(022)	17.801(048)	17.558(031)	AndyCam/SAO
2450925.89	···	19.703(037)	19.081(021)	19.096(036)	18.797(045)	4Sh-chip1/SAO
2450980.80	···	20.604(082)	20.494(059)	20.692(086)	20.134(198)	4Sh-chip1/SAO
2450987.78	···	20.809(083)	20.590(060)	···	···	4Sh-chip1/SAO

Table 3.15. Photometry of SN 1998V

HJD	*U*	*B*	*V*	*R*	*I*	Detector/Filterset
2450894.00	15.738(039)	15.917(016)	15.698(010)	15.486(017)	15.757(015)	AndyCam/SAO
2450894.98	15.918(037)	15.972(014)	15.761(009)	15.521(011)	···	AndyCam/SAO
2450896.01	15.960(038)	15.996(014)	15.736(007)	15.558(010)	15.807(011)	AndyCam/SAO
2450900.93	16.362(036)	16.337(011)	15.913(007)	15.812(008)	16.036(012)	AndyCam/SAO
2450904.00	16.906(036)	16.601(011)	16.159(007)	16.090(010)	16.248(013)	AndyCam/SAO
2450906.99	17.296(041)	16.975(018)	16.285(012)	16.140(016)	16.213(018)	AndyCam/SAO
2450921.99	18.995(076)	18.526(032)	17.147(011)	16.526(017)	16.100(025)	4Sh-chip1/SAO
2450925.95	19.186(056)	18.761(028)	17.408(010)	16.779(016)	16.364(022)	4Sh-chip1/SAO
2450957.98	19.952(199)	19.345(060)	18.395(022)	18.072(038)	17.895(063)	4Sh-chip1/SAO
2450980.86	20.362(160)	19.683(035)	18.960(021)	18.710(030)	18.735(043)	4Sh-chip1/SAO
2450987.83	···	19.823(035)	19.137(018)	18.987(036)	19.057(049)	4Sh-chip1/SAO
2451013.79	···	20.172(049)	19.702(032)	19.700(065)	19.815(111)	AndyCam/SAO
2451077.66	···	21.350(266)	20.626(199)	21.282(280)	···	4Sh-chip1/SAO

Table 3.16. Photometry of SN 1998ab

HJD	*U*	*B*	*V*	*R*	*I*	Detector/Filterset
2450906.82	15.974(038)	16.602(015)	16.570(008)	16.478(013)	16.565(015)	AndyCam/SAO
2450920.66	16.216(044)	16.384(019)	16.216(008)	16.082(011)	16.473(017)	4Sh-chip1/SAO
2450922.65	16.438(040)	16.533(015)	16.277(009)	16.153(012)	16.520(014)	4Sh-chip1/SAO
2450925.84	16.850(040)	16.850(015)	16.388(008)	16.280(012)	16.606(014)	4Sh-chip1/SAO
2450930.76	17.673(045)	17.431(018)	16.746(009)	16.503(013)	16.605(015)	4Sh-chip1/SAO
2450931.81	17.865(046)	17.583(020)	16.781(011)	16.571(015)	16.583(017)	4Sh-chip1/SAO
2450936.68	18.425(065)	18.132(027)	17.106(011)	16.695(017)	16.617(021)	4Sh-chip1/SAO
2450938.71	18.840(104)	18.300(032)	17.211(015)	16.772(021)	16.668(023)	4Sh-chip1/SAO
2450952.69	···	19.096(037)	17.914(015)	17.311(024)	17.030(028)	4Sh-chip1/SAO
2450955.65	19.568(075)	···	18.035(012)	17.452(021)	17.213(031)	4Sh-chip1/SAO
2450961.69	19.522(071)	19.365(028)	18.255(013)	17.686(019)	17.520(024)	AndyCam/SAO
2450964.65	···	19.505(086)	18.349(029)	17.824(043)	17.683(042)	4Sh-chip1/SAO
2450980.69	19.721(113)	19.649(063)	18.702(026)	18.369(042)	18.330(058)	4Sh-chip1/SAO
2450987.73	19.882(075)	19.661(052)	18.863(016)	18.542(028)	18.406(067)	4Sh-chip1/SAO

Table 3.17. Photometry of SN 1998bp

HJD	*U*	*B*	*V*	*R*	*I*	Detector/Filterset
2450934.88	15.655(037)	15.641(014)	15.439(008)	15.162(011)	15.230(014)	4Sh-chip1/SAO
2450937.90	15.801(040)	15.672(017)	15.313(010)	15.070(015)	15.134(016)	4Sh-chip1/SAO
2450938.95	15.923(037)	15.739(014)	15.298(008)	15.054(012)	15.135(013)	4Sh-chip1/SAO
2450939.93	···	15.849(029)	15.307(019)	15.052(026)	15.160(025)	4Sh-chip1/SAO
2450949.93	17.921(053)	17.416(026)	16.077(011)	15.607(015)	15.295(019)	4Sh-chip1/SAO
2450951.87	18.184(069)	17.636(038)	16.266(013)	15.751(021)	15.403(025)	4Sh-chip1/SAO
2450953.85	18.250(049)	17.883(029)	16.416(012)	15.870(019)	15.482(023)	4Sh-chip1/SAO
2450955.89	18.417(053)	18.028(032)	16.653(013)	16.058(019)	15.622(022)	4Sh-chip1/SAO
2450959.94	18.700(046)	18.239(023)	16.941(016)	16.441(021)	16.022(022)	AndyCam/SAO
2450962.88	18.770(062)	18.422(042)	17.125(019)	16.680(026)	16.237(035)	4Sh-chip1/SAO
2450980.84	19.263(088)	18.939(064)	17.787(039)	17.481(051)	17.203(053)	4Sh-chip1/SAO
2450983.81	19.434(053)	18.958(031)	17.891(013)	17.610(022)	17.307(029)	4Sh-chip1/SAO
2450987.82	19.476(083)	19.025(038)	18.014(017)	17.770(027)	17.529(038)	4Sh-chip1/SAO
2450996.78	···	19.204(049)	18.301(025)	18.121(036)	17.836(059)	4Sh-chip1/SAO
2451013.74	20.311(106)	19.456(037)	18.721(025)	18.835(053)	18.538(106)	AndyCam/SAO
2451077.63	···	20.705(082)	···	···	20.114(175)	4Sh-chip1/SAO

Table 3.18. Photometry of SN 1998co

HJD	*U*	*B*	*V*	*R*	*I*	Detector/Filterset
2450990.90	15.934(042)	15.930(016)	15.739(010)	15.608(017)	15.897(016)	4Sh-chip1/SAO
2450993.96	16.319(045)	16.228(016)	15.867(009)	15.796(012)	15.961(020)	4Sh-chip1/SAO
2451077.71	20.381(238)	19.951(141)	19.484(084)	19.522(135)	18.896(173)	4Sh-chip1/SAO
2451110.66	···	20.441(156)	20.279(100)	···	···	4sh-chip3/SAO
2451136.58	···	20.971(192)	20.920(134)	···	19.618(175)	AndyCam/SAO

Table 3.19. Photometry of SN 1998de

HJD	*U*	*B*	*V*	*R*	*I*	Detector/Filterset
2451021.95	18.587(049)	17.979(019)	17.336(010)	17.085(015)	17.175(016)	4Sh-chip1/SAO
2451022.96	18.389(064)	17.781(022)	17.176(011)	16.952(024)	16.937(021)	4Sh-chip1/SAO
2451024.98	18.291(056)	17.572(029)	16.974(017)	16.740(023)	16.701(026)	4Sh-chip1/SAO
2451047.85	···	19.972(072)	18.554(042)	17.866(056)	17.419(057)	4Sh-chip1/SAO
2451055.90	···	20.193(040)	18.879(017)	18.321(024)	17.925(028)	4Sh-chip1/SAO
2451074.74	···	20.621(055)	19.489(027)	19.176(037)	18.598(085)	4Sh-chip1/SAO
2451077.84	···	20.663(075)	19.619(046)	19.315(060)	18.839(071)	4Sh-chip1/SAO
2451110.84	···	21.203(112)	20.540(067)	20.582(101)	19.893(188)	4sh-chip3/SAO
2451136.81	···	21.760(133)	21.139(085)	21.654(198)	20.523(175)	AndyCam/SAO

Table 3.20. Photometry of SN 1998dh

HJD	*U*	*B*	*V*	*R*	*I*	Detector/Filterset
2451021.94	14.427(039)	14.745(015)	14.718(007)	14.475(010)	14.453(012)	4Sh-chip1/SAO
2451026.89	13.929(038)	14.193(013)	14.138(008)	13.987(011)	14.105(011)	4Sh-chip1/SAO
2451045.84	15.743(052)	15.534(036)	14.665(024)	···	14.709(047)	4Sh-chip1/SAO
2451047.84	15.994(045)	15.753(021)	14.782(009)	14.618(014)	14.580(015)	4Sh-chip1/SAO
2451055.89	16.804(042)	16.574(019)	15.235(007)	14.790(011)	14.472(015)	4Sh-chip1/SAO
2451069.87	17.455(051)	17.293(023)	16.045(010)	15.634(014)	15.343(016)	4Sh-chip1/SAO
2451077.76	17.652(042)	17.407(022)	16.289(010)	15.922(014)	15.739(016)	4Sh-chip1/SAO
2451110.75	18.467(059)	17.855(038)	17.128(025)	17.049(036)	17.058(040)	4sh-chip3/SAO
2451136.68	19.097(045)	18.229(017)	17.730(011)	17.847(015)	17.971(032)	AndyCam/SAO

Table 3.21. Photometry of SN 1998dk

HJD	*U*	*B*	*V*	*R*	*I*	Detector/Filterset
2451075.72	16.700(055)	16.494(023)	15.566(012)	15.434(020)	15.456(019)	4Sh-chip1/SAO
2451077.82	16.961(042)	16.750(020)	15.667(008)	15.435(013)	15.402(014)	4Sh-chip1/SAO
2451079.76	17.234(048)	16.941(026)	15.743(013)	15.469(017)	15.369(021)	4Sh-chip1/SAO
2451102.62	18.321(081)	18.192(028)	16.951(013)	16.498(020)	16.200(023)	4sh-chip3/SAO
2451110.79	18.500(065)	18.311(022)	17.196(013)	16.760(019)	16.588(021)	4sh-chip3/SAO
2451136.73	19.231(058)	18.661(018)	17.899(011)	17.613(018)	17.762(018)	AndyCam/SAO

Table 3.22. Photometry of SN 1998dm

HJD	U	B	V	R	I	Detector/Filterset
2451071.82	···	15.398(023)	14.843(006)	14.743(010)	14.832(011)	4Sh-chip1/SAO
2451077.86	16.171(040)	16.008(017)	15.158(008)	15.040(013)	14.962(014)	4Sh-chip1/SAO
2451080.88	16.545(046)	16.321(021)	15.328(009)	15.094(015)	14.909(014)	4Sh-chip1/SAO
2451104.74	18.325(083)	17.866(022)	16.529(008)	16.037(016)	15.544(012)	4sh-chip3/SAO
2451110.80	18.363(062)	18.027(021)	16.736(011)	16.251(019)	15.816(017)	4sh-chip3/SAO
2451136.77	19.000(173)	18.454(017)	17.417(011)	17.071(016)	16.947(016)	AndyCam/SAO
2451195.64	···	19.317(023)	18.749(014)	18.759(021)	18.831(094)	4sh-chip3/Harris+I_{SAO}

Table 3.23. Photometry of SN 1998dx

HJD	U	B	V	R	I	Detector/Filterset
2451072.62	17.269(095)	17.689(057)	17.729(030)	17.578(045)	17.895(062)	4Sh-chip1/SAO
2451077.64	17.951(046)	17.999(023)	17.852(014)	17.708(020)	18.046(027)	4Sh-chip1/SAO
2451078.64	18.059(046)	18.050(024)	17.865(015)	17.735(022)	18.118(085)	4Sh-chip1/SAO
2451083.73	18.904(078)	18.598(021)	18.179(012)	18.158(019)	18.343(036)	AndyCam/SAO
2451100.62	···	20.642(175)	19.559(093)	18.882(142)	18.808(174)	4sh-chip3/SAO
2451136.60	22.432(242)	21.552(184)	20.751(123)	20.097(181)	20.270(212)	AndyCam/SAO

Table 3.24. Photometry of SN 1998ec

HJD	U	B	V	R	I	Detector/Filterset
2451101.96	17.587(044)	17.296(014)	16.663(008)	16.620(011)	16.901(014)	4sh-chip3/SAO
2451106.02	18.128(049)	17.757(017)	16.920(009)	16.836(013)	16.928(017)	4sh-chip3/SAO
2451110.97	18.800(059)	18.324(024)	17.182(013)	16.873(019)	16.823(018)	4sh-chip3/SAO
2451114.01	19.255(116)	18.622(026)	17.366(013)	16.859(019)	16.724(020)	4sh-chip3/SAO
2451136.88	19.983(113)	19.762(032)	18.469(012)	17.972(019)	17.678(023)	AndyCam/SAO
2451195.74	21.003(226)	20.717(064)	19.964(036)	19.929(048)	20.149(108)	4sh-chip3/Harris+I_{SAO}
2451217.84	···	21.050(160)	20.421(121)	20.439(151)	20.401(210)	AndyCam/Harris+I_{SAO}
2451224.68	···	21.187(171)	20.504(121)	20.535(152)	···	AndyCam/Harris+I_{SAO}
2451232.67	···	···	20.853(298)	···	···	4sh-chip3/Harris+I_{SAO}
2451275.62	···	21.938(296)	21.584(153)	21.411(261)	···	4sh-chip3/Harris+I_{SAO}

Table 3.25. Photometry of SN 1998ef

HJD	U	B	V	R	I	Detector/Filterset
2451106.62	15.412(043)	15.628(018)	15.684(011)	15.557(016)	15.513(017)	4sh-chip3/SAO
2451107.75	15.317(040)	15.487(013)	15.521(007)	15.431(010)	15.367(012)	AndyCam/SAO
2451109.86	14.972(038)	15.266(016)	15.320(010)	15.233(013)	15.251(014)	AndyCam/SAO
2451110.78	14.898(039)	15.167(016)	15.209(010)	15.157(013)	15.242(013)	4sh-chip3/SAO
2451136.86	17.707(041)	17.380(014)	16.220(008)	15.845(013)	15.564(014)	AndyCam/SAO
2451195.70	19.901(130)	18.921(038)	18.369(023)	18.465(031)	18.233(047)	4sh-chip3/Harris+I_{SAO}
2451216.62	...	19.230(030)	18.928(017)	19.000(024)	19.011(046)	AndyCam/Harris+I_{SAO}
2451224.59	...	19.399(056)	19.066(034)	19.618(067)	...	AndyCam/Harris+I_{SAO}

Table 3.26. Photometry of SN 1998eg

HJD	U	B	V	R	I	Detector/Filterset
2451110.67	16.367(042)	16.615(022)	16.480(014)	16.340(021)	16.467(020)	4sh-chip3/SAO
2451111.66	16.409(041)	16.594(019)	16.486(011)	16.303(017)	16.545(018)	4sh-chip3/SAO
2451113.58	16.552(043)	16.680(022)	16.490(012)	16.314(018)	16.510(028)	4sh-chip3/SAO
2451136.64	19.506(099)	18.926(064)	17.714(048)	17.217(062)	17.014(062)	AndyCam/SAO
2451195.61	...	20.415(096)	19.669(062)	19.397(093)	...	4sh-chip3/Harris+I_{SAO}

Table 3.27. Photometry of SN 1998es

HJD	U	B	V	R	I	Detector/Filterset
2451133.84	...	...	...	14.391(039)	...	AndyCam/SAO
2451134.80	...	...	...	14.228(039)	...	AndyCam/SAO
2451135.67	13.827(045)	14.288(021)	14.270(012)	14.205(018)	...	AndyCam/SAO
2451136.84	13.725(084)	14.231(032)	14.131(019)	14.073(031)	14.159(027)	AndyCam/SAO
2451137.77	...	14.090(027)	14.061(014)	13.994(021)	14.095(019)	4sh-chip3/SAO
2451138.64	13.537(047)	14.032(022)	13.995(013)	13.913(023)	14.110(021)	4sh-chip3/SAO
2451140.78	13.461(045)	13.945(023)	13.927(016)	13.850(024)	14.079(027)	4sh-chip3/SAO
2451141.82	13.450(065)	13.958(026)	13.889(019)	13.807(025)	14.056(027)	4sh-chip3/SAO
2451142.84	13.507(041)	13.975(022)	13.857(015)	13.801(022)	14.072(030)	4sh-chip3/SAO
2451143.86	13.524(039)	13.974(017)	13.857(008)	13.773(014)	14.100(018)	4sh-chip3/SAO
2451144.72	13.584(042)	14.022(025)	13.841(017)	...	14.184(023)	4sh-chip3/SAO
2451158.65	15.029(113)	14.877(059)	14.459(040)	14.492(058)	14.765(079)	4sh-chip3/Harris+I_{SAO}
2451159.71	15.045(053)	14.970(022)	14.453(013)	14.475(018)	14.703(034)	4sh-chip3/Harris+I_{SAO}
2451164.62	15.863(063)	15.532(036)	14.718(023)	14.587(031)	14.644(040)	4sh-chip3/Harris+I_{SAO}
2451188.58	17.419(066)	17.009(036)	15.897(023)	15.493(030)	15.218(037)	4sh-chip3/Harris+I_{SAO}
2451195.66	17.492(084)	17.187(051)	16.106(028)	15.754(039)	15.544(047)	4sh-chip3/Harris+I_{SAO}
2451196.60	17.702(119)	17.187(059)	16.120(034)	15.787(047)	15.601(054)	4sh-chip3/Harris+I_{SAO}
2451216.60	18.016(171)	17.490(115)	16.728(079)	16.510(109)	16.647(144)	AndyCam/Harris+I_{SAO}
2451224.63	...	17.573(131)	16.938(074)	16.845(116)	17.001(202)	AndyCam/Harris+I_{SAO}
2451233.60	18.418(195)	17.954(125)	17.446(088)	17.287(207)	...	4sh-chip3/Harris+I_{SAO}

Table 3.28. Photometry of SN 1999X

HJD	*U*	*B*	*V*	*R*	*I*	Detector/Filterset
2451217.81	17.150(065)	17.007(041)	16.640(031)	16.602(046)	16.969(054)	AndyCam/Harris+I_{SAO}
2451218.89	17.356(063)	17.086(046)	16.717(034)	16.744(042)	16.991(043)	AndyCam/Harris+I_{SAO}
2451219.86	...	17.215(043)	16.765(032)	16.779(038)	17.016(038)	AndyCam/Harris+I_{SAO}
2451224.71	18.214(082)	17.842(067)	17.074(047)	16.907(058)	16.963(059)	AndyCam/Harris+I_{SAO}
2451233.68	19.056(158)	18.803(105)	17.568(080)	17.078(097)	16.867(103)	4sh-chip3/Harris+I_{SAO}
2451275.67	20.175(259)	19.924(172)	...	18.764(038)	...	4sh-chip3/Harris+I_{SAO}
2451284.69	20.444(209)	...	...	18.976(046)	...	4sh-chip3/Harris+I_{SAO}
2451312.68	...	...	19.906(031)	19.922(045)	...	4sh-chip3/Harris

Table 3.29. Photometry of SN 1999aa

HJD	*U*	*B*	*V*	*R*	*I*	Detector/Filterset
2451222.90	14.986(036)	15.603(013)	15.633(008)	15.573(011)	15.704(013)	AndyCam/Harris+I_{SAO}
2451223.84	14.818(037)	15.417(012)	15.466(007)	15.439(009)	15.534(011)	AndyCam/Harris+I_{SAO}
2451224.79	14.693(043)	15.276(022)	15.351(009)	15.346(012)	15.415(020)	AndyCam/Harris+I_{SAO}
2451226.76	14.477(041)	15.088(021)	15.147(016)	15.145(019)	15.282(020)	AndyCam/Harris+I_{SAO}
2451227.80	14.422(036)	14.960(013)	15.079(009)	15.064(012)	...	AndyCam/Harris+I_{SAO}
2451230.64	...	14.933(014)	14.994(007)	...	15.238(010)	4sh-chip3/Harris+I_{SAO}
2451232.69	14.442(038)	14.876(015)	14.911(007)	14.890(008)	15.214(010)	4sh-chip3/Harris+I_{SAO}
2451233.62	14.486(036)	14.895(012)	14.909(008)	14.888(011)	15.290(023)	4sh-chip3/Harris+I_{SAO}
2451234.64	14.526(055)	14.899(037)	14.905(029)	14.882(035)	15.277(038)	4sh-chip3/Harris+I_{SAO}
2451246.75	15.531(036)	15.629(012)	15.371(007)	15.448(010)	15.682(010)	4sh-chip3/Harris+I_{SAO}
2451248.63	15.826(036)	15.806(012)	15.454(007)	15.531(009)	15.779(012)	4sh-chip3/Harris+I_{SAO}
2451250.74	16.199(037)	16.058(013)	15.554(008)	15.572(010)	15.837(011)	AndyCam/Harris+I_{SAO}
2451252.69	16.506(038)	16.302(016)	15.688(008)	15.646(011)	15.772(012)	AndyCam/Harris+I_{SAO}
2451258.72	17.236(055)	16.914(040)	...	15.710(037)	15.630(039)	4sh-chip3/Harris+I_{SAO}
2451261.62	17.409(040)	17.130(015)	16.051(010)	15.729(013)	15.609(017)	4sh-chip3/Harris+I_{SAO}
2451275.65	18.123(060)	18.025(043)	...	...	16.235(041)	4sh-chip3/Harris+I_{SAO}
2451279.64	18.184(042)	17.973(018)	16.982(010)	16.622(013)	16.432(024)	4sh-chip3/Harris+I_{SAO}
2451281.64	...	17.983(017)	17.033(010)	16.700(013)	16.517(019)	4sh-chip3/Harris+I_{SAO}
2451284.67	18.123(058)	18.032(024)	17.123(011)	16.787(017)	16.684(067)	4sh-chip3/Harris+I_{SAO}
2451285.61	18.271(054)	18.009(023)	17.124(014)	16.825(017)	16.722(025)	4sh-chip3/Harris+I_{SAO}
2451291.62	18.210(107)	18.218(065)	17.192(029)	16.934(045)	16.933(143)	4sh-chip3/Harris+I_{SAO}
2451306.66	18.529(049)	18.311(020)	17.654(011)	17.489(017)	17.554(032)	4sh-chip3/Harris
2451312.65	18.650(090)	18.399(046)	17.826(033)	17.655(041)	17.804(046)	4sh-chip3/Harris

Table 3.30. Photometry of SN 1999ac

HJD	U	B	V	R	I	Detector/Filterset
2451246.89	14.081(035)	14.361(012)	14.392(007)	···	14.335(011)	4sh-chip3/Harris+I_{SAO}
2451247.95	14.039(046)	14.316(028)	14.356(022)	14.271(027)	14.303(027)	4sh-chip3/Harris+I_{SAO}
2451249.99	···	14.274(012)	14.253(007)	14.200(010)	14.290(011)	AndyCam/Harris+I_{SAO}
2451252.00	14.168(037)	14.270(012)	14.237(008)	14.167(010)	14.344(012)	AndyCam/Harris+I_{SAO}
2451253.99	14.276(038)	14.372(015)	14.211(008)	14.178(012)	14.373(013)	AndyCam/Harris+I_{SAO}
2451258.00	14.690(045)	14.698(015)	14.278(010)	14.237(012)	14.482(014)	4sh-chip3/Harris+I_{SAO}
2451260.96	15.057(038)	15.043(013)	14.473(007)	14.383(010)	14.600(011)	4sh-chip3/Harris+I_{SAO}
2451275.90	16.888(047)	16.430(022)	15.319(009)	14.901(024)	14.712(017)	4sh-chip3/Harris+I_{SAO}
2451280.98	17.153(043)	16.743(022)	15.593(012)	15.123(017)	14.826(023)	4sh-chip3/Harris+I_{SAO}
2451282.98	17.205(043)	16.853(020)	15.711(008)	15.246(010)	14.927(017)	4sh-chip3/Harris+I_{SAO}
2451284.92	17.424(044)	16.969(022)	15.843(009)	15.400(012)	15.085(018)	4sh-chip3/Harris+I_{SAO}
2451287.97	17.471(053)	17.078(028)	16.028(016)	15.603(020)	15.262(029)	4sh-chip3/Harris+I_{SAO}
2451290.97	17.560(050)	17.208(024)	16.180(009)	15.789(011)	15.486(017)	4sh-chip3/Harris+I_{SAO}
2451308.85	17.988(058)	17.616(033)	16.668(007)	16.387(009)	16.298(013)	4sh-chip3/Harris
2451312.86	18.120(058)	17.667(033)	16.751(007)	16.525(010)	16.365(014)	4sh-chip3/Harris
2451343.78	18.816(080)	18.116(048)	17.461(011)	17.501(015)	17.411(032)	4sh-chip3/Harris
2451434.62	···	19.643(191)	19.297(050)	19.860(079)	19.444(085)	4sh-chip3/Harris

Table 3.31. Photometry of SN 1999cc

HJD	U	B	V	R	I	Detector/Filterset
2451312.84	16.702(039)	16.947(017)	16.955(011)	16.818(015)	16.914(022)	4sh-chip3/Harris
2451317.90	16.878(040)	16.907(019)	16.884(013)	16.716(017)	17.128(025)	4sh-chip3/Harris
2451336.80	19.439(136)	19.099(068)	17.935(042)	17.462(051)	17.355(067)	4sh-chip3/Harris
2451339.79	19.718(091)	19.386(042)	18.190(021)	17.640(026)	17.530(037)	4sh-chip3/Harris
2451343.79	19.966(139)	19.659(046)	18.510(023)	17.987(028)	17.809(039)	4sh-chip3/Harris
2451434.65	···	21.494(276)	20.843(181)	···	···	4sh-chip3/Harris

Table 3.32. Photometry of SN 1999cl

HJD	U	B	V	R	I	Detector/Filterset
2451335.69	16.071(184)	···	14.354(035)	13.702(046)	13.346(049)	4sh-chip3/Harris
2451338.65	15.793(061)	15.126(043)	14.022(028)	13.455(034)	13.147(035)	4sh-chip3/Harris
2451340.65	15.777(064)	15.066(046)	13.933(030)	13.387(036)	13.147(042)	4sh-chip3/Harris
2451342.65	15.838(060)	15.076(041)	13.887(027)	13.326(038)	13.131(041)	4sh-chip3/Harris
2451343.69	15.904(060)	15.091(037)	13.878(022)	13.323(028)	13.175(031)	4sh-chip3/Harris
2451346.70	···	···	13.869(031)	···	···	4sh-chip3/Harris
2451348.68	16.405(066)	15.395(043)	13.946(027)	13.471(032)	13.340(035)	4sh-chip3/Harris
2451350.66	16.531(072)	15.530(054)	14.044(036)	13.567(051)	13.429(054)	4sh-chip3/Harris
2451362.72	18.588(087)	16.846(040)	14.709(026)	13.934(032)	13.394(036)	4sh-chip3/Harris

Table 3.33. Photometry of SN 1999cw

HJD	*U*	*B*	*V*	*R*	*I*	Detector/Filterset
2451376.96	16.185(064)	15.925(043)	15.044(022)	14.821(041)	14.895(044)	4sh-chip3/Harris
2451434.86	17.991(042)	17.624(016)	17.003(007)	16.828(015)	16.982(019)	4sh-chip3/Harris
2451461.79	18.441(057)	18.044(023)	17.606(016)	17.639(020)	17.849(028)	4sh-chip3/Harris
2451487.71	18.998(074)	18.445(030)	18.103(018)	18.325(024)	18.602(065)	4sh-chip3/Harris
2451521.60	19.794(190)	18.916(050)	18.663(033)	19.102(046)	19.229(103)	4sh-chip3/Harris
2451546.62	20.297(161)	19.367(045)	19.073(030)	19.689(056)	...	4sh-chip3/Harris

Table 3.34. Photometry of SN 1999dq

HJD	*U*	*B*	*V*	*R*	*I*	Detector/Filterset
2451426.99	15.027(043)	15.477(022)	15.325(014)	15.202(017)	15.147(022)	4sh-chip3/Harris
2451427.97	14.831(037)	15.322(015)	15.162(010)	15.027(013)	15.029(015)	4sh-chip3/Harris
2451428.88	14.663(054)	15.199(021)	15.074(014)	14.943(018)	14.960(020)	4sh-chip3/Harris
2451429.99	14.613(038)	15.092(018)	14.955(010)	14.843(014)	14.861(017)	4sh-chip3/Harris
2451431.93	14.491(046)	14.953(023)	14.766(016)	14.689(020)	14.808(026)	4sh-chip3/Harris
2451432.97	14.472(064)	...	...	14.594(038)	...	4sh-chip3/Harris
2451434.00	14.431(040)	14.895(020)	14.740(013)	14.644(016)	14.760(021)	4sh-chip3/Harris
2451434.95	14.466(039)	14.853(021)	14.697(015)	14.587(021)	14.788(021)	4sh-chip3/Harris
2451435.90	14.481(036)	14.864(014)	14.710(010)	14.608(015)	14.743(015)	4sh-chip3/Harris
2451436.87	14.619(064)	14.845(039)	14.696(015)	14.563(019)	14.749(021)	4sh-chip3/Harris
2451437.86	14.621(038)	14.892(017)	14.675(011)	14.565(016)	14.783(016)	4sh-chip3/Harris
2451438.89	14.652(038)	14.889(012)	14.697(008)	14.565(010)	14.813(013)	4sh-chip3/Harris
2451439.91	14.738(038)	14.918(018)	14.681(013)	14.555(018)	14.851(019)	4sh-chip3/Harris
2451441.92	14.883(111)	14.985(015)	14.712(010)	14.601(014)	14.914(019)	4sh-chip3/Harris
2451453.94	16.306(038)	16.009(015)	15.273(007)	15.168(010)	15.280(016)	4sh-chip3/Harris
2451454.90	...	...	15.396(012)	15.210(015)	15.349(017)	AndyCam/Harris
2451458.89	16.928(057)	16.608(015)	15.558(010)	15.263(013)	15.178(014)	4sh-chip3/Harris
2451461.89	17.319(036)	16.911(011)	15.698(007)	15.298(009)	15.098(011)	4sh-chip3/Harris
2451463.90	17.565(039)	17.071(014)	15.808(009)	15.337(011)	15.068(013)	4sh-chip3/Harris
2451466.87	...	17.299(022)	15.983(012)	15.461(016)	15.094(016)	4sh-chip3/Harris
2451468.85	17.939(051)	17.443(021)	16.092(013)	15.556(017)	15.172(018)	4sh-chip3/Harris
2451487.83	18.397(047)	18.016(016)	16.871(010)	16.470(012)	16.174(017)	4sh-chip3/Harris
2451512.78	19.212(067)	18.329(038)	17.518(026)	17.258(032)	17.133(037)	4sh-chip3/Harris
2451521.78	...	18.528(026)	17.619(013)	17.476(019)	17.683(049)	4sh-chip3/Harris
2451527.72	...	...	17.825(028)	17.694(035)	17.824(065)	4sh-chip3/Harris
2451546.76	19.824(082)	18.867(041)	18.270(023)	18.277(032)	18.446(059)	4sh-chip3/Harris
2451547.74	...	...	18.292(029)	...	...	4sh-chip3/Harris
2451589.65	...	19.479(090)	19.031(065)	19.235(092)	18.941(148)	4sh-chip3/Harris
2451590.65	...	19.315(059)	18.922(038)	19.483(092)	18.862(094)	4sh-chip3/Harris

Table 3.35. Photometry of SN 1999ef

HJD	*U*	*B*	*V*	*R*	*I*	Detector/Filterset
2451464.81	17.842(047)	17.720(022)	17.491(015)	17.316(019)	17.909(031)	4sh-chip3/Harris
2451467.73	18.109(041)	17.945(018)	17.627(011)	17.586(016)	18.131(029)	4sh-chip3/Harris
2451469.85	18.301(081)	18.146(020)	17.765(012)	17.742(020)	18.343(080)	4sh-chip3/Harris
2451487.74	20.248(116)	19.955(039)	18.763(024)	18.173(031)	18.174(041)	4sh-chip3/Harris
2451521.62	···	20.953(081)	20.032(046)	19.573(074)	20.215(120)	4sh-chip3/Harris
2451546.68	···	21.313(258)	20.487(177)	20.464(234)	···	4sh-chip3/Harris
2451581.62	···	21.798(280)	20.858(177)	···	···	4sh-chip3/Harris

Table 3.36. Photometry of SN 1999ej

HJD	*U*	*B*	*V*	*R*	*I*	Detector/Filterset
2451487.75	15.728(038)	15.833(016)	15.632(010)	15.531(013)	15.795(014)	4sh-chip3/Harris
2451494.83	16.801(041)	16.629(018)	16.072(011)	16.060(014)	16.267(016)	4sh-chip3/Harris
2451521.70	18.902(135)	18.831(075)	···	17.373(044)	17.174(045)	4sh-chip3/Harris
2451527.64	···	···	17.968(256)	···	···	4sh-chip3/Harris
2451546.71	19.690(133)	19.332(048)	18.529(019)	18.326(029)	18.372(052)	4sh-chip3/Harris
2451589.59	···	20.087(164)	···	19.604(161)	···	4sh-chip3/Harris
2451590.61	···	19.981(118)	19.615(074)	19.684(110)	19.818(197)	4sh-chip3/Harris

The *UBVRI* light curves of the 44 SNe Ia are shown in Figure 3.2 relative to maximum light (defined in the *B*-band) and corrected for time-dilation to the rest-frame (cf. Table 3.49, §3.3.2).

We have used linear color transformations between the supernova instrumental magnitudes and standard magnitudes as has been conventional when presenting SN Ia light curves, but these may be inappropriate due to the strong, broad features present in SN spectra, as compared to the stars from which the color terms are derived. Fortunately, our primary concern is accurate photometry of SN Ia near and soon after maximum light, when the SN flux is still dominated by the continuum in this "photospheric" phase, where the linear transformations derived from stars would be most appropriate. Furthermore, the color terms give no clear indication

Table 3.37. Photometry of SN 1999ek

HJD	*U*	*B*	*V*	*R*	*I*	Detector/Filterset
2451487.91	18.629(058)	18.186(021)	17.324(011)	16.905(015)	16.803(017)	4sh-chip3/Harris
2451495.91	19.737(083)	18.924(030)	17.757(012)	17.401(016)	17.272(022)	4sh-chip3/Harris
2451517.87	...	20.934(130)	19.077(038)	18.296(049)	17.609(049)	4sh-chip3/Harris
2451521.81	...	20.988(150)	19.231(044)	18.505(060)	17.712(064)	4sh-chip3/Harris
2451545.84	...	21.286(121)	19.890(067)	19.251(083)	18.888(085)	4sh-chip3/Harris
2451584.62	...	...	20.825(161)	20.616(209)	20.719(224)	4sh-chip3/Harris
2451590.70	...	...	20.966(201)	...	...	4sh-chip3/Harris

Table 3.38. Photometry of SN 1999gd

HJD	*U*	*B*	*V*	*R*	*I*	Detector/Filterset
2451521.93	17.325(059)	17.144(015)	16.680(010)	16.381(014)	16.470(027)	4sh-chip3/Harris
2451527.95	17.987(078)	17.563(020)	16.842(011)	16.627(014)	16.783(019)	4sh-chip3/Harris
2451545.91	20.109(055)	19.482(016)	17.923(007)	17.242(011)	16.812(012)	4sh-chip3/Harris
2451556.84	20.785(135)	20.343(045)	18.691(021)	18.028(026)	17.502(028)	4sh-chip3/Harris
2451581.82	...	20.486(052)	19.312(021)	18.860(027)	18.525(038)	4sh-chip3/Harris
2451589.86	...	20.521(118)	19.563(046)	19.096(065)	18.716(120)	4sh-chip3/Harris
2451590.89	...	20.531(101)	19.508(045)	19.068(071)	18.651(140)	4sh-chip3/Harris
2451640.77	...	...	20.791(091)	20.549(123)	...	4sh-chip3/Harris
2451670.68	...	...	21.398(257)	...	...	4sh-chip3/Harris

Table 3.39. Photometry of SN 1999gh

HJD	*U*	*B*	*V*	*R*	*I*	Detector/Filterset
2451520.95	15.381(040)	15.172(011)	14.507(007)	14.450(008)	14.651(013)	4sh-chip3/Harris
2451522.01	15.568(040)	15.321(011)	14.587(007)	14.524(011)	14.687(015)	4sh-chip3/Harris
2451523.00	15.733(037)	15.477(014)	14.657(010)	14.570(012)	14.679(015)	4sh-chip3/Harris
2451524.97	16.067(038)	15.814(015)	14.813(010)	14.661(012)	14.707(015)	4sh-chip3/Harris
2451527.04	16.420(043)	16.099(016)	14.991(009)	14.712(012)	14.589(014)	4sh-chip3/Harris
2451541.95	17.656(051)	17.477(017)	16.247(009)	15.799(012)	15.520(016)	4sh-chip3/Harris
2451545.95	17.810(113)	17.631(015)	16.442(010)	15.986(014)	15.737(019)	4sh-chip3/Harris
2451549.92	17.902(052)	17.728(019)	16.589(008)	16.190(012)	15.973(020)	4sh-chip3/Harris
2451552.93	...	17.800(017)	16.688(007)	16.320(011)	16.129(026)	4sh-chip3/Harris
2451554.89	18.079(051)	17.800(018)	16.730(009)	16.382(014)	16.238(019)	4sh-chip3/Harris
2451575.81	18.628(125)	18.148(028)	17.359(019)	17.182(030)	17.052(067)	4sh-chip3/Harris
2451581.85	18.804(091)	18.270(019)	17.524(009)	17.386(019)	17.424(076)	4sh-chip3/Harris
2451584.82	18.885(087)	18.331(031)	17.596(021)	17.509(029)	17.521(059)	4sh-chip3/Harris
2451588.79	19.003(172)	18.419(039)	17.711(023)	17.653(033)	17.664(097)	4sh-chip3/Harris
2451589.81	...	...	17.749(028)	17.638(054)	17.550(113)	4sh-chip3/Harris
2451590.83	18.800(095)	18.417(023)	17.777(015)	17.730(026)	17.701(065)	4sh-chip3/Harris
2451600.79	19.087(240)	18.614(079)	17.990(023)	18.070(046)	18.023(099)	4sh-chip3/Harris
2451640.68	19.873(154)	19.287(069)	18.980(042)	19.197(068)	18.902(168)	4sh-chip3/Harris

Table 3.40. Photometry of SN 1999gp

HJD	*U*	*B*	*V*	*R*	*I*	Detector/Filterset
2451545.81	15.756(037)	16.330(012)	16.338(008)	16.243(011)	16.352(012)	4sh-chip3/Harris
2451546.74	15.758(041)	16.285(016)	16.206(008)	16.177(012)	16.330(012)	4sh-chip3/Harris
2451548.65	15.760(036)	16.199(013)	16.226(009)	16.145(012)	16.366(015)	4sh-chip3/Harris
2451551.63	15.874(037)	16.251(013)	16.140(007)	16.023(011)	16.406(016)	4sh-chip3/Harris
2451553.57	16.050(038)	16.291(013)	16.136(008)	16.015(011)	16.472(014)	4sh-chip3/Harris
2451555.62	16.150(037)	16.475(014)	16.280(009)	16.171(012)	16.568(014)	4sh-chip3/Harris
2451564.64	17.109(048)	17.011(019)	16.564(012)	16.527(017)	17.048(041)	4sh-chip3/Harris
2451570.58	17.857(072)	17.589(021)	16.872(011)	...	17.142(033)	4sh-chip3/Harris
2451580.58	18.870(066)	18.463(031)	17.306(017)	16.851(026)	16.831(029)	4sh-chip3/Harris
2451581.67	18.985(063)	18.578(017)	17.324(010)	16.849(017)	16.850(017)	4sh-chip3/Harris
2451589.67	19.378(193)	18.999(028)	17.822(016)	17.249(024)	17.053(032)	4sh-chip3/Harris

Table 3.41. Photometry of SN 2000B

HJD	*U*	*B*	*V*	*R*	*I*	Detector/Filterset
2451578.83	17.654(036)	17.333(012)	16.462(007)	16.374(010)	16.632(013)	4sh-chip3/Harris
2451581.74	18.102(043)	17.731(017)	16.603(010)	16.429(014)	16.470(016)	4sh-chip3/Harris
2451590.78	19.055(086)	18.624(024)	17.368(012)	16.793(016)	16.544(019)	4sh-chip3/Harris
2451601.65	19.436(118)	19.145(025)	17.946(014)	17.455(018)	17.268(023)	4sh-chip3/Harris
2451607.67	19.728(123)	19.238(024)	18.141(011)	17.701(016)	17.562(022)	4sh-chip3/Harris
2451640.66	20.254(212)	19.691(042)	19.018(030)	18.789(043)	18.892(066)	4sh-chip3/Harris

Table 3.42. Photometry of SN 2000ce

HJD	*U*	*B*	*V*	*R*	*I*	Detector/Filterset
2451674.63	17.842(083)	17.615(030)	16.835(016)	16.504(022)	16.528(024)	4sh-chip3/Harris
2451675.64	18.156(081)	17.674(028)	16.882(015)	16.564(021)	16.595(029)	4sh-chip3/Harris
2451677.66	18.202(083)	17.837(020)	17.010(012)	16.711(019)	16.739(031)	4sh-chip3/Harris
2451678.63	18.292(126)	17.924(038)	17.067(015)	16.761(022)	16.818(033)	4sh-chip3/Harris
2451679.63	18.525(210)	18.068(050)	17.091(021)	16.804(027)	16.821(036)	4sh-chip3/Harris
2451689.66	19.669(141)	19.169(048)	17.648(026)	17.113(033)	16.787(040)	4sh-chip3/Harris

Table 3.43. Photometry of SN 2000cf

HJD	*U*	*B*	*V*	*R*	*I*	Detector/Filterset
2451676.85	17.173(077)	17.256(022)	17.194(012)	17.063(020)	17.491(037)	4sh-chip3/Harris
2451677.80	17.334(063)	17.302(027)	17.191(018)	17.126(024)	17.524(034)	4sh-chip3/Harris
2451678.74	17.410(097)	...	...	17.151(038)	...	4sh-chip3/Harris
2451679.78	17.648(085)	17.445(023)	17.270(014)	17.180(018)	17.604(027)	4sh-chip3/Harris
2451688.81	...	18.437(038)	17.751(020)	17.648(029)	18.046(045)	4sh-chip3/Harris
2451691.79	...	18.851(035)	17.989(015)	17.731(023)	17.993(041)	4sh-chip3/Harris
2451693.83	19.559(185)	18.996(070)	18.128(023)	17.778(031)	17.980(059)	4sh-chip3/Harris
2451695.73	...	19.302(053)	18.245(022)	17.793(028)	17.995(043)	4sh-chip3/Harris
2451696.78	19.822(216)	19.436(057)	18.278(022)	17.844(031)	17.864(038)	4sh-chip3/Harris
2451730.67	...	20.721(176)	19.746(069)	19.269(099)	19.252(118)	4sh-chip3/Harris
2451758.68	...	...	20.377(174)	20.052(236)	...	4sh-chip3/Harris
2451795.67	22.525(201)	...	...	...	...	4sh-chip3/Harris
2451806.62	...	...	20.964(205)	...	...	4sh-chip3/Harris

Table 3.44. Photometry of SN 2000cn

HJD	*U*	*B*	*V*	*R*	*I*	Detector/Filterset
2451699.85	17.567(047)	17.618(020)	17.471(013)	17.264(019)	17.254(025)	4sh-chip3/Harris
2451700.84	17.258(043)	17.349(024)	17.260(018)	17.049(023)	17.008(028)	4sh-chip3/Harris
2451701.90	17.024(038)	17.178(017)	17.033(011)	16.843(015)	16.879(017)	4sh-chip3/Harris
2451702.98	...	16.982(028)	16.892(016)	16.701(021)	16.789(027)	4sh-chip3/Harris
2451703.80	16.888(039)	16.921(018)	16.856(013)	16.647(017)	16.673(022)	4sh-chip3/Harris
2451709.89	17.003(090)	16.896(018)	16.591(012)	16.437(017)	16.785(027)	4sh-chip3/Harris
2451710.83	17.085(070)	16.958(037)	16.580(026)	16.432(041)	16.751(051)	4sh-chip3/Harris
2451711.71	17.195(049)	17.017(022)	16.611(014)	16.476(019)	16.781(023)	4sh-chip3/Harris
2451712.78	17.474(061)	17.074(028)	16.645(018)	16.538(024)	16.867(031)	4sh-chip3/Harris
2451715.86	17.698(071)	17.460(030)	16.821(020)	16.790(028)	17.061(046)	4sh-chip3/Harris
2451716.74	17.889(047)	17.557(020)	16.930(013)	16.857(018)	17.128(027)	4sh-chip3/Harris
2451728.97	...	19.301(044)	17.883(027)	17.355(033)	17.119(039)	4sh-chip3/Harris
2451758.72	...	20.148(070)	19.154(038)	18.967(059)	...	4sh-chip3/Harris
2451789.79	...	...	19.879(252)	...	...	4sh-chip3/Harris
2451790.67	...	...	19.992(244)	...	...	4sh-chip3/Harris
2451791.64	...	...	20.076(104)	20.225(206)	...	4sh-chip3/Harris
2451794.65	...	20.616(147)	20.075(101)	20.242(167)	...	4sh-chip3/Harris
2451796.66	...	20.656(182)	...	...	...	4sh-chip3/Harris
2451803.62	...	...	20.333(101)	20.769(175)	...	4sh-chip3/Harris
2451810.65	...	...	20.659(251)	...	...	4sh-chip3/Harris

Table 3.45. Photometry of SN 2000cx

HJD	*U*	*B*	*V*	*R*	*I*	Detector/Filterset
2451751.97	13.223(051)	13.422(021)	13.285(013)	13.338(017)	13.639(029)	4sh-chip3/Harris
2451789.96	16.571(092)	16.390(035)	15.516(012)	15.227(016)	15.129(028)	4sh-chip3/Harris
2451792.99	16.667(046)	16.512(018)	15.643(010)	15.365(015)	15.315(028)	4sh-chip3/Harris
2451794.95	16.768(049)	16.555(018)	15.718(010)	15.452(014)	15.429(025)	4sh-chip3/Harris
2451800.96	16.911(072)	16.677(048)	15.919(024)	15.700(030)	15.753(060)	4sh-chip3/Harris
2451801.88	16.961(065)	16.701(039)	15.973(028)	15.751(035)	15.828(041)	4sh-chip3/Harris
2451805.86	16.990(050)	16.780(026)	16.099(017)	15.877(024)	16.038(030)	4sh-chip3/Harris
2451810.85	17.126(047)	16.889(021)	16.250(012)	16.067(017)	16.248(027)	4sh-chip3/Harris
2451814.76	17.157(061)	16.971(016)	16.391(009)	16.219(012)	16.446(021)	4sh-chip3/Harris
2451819.93	17.271(047)	17.063(021)	16.563(010)	16.412(014)	16.730(025)	4sh-chip3/Harris
2451822.99	17.275(048)	17.120(021)	16.654(011)	16.524(016)	16.868(028)	4sh-chip3/Harris
2451843.64	17.833(095)	17.535(064)	17.263(033)	17.231(044)	17.667(054)	4sh-chip3/Harris
2451868.70	18.465(073)	18.018(030)	17.816(020)	17.963(029)	18.403(050)	4sh-chip3/Harris
2451875.70	...	18.111(027)	17.918(016)	18.071(027)	18.377(055)	4sh-chip3/Harris
2451878.77	18.779(060)	18.189(029)	18.036(020)	18.164(029)	18.548(050)	4sh-chip3/Harris
2451900.66	19.063(057)	18.550(031)	18.418(020)	18.760(038)	18.929(058)	4sh-chip3/Harris
2451906.64	19.252(055)	18.604(026)	18.520(017)	18.842(029)	19.026(066)	4sh-chip3/Harris
2451933.64	19.817(120)	19.025(084)	18.942(063)	19.404(077)	19.734(152)	4sh-chip3/Harris

Table 3.46. Photometry of SN 2000dk

HJD	*U*	*B*	*V*	*R*	*I*	Detector/Filterset
2451807.88	15.500(038)	15.917(016)	15.896(010)	15.724(012)	15.871(016)	4sh-chip3/Harris
2451809.88	15.431(037)	15.699(012)	15.692(007)	15.558(009)	15.713(011)	4sh-chip3/Harris
2451810.80	15.405(037)	15.664(015)	15.652(009)	15.498(011)	15.696(014)	4sh-chip3/Harris
2451811.84	15.423(036)	15.630(012)	15.578(007)	15.456(008)	15.742(012)	4sh-chip3/Harris
2451813.71	15.562(037)	15.637(014)	15.568(008)	15.468(011)	15.803(014)	4sh-chip3/Harris
2451818.71	16.146(038)	16.004(015)	15.667(009)	15.653(011)	16.114(014)	4sh-chip3/Harris
2451821.97	16.650(039)	16.435(017)	15.906(010)	15.876(013)	16.260(018)	4sh-chip3/Harris
2451825.81	17.359(040)	17.021(015)	16.153(009)	15.996(011)	16.166(016)	4sh-chip3/Harris
2451844.60	18.995(117)	18.682(039)	17.585(016)	17.201(024)	16.970(042)	4sh-chip3/Harris
2451873.73	19.918(229)	19.392(052)	18.529(027)	18.366(041)	18.422(066)	4sh-chip3/Harris
2451875.64	...	19.296(070)	18.610(032)	18.364(047)	18.567(068)	4sh-chip3/Harris
2451906.66	...	19.866(121)	19.515(067)	19.450(103)	19.371(137)	4sh-chip3/Harris
2451933.61	...	20.347(215)	20.245(143)	...	...	4sh-chip3/Harris

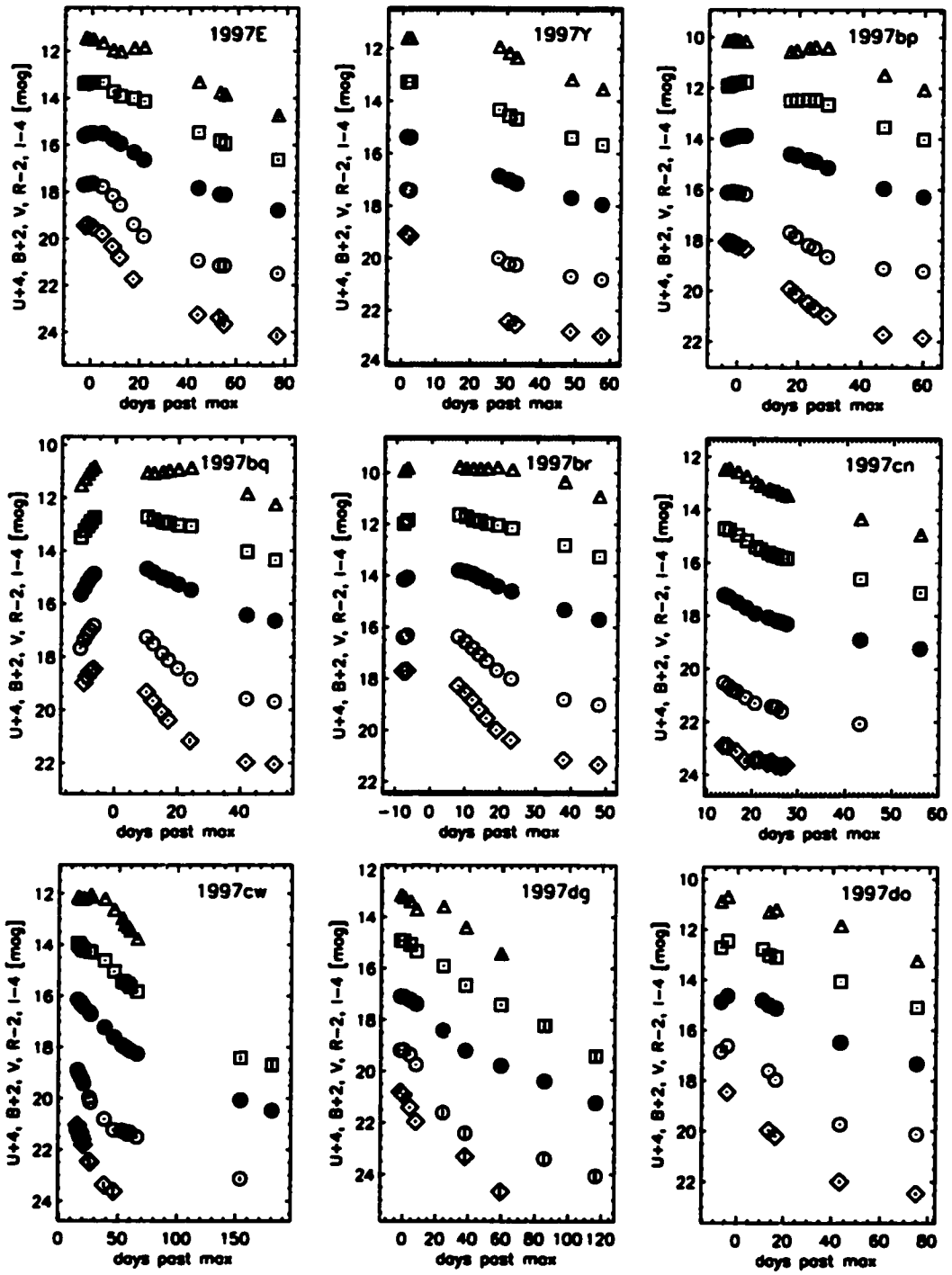

Figure 3.2.— *UBVRI* photometry of 44 SNe Ia. The U (diamonds), B (open circles), V (filled circles), R (squares), and I (triangles) light curves are shown shown relative to B maximum and have been corrected for time-dilation to the rest frame.

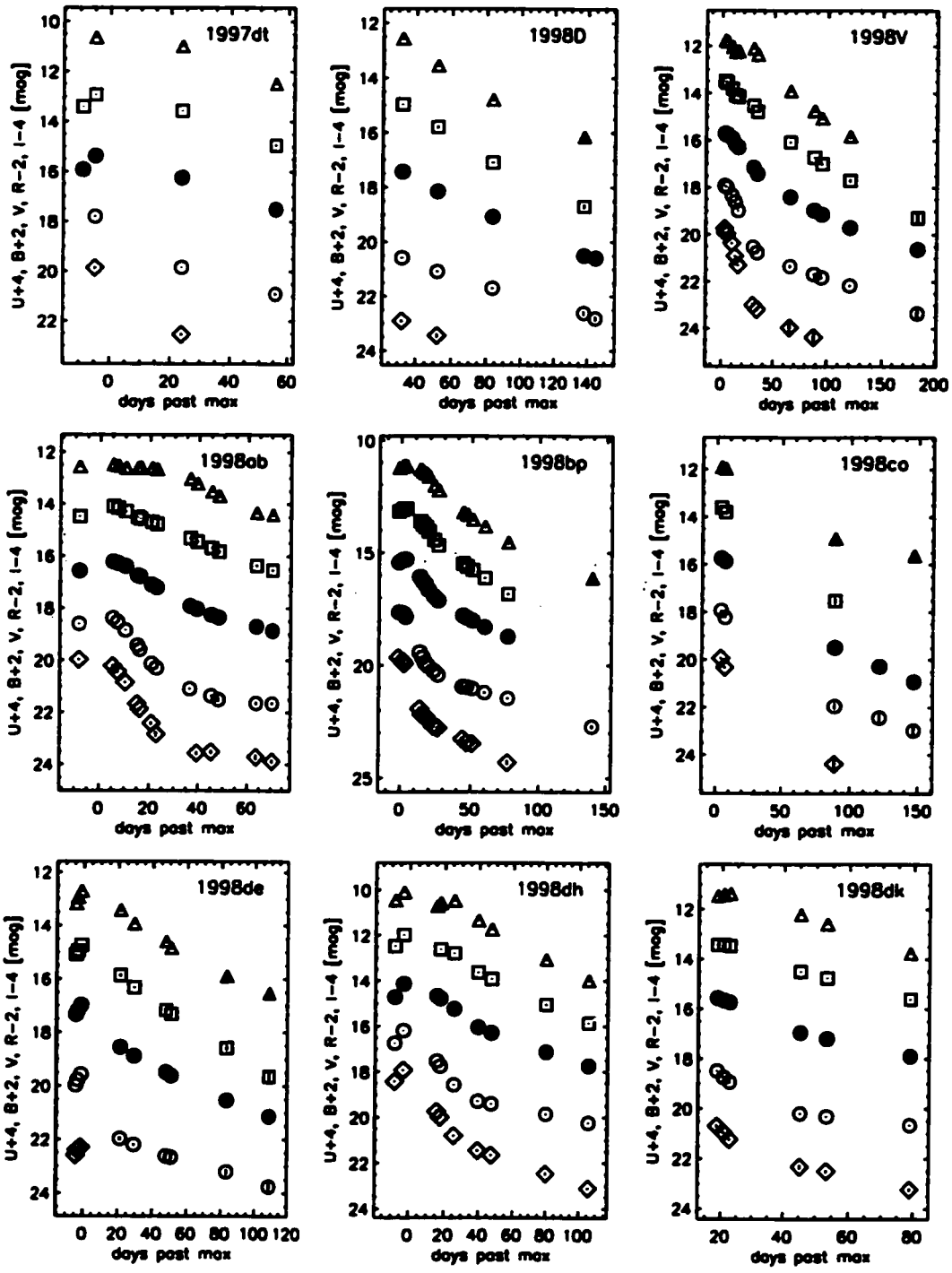

Figure 3.2.— Continued

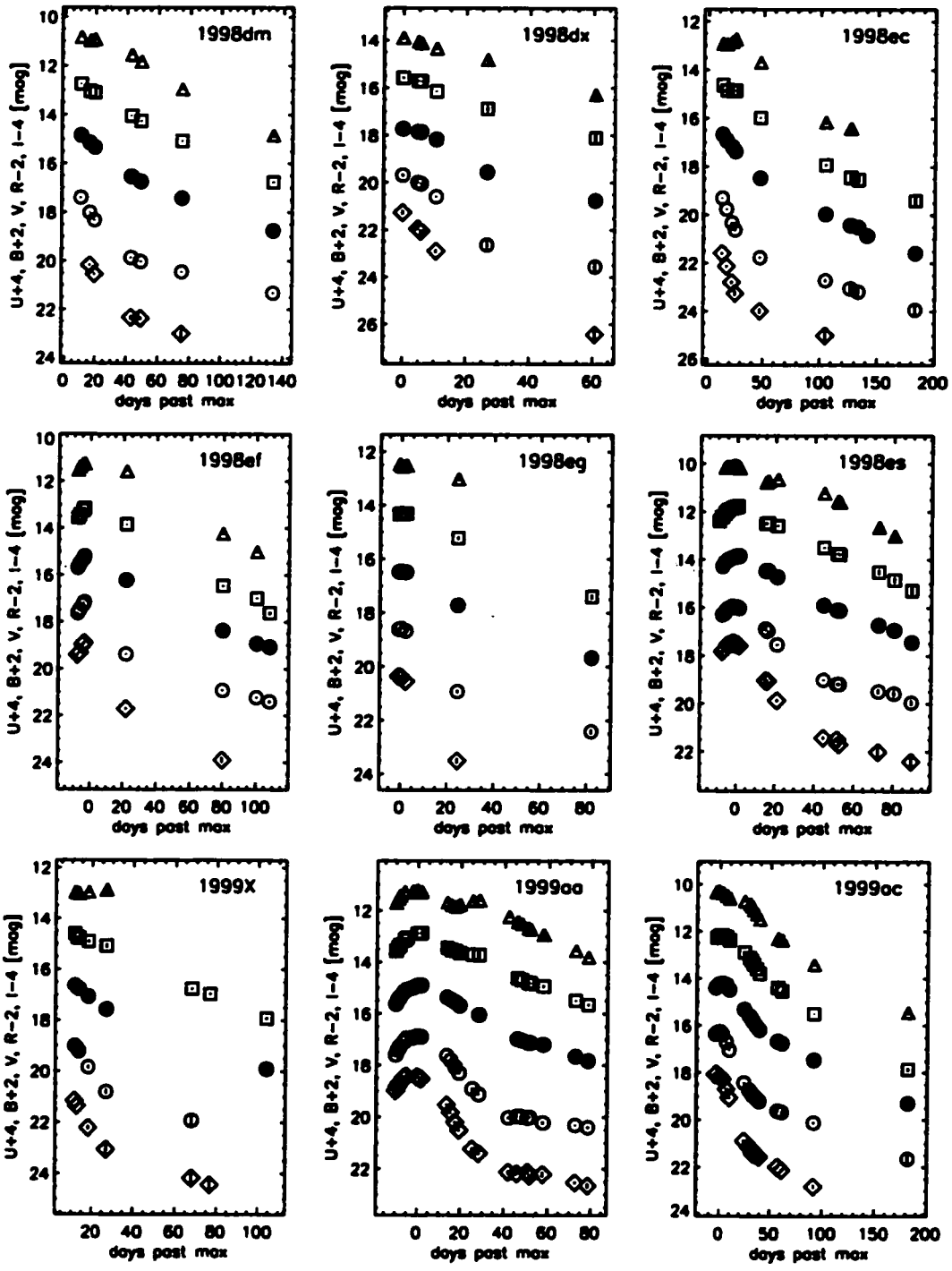

Figure 3.2.— Continued

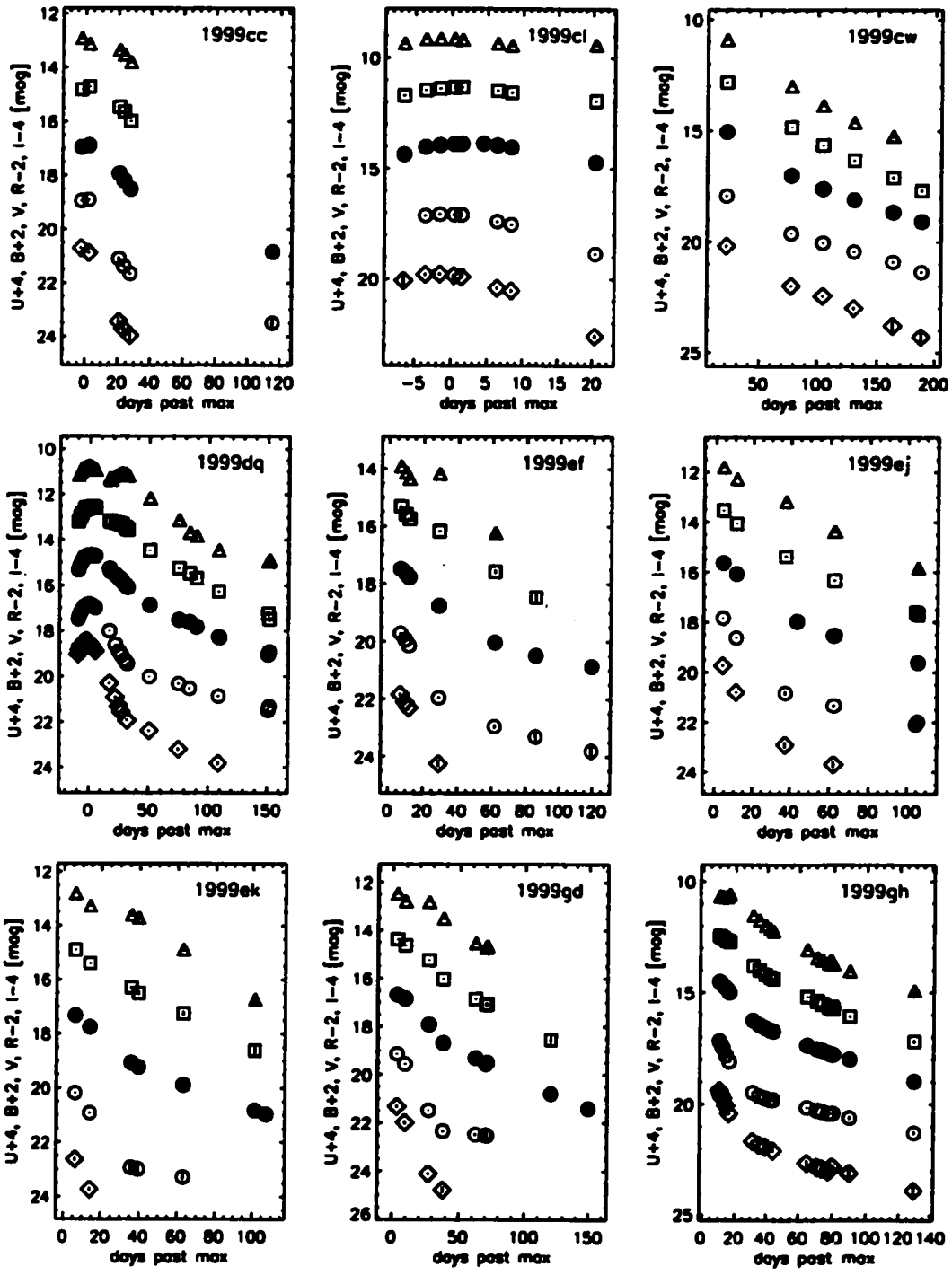

Figure 3.2.— Continued

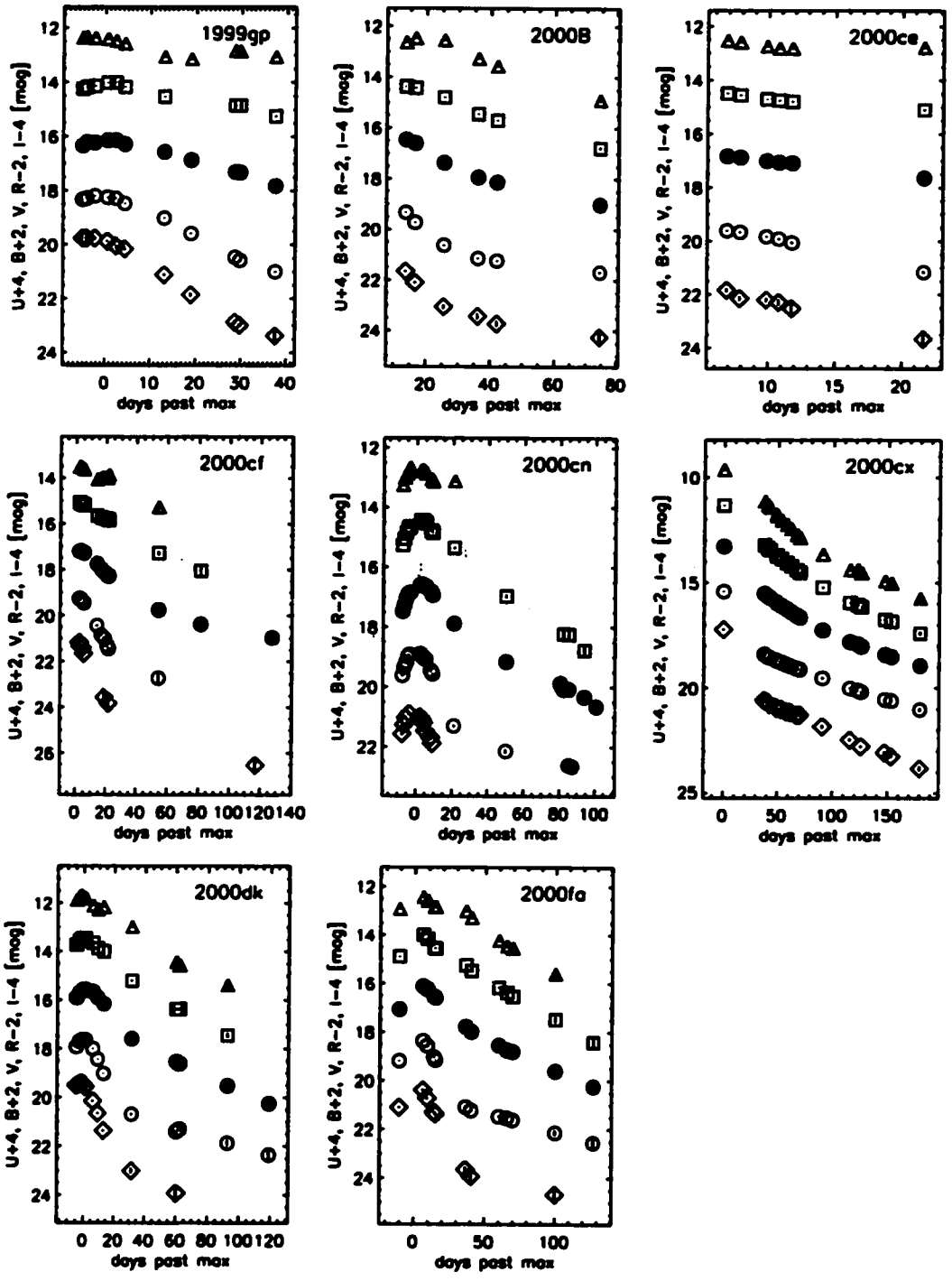

Figure 3.2.— Continued

Table 3.47. Photometry of SN 2000fa

HJD	*U*	*B*	*V*	*R*	*I*	Detector/Filterset
2451881.91	17.095(041)	17.184(017)	17.059(011)	16.889(016)	16.919(019)	4sh-chip3/Harris
2451898.83	16.386(036)	16.364(011)	16.110(007)	15.993(010)	16.424(015)	4sh-chip3/Harris
2451901.83	16.718(037)	16.566(013)	16.237(008)	16.155(011)	16.580(018)	4sh-chip3/Harris
2451906.82	17.295(041)	17.039(015)	16.546(010)	16.531(012)	16.833(021)	4sh-chip3/Harris
2451907.74	17.368(052)	17.148(012)	16.584(007)	16.560(010)	16.836(017)	4sh-chip3/Harris
2451929.83	19.642(113)	19.082(054)	17.777(014)	17.246(019)	17.007(025)	4sh-chip3/Harris
2451933.83	19.921(159)	19.220(031)	17.984(017)	17.472(021)	17.284(025)	4sh-chip3/Harris
2451953.73	...	19.463(040)	18.537(024)	18.167(030)	18.219(044)	4sh-chip3/Harris
2451959.61	...	19.526(048)	18.737(034)	18.372(043)	18.451(063)	4sh-chip3/Harris
2451963.76	...	19.613(043)	18.804(020)	18.537(027)	18.541(080)	4sh-chip3/Harris
2451994.70	20.665(226)	20.133(114)	19.601(076)	19.478(116)	19.591(153)	4sh-chip3/Harris
2452022.66	...	20.550(239)	20.237(155)	20.422(227)	...	4sh-chip3/Harris

that the detector/filterset effective wavelengths are far from those of the standard bandpasses. The ultimate test, though, is in the light curves, which also give no evidence for systematic differences between observations taken with different detector/filterset combinations. For instance, the smoothness of the light curve of SN 1998es (Table 3.27), observed with both instruments with multiple filtersets, is evidence of the internal consistency and homogeneity of the photometry. This is particularly important in the U-band, for which this sample represents the first large collection of SN Ia photometry, but which is also notoriously difficult to transform to a standard system (see, e.g., Suntzeff et al. 1999; Jha et al. 1999, Chapter 2).

Though we have strived to ensure the transformations to the standard system result in consistent, homogeneous photometry, the future uses of this data might nonetheless be limited by the accuracy of these transformations. It may be more convenient and useful to have the data as measured on the natural system. Given the color terms in Table 3.3, it is straightforward to transform the data back to the natural system (and the natural system magnitudes are available on request).

This is only useful, however, in conjunction with the natural system passbands. We have synthesized these passbands by combining the primary and secondary mirror reflectivities (taken simply as two reflections off an aluminum surface), the measured filter transmissions, and the measured detector quantum efficiencies (QE).[1] We have assumed that the QE curve for each 4Shooter chip is identical. The synthesized passbands are shown in Figure 3.3, along with the standard *UX* and *BVRI* passbands of Bessell (1990). Because the *U* passband is defined by the atmospheric cutoff in the blue, we follow the Bessell convention of realizing this passband at airmass 1.0 (using the IRAF Kitt Peak atmospheric extinction curve, adjusted to match the average observed extinction coefficients), whereas the *BVRI* passbands are extra-atmospheric (i.e., airmass 0). As shown in Figure 3.3, the correspondence between the natural system passbands and the Bessell standard response curves is quite good, save for the *I*-band in the SAO filterset. The synthesized passbands are also tabulated in Table 3.48.

[1] We reiterate the footnote of Suntzeff et al. (1999), that the Bessell (1990) passband convention that we adopt also includes a term in the passband that is a linearly increasing function of wavelength. In this convention, then, the magnitude measured with a photon counting detector is $m = -2.5 \log \{ \int F_\lambda(\lambda)\, R(\lambda)\, d\lambda \} + \text{const}$, where $F_\lambda(\lambda)$ is the source flux density and $R(\lambda)$ is the bandpass response.

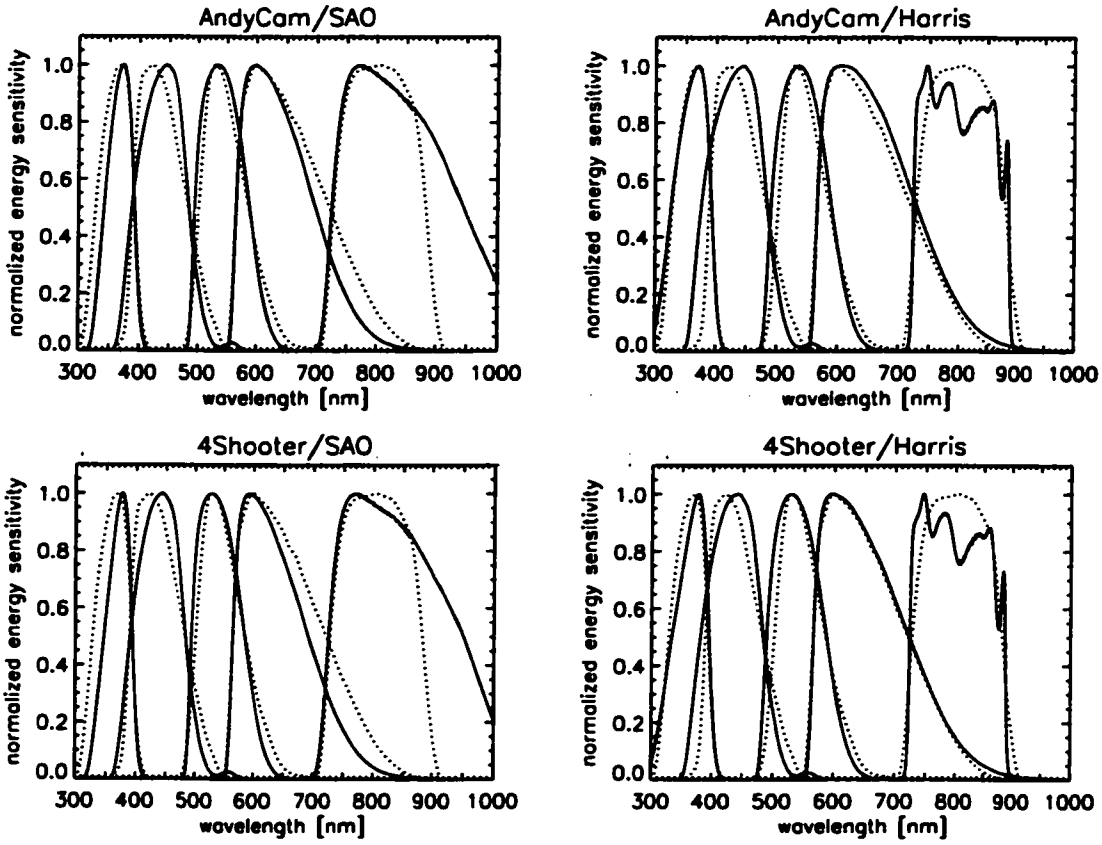

Figure 3.3.— Synthesized natural system *UBVRI* passbands (solid curves) with standard *UX* and *BVRI* passbands (dotted curves) of Bessell (1990) shown for each detector/filterset combination.

Table 3.48. Natural System *UBVRI* passbands

Wavelength (nm)	Detector/filterset normalized response			
	AndyCam/SAO	AndyCam/Harris	4Shooter/SAO	4Shooter/Harris
		U		
290	0.000	0.000	0.000	0.000
295	0.000	0.025	0.000	0.021
300	0.000	0.070	0.000	0.056
305	0.000	0.132	0.000	0.105
310	0.000	0.202	0.000	0.159
315	0.002	0.289	0.002	0.226
320	0.024	0.385	0.018	0.298
325	0.089	0.493	0.067	0.382
330	0.194	0.592	0.148	0.459
335	0.326	0.673	0.250	0.527
340	0.465	0.745	0.362	0.591
345	0.595	0.815	0.472	0.659
350	0.713	0.876	0.581	0.727
355	0.814	0.924	0.686	0.794
360	0.897	0.965	0.786	0.861
365	0.960	0.991	0.878	0.924
370	0.997	1.000	0.953	0.974
375	1.000	0.981	1.000	1.000
380	0.943	0.924	0.985	0.983
385	0.816	0.808	0.888	0.896
390	0.616	0.632	0.696	0.727
395	0.384	0.421	0.448	0.501
400	0.189	0.230	0.226	0.281
405	0.071	0.101	0.086	0.125
410	0.020	0.035	0.025	0.045
415	0.005	0.011	0.006	0.014
420	0.001	0.003	0.001	0.004
425	0.000	0.001	0.000	0.001
430	0.000	0.000	0.000	0.000
		B		
345	0.000	0.000	0.000	0.000
350	0.000	0.005	0.000	0.004
355	0.000	0.040	0.000	0.027
360	0.007	0.130	0.005	0.092
365	0.040	0.255	0.030	0.188
370	0.113	0.383	0.087	0.296
375	0.215	0.494	0.174	0.399
380	0.331	0.586	0.280	0.494
385	0.443	0.661	0.390	0.581
390	0.545	0.723	0.498	0.660
395	0.631	0.774	0.597	0.729
400	0.705	0.816	0.683	0.789
405	0.767	0.851	0.758	0.840

Table 3.48—Continued

Wavelength (nm)	Detector/filterset normalized response AndyCam/SAO	AndyCam/Harris	4Shooter/SAO	4Shooter/Harris
410	0.821	0.884	0.823	0.884
415	0.866	0.913	0.876	0.921
420	0.907	0.940	0.921	0.952
425	0.938	0.960	0.953	0.973
430	0.963	0.978	0.977	0.989
435	0.981	0.990	0.991	0.997
440	0.994	0.997	0.999	1.000
445	1.000	1.000	1.000	0.997
450	0.991	0.989	0.986	0.981
455	0.977	0.973	0.967	0.961
460	0.948	0.944	0.935	0.929
465	0.896	0.894	0.882	0.877
470	0.814	0.814	0.799	0.797
475	0.711	0.715	0.696	0.698
480	0.602	0.608	0.588	0.592
485	0.488	0.497	0.475	0.482
490	0.386	0.396	0.374	0.383
495	0.305	0.315	0.295	0.303
500	0.246	0.254	0.236	0.244
505	0.183	0.191	0.174	0.182
510	0.126	0.133	0.119	0.126
515	0.087	0.093	0.082	0.087
520	0.056	0.060	0.052	0.056
525	0.034	0.037	0.031	0.034
530	0.021	0.023	0.019	0.021
535	0.015	0.018	0.013	0.016
540	0.013	0.015	0.012	0.013
545	0.014	0.015	0.012	0.014
550	0.018	0.018	0.016	0.016
555	0.025	0.024	0.022	0.021
560	0.029	0.027	0.025	0.024
565	0.025	0.024	0.022	0.021
570	0.018	0.018	0.015	0.015
575	0.009	0.009	0.008	0.008
580	0.004	0.004	0.003	0.003
585	0.001	0.001	0.001	0.001
590	0.000	0.001	0.000	0.000
595	0.000	0.000	0.000	0.000
		V		
470	0.000	0.000	0.000	0.000
475	0.000	0.010	0.000	0.011
480	0.001	0.094	0.001	0.100
485	0.040	0.285	0.043	0.304
490	0.245	0.496	0.260	0.527
495	0.531	0.662	0.562	0.700
500	0.732	0.777	0.770	0.817
505	0.845	0.854	0.883	0.892

Table 3.48—Continued

Wavelength (nm)	Detector/filterset normalized response AndyCam/SAO	AndyCam/Harris	4Shooter/SAO	4Shooter/Harris
510	0.908	0.907	0.942	0.941
515	0.946	0.944	0.975	0.971
520	0.971	0.970	0.992	0.990
525	0.988	0.987	1.000	0.999
530	0.997	0.998	1.000	1.000
535	1.000	1.000	0.994	0.994
540	0.994	0.995	0.980	0.980
545	0.981	0.981	0.959	0.959
550	0.958	0.960	0.930	0.931
555	0.925	0.930	0.891	0.895
560	0.882	0.891	0.845	0.852
565	0.829	0.841	0.789	0.800
570	0.768	0.787	0.727	0.744
575	0.700	0.723	0.659	0.680
580	0.625	0.654	0.586	0.612
585	0.548	0.581	0.511	0.541
590	0.470	0.508	0.435	0.471
595	0.393	0.435	0.363	0.401
600	0.321	0.365	0.295	0.335
605	0.256	0.300	0.233	0.273
610	0.198	0.241	0.180	0.219
615	0.149	0.190	0.134	0.171
620	0.108	0.146	0.097	0.131
625	0.076	0.110	0.068	0.098
630	0.052	0.081	0.046	0.072
635	0.034	0.058	0.030	0.051
640	0.021	0.041	0.019	0.036
645	0.013	0.028	0.011	0.024
650	0.008	0.019	0.007	0.016
655	0.004	0.013	0.004	0.012
660	0.002	0.009	0.002	0.007
665	0.001	0.005	0.001	0.005
670	0.001	0.003	0.000	0.003
675	0.000	0.002	0.000	0.002
680	0.000	0.001	0.000	0.001
685	0.000	0.001	0.000	0.001
690	0.000	0.000	0.000	0.000
		R		
540	0.000	0.000	0.000	0.000
550	0.001	0.000	0.001	0.000
560	0.173	0.129	0.179	0.135
570	0.718	0.690	0.735	0.711
580	0.944	0.927	0.958	0.947
590	0.996	0.986	1.000	0.997
600	1.000	0.999	0.994	1.000
610	0.986	1.000	0.969	0.989
620	0.960	0.993	0.933	0.971

Table 3.48—Continued

Wavelength (nm)	Detector/filterset normalized response AndyCam/SAO	AndyCam/Harris	4Shooter/SAO	4Shooter/Harris
630	0.922	0.977	0.886	0.944
640	0.876	0.952	0.833	0.910
650	0.823	0.920	0.775	0.871
660	0.764	0.883	0.713	0.830
670	0.701	0.842	0.651	0.786
680	0.633	0.794	0.584	0.738
690	0.559	0.739	0.514	0.685
700	0.486	0.681	0.446	0.629
710	0.417	0.621	0.383	0.574
720	0.353	0.562	0.324	0.519
730	0.294	0.505	0.270	0.466
740	0.240	0.448	0.221	0.413
750	0.193	0.391	0.177	0.361
760	0.152	0.337	0.139	0.310
770	0.117	0.287	0.106	0.263
780	0.088	0.241	0.080	0.221
790	0.065	0.201	0.059	0.184
800	0.048	0.165	0.044	0.151
810	0.035	0.135	0.032	0.124
820	0.025	0.110	0.023	0.101
830	0.018	0.088	0.016	0.081
840	0.012	0.070	0.011	0.065
850	0.009	0.056	0.008	0.052
860	0.005	0.044	0.005	0.041
870	0.004	0.034	0.003	0.032
880	0.002	0.027	0.002	0.024
890	0.002	0.021	0.002	0.019
900	0.001	0.016	0.001	0.015
910	0.000	0.012	0.000	0.011
920	0.000	0.009	0.000	0.008
930	0.000	0.007	0.000	0.007
940	0.000	0.005	0.000	0.005
950	0.000	0.004	0.000	0.004
960	0.000	0.003	0.000	0.003
970	0.000	0.002	0.000	0.002
980	0.000	0.002	0.000	0.001
990	0.000	0.001	0.000	0.001
1000	0.000	0.001	0.000	0.001
1010	0.000	0.001	0.000	0.000
1020	0.000	0.000	0.000	0.000
		I		
690	0.000	0.000	0.000	0.000
700	0.003	0.000	0.003	0.000
710	0.077	0.001	0.077	0.001
720	0.326	0.073	0.328	0.073
730	0.630	0.927	0.634	0.928
740	0.841	0.993	0.846	0.994

Table 3.48—Continued

Wavelength (nm)	Detector/filterset normalized response			
	AndyCam/SAO	AndyCam/Harris	4Shooter/SAO	4Shooter/Harris
750	0.946	1.000	0.950	1.000
760	0.989	0.886	0.992	0.885
770	1.000	0.945	1.000	0.940
780	0.994	0.976	0.991	0.969
790	0.979	0.938	0.976	0.930
800	0.970	0.826	0.967	0.819
810	0.950	0.799	0.948	0.795
820	0.932	0.837	0.935	0.836
830	0.916	0.879	0.923	0.882
840	0.895	0.886	0.905	0.892
850	0.876	0.875	0.886	0.881
860	0.843	0.917	0.849	0.920
870	0.829	0.697	0.830	0.694
880	0.800	0.597	0.795	0.591
890	0.765	0.278	0.757	0.273
900	0.726	0.009	0.719	0.009
910	0.681	0.000	0.681	0.000
920	0.633	0.000	0.642	0.000
930	0.581	0.000	0.601	0.000
940	0.529	0.000	0.556	0.000
950	0.476	0.000	0.505	0.000
960	0.426	0.000	0.447	0.000
970	0.377	0.000	0.385	0.000
980	0.330	0.000	0.323	0.000
990	0.284	0.000	0.263	0.000
1000	0.239	0.000	0.208	0.000
1010	0.195	0.000	0.161	0.000
1020	0.154	0.000	0.122	0.000
1030	0.117	0.000	0.091	0.000
1040	0.085	0.000	0.066	0.000
1050	0.059	0.000	0.046	0.000
1060	0.040	0.000	0.032	0.000
1070	0.026	0.000	0.021	0.000
1080	0.016	0.000	0.014	0.000
1090	0.009	0.000	0.008	0.000
1100	0.004	0.000	0.004	0.000
1110	0.000	0.000	0.000	0.000

Through synthetic photometry, we have verified that the natural system passbands yield color terms consistent with those directly measured, c.f. Table 3.3. We have also tried to constrain the natural system passbands directly, though observations of spectrophotometric standard stars on the photometric night of 2001 October 24 UT with the FLWO 1.2m telescope using chip 3 of the 4Shooter and the Harris filterset. We took multiple *UBVRI* observations of the following eight

tertiary spectrophotometric standard stars (Massey et al 1988; Hamuy et al. 1992), over a wide airmass range throughout the night: BD +28°4211, Feige 34, Feige 110, G191B2B, Hiltner 600, LTT 9239, LTT 9491, and Wolf 1346. All of these stars also have published spectrophotometry in the red to 1μm (Massey & Gronwall 1990; Hamuy et al. 1994), allowing us to measure synthetic *BVRI* magnitudes. The ground-based spectrophotometry does not extend far enough to the blue with enough precision to synthesize U magnitudes (the Bessell UX passband extends down to 300 nm), and so for the U-band we have used the results of Bohlin, Dickinson, & Calzetti (2001), who give HST/STIS fluxes for five of the standards (BD +28°4211, Feige 34, Feige 110, G191B2B, and LTT 9491) extending below the atmospheric limit.

For each passband, we model the response curve as a cubic spline through a number of spline points spaced equally over the wavelength region where we expect a nonzero response. For each observation in the passband (~20 each in *BVRI* and 13 in U), we correct the standard star spectrum for atmospheric extinction (as above, to zero airmass for *BVRI* and 1.0 airmass for U), and synthesize photometry using the model passband. We find the best-fit model passband by minimizing the residuals between the synthetic and observed magnitudes, using a downhill-simplex (amoeba) method (Press et al. 1992). Our model is specified by the amplitudes (restricted to between zero and one) at the fixed spline points, with the normalization adjusted to yield a fixed zeropoint. The number of spline points in our model is somewhat arbitrary, limited by the number of individual measurements (~20 in *BVRI* and 13 in U). We have found that, in general, having fewer spline points is generally advantageous, avoiding pathological cases and overfitting the measurements at the

expense of detailed information about the shape of the response curve. We have also imposed constraints that the model passband is "reasonable"; it is forced to zero at the ends and not allowed to be wildly oscillatory.

Given these constraints, the best-fit model passbands from the spectrophotometric data are shown in Figure 3.4, along with the 4Shooter/Harris passbands synthesized from the CCD QE curves, filter transmissions, etc. from Figure 3.3, and the Bessell (1990) passbands. Because of the somewhat arbitrary nature of the model, as well as uncertainties in the photometry, these best-fit response curves should be viewed as "typical" realizations of the true response, rather than exact representations. There is a range of models that fit the data reasonably well (with a dispersion of $\sim$0.02 mag in *BVRI* and $\sim$0.04 mag in *U*, similar to the scatter typically exhibited by the Landolt standards), and this range overlaps well with the calculated passbands. A few of the discrepancies between the solid and dashed curves seem to be robust; in particular, the spectrophotometric data favor a *B* response which is narrower than the filter transmission would predict. To thest this definitively, we would need a larger data set, with more spectrophotometric standards.

Though we have only tried this exercise with one detector/filterset combination, the results suggest that the match between the best-fit model passband and the calculated passbands is generally good. Furthermore, the constancy of the color terms for a particular detector/filterset indicates that effects such variable detector response or mirror reflectivity (due to cleanliness, for instance) do not significantly affect the natural system bandpasses. We thus conclude that the response curves shown in Figure 3.3 and Table 3.48 are good representations of the natural system.

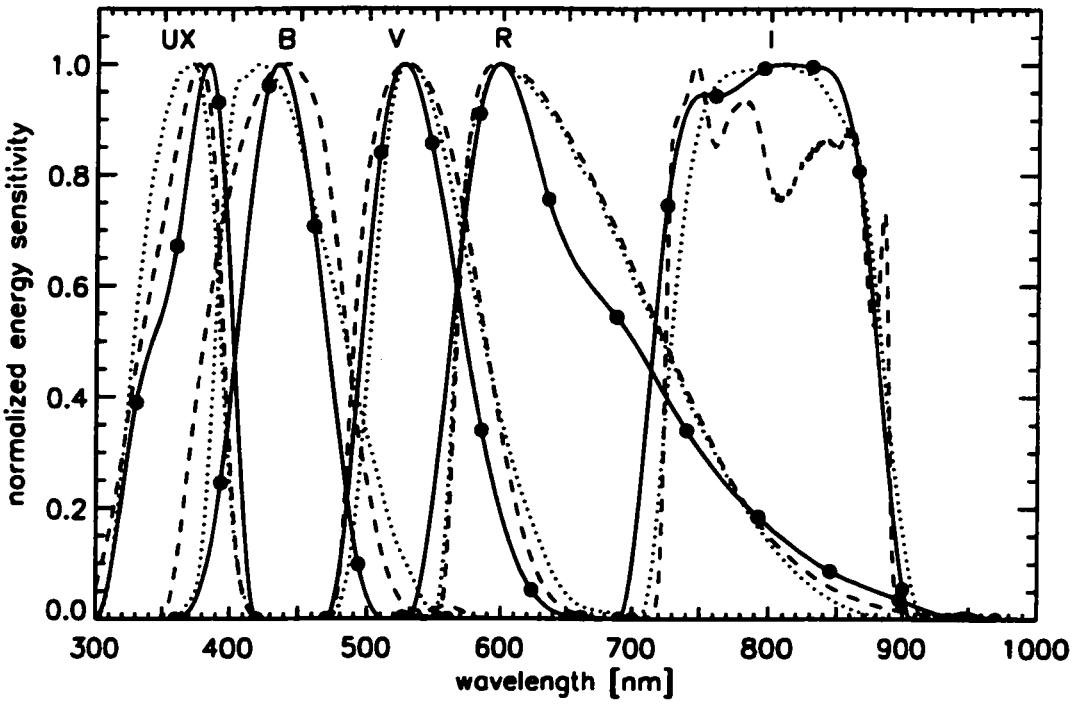

Figure 3.4.— Model 4Shooter/Harris *UBVRI* passbands derived from observations of spectrophotometric standard stars (solid curves), calculated passbands from optics + filter transmission + detector response (dashed curves), and standard *UX* and *BVRI* passbands of Bessell (1990; dotted curves). The solid points show the location of the model spline points; see text for details.

3.3 Results

3.3.1 Comparison with Published Photometry

A number of the supernovae presented here have published photometry from other groups. Because of the difficulties in supernova photometry (correcting for galaxy contamination, transformation to the standard system, etc.), systematic differences between SN photometry from different telescopes are common. This differences are generally small, at the level of a few hundredths of a magnitude (see, e.g., comparisons of photometry of SN 1998bu, in Chapter 2; Suntzeff et al. 1999; Jha et al. 1999; Riess et al. 1999), though larger differences can occur with worse filter mismatches. In this paper, we strive to present photometry that is internally as homogeneous as possible, but it is still useful to compare this data with independent observations. When the systematic differences are small, combining these independent data sets is highly desirable, producing dramatic improvements in the light curve sampling.

3.3.1.1 SN 1997br

Li et al. (1999) present extensive *BVRI* photometry of SN 1997br in ESO 576-40 from observations at the Beijing Astronomical Observatory 0.6m and the Lick Observatory 0.76m Katzman Automatic Imaging Telescope (KAIT). There is good agreement in the *BVI* photometry presented by Li et al. and that presented here, but there are significant, systematic differences in the R photometry, at the level of 0.25 mag, even at maximum light. The comparison stars we have in common show

good agreement[2]. However, the color terms presented by Li et al. are relatively large in R, e.g., $(v-r)/(V-R) = 1.20$ for the KAIT observations, and the photometry differences correlate well with the SN color, implying that the transformation to the standard system is the likely culprit.

3.3.1.2 SN 1997cn

Turatto et al. (1998) present *UBVRI* photometry of SN 1997cn in NGC 5490 from a number of telescopes at ESO, La Silla. Our photometry agrees well with theirs in *BVR* ; in U our photometry is generally brighter by $\sim$0.15 mag, but is consistent within the photometric uncertainties for this faint object. Our I-band photometry is also brighter, by $\sim$0.1 mag. We have one comparison star in common with Turatto et al. (their star 2 is our star 9), and the agreement is good in all bands. We note that the Turatto et al. U-band photometry is the only other published U photometry for any of the 44 SNe presented in this paper.

3.3.1.3 SN 1998de

Extensive *BVRI* observations of SN 1998de in NGC 252 are presented by Modjaz et al. (2001). The data presented there have been K-corrected to the rest-frame, and to facilitate direct comparison with our observations, M. Modjaz has kindly supplied us with their standard magnitudes before K-correction. Our data set is relatively

[2]We note in passing that the finder chart presented by Li et al. (1999) seems to indicate their star E corresponds to our comparison star 6, but the photometry in their Table 1 matches our photometry of comparison star 5, which is somewhat fainter and much redder than star 6. Because of its faintness, Li et al. do not assign much weight to this star, so it is unlikely to explain the discrepant R magnitudes.

sparse compared to that presented by Modjaz et al.[3] but the agreement is very good before maximum light. Our I-band data taken about 45 days past maximum light shows a relatively large discrepancy (~ 0.4 mag), but this is still likely a result of the transformation to the standard system at a phase when the SN spectrum is highly non-stellar. Comparison star C of Modjaz et al. is the same as our star 8, and its photometry agrees very well.

3.3.1.4 SN 1999aa and SN 1999cl

Krisciunas et al. (2000) present *BVRI* observations of three SNe Ia: SN 1999aa, SN 1999cl, and SN 1999cp, for two of which we have independent data. The agreement between our photometry of SN 1999aa and that of Krisciunas et al. is superb. In addition, the data sets complement each other very nicely in terms of phase coverage; the combined light curves are excellent.

Neither set of data on the nearby SN 1999cl in NGC 4501 (M88) is as extensive as for SN 1999aa, nor is the photometric agreement as good. The two sets agree relatively well in all bands at maximum light, but the photometry of Krisciunas et al. at about a month past maximum is brighter than our (single) late time point at that epoch in all bands. Moreover, the discrepancy is larger in the redder bands. This is a good indication of contamination from the host galaxy; indeed, Krisciunas et al. note that SN 1999cl might be an object where galaxy subtraction would improve their aperture photometry. Our late-time template images show that the host galaxy makes a non-negligible contribution to the flux at the position of the

[3]This is due to the fact that the SN peaked at the end of July, just as FLWO undergoes a month-long shutdown because of the southern Arizona monsoons.

supernova. It would be very useful to reanalyze the Krisciunas et al. data for SN 1999cl using image subtraction, as they present four epochs of data later than the last point presented here which would significantly enhance the quality of the light curve for this important object.

3.3.1.5 SN 1999gp and SN 2000ce

Krisciunas et al. (2001) present *BVRI* photometry of five SNe Ia, including SN 1999gp in UGC 1993 (with galaxy subtraction) and SN 2000ce in UGC 4195. For SN 1999gp, the two sets of photometry match extremely well, with only a small ($\sim$ 0.05 mag) consistent difference in the R band photometry. This discrepancy can be traced directly to the comparison stars, as the ones in common show an identical offset. Our comparison star photometry for the SN 1999gp field comes from 5 photometric nights, with consistent R photometry on all epochs. We thus recommend that the Krisciunas et al. SN 1999gp R photometry be adjusted 0.05 mag brighter to be consistent with the data presented here. As in the case of SN 1999aa, the data sets are nicely complementary.

The light curve of SN 2000ce also benefits from the combined data sets. In fact, the overlap is very slight (we have two epochs in common, and only one for all the bands simultaneously). Nonetheless, the agreement of the photometry at these epochs is quite good.

3.3.1.6 SN 2000cx

Li et al. (2001) present an immense data set in *BVRI* for the unique SN 2000cx in NGC 524. The photometry presented here is also quite extensive, except for the fact the SN was discovered in mid July, just prior to the aforementioned August shutdown of FLWO. Thus, our data set consists of only point near maximum light, before a large number of observations beginning a month later. Nevertheless, the agreement between our photometry and that of Li et al. is excellent as far as 100 days past maximum light.

3.3.2 SN and Host Galaxy Properties

In Table 3.49 we list basic data about each SN Ia. The host-galaxy heliocentric redshifts listed are taken from the Updated Zwicky Catalog (Falco et al. 1999) if possible, and from the NASA/IPAC Extragalactic Database (NED) otherwise, where we favor optical redshifts over H I redshifts if there is a discrepancy. For three objects, host galaxy redshifts were not available, and we report them here based on spectroscopy with the FLWO 1.5m telescope plus FAST spectrograph (Fabricant et al. 1998) and cross-correlation with galaxy templates: the host of SN 1997dg, $cz_{\rm helio} = 9238 \pm 14$ km s^{-1}; the host of SN 1998dx (UGC 11149), $cz_{\rm helio} = 16197 \pm 32$ km s^{-1}; and the host of SN 2000cf (MCG +11−19−25), $cz_{\rm helio} = 10920 \pm 20$ km s^{-1}.

Table 3.49. SN Ia and Host Basic Data

SN Ia	Host galaxy	$cz_{\rm helio}$ km s^{-1}	Morphology	SN Offsets ″N	″E	$E(B-V)_{\rm Galactic}$ mag
1997E	NGC 2258	4001	S0	+57	−32	0.124
1997Y	NGC 4675	4806	Sb	+2	−8	0.017
1997bp	NGC 4680	2492	Sd/Irr	−20	−15	0.044
1997bq	NGC 3147	2780	Sbc	−60	+50	0.024
1997br	ESO 576-40	2085	Sd/Irr	+52	−21	0.113
1997cn	NGC 5490	4855	E	−12	+7	0.027
1997cw	NGC 105	5133	Sab	+4	+8	0.073
1997dg	anonymous	9238	···	0	+2	0.078
1997do	UGC 3845	3034	Sbc	−4	−3	0.063
1997dt	NGC 7448	2194	Sbc	+1	−9	0.057
1998D	NGC 5440	3765	Sa	−7	−26	0.015
1998V	NGC 6627	5268	Sb	+21	−21	0.196
1998ab	NGC 4704	8134	Sc	+12	+2	0.017
1998bp	NGC 6495	3127	E	+13	−1	0.076
1998co	NGC 7131	5418	S0	+5	+2	0.043
1998de	NGC 252	4990	S0	+3	+72	0.057
1998dh	NGC 7541	2678	Sbc	+10	−54	0.068
1998dk	UGC 139	3963	Sc	+3	+5	0.044
1998dm	MCG-01-4-44	1968	Sc	−37	−14	0.044
1998dx	UGC 11149	16197	Sb	−12	+21	0.041
1998ec	UGC 3576	5966	Sb	−20	−9	0.085
1998ef	UGC 646	5319	Sa	−2	+6	0.073
1998eg	UGC 12133	7423	Sc	−25	−26	0.123
1998es	NGC 632	3168	S0	+11	0	0.032
1999X	CGCG 180-22	7503	···	+6	+4	0.032
1999aa	NGC 2595	4330	Sc	+28	+1	0.040
1999ac	NGC 6063	2848	Scd	−30	+24	0.046
1999cc	NGC 6038	9392	Sc	+2	+17	0.023
1999cl	NGC 4501 (M88)	2281	Sb	+23	−46	0.038
1999cw	MCG-01-02-001	3725	Sab	−2	+21	0.036
1999dq	NGC 976	4295	Sc	−6	−4	0.110

Table 3.49—Continued

SN Ia	Host galaxy	$cz_{\rm helio}$ km s^{-1}	Morphology	SN Offsets "N	"E	$E(B-V)_{\rm Galactic}$ mag
1999ef	UGC 607	11733	Scd	−10	+20	0.087
1999ej	NGC 495	4114	S0/Sa	−20	+18	0.071
1999ek	UGC 3329	5253	Sbc	−12	−12	0.561
1999gd	NGC 2623	5535	···	+17	+7	0.041
1999gh	NGC 2986	2302	E	+16	+52	0.058
1999gp	UGC 1993	8018	Sb	+10	−11	0.056
2000B	NGC 2320	5901	E	+19	−14	0.068
2000ce	UGC 4195	4888	Sb	+17	+15	0.057
2000cf	MCG+11-19-25	10920	···	+4	+3	0.032
2000cn	UGC 11064	7043	Scd	−7	−7	0.057
2000cx	NGC 524	2379	S0	−109	−23	0.082
2000dk	NGC 382	5228	E	+9	−5	0.070
2000fa	UGC 3770	6378	Sd/Irr	+4	+7	0.069

The supernovae in the sample range from heliocentric redshifts of 1968 to 16197 km s^{-1}, with median and mean redshifts of 4888 and 5274 km s^{-1}, respectively. The mean redshift is significantly less than both the original CfA sample of Riess et al. (1999; $\overline{cz} \simeq 7500$ km s^{-1}) and the Calán/Tololo sample of Hamuy et al. (1996a; $\overline{cz} \simeq 13500$ km s^{-1}). Nonetheless, most of the objects are in the Hubble flow; 39 of the 44 SNe Ia have $cz \geq 2500$ km s^{-1} in the CMB rest-frame, a slightly larger fraction than the original CfA sample (17 out of 22).

The host-galaxy morphology information shown in Table 3.49 is taken from NED, and the supernova offset from the nucleus is taken from the IAU CBAT list of supernovae[4]. We also list the Galactic reddening towards each supernova, derived from the dust maps of Schlegel, Finkbeiner & Davis (1998).

[4]`http://cfa-www.harvard.edu/iau/lists/Supernovae.html`

3.3.3 Light Curve Properties

In Table 3.50 we list the times of maximum light in B for each supernova, as determined from either a direct polynomial fit to the B light curve, or from MLCS2k2 fits (Jha et al. 2002; Chapter 4). We also present the epoch of the first observation in our data set (measured in the rest frame). Over half the objects (25 out of 44) have observations before maximum light, and seventy percent (31 out of 44) have observations earlier than 5 days past maximum light.

We have also fit the BVI light curves of our supernova sample to determine maximum light magnitudes and the parameter $\Delta m_{15}(B)$, which has been shown to correlate with the supernova intrinsic luminosity (Phillips 1993). Though originally defined as the measured decline rate of the supernova in B from maximum to 15 days past maximum light, we follow Hamuy et al. (1995, 1996a) where $\Delta m_{15}(B)$ is a parameter in a multi-dimensional fit to template light curves (each with a predefined $\Delta m_{15}(B)$). We have followed the recipe of Hamuy et al. (1996a) in our fits, using a parabolic fit through the minimum reduced χ^2 in a fit of the BVI light curves to each of a set of templates ("de"-K-corrected and time-dilated to the observed frame, for each SN). We have used the six BVI templates presented by Hamuy et al. (1996b), and augmented this sample with templates based on an additional four well-observed SNe Ia in order to produce more robust measurements of $\Delta m_{15}(B)$: SN 1995al (Riess et al. 1999; $\Delta m_{15}(B) = 0.83$), SN 1998aq (Boffi et al. 2002, in preparation; $\Delta m_{15}(B) = 1.13$), SN 1998bu (Suntzeff et al. 1999; Jha et al. 1999, Chapter 2; $\Delta m_{15}(B) = 1.01$) and SN 1999by (Garnavich et al. 2002; $\Delta m_{15}(B) = 1.90$). We were able to

get reliable $\Delta m_{15}(B)$ measurements for all but four of the SNe Ia[5]; these values (not corrected for host-galaxy reddening) and their uncertainties are listed in Table 3.50. We also present the *BVI* magnitudes at maximum light (in *B*) for each SN determined from the best-fit template.

[5]The four objects include SN 1998D and SN 1999cw, for which the first observation was well after maximum light; SN 1998co, for which the data are quite sparse; and SN 2000cx, whose light curve is unique among all SNe Ia (Li et al. 2001).

Table 3.50. Light Curve Data and $\Delta m_{15}(B)$ Template Fits

SN Ia	HJD_{Bmax}	First Obs.	$\Delta m_{15}(B)$ fits			
			$\Delta m_{15}(B)$	B_{Bmax}	V_{Bmax}	I_{Bmax}
1997E	2450468.0	−3.1	1.39(06)	15.59	15.47	15.50
1997Y	2450487.5	1.4	1.25(10)	15.28	15.31	15.39
1997bp	2450550.3	−3.5	1.00(05)	14.15	13.89	14.10
1997bq	2450558.5	−10.8	1.01(05)	14.57	14.27	14.38
1997br	2450559.7	−7.8	1.02(06)	14.02	13.61	13.45
1997cn	2450583.9	13.6	1.90(05)	16.93	16.44	16.24
1997cw	2450627.1	15.6	1.02(10)	16.00	15.52	15.34
1997dg	2450722.6	−1.6	1.13(09)	17.20	17.11	17.16
1997do	2450767.0	−7.0	0.99(10)	14.56	14.46	14.60
1997dt	2450786.6	−8.9	1.04(15)	15.64	15.08	14.55
1998D	2450841.2	32.4	...	...	...	...
1998V	2450891.1	2.9	1.06(05)	15.88	15.71	15.63
1998ab	2450915.2	−8.2	0.88(17)	15.94	15.93	15.99
1998bp	2450936.4	−1.5	1.83(06)	15.73	15.29	15.09
1998co	2450987.2	3.7	...	...	...	...
1998de	2451026.2	−4.2	1.93(05)	17.55	16.83	16.58
1998dh	2451030.0	−8.0	1.23(17)	14.24	13.99	14.07
1998dk	2451056.8	18.7	1.05(10)	14.93	14.74	14.82
1998dm	2451061.2	10.5	1.07(06)	14.70	14.48	14.29
1998dx	2451072.6	0.0	1.55(09)	17.71	17.76	17.90
1998ec	2451088.6	13.1	1.08(09)	16.44	16.21	16.23
1998ef	2451114.5	−7.7	0.97(10)	15.21	15.18	15.29
1998eg	2451111.4	−0.7	1.15(09)	16.62	16.50	16.51
1998es	2451143.4	−9.4	0.87(08)	13.99	13.87	14.12
1999X	2451206.0	11.5	1.11(08)	16.45	16.29	16.32
1999aa	2451233.0	−9.9	0.85(08)	14.91	14.91	15.25
1999ac	2451251.2	−4.2	1.00(08)	14.34	14.28	14.33
1999cc	2451315.5	−2.5	1.46(05)	16.85	16.85	17.08
1999cl	2451342.2	−6.5	1.19(19)	15.11	13.90	13.10
1999cw	2451355.9	20.8	...	...	...	...
1999dq	2451436.7	−9.5	0.88(08)	14.88	14.68	14.77

Table 3.50—Continued

SN Ia	HJD_{Bmax}	First Obs.	$\Delta m_{15}(B)$ fits			
			$\Delta m_{15}(B)$	B_{Bmax}	V_{Bmax}	I_{Bmax}
1999ef	2451457.7	6.9	1.06(05)	17.52	17.39	17.70
1999ej	2451483.7	4.0	1.41(05)	15.65	15.63	15.71
1999ek	2451481.6	6.2	1.13(09)	17.97	17.19	16.56
1999gd	2451518.5	3.4	1.16(06)	17.02	16.61	16.29
1999gh	2451510.4	10.4	1.69(05)	14.46	14.27	14.27
1999gp	2451551.1	−5.1	0.87(08)	16.25	16.12	16.44
2000B	2451564.8	13.8	1.46(05)	15.94	15.80	15.99
2000ce	2451667.6	6.9	1.06(10)	17.39	16.71	16.23
2000cf	2451674.4	2.4	1.27(12)	17.15	17.12	17.34
2000cn	2451707.5	−7.5	1.58(12)	16.82	16.64	16.71
2000cx	2451752.2	−0.2	...	...	...	...
2000dk	2451812.5	−4.5	1.57(09)	15.63	15.57	15.77
2000fa	2451892.7	−10.5	1.00(10)	15.99	15.95	16.13

To further explore the light curve properties of this sample, and in particular, to study the U-band light curves, we have also fit the light curves to templates, based on the timescale stretch parameterization developed by the Supernova Cosmology Project (Perlmutter et al. 1997, 1999; Goldhaber et al. 2001). The stretch template presented by Goldhaber et al. (2001) is only for the B-band; we would like to fit the UBV light curves, for which the simple stretching of the time axis does a good job of fitting the observed data. To construct U and V-band templates, one possibility is to use composite light curves, combining a large number of supernovae to produce an average template. However, because some objects are better sampled in different bands, the average templates produced this way might not consistently represent a supernova of "average" light curve shape and/or luminosity. For this reason, we have constructed UBV templates based on photometry of a single supernova, the

well-observed SN 1998aq (Boffi et al. 2002, in preparation). To retain consistency with the Goldhaber et al. (2001) normalization, we have corrected our SN 1998aq *UBV* stretch templates to $s = 1$, by fitting the B template to the SCP1997 template presented in that paper.

In fitting our stretch templates to the data, we generally follow the methodology of Goldhaber et al. (2001) as applied in their analysis of the Calán/Tololo sample (Hamuy et al. 1996a). We restrict the light curves to between -10 and $+40$ days in the rest-frame, and we only include objects with photometry commencing earlier than 5 days after maximum light. Because we are interested in understanding the general light-curve properties of these SNe Ia, we allow the fits to be as unrestrictive as possible: we fit for the stretch individually in each of the three bands, and allow the times of maxima to vary in each band (plus or minus a few days), as well as individually fitting for the *UBV* peak magnitudes[6]. We also impose an error floor on the photometry equal to 0.007 times the peak flux, as did Goldhaber et al. (2001, see their Table 7); while this is negligible near maximum, it becomes the dominant uncertainty in the photometry at late times (for instance, corresponding to ± 0.2 mag in the U-band at $+40$ days). As in the $\Delta m_{15}(B)$ fits above, we fit the data in the observed-frame (de-K-correcting and time-dilating the templates).

The limits on the epoch of first observation, and the requirement that we need $\gtrsim 5$ points between -10 and $+40$ days in each of the three bands for a meaningful

[6]We fit the data in magnitude space, rather than flux space, out of convenience. Because we are only fitting the light curves between -10 and $+40$ days, the difference between the two approaches is negligible. Determining rise-time information at very early epochs clearly benefits from fitting in flux space, where negative and zero fluxes are common.

fit limits the application of this method to 22 of the 44 SNe Ia presented here. The results are presented in Table 3.51, listing the *UBV* peak magnitudes and timescale stretch factors, along with the differences in the time of maximum light in U and V relative to $t_{\rm Bmax}$.

3.4 Discussion: U-band Light Curves

The U-band photometry presented here, while just a fraction of the whole dataset, is the first large sample of homogeneously observed and reduced U photometry of SNe Ia. The *BVRI* properties of SNe Ia are well-studied, and while our data provide a much expanded sample of *BVRI* light curves, here we focus on the new element, the U-band data. Though a number of other SN Ia individually also have published U-band photoelectric or CCD photometry, the difficulties of transforming this photometry (with the variety of instruments, filters, sensitivities, etc.; see, e.g., Schaefer 1995; Suntzeff et al. 1999) to a standard system leads us first to examine the U-band properties of SNe Ia from FLWO observations alone, as we have taken care to ensure internal consistency. We will explore the comparisons between other U-band photometry with the results derived here in a future paper.

Figure 3.5 shows the composite U-band light curve of the 44 SNe Ia presented in this paper, along with six other SNe Ia with U data from the FLWO 1.2m: SN 1995al and SN 1996X (for which *BVRI* light curves were presented by Riess et al. 1999), SN 1998aq (Boffi et al. 2002, in preparation), SN 1998bu (Jha et al. 1999, Chapter 2), SN 1999by (Garnavich et al. 2002), and SN 2001V (Mandel et al. 2002, in preparation). Of the *UBVRI* passbands, the SN Ia light curve declines fastest

Table 3.51. *UBV* Stretch Template Fits

SN Ia	$U_{\rm Bmax}$	$B_{\rm Bmax}$	$V_{\rm Bmax}$	s_U	s_B	s_V	$t_U - t_B$	$t_V - t_B$	χ^2/dof
1997E	15.40(05)	15.62(02)	15.47(02)	0.79(04)	0.83(02)	0.87(03)	−1.8(0.8)	0.7(0.3)	2.3
1997Y	14.90(07)	15.35(08)	15.39(02)	0.96(08)	0.93(03)	0.91(04)	−1.9(1.3)	1.6(0.7)	0.2
1997bp	14.05(05)	14.10(02)	13.91(02)	1.12(03)	0.97(03)	1.07(03)	−3.1(1.0)	2.1(0.4)	2.3
1997bq	14.23(04)	14.53(02)	14.44(02)	0.89(02)	0.92(02)	1.02(02)	−2.1(0.2)	1.6(0.1)	0.7
1997br	13.29(12)	13.88(05)	13.62(02)	0.81(05)	0.91(03)	1.04(03)	−2.6(0.4)	1.1(0.2)	2.1
1998V	15.62(07)	15.91(04)	15.73(03)	0.89(07)	0.99(05)	0.96(04)	−1.8(1.8)	0.7(0.9)	4.0
1998ab	15.51(06)	16.08(03)	16.10(02)	0.83(03)	0.92(02)	1.02(02)	−2.0(0.2)	0.5(0.2)	1.1
1998bp	15.56(07)	15.63(02)	15.31(02)	0.71(04)	0.65(02)	0.66(02)	−3.1(1.2)	2.1(0.4)	2.7
1998dh	13.91(06)	14.15(02)	14.04(02)	0.90(03)	0.91(02)	0.98(02)	−1.9(0.3)	1.1(0.2)	0.7
1998dx	17.02(13)	17.69(05)	17.74(03)	0.70(06)	0.85(04)	0.81(04)	−2.0(1.3)	1.2(0.7)	1.4
1998eg	16.20(06)	16.61(02)	16.50(02)	0.88(06)	0.96(04)	0.98(04)	−2.3(0.9)	1.3(0.6)	0.6
1998es	13.45(04)	13.97(02)	13.87(01)	0.98(03)	1.13(02)	1.10(02)	−1.6(0.3)	0.4(0.2)	1.0
1999aa	14.37(04)	14.89(03)	14.94(02)	1.05(02)	1.11(03)	1.13(02)	−2.2(0.3)	0.0(0.2)	2.9
1999ac	14.03(06)	14.28(03)	14.22(02)	1.04(04)	0.93(05)	0.99(02)	−2.7(0.9)	2.0(0.4)	4.0
1999cc	16.60(06)	16.88(03)	16.89(02)	0.86(05)	0.81(03)	0.87(03)	−2.0(0.9)	0.3(0.5)	1.8
1999cl	15.76(05)	15.07(03)	13.88(02)	0.82(04)	0.97(04)	1.02(03)	−1.9(0.6)	1.7(0.4)	0.5
1999dq	14.43(04)	14.86(02)	14.69(02)	0.98(02)	1.08(02)	1.13(02)	−2.3(0.2)	0.3(0.2)	1.5
1999gp	15.67(07)	16.26(03)	16.19(02)	1.04(07)	1.17(06)	1.20(04)	−2.0(1.2)	0.8(0.6)	6.2
2000cf	16.84(11)	17.18(04)	17.21(02)	0.83(06)	0.87(02)	0.92(03)	−2.2(1.3)	1.4(0.7)	0.6
2000cn	16.76(07)	16.81(03)	16.59(02)	0.76(06)	0.77(03)	0.82(02)	−1.7(0.3)	1.2(0.2)	2.3
2000dk	15.36(05)	15.63(02)	15.57(02)	0.73(04)	0.74(02)	0.81(03)	−2.5(0.5)	1.1(0.2)	2.7
2000fa	15.82(08)	16.13(04)	16.04(03)	1.01(03)	1.04(03)	0.97(03)	−2.3(1.0)	1.4(0.8)	1.2

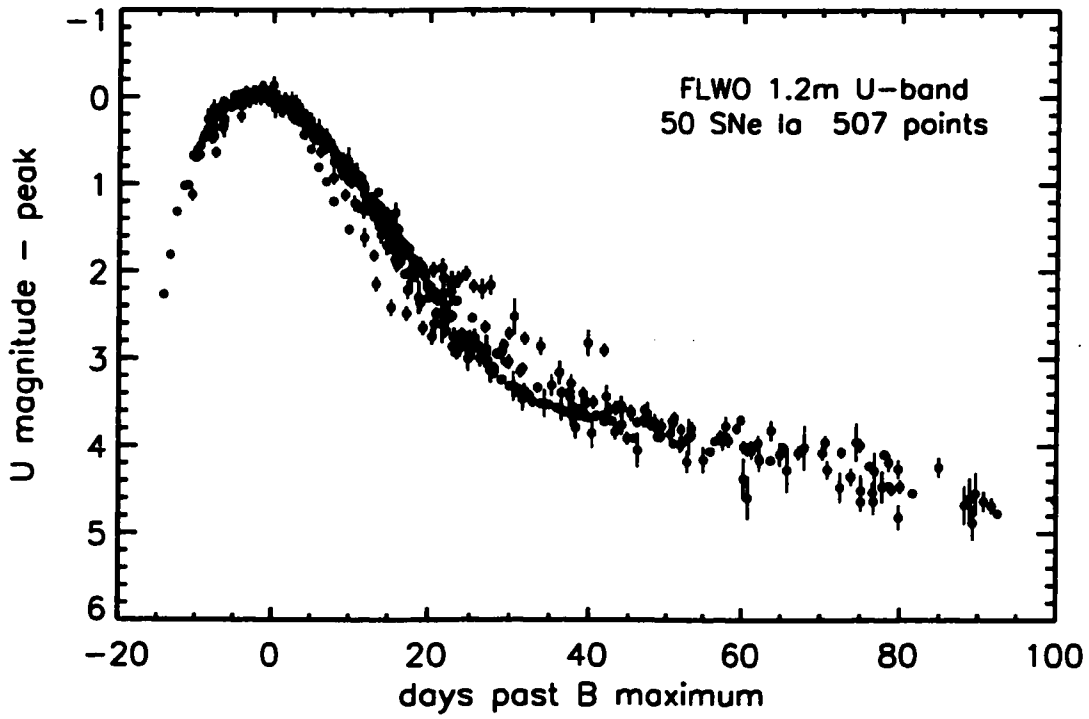

Figure 3.5.— Composite U-band light curve of 50 SNe Ia observed with the FLWO 1.2m telescope. The data were K-corrected and time-dilated to the rest frame. There are 507 individual points in the time interval displayed, from −20 to +100 days after maximum light in B.

in U, with an average SN Ia dropping $\sim$ 1.5 mag in U over the first 15 days after $B_{\rm max}$, as compared to only a $\sim$ 1.1 mag drop in B and $\sim$ 0.5 mag drop in V over that time period. Over the first 30 days after $B_{\rm max}$, the declines in U,B, and V are $\sim$3.2, $\sim$2.6, and $\sim$1.4 mag, respectively. At late time, $t \gtrsim 35$ days after B maximum light, the U-band light curves follow the typical exponential decline, decaying at 0.020 ± 0.001 mag day^{-1}.

In Figure 3.6 we plot the distribution of the epoch of U-band maximum light relative to B-band maximum light, using the stretch templates results for the 22 SNe Ia listed in Table 3.51, along with the 6 additional SNe Ia listed above. As can also be seen in Figure 3.5, the SNe Ia clearly peak earlier in the U-band than in B, with an average time offset of -2.3 days and a dispersion of only 0.4 days. The earlier peak in U also implies the decline rate in U relative to maximum light in U is not so different from the decline rate in B relative to maximum light in B. A typical SN Ia that drops $\sim$1.1 mag in B over the first 15 days after maximum light (as above), declines by $\sim$1.2 mag in U over the first 15 days after U maximum. We note that our precise photometry confirms the result of Leibundgut et al. (1991), who found that maximum in light in U occurs $\sim$2.8 days before maximum light in B, based on a compilation of heterogeneous photoelectric UBV photometry.

We plot the relation between the timescale stretch factors in U and B for the 28 SNe Ia described above in Figure 3.7, where it is clear that the decline rate in U is well correlated with the decline rate in B. However, as the figure also illustrates, there is a significant scatter. The relationship between the stretch factor in V and the stretch factor in B is considerably tighter. Nonetheless, these correlations imply that U light curves can provide leverage in determining the intrinsic luminosities

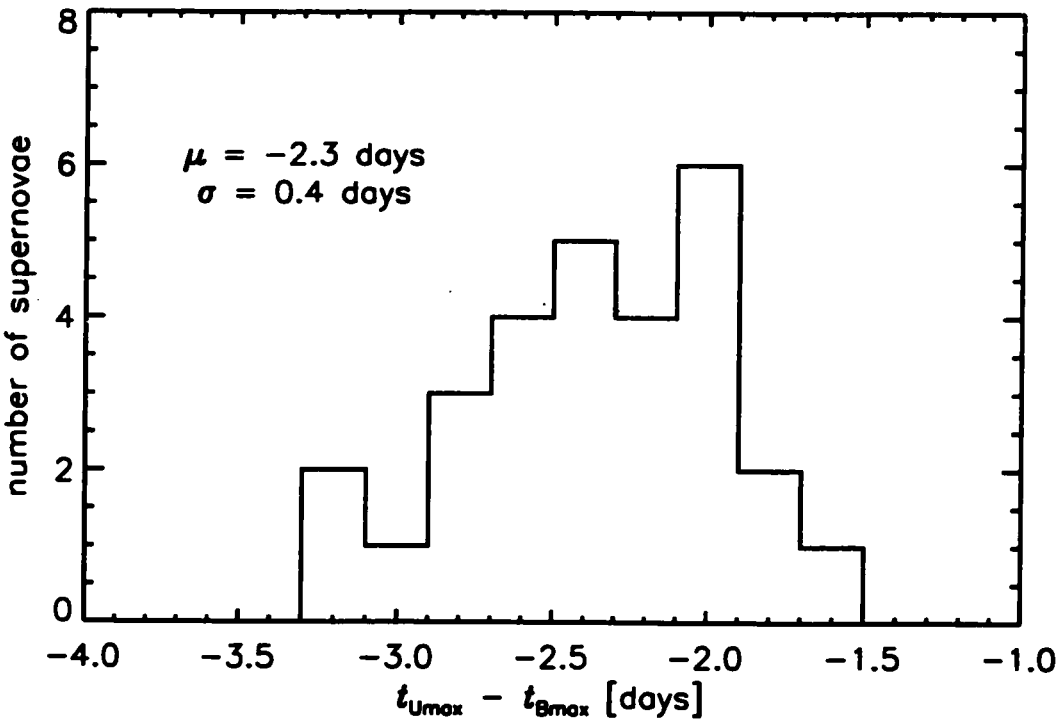

Figure 3.6.— Distribution of the times of maximum light in U relative to maximum light in B, measured in the rest-frame.

of SNe Ia. The best-fit linear relations between s_U, s_B, and s_V are given in the figure. Given the scatter, the relations are consistent with a "universal" stretch, $s = s_U = s_B = s_V$, though the data for a number of objects individually favor slightly different stretch factors in each band. The slope of the luminosity/stretch relation is ~ 1.7 (Nugent, Kim, & Perlmutter 2002), meaning that the dispersion in the s_U-s_B relation ($\sigma \simeq 0.08$) translates into an uncertainty of $\sigma \simeq 0.14$ mag in luminosity, comparable to the typical dispersion in measuring SN Ia distances (e.g., in the stretch/luminosity relation itself). Similarly, the dispersion in the s_V-s_B relation corresponds to $\sigma \simeq 0.09$ mag.

We can also examine the correlation between the timescale stretch factors and $\Delta m_{15}(B)$ for these 28 SNe Ia (cf. Table 3.50); the results are shown in Figure 3.8. The correlation between $\Delta m_{15}(B)$ and s is clear, with s_V and s_B producing a tighter relationship. It also appears that much of the dispersion comes at the low $\Delta m_{15}(B)$ (large s) end of the diagram, implying that there may be larger intrinsic variation in the light curves of the most luminous SNe Ia. The dispersions in $\Delta m_{15}(B)$ are 0.17, 0.12, 0.10 for the relations with s_U, s_B, and s_V, respectively. Using the luminosity-$\Delta m_{15}(B)$ relationship presented by Phillips et al. (1999), the luminosity scatter corresponding to these dispersions are 0.14, 0.10 and 0.08 mag, similar to the results above directly comparing stretch to luminosity. We note that the relations between $\Delta m_{15}(B)$ and s presented in Figure 3.8 match well the results of Garnavich et al. (2002; see their Figure 5).

In addition to the U-band light curve shapes, we can explore the $U-B$ color with this data set. Schaefer (1995) and Branch, Nugent, & Fisher (1997), display relations between the $U-B$ and $B-V$ maximum light colors of SNe Ia, based on a

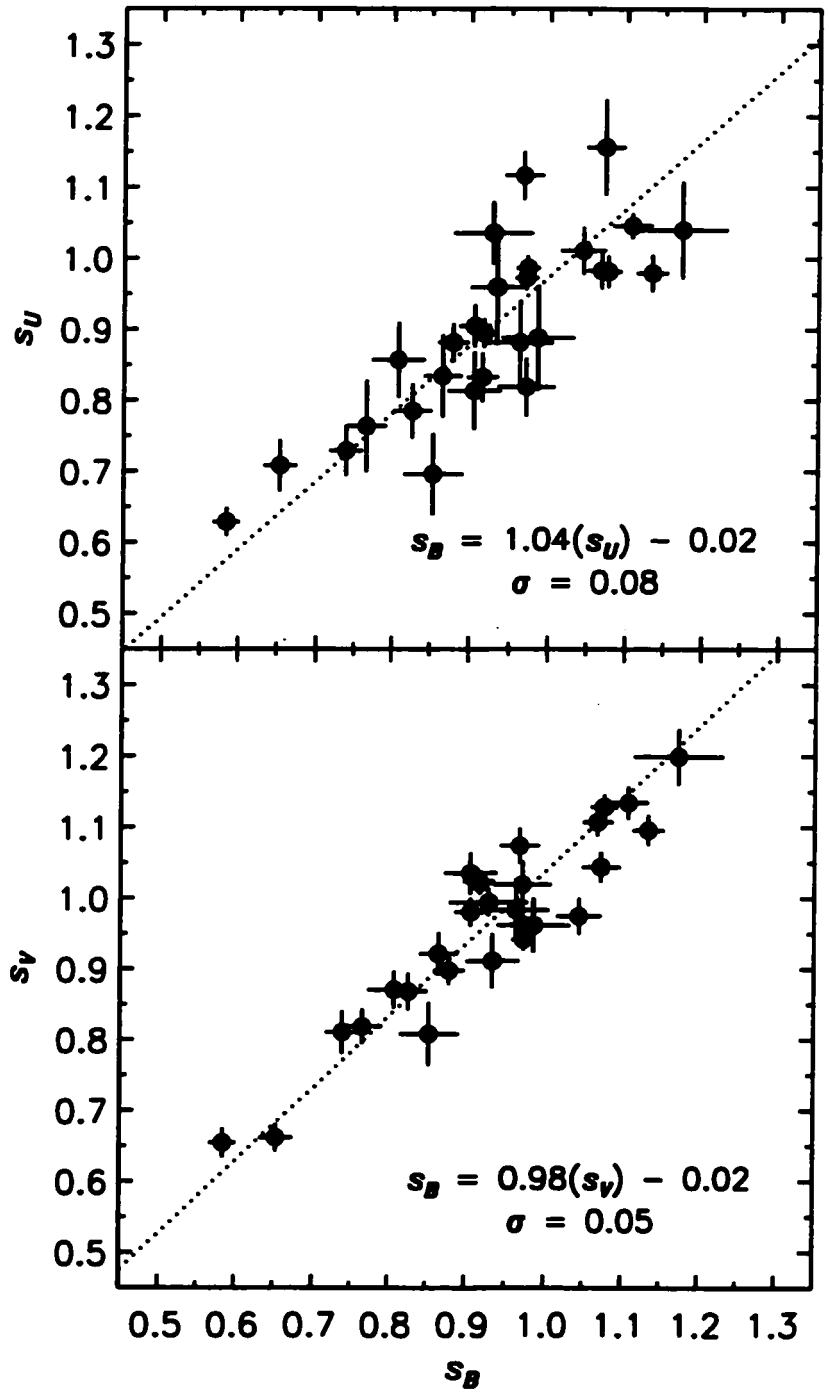

Figure 3.7.— Relation between timescale stretch factors in U, B, and V, based on the stretch-corrected SN 1998aq templates (see text for details). The best linear fits are: $s_B = (1.04 \pm 0.06)s_U - (0.02 \pm 0.05)$ and $s_B = (0.98 \pm 0.05)s_V - (0.02 \pm 0.05)$.

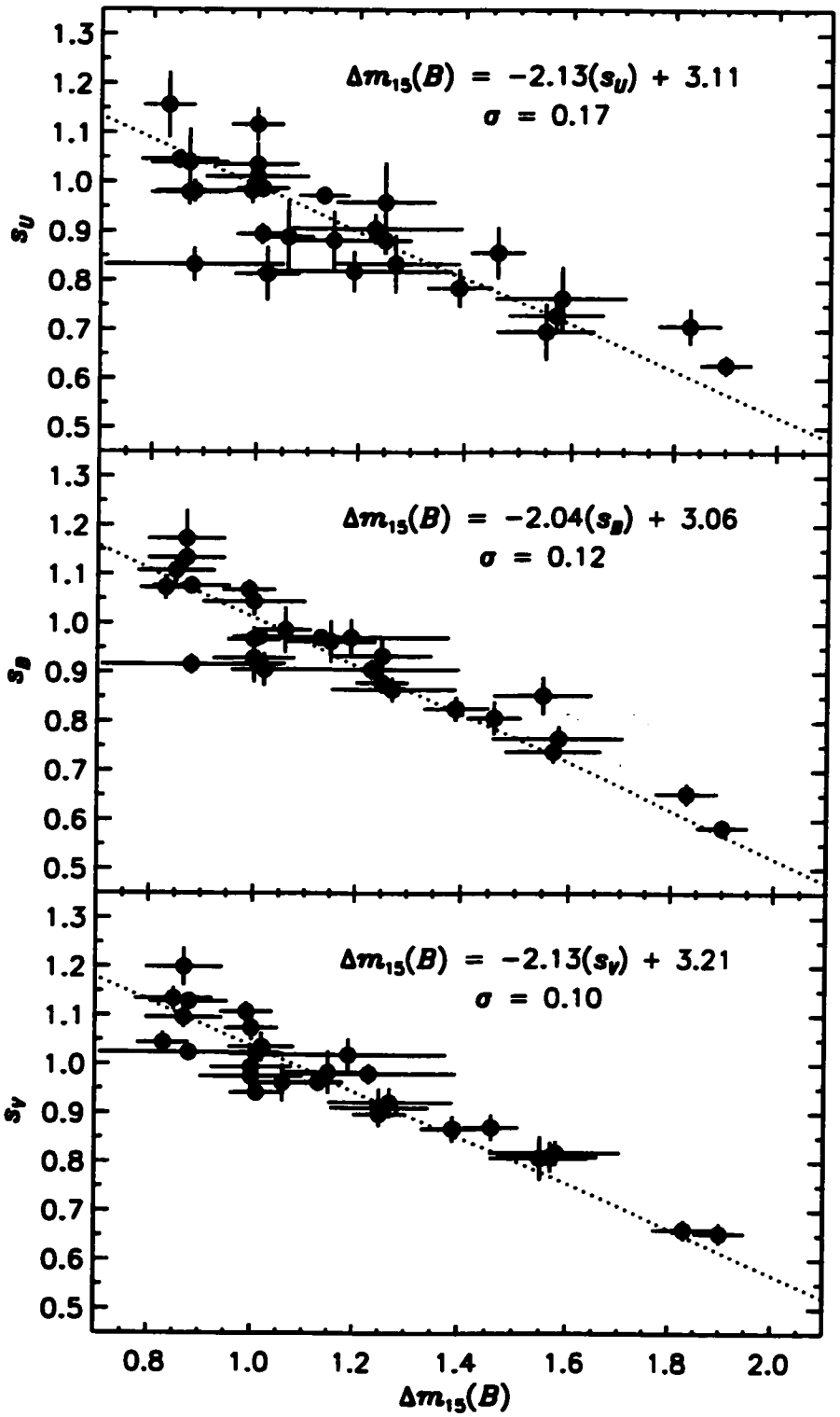

Figure 3.8.— Relation between timescale stretch factors and $\Delta m_{15}(B)$. The best linear fits are $\Delta m_{15}(B) = (-2.13 \pm 0.14)s_U + (3.11 \pm 0.13)$, $\Delta m_{15}(B) = (-2.04 \pm 0.11)s_B + (3.06 \pm 0.10)$, and $\Delta m_{15}(B) = (-2.13 \pm 0.12)s_V + (3.21 \pm 0.11)$.

handful of objects, with heterogeneous photometry from diverse sources. We display 27 SNe Ia[7] in the color-color diagram shown in the top panel of Figure 3.9. We note that the stretch-template fits to the peak magnitudes include the effects of K-correction, which can be significant, particularly in the U-band (Jha et al. 2002, Chapter 4). We have also corrected the colors for (the generally small) Galactic reddening (cf. Table 3.49), assuming the $R_V = 3.1$ extinction law of Cardelli, Clayton, & Mathis (1989). For 23 of the 27 SNe Ia, we were also able to correct for the host-galaxy extinction, via measurement of the tail $B-V$ evolution and the method of Lira (1995) and Phillips et al. (1999), as described in detail in Chapter 4. The colors corrected for host-galaxy reddening are shown in the bottom panel of Figure 3.9.

The lower panel figure shows a tight relation between the intrinsic $B-V$ and $U-B$ color at maximum light. In this plot, normal SNe Ia have $B-V \simeq -0.1$ (e.g., Phillips et al. 1999)[8], and there is a strong clustering of objects at this value. Note, however, the wide span of $U-B$ colors (from about -0.2 to -0.8) for these normal SNe Ia. This is not an artifact of the reddening correction, nor can it be explained by variation in the extinction law in these external galaxies. If there were strong variations in the extinction law, because of the patchiness of interstellar dust, we would expect the top panel of Figure 3.9 to show a swarm of points at the

[7]We show 27 SNe Ia rather than 28, because we exclude the highly-reddened SN 1999cl, for which there is strong evidence from near-infrared photometry that the extinction law varies significantly from the canonical $R_V = 3.1$ law (Krisciunas et al. 2000; Jha et al. 2002, Chapter 4).

[8]Phillips et al. (1999) find the "pseudo"-color $B_{\rm Bmax} - V_{\rm Vmax} \simeq -0.07$ for normal SNe Ia. Because $V_{\rm Vmax} \simeq V_{\rm Bmax} - 0.02$, their result implies $(B-V)_{\rm Bmax} \simeq -0.09$ for normal SNe Ia.

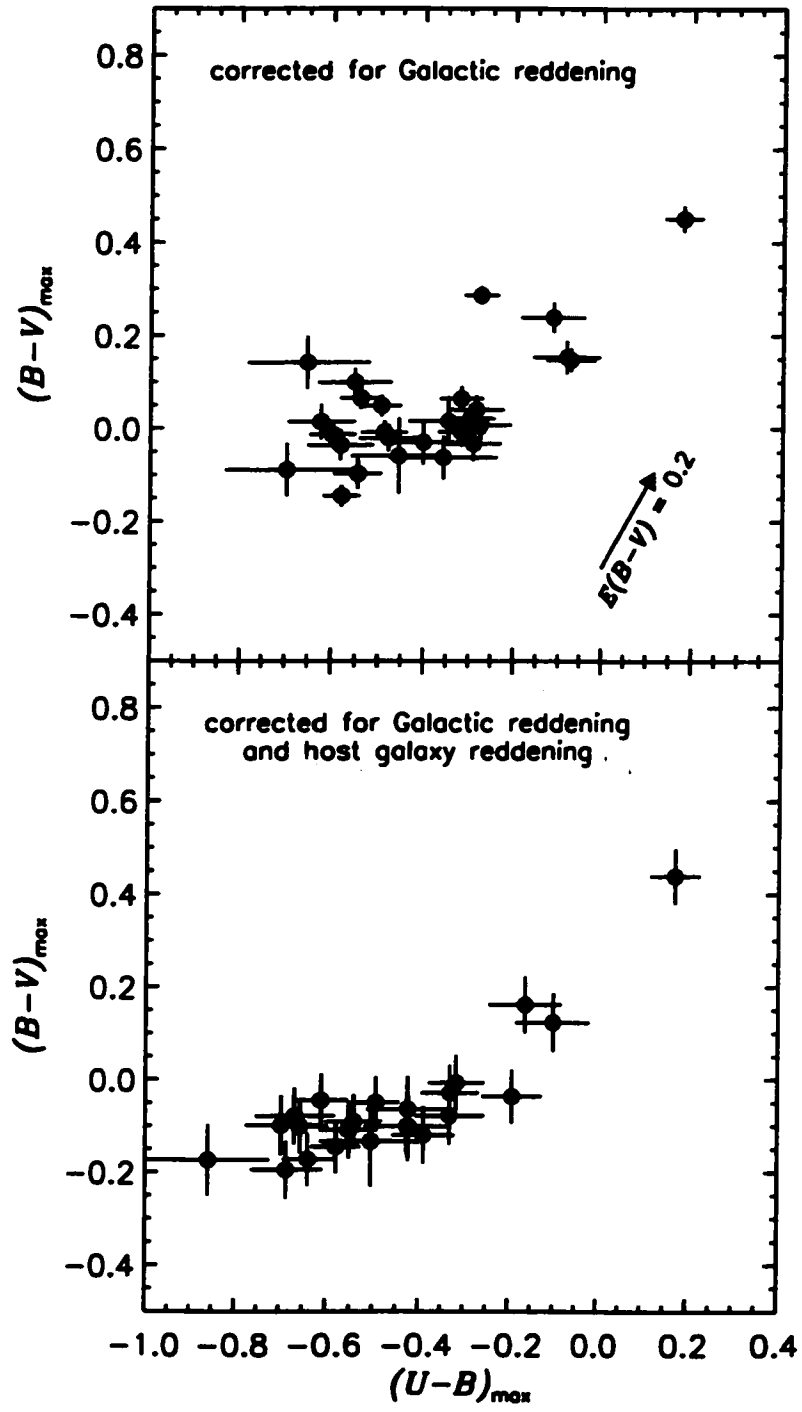

Figure 3.9.— SN Ia colors at maximum light. The top panel shows maximum light colors corrected for Galactic extinction, while the bottom panel includes a correction for extinction in the host galaxy. The arrow indicates a reddening vector corresponding to $E(B-V)_{\rm true} = 0.2$ mag.

lower left (corresponding to an unreddened locus) with the remainder of the points fanning out toward the upper right (corresponding to different amounts of extinction and reddening), which is clearly not what we see. We conclude that the intrinsic variation in $U-B$ color at maximum light is significantly greater than the variation seen in $B-V$.

Do these color variations correlate with light-curve shape or luminosity? There is strong evidence that objects with intrinsically red $B-V$ colors at maximum are the fast-declining, low-luminosity SNe Ia (see, e.g., Garnavich et al. 2002 and references therein). The bottom panel of Figure 3.9 shows that the red objects in $B-V$ are also red in $U-B$. We can check this relationship between color and light-curve shape directly, as shown in Figure 3.10, we we plot the intrinsic $U-B$ and $B-V$ maximum light colors against the measured timescale stretch factor (in V). The relationship between $B-V$ and s_V shown in the lower panel is in good accord with the results presented by Phillips et al. (1999) and Garnavich et al. (2002). The $U-B$ results in the top panel show that the $U-B$ color is well-correlated with stretch (and therefore, luminosity) over the whole range of luminosity in the sample. However, the scatter is also greater in $U-B$, implying that there is a significant intrinsic dispersion U-band peak brightness even after accounting for variations in light-curve shape. A simple linear fit to the data in the top panel of Figure 3.10 implies that this intrinsic dispersion is $\sigma_U \simeq 0.12$ mag. It would be interesting to check whether this increased dispersion is related to other factors, such as progenitor metallicty, as some theoretical studies have indicated that the these factors may have more significant effects in U than in $BVRI$ (e.g., Höflich, Wheeler, & Thielemann 1998).

It is clear that the analysis of these U-band light curves and their relation

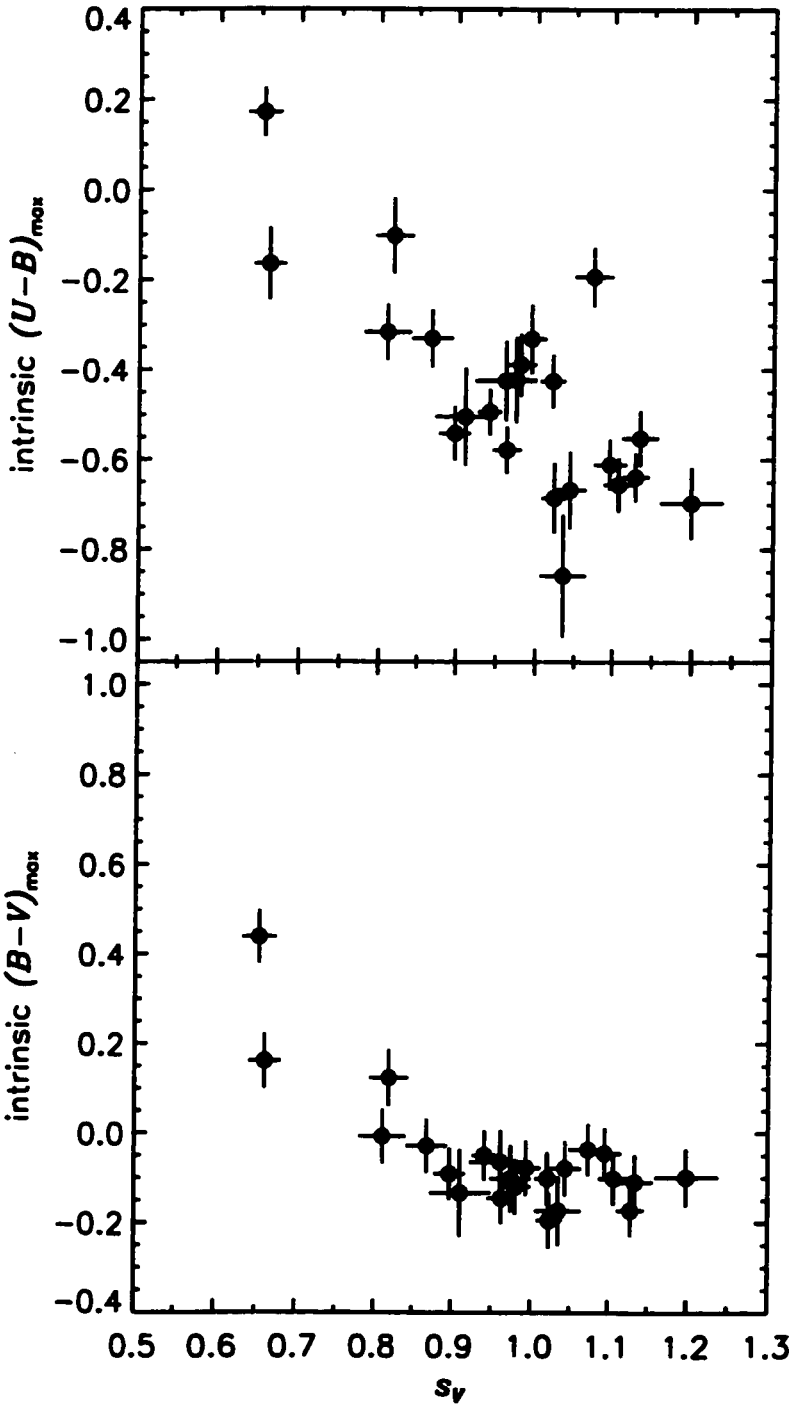

Figure 3.10.— Relation between SN Ia maximum light *UBV* colors and the *V*-band timescale stretch factor. The colors have been corrected for Galactic and host-galaxy reddening.

to light curves in *BVRI* and ultimately, precise distances, is intimately tied to the luminosity and extinction of each SN. To further explore these relations, a profitable strategy would be to incorporate the *U*-band light curves into the general framework of the Multicolor Light Curve Shape analysis presented by Riess, Press, & Kirshner (1996). We present the methods and results of this incorporation in Chapter 4.

We thank the numerous observers who have helped in obtaining this photometry presented here, as well as the avid supernova searchers who allow us to be successful searching our email. Special thanks also to the staff of the F. L. Whipple Observatory as well as the telescope Time Allocation Committees who have steadfastly supported this endeavor. This work was supported in part by an NSF Graduate Research Fellowship.

3.5 References

Alard, C., & Lupton, R. 1998, ApJ, 503, 325

Armstrong, M, & Hurst, G. M. 1996, IAU Circ.6497

Bessell, M.S. 1990, PASP, 102, 1181

Bohlin, R.C., Dickinson, M.E., & Calzetti, D. 2001, AJ, 122, 2118

Boisseau, J.R., & Wheeler, J.C. 1991, AJ, 101, 1281

Branch, D., Nugent, P., & Fisher, A. 1997, in Thermonuclear Supernovae, eds. P. Ruiz-Lapuente, R. Canal, & J. Isern, Dordrecht: Kluwer Academic Publishers, 715

Cardelli, J.A., Clayton, G.C., & Mathis, J.S. 1989, ApJ, 345, 245

Fabricant, D., Cheimets, P., Caldwell, N., & Geary, J. 1998, PASP, 110, 79

Falco, E.E., Kurtz, M.J., Geller, M.J., Huchra, J.P., Peters, J., Berlind, P., Mink, D.J., Tokarz, S.P., & Elwell, B. 1999, PASP, 111, 438

Garnavich, P.M., Bonanos, A.Z., Jha, S., Kirshner, R.P., Schlegel, E.M., Challis, P., Macri, L.M., Hatano, K., Branch, D., Bothun, G.D., & Freedman, W.L. 2002, in press (astro-ph/0105490)

Goldhaber, G., et al. 2001, ApJ, 558, 359

Hamuy, M., Walker, A.R., Suntzeff, N.B., Gigoux, P., Heathcote, S.R., & Phillips, M.M. 1992, PASP, 104, 533

Hamuy, M., et al. 1993, AJ, 106, 2392

Hamuy, M., Suntzeff, N.B., Heathcote, S.R., Walker, A.R., Gigoux, P., & Phillips, M.M. 1994, PASP, 106, 566

Hamuy, M., Phillips, M.M., Maza, J., Suntzeff, N.B., Schommer, R.A., & Avilés, R. 1995, AJ, 109, 1

Hamuy, M., et al. 1996a, AJ, 112, 2408

Hamuy, M., Phillips, M.M., Suntzeff, N.B., Schommer, R.A., Maza, J., Smith, R.C., Lira, P., & Avilés, R. 1996b, 112, 2438

Hamuy, M., & Pinto, P. A. 1999, AJ, 117, 1185

Harris, W.E., Fitzgerald, M.P., & Reed, B.C. 1981, PASP, 93, 507

Höflich, P., Wheeler, J.C., & Thielemann, F.K. 1998, ApJ, 495, 617

Jha, S., et al. 1999, ApJS, 125, 73

Krisciunas, K., Hastings, N.C., Loomis, K., McMillan, R.. Rest, A., Riess, A.G., & Stubbs, C. 2000, ApJ, 539, 658

Krisciunas, K., Phillips, M.M., Stubs, C., Rest, A., Miknaitis, G., Riess, A.G., Suntzeff, N.B., Roth, M., Persson, S.E., & Freedman, W.L. 2001, AJ, 122, 1616

Landolt, A.U. 1992, AJ, 104, 340

Leibundgut, B., Tammann, G.A., Cadonau, R., & Cerrito, D. 1991, A&AS, 89, 537

Li, W.D., Qiu, Y.L., Qiao, Q.Y., Ma, J., & Hu, J.Y. 1996, IAU Circ.6379

Li, W.D., Qiu, Y.L., Qiao, Q.Y., Zhu, X.H., Hu, J.Y., Richmond, M.W., Filippenko, A.V., Treffers, R.R., Peng, C.Y., & Leonard, D.C. 1999, AJ, 117, 2709

Li, W.D., Filippenko, A.V., Gates, E., Chornock, R., Gal-Yam, A., Ofek, E.O., Leonard, D.C., Modjaz, M., Rich, R.M., Riess, A.G., & Treffers, R.R. 2001, PASP, 113, 1178

Lira, P. 1995, Master's Thesis, University of Chile

Massey, P., Strobel, K., Barnes, J.V., & Anderson, E. 1988, ApJ, 328, 315

Massey, P., & Gronwall, C. 1990, ApJ, 358, 344

Modjaz, M., Li, W.D., Filippenko, A.V., King, J.Y., Leonard, D.C., Matheson, T., & Treffers, R.R. 2001, PASP, 113, 308

Monet, D., et a. 1998, The USNO-A2.0 Catalogue, (U.S. Naval Observatory, Washington DC)

Nugent, P., Kim, A., & Perlmutter, S. 2002, in press

Perlmutter, S., et al. 1997, ApJ, 483, 565

Perlmutter, S., et al. 1999, ApJ, 517, 565

Phillips, M.M. 1993, ApJ, 413, L105

Phillips, M.M., Lira, P., Suntzeff, N.B., Schommer, R.A., Hamuy, M., & Maza, J. 1999, AJ, 118, 1766

Press, W.H., Teukolsky, S.A., Vetterling, W.T., & Flannery, B.P. 1992, Numerical Recipes in C, 2nd ed., New York: Cambridge University Press

Puckett, T. 1998, IAU Circ.6957

Riess, A.G., Press, W.H., & Kirshner, R.P. 1996, ApJ, 473, 88

Riess, A.G., et al. 1999, AJ, 117, 707

Schaefer, B.E. 1995, ApJ, 450, L5

Schechter, P.L., Mateo, M., & Saha, A. 1993, PASP, 105, 1342

Schlegel, D. J., Finkbeiner, D. P., & Davis, M. 1998, ApJ, 500, 525

Schmidt, B. P., et al. 1998, ApJ, 507, 46

Schwartz, M. 1997, IAU Circ.6700

Schwartz, M., Li, W.D., Filippenko, A.V., Modjaz, M., & Treffers, R.R. 2000, IAU Circ.7514

Stetson, P. 1987, PASP, 99, 191

Stetson, P. 1994, PASP, 106, 250

Suntzeff, N.B., et al. 1999, AJ, 117, 1175

Treffers, R.R., Peng, C.Y., Filippenko, A.V., & Richmond, M.W. 1997, IAU Circ.6627

Turatto, M., Piemonte, A., Benetti, S., Cappellaro, E., Mazzali, P.A., Danziger, I.J., & Patat, F. 1998, AJ, 116, 2431

Chapter 4

MLCS 2k2: New Distances to Type Ia Supernovae and the Hubble Constant

Saurabh Jha, Adam G. Riess, & Robert P. Kirshner 2002, to be submitted to *The Astrophysical Journal*

Abstract

We present an updated version of the Multicolor Light Curve Shape method to measure distances to type Ia supernovae. We incorporate new procedures for K-correction and extinction corrections, as well as expand the method to incorporate U-band light curves and more easily accomodate prior constraints on any of the model parameters. Application of this method to a new sample of SNe Ia, nearly

doubling the number of Hubble-flow objects and also doubling the number of Cepheid-based calibrators compared to the results presented by Jha et al. (1999, Chapter 2), yields the best estimate of the Hubble Constant from SNe Ia to date, with $H_0 = 66 \pm 3 \pm 7$ or $76 \pm 3 \pm 8$ km s Mpc^{-1} (statistical and systematic uncertainties), depending on the choice of Cepheid distances used.

4.1 Introduction

The cosmological uses of type Ia supernovae (SNe Ia) result from precise distances to these calibrated candles. It has been well established that the intrinsic luminosity of SNe Ia is correlated with the shape of their optical light curves (Phillips 1993; Hamuy et al. 1995; Riess, Press, & Kirshner 1995; Hamuy et al. 1996a; Riess, Press, & Kirshner 1996a). Determining the precise distance we seek, then, requires well-observed SN Ia light curves in multiple passbands, to constrain the intrinsic luminosity and extinction by dust along the line of sight to each SN Ia.

A number of methods have been developed to measure distances from SN Ia multicolor light curves, with each enjoying a similar level of success. The first of these was introduced by Phillips (1993), who noted that the parameter $\Delta m_{15}(B)$, the amount by which a SN Ia declined in the B-band during the first fifteen days after maximum light, was well-correlated with SN Ia intrinsic luminosity. The $\Delta m_{15}(B)$ method was transformed by Hamuy et al. (1996a), in which $\Delta m_{15}(B)$ became a parameter in a multi-dimensional fit to six template BVI light curves spanning a wide range in $\Delta m_{15}(B)$ as it was originally defined. Phillips et al. (1999) present the current version of this method, which incorporates measurement of the extinction via

late-time $B-V$ color measurements (roughly independent of $\Delta m_{15}(B)$) and $B-V$ and $V-I$ measurements at maximum light (for the measured $\Delta m_{15}(B)$, determined in an iterative fashion).

Other methods include the stretch correction of Perlmutter et al. (1997), in which the SN Ia intrinsic luminosity is correlated to a simple stretching of the time axis to a fiducial light curve. Currently this method is only presented in detail for the B band (Goldhaber et al. 2001), though it seems to be applicable in U and V (but not in R or I; Jha et al. 2002, Chapter 3; Nugent, Kim, & Perlmutter 2002). Tripp & Branch (1999) present a two-parameter method, empirically correlating SN Ia luminosity to $\Delta m_{15}(B)$ and maximum light $B-V$ color, but without regard to the source of the color variation (i.e., extinction or intrinsic variation). Parodi et al. (2000) present a similar study, with empirical correlations between SN Ia maximum light magnitudes in BVI and $\Delta m_{15}(B)$ and color, using a color-selected sample.

Here we present an updated version of the Multicolor Light Curve Shape method, denoted here as MLCS2k2. Riess et al. (1995) presented the first incarnation of this method (called LCS as it was based only on V band data), in which a continuum of template light curves was created based on a "training set" of SN Ia with known relative distances and the parameter Δ, a particular SN's under- or over-luminosity relative to some fiducial value. The luminosity correction, Δ, was used as a parameter in a least-squares fit, resulting in a best-fit distance for each SN, along with a quantitative estimate of the uncertainty. The MLCS method, presented by Riess et al. (1996a) gave the details of the model, as well as incorporating $BVRI$ light curves and providing an estimate of extinction by dust.

Riess et al. (1998a) updated the training set, using reliable distances measured by the Hubble Law in favor of other methods, added a quadratic term in Δ to create the template light curves, and included the effects of covariance in the model. The application of this version of MLCS to nearby SN Ia and the Hubble Constant is given by Jha et al. (1999; Chapter 2).

The MLCS approach has some advantages: by using a relatively large training set to define a continuum of templates, we become less sensitive to peculiarities of individual objects. During the training process, we keep track of variance and covariance in the residuals to the model fit, and use these to determine statistically reliable indications of goodness-of-fit and parameter uncertainties when the model is applied to other objects. The model also attempts to separate extinction from intrinsic color variations, and uses all of the light curves (at all epochs) to constrain the extinction. Finally the model is easily extensible with new data (for example, the inclusion of a quadratic term in Δ, or the incorporation of the U-band presented here). The major disadvantage is that the method requires accurate estimates of luminosity and extinction for the training set sample in order to construct reliable templates.

We use multicolor photoelectric and CCD *UBVRI* data from a variety of sources, relying most heavily on the compilations of Hamuy et al. (1996b) from the Calán/Tololo survey (29 SNe Ia), as well as those of Riess et al. (1999) and Jha et al. (2002, Chapter 3), consisting of 22 and 44 SNe Ia, respectively, from the CfA monitoring campaign. We also use unpublished photometry from the Lick Observatory Supernova Search (W. Li, personal communication) for a 7 SNe Ia, in addition to photometry of SN 1997br (Li et al. 1999), SN 1998de (Modjaz et al. 2000),

and SN 2000cx (Li et al. 2001). Krisciunas et al. (2000, 2001) present additional photometry for 8 SNe Ia, largely from Apache Point Observatory. We also use the following data for individual objects: SN 1972E (photoelectric *UBV* photometry compiled by Leibundgut et al. 1991), SN 1980N (Hamuy et al. 1991), SN 1981B (Buta & Turner 1982; Tsvetkov 1982), SN 1981D (Hamuy et al. 1991), SN 1986G (Phillips et al. 1987), SN 1989B (Wells et al. 1994), SN 1990N and SN 1991T (Lira et al. 1998), SN 1991bg (Filippekno et al. 1992; Leibundgut et al. 1993; Turatto et al. 1996), SN 1992A (N. Suntzeff, personal communication), SN 1994D (Richmond et al. 1995; Patat et al. 1996; Meikle et al. 1996), SN 1997cn (Turatto et al. 1998), SN 1998aq (Boffi et al. 2002, in preparation), SN 1998bu (Suntzeff et al. 1999; Jha et al. 1999, Chapter 2), SN 1999by (Garnavich et al. 2002) and SN 2001V (Mandel et al. 2002, in preparation). For a number of objects, we have combined data sets from different sources (cf. §3.3.1). The data set consists of 114 SNe Ia in all.

4.2 Groundwork

Intercomparison of the light curves of many SNe Ia requires understanding and correction for a number of effects to bring the photometry to a common frame. These include correction for Galactic extinction, correction for time-dilation and the K-correction. We have updated a number of these foundations in our development of MLCS2k2.

4.2.1 K-correction

The stretching and shifting of spectra due to the cosmological expansion leads to changes in measured flux observed through a fixed detector passband as a function of redshift. K-corrections for SNe Ia in B and V have been presented by Hamuy et al. (1993), based on spectra of three objects. Kim, Goobar, & Perlmutter (1996) provide additional K-corrections in R, as well as developing a method of "cross-filter" K-corrections used at high-redshift. These methods have used a fixed set of spectra to define the K-correction for all objects, and do not include spectral energy distribution (SED) variations arising from intrinsic differences among supernovae (either in the detailed spectral features or in the continuum shape) or changes in in the SED due to extinction.

Nugent, Kim, & Perlmutter (2002) have developed a method that accounts for these variations with a simple, yet effective, "trick" in which both the intrinsic and extinction-related SED variations are effected by adjusting the SED by the $R_V = 3.1$ extinction law of Cardelli, Clayton & Mathis (1989; hereinafter CCM89) to match the color of the SN as observed.[1] This procedure is reasonably well-motivated; at early times, SN Ia are in the photospheric phase and the SED is continuum dominated, so that adjustment of the SED by a relatively slowly varying function like the CCM89 extinction law to match the observed color will do a good job of mimicking the true SED. At late times, much of the color variation is due, in fact, to extinction and so the adjustment is appropriate. Furthermore, the adjustment is done using a color "local" to the spectral region being adjusted, minimizing

[1]Here we use the extinction law to adjust the SED redder *or bluer*, to match the observed SN color.

any adverse effects. The difference in the K-correction accounting for these color variations and assuming a constant color for all objects is typically small (generally $\lesssim 0.1$ mag), but systematic. Nugent et al. (2002) show the efficacy of this color-based procedure.

Our concern in this paper is for accurate K-corrections at low redshift ($z \lesssim 0.1$), so we restrict our attention to K-corrections in the same passband (i.e., not the cross-filter K-correction). We have implemented the Nugent et al. (2002) procedure using a sample of 91 SN Ia spectra covering phases from -14 to $+92$ days past maximum light. Of these, 57 spectra extend far enough to the red to cover the I passband, while 32 spectra cover the U passband in the blue. The number of spectra that cover the U-band decreases quickly as the spectra are redshifted; however, of the 114 SNe Ia described here, the maximum redshift for which there are U observations is only $z \simeq 0.06$, meaning that is the extent to which we need to calculate K_{UU}.

To derive the K-corrections, the basic procedure is as follows. For each of *UBVRI* (we adopt the standard Bessell 1990 passbands), we choose standard colors including that passband (specifically, for U: $U-B$; B: $U-B$ and $B-V$; V: $B-V$, $V-R$, and $V-I$; R: $V-R$ and $R-I$; I: $V-I$ and $R-I$). Then for a particular combination of passband and color, we calculate K-corrections in that passband, such that the spectra are forced to take on a range of observed colors, using the CCM89 extinction law to adjust the spectra to any particular color. Thus, we tabulate the K-correction as a function of three parameters: epoch (i.e., days after maximum light), redshift and color. We measure the colors in the observed frame, so that for example, to determine the K-correction in the V-band for a supernova at maximum light at redshift $z = 0.05$ with an observed $B-V = 0.0$ mag, we have taken

our maximum light spectra, redshifted them to $z = 0.05$, adjusted them using the CCM89 extinction law to have $B-V= 0.0$ as measured with synthetic photometry, and calculated the K-correction for that adjusted spectrum. In this example, the answer is $K_{VV} = -0.04 \pm 0.02$ mag, where the uncertainty is measured from the scatter among the individual spectra about a smooth curve. If the observed color had been redder, e.g., $B-V= 0.5$ mag, then $K_{VV} = 0.06 \pm 0.01$ mag.

The advantage of tabulating the K-correction as a function of observed-frame color (as opposed to the rest-frame color) is that no iteration is then required in determining the K-corrections. However, in making the K-correction a function of color, the process of K-correcting observations to the rest frame and "de"-K-correcting templates to the observed frame becomes somewhat asymmetric, in that for the former case we use the observed-frame color, and for the latter it is more convenient to use the rest-frame color. As long as the observed-frame colors are measured relatively precisely (say, to better than $\sim$0.1 mag), there is no advantage to de-K-correcting templates (with presumably known colors) to the observed-frame over K-correcting observations to the rest frame.

In Figure 4.1 we show the derived K-corrections in the U-band. It is interesting to note that the K-corrections in U at maximum light are quite significant ($\sim$0.1 mag), even for very modest redshifts. Ignoring the K-correction can lead to spurious correlations with redshift and distance.

Nugent et al. (2002) caution against using the CCM89 extinction law adjustment procedure to determine K-corrections for SNe Ia with SN 1991bg-like spectra, in which deep Ti II spectral features can dominate the photometric colors (particularly

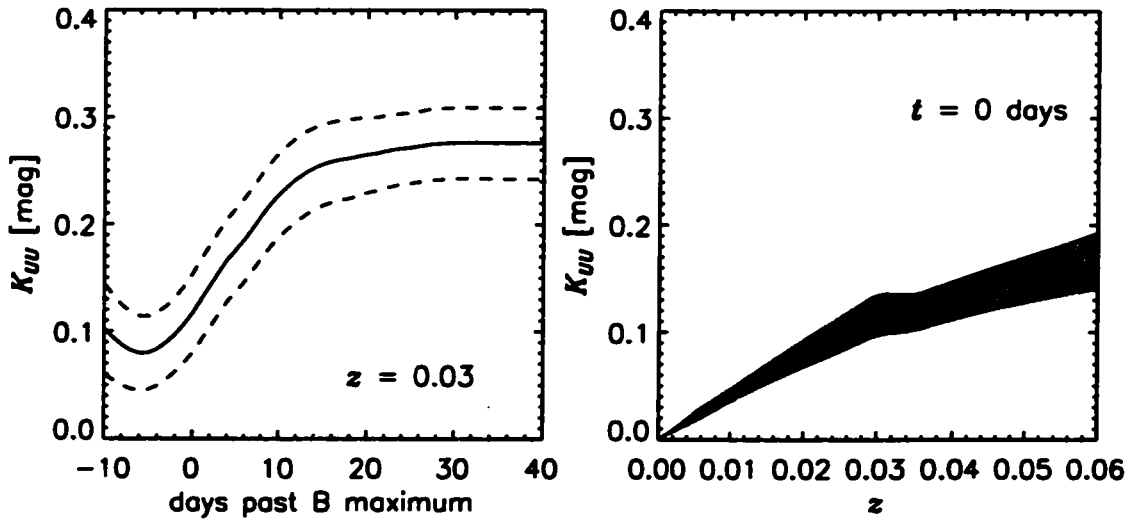

Figure 4.1.— K-corrections in the U-band. The left panel shows K_{UU} as a function of supernova age at a redshift of $z = 0.03$. The solid line corresponds to an observed maximum-light $U-B = -0.35$ (corresponding to a rest-frame maximum-light color $U-B = -0.50$). The dashed lines above and below the solid line correspond to SNe Ia that are 0.2 mag redder and bluer, respectively, in $U-B$ at all epochs. The right panel shows K_{UU} at maximum light as a function of redshift, assuming a rest-frame color of $U-B = -0.50$. The shaded region indicates the K-correction uncertainty. The "kinks" in the right panel occur because of individual spectra dropping out of the K-correction calculation as their wavelength coverage ceases to encompass the the entire U-band beyond a maximum redshift.

in B), even at early times. We have thus calculated K-corrections independently for this class of SN Ia, a small minority of the entire sample.

4.2.2 Extinction

Extinction by dust along the line of sight to a SN Ia is recognized by its reddening effect on the SN colors. As discussed by Phillips et al. (1999) and Nugent et al. (2002), the evolution of the SN Ia SED over time leads to variations in the observed extinction in any given passband. Furthermore the extinction itself alters the SED such that the reddening is a nonlinear function of the total extinction. These effects are generally small, but again, systematically affect the observed light curves, making them important to quantify.

The dust extinction along a particular line of sight is typically parameterized by the extinction in a given band X, A_X and by the amount of reddening, given by the color excess, typically $E(B-V)$. Following Phillips et al. (1999) and Nugent et al. (2002), we distinguish between the "true" reddening $E(B-V)_{\rm true}$ which depends only on the dust itself (and is calculated from the effects of that dust on idealized stellar spectra; CCM89), and the "observed" reddening $E(B-V)_{\rm obs} \equiv A_B - A_V$, which varies with time as the supernova spectrum evolves. From these, we can construct the ratio $R_X^{\rm true} \equiv A_X/E(B-V)_{\rm true}$, which varies in time as the numerator varies, and $R_X^{\rm obs} \equiv A_X/E(B-V)_{\rm obs}$, for which both the numerator and denominator vary in time. We have calculated both of these ratios similarly to Phillips et al. (1999) and Nugent et al. (2002), by simulating the effects of extinction on the sample of 91 spectra described in §4.2.1, using the $R_V = 3.1$ extinction law of

CCM89,[2] as modified by O'Donnell (1994), and synthetic photometry through the Bessell (1990) standard passbands.[3]

We present our calculations of $R_X^{\rm true}$ and $R_X^{\rm obs}$ in Figures 4.2 and 4.3, respectively. We find a good match in general to the results of Nugent et al. (2002) and Phillips et al. (1999), which is not surprising, as we have many of the input spectra in common. The figures show the time variation of these two ratios as well as its variation over two magnitudes in $E(B-V)_{\rm true}$. Both of these ratios have their uses, depending on whether one knows the extinction *a priori* (for instance, using a Galactic reddening map) or is measuring it from the observed SN colors. Because we have used the SED of SNe Ia themselves to calculate these quantities (and their time variation), it is preferable to use these results rather than those from standard filter tables (e.g., Schlegel, Finkbeiner & Davis 1998, their Table 6).

So far we have restricted ourselves to the standard $R_V = 3.1$ extinction law of CCM89, but we would like our distance measuring technique to be flexible and allow for variations in the properties of the dust. CCM89 have shown that in the optical passbands, dust in our Galaxy follow extinction laws that can be expressed in terms R_V.[4] Clearly, using extinction laws with different values of R_V will lead directly to variations in $R_X^{\rm true}$ and $R_X^{\rm obs}$. The variation with the total extinction itself adds further complications and makes using these ratios cumbersome. For instance,

[2]We have also explored using the extinction law presented by Fitzpatrick (1999), with similar results.

[3]We note in passing that the previous incarnations of MLCS used extinction coefficients tabulated for the Johnson R and I passbands, rather than the Kron/Cousins passbands. We have rectified this here.

[4]We adopt the notation that without a superscript "true" or "obs", R_V corresponds to the R_V of CCM89, i.e., derived from photoelectric measurements of Galactic stars.

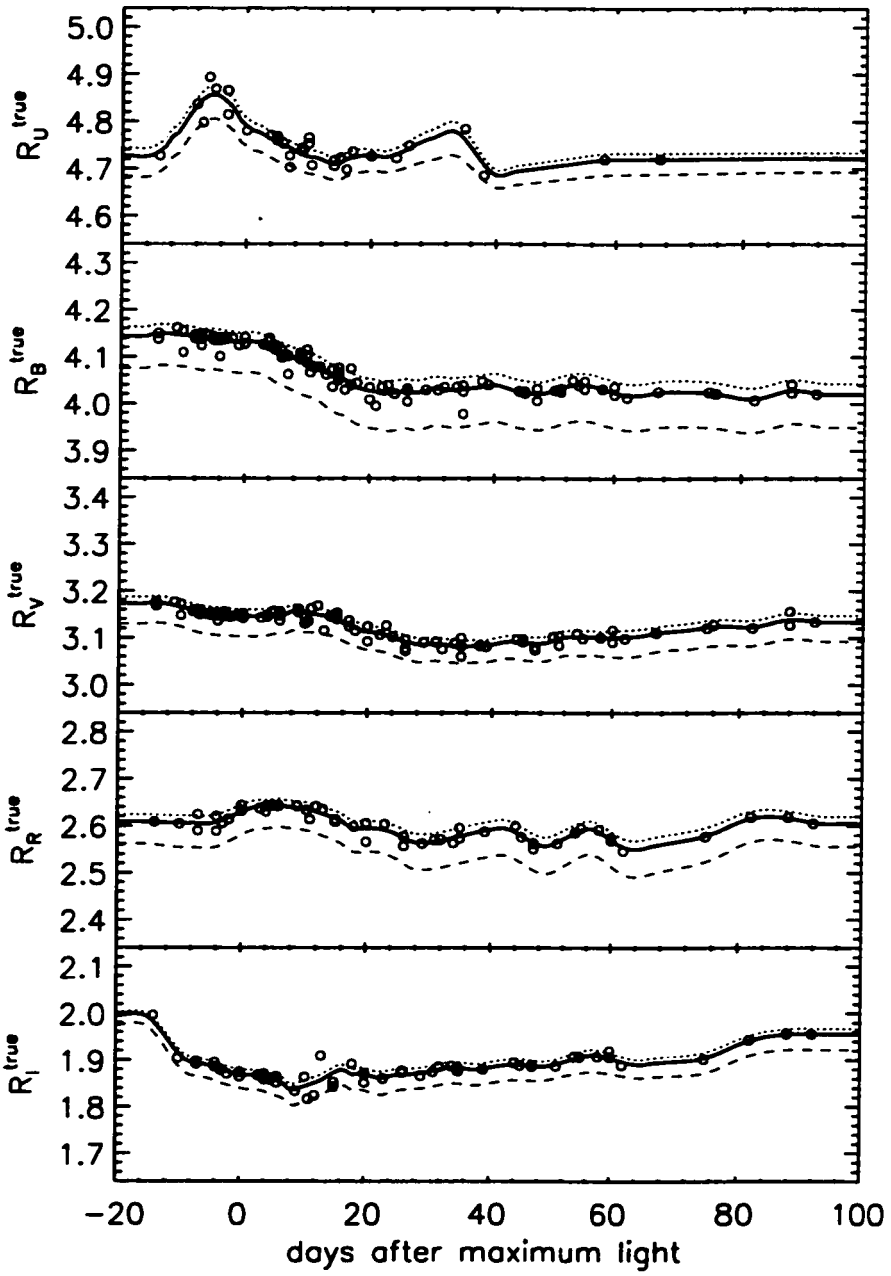

Figure 4.2.— Variation of $R_X^{\rm true} \equiv A_X/E(B-V)_{\rm true}$ in *UBVRI* as a function of supernova phase. The open circles represent the measurement from the individual spectra and the heavy solid line is the smoothed representation. The dotted and dashed lines show the variation of $R_X^{\rm true}$ with the total extinction (cf. Phillips et al. 1999, their Figure 2). The dashed line corresponds to $E(B-V)_{\rm true} = +1.0$ mag relative to the solid line (which was calculated for $E(B-V)_{\rm true}$ approaching zero). The dotted line corresponds to $E(B-V)_{\rm true} = -0.5$ mag relative to the solid line (for illustration only, as it would be unphysical unless the extinction zeropoint for the solid line was significantly underestimated).

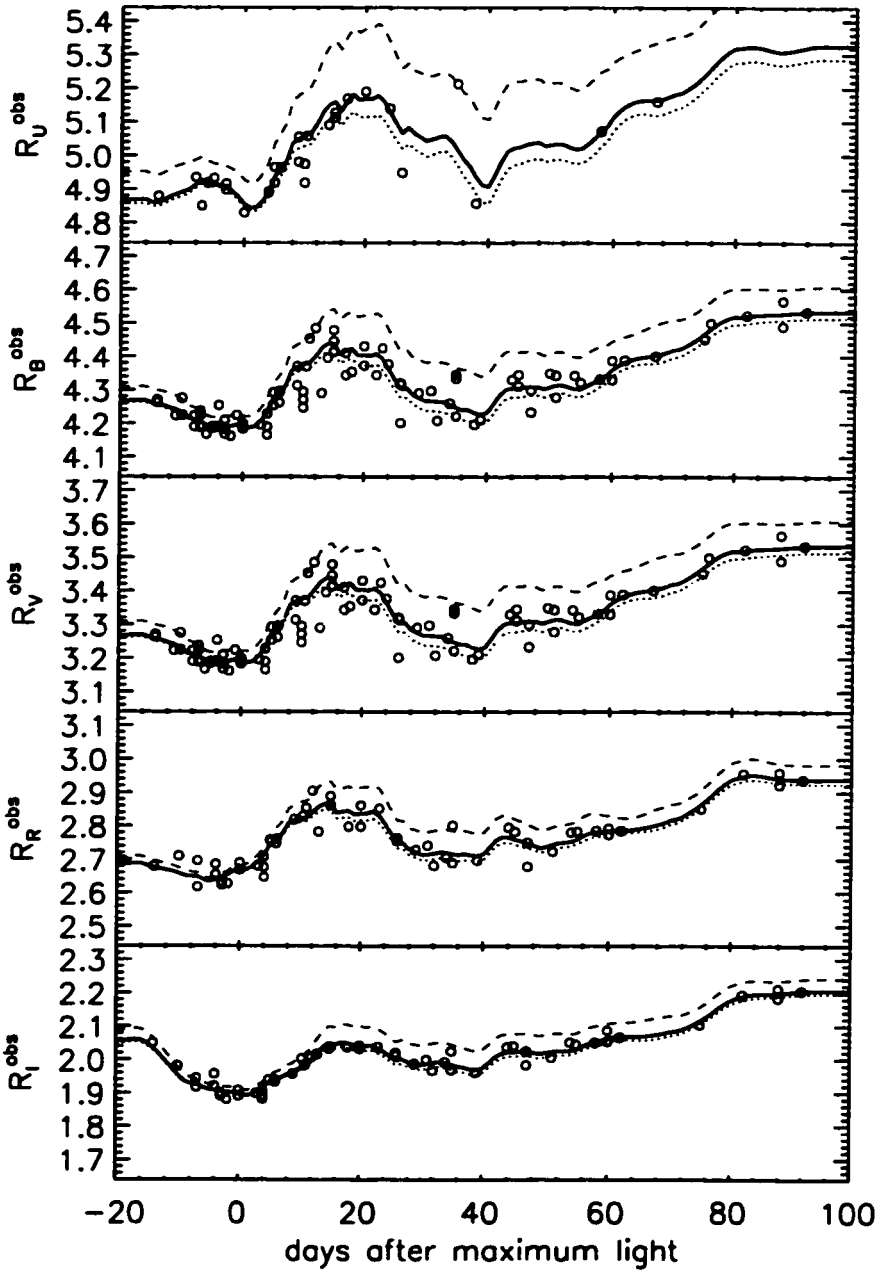

Figure 4.3.— Same as Figure 4.2, except showing the variation of $R_X^{\rm obs} \equiv A_X/E(B-V)_{\rm obs}$. Note that the y-axis ranges have been increased in this figure, to encompass the larger variations in $R_X^{\rm obs}$, and that $R_B^{\rm obs} = R_V^{\rm obs} + 1$ by definition.

calculating $R_I^{\rm obs} \equiv A_I/(A_B - A_V)$ involves three terms, each varying individually with epoch, total extinction and extinction law.

To make things simpler, we have chosen to work in the more natural space of A_X rather than using color excesses to parameterize the extinction. This is convenient because we fit the light curves in each passband directly (rather than fitting color curves), which is advantageous as it does not require light curves to have multiple color measurements at each epoch. Secondly, the extinction laws themselves are better characterized in ratios of extinctions, e.g., A_B/A_V, rather than in ratios of extinctions to differences in extinctions (color excesses).[5]

The first part of this framework is to separate out the time-dependence of the extinction. For each passband X, we define the quantity,

$$\vec{\zeta_X} \equiv \frac{\vec{A_X}}{A_X^0}, \tag{4.1}$$

where we denote quantities that are functions of SN phase with vector arrows (i.e., $\vec{\zeta_X} = \vec{\zeta_X}(t)$, and A_X^0 is defined as the extinction in passband X at maximum light in B. Thus, $\vec{\zeta_X}(t = 0) \equiv 1$ by definition (all times are defined relative to maximum light in B). In Figure 4.4 we show our calculation of $\vec{\zeta_X}$ in *UBVRI* . The useful result is that $\vec{\zeta_X}$ captures all of the time-dependence in the extinction *and* is insensitive to both the total extinction $E(B-V)_{\rm true}$ and the extinction law R_V. This point is also illustrated in Figure 4.4, where the dark gray bands show the variation in $\vec{\zeta_X}$ over the very wide range of 3 magnitudes of $E(B-V)_{\rm true}$ and the light gray bands show the variation of a wide range of R_V from 1.7 to 5.7 (including the full variation in

[5]This point is made explicitly by CCM89 who note that "There are some relationships which emerge more clearly when $A(\lambda)/A(V)$ is considered than when normalization by $E(B-V)$ is used."

$E(B-V)_{\rm true}$). While the figure shows some differences in $\vec{\zeta_X}$ at levels greater than a few percent (for instance, in I at early times), these are only realized for extreme values of both R_V and $E(B-V)_{\rm true}$. We can then confidently fix $\vec{\zeta_X}$ as shown by the heavy solid lines in the figure, independent of the reddening law and total extinction.

With the time-dependence separated, we can relate the extinction in any passband at any epoch to the maximum light extinction A_X^0. These are of course inter-related, and so we can define the relations between these (currently, five) parameters as a function of the total extinction and the reddening law. CCM89 show that the ratio A_X/A_V is a simple linear function of $R_V^{-1} = (1/R_V)$. We have calculated this relationship at maximum light explicitly using our sample of spectra near that epoch, and fit for the coefficients α_X and β_X, defined by

$$\frac{A_X^0}{A_V^0} = \alpha_X + \frac{\beta_X}{R_V}. \tag{4.2}$$

The results are presented graphically in Figure 4.5, and listed in Table 4.1 (which also shows explicitly the relations for an $R_V = 3.1$ extinction law). Furthermore, the figure illustrates that A_X^0/A_V^0 is a very weak function of $E(B-V)_{\rm true}$ (in most cases the three open circles are indistinguishable), and we are justified in ignoring the dependence on the total extinction.

In the framework developed, then, we parameterize the extinction by a two numbers: A_V^0, corresponding to the extinction in the V passband at maximum light, and R_V, describing the shape of the extinction law. The fixed coefficients α_X and β_X provide the maximum light extinctions in other passbands, and the vectors $\vec{\zeta_X}$ contain the time variation. While the parameterization in terms of $R_X^{\rm true}$ and $R_X^{\rm obs}$ is still useful for certain tasks (see below), we switch to this new framework in the

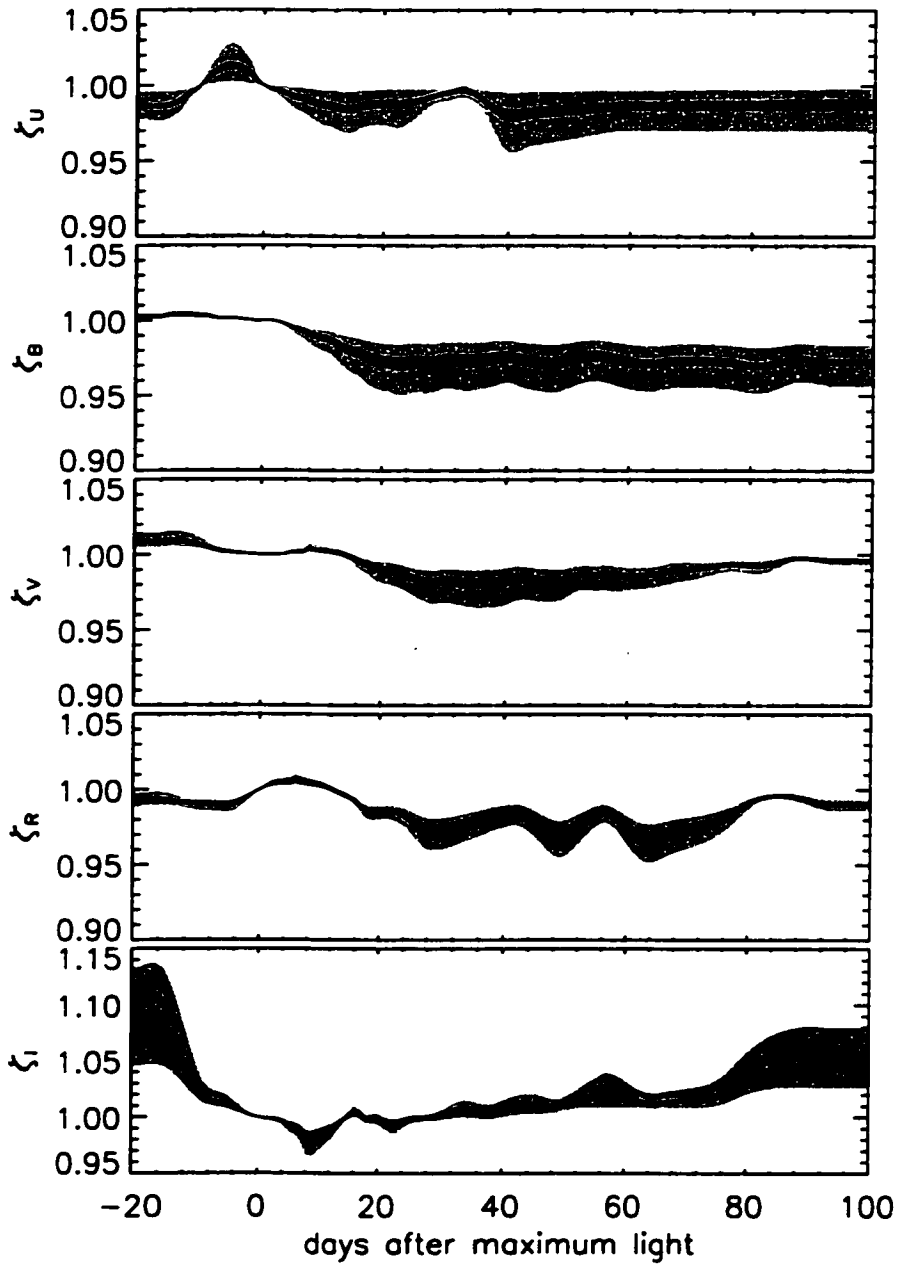

Figure 4.4.— Calculation of $\vec{\zeta_X} \equiv \vec{A_X}/A_X^0$ in *UBVRI* . The dark solid line shows the result for $R_V = 3.1$ and $E(B-V)_{\rm true}$ approaching zero. The dark gray shaded area shows the range of variation in $\vec{\zeta_X}$ over 3 magnitudes in $E(B-V)_{\rm true}$, while the light gray shaded area indicates the variation in $\vec{\zeta_X}$ over that reddening range and over the range $1.7 \leq R_V \leq 5.7$.

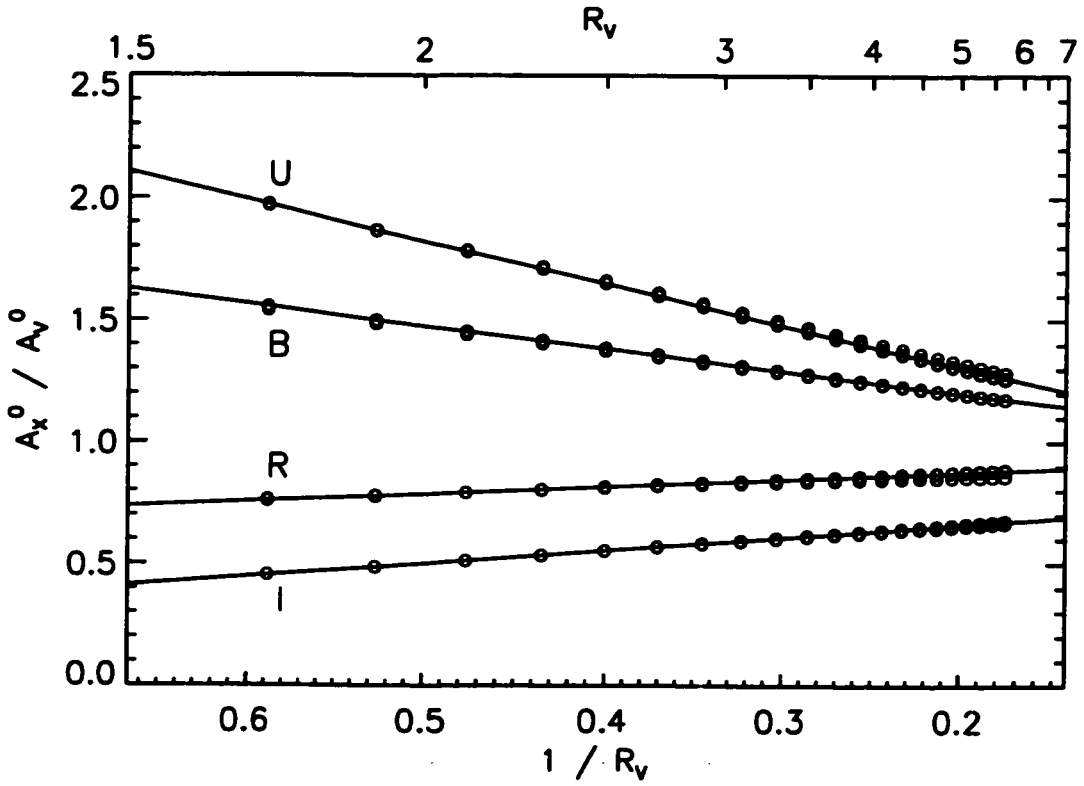

Figure 4.5.— Variation of A_X^0/A_V^0 as a function of R_V^{-1}. The sold lines indicate the best linear fit. The open circles show the calculated points; for each passband and R_V there are three open circles, with $E(B-V)_{\rm true} \simeq -0.5$, 0.0, and +2.5 mag, showing the small differences in the relations as a function of the total extinction.

Table 4.1. Maximum Light Extinction Coefficients

Passband (X)	$A_X^0/A_V^0 = \alpha_X + \beta_X/R_V$		
	α_X	β_X	$\alpha_X + \beta_X/3.1$
U	0.964	1.716	1.518
B	1.016	0.919	1.313
V	1.000	0.000	1.000
R	0.935	−0.300	0.839
I	0.767	−0.534	0.595

MLCS2k2 fits.

4.2.3 Extinction Zeropoint

To define the training set that yield our desired template light curves, we need an estimate of the extinction in the host galaxy of each object. Various approaches are possible, e.g., assuming that SNe Ia in early-type host galaxies or the bluest SNe Ia define an extinction-free sample. Knowing the zeropoint of color (i.e., the true, unreddened color of a SN Ia) is not strictly necessary if we are interested only in relative distances (or in tying the SN Ia distances to another set, such as the Cepheid scale), but it becomes essential if we want to use the positivity of the extinction (dust cannot brighten a source or make it appear bluer) as a constraint on our derived distances. We employ an observational coincidence, independently discovered by Lira (1995) and Riess et al. (1996a), who noticed that the late time ($t \gtrsim +30$ days) $B-V$ color evolution of SNe Ia was remarkably similar, regardless of light curve shape near maximum light. SNe Ia undergoing this transition to the nebular phase also show very similar spectra (e.g., see Filippenko 1997). Phillips et al. (1999) used this "Lira Law," $(B-V)_0 = 0.725 - 0.0118(t_V - 60)$, giving the intrinsic color in terms of the number of days past V maximum light, to measure extinctions and to constrain the $B-V$ and $V-I$ maximum light colors of SN Ia (as a function of $\Delta m_{15}(B)$). The Lira Law as quoted was derived from a fit of late-time photometry of four objects (SNe 1992A, 1992bc, 1992bo and 1994D), estimated to be free of host-galaxy extinction. Phillips et al. (1999) estimate that the intrinsic dispersion about the relation is 0.05 mag.

We have attempted to check the Lira relation with another approach. Rather than trying to choose an extinction-free subsample of the data, we use all the data we can. Beginning with the sample of 114 SNe Ia described above, we have corrected the photometry for Galactic extinction, using the reddening maps of Schlegel et al. (1998) and our calculation of $R_X^{\rm true}$ above, with the assumption that the Galactic component is described by an $R_V = 3.1$ extinction law. We have also applied the K-correction (cf. §4.2.1) and corrected for time-dilation to bring the data to the rest frame. We have then constructed $B-V$ color curves for the sample, and attempted to measure the late-time color evolution. We find that the Lira late-time $B-V$ slope of -0.0118 mag day^{-1} does an excellent job of fitting the bulk of the observations, so we fix the slope and measure only the zeropoint, which we reference to a fiducial epoch of $t = +35$ days past B maximum light. Of the 114 objects, 60 have sufficient data to determine the late-time color well. We show a histogram of these late time color measurements in Figure 4.6.

We assume that this distribution is a result of two independent factors: first, an intrinsic $B-V$color with an unknown dispersion, and second, reddening by dust in the host galaxy. We then model the distribution of the intrinsic component as a Gaussian with mean $(B-V)_{+35}$ and standard deviation σ_{B-V}, and the distribution of the reddening as an exponential with scale length $\tau_{E(B-V)}$ (such that the probability density of the reddening peaks at zero, and falls to $1/e$ of the peak at $\tau_{E(B-V)}$. The probability distribution function of the sum of these two components is just the convolution of the individual distributions, and we perform a maximum-likelihood analysis using each point to determine the best-fit model parameters. The results are also shown in Figure 4.6, with the convolution

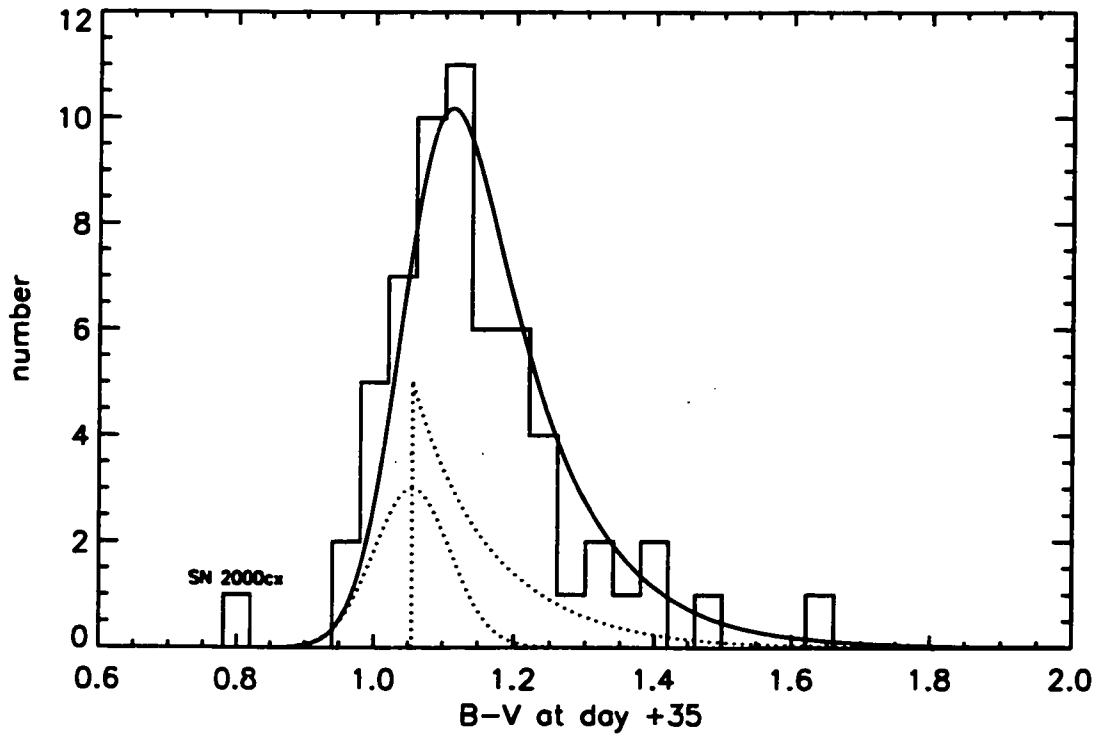

Figure 4.6.— Histogram of 60 SNe Ia with well-measured late-time $B-V$color evolution. The data were corrected for Galactic extinction and the K-correction, and referenced to +35 days after B maximum, adopting a late-time color evolution slope of -0.0118 mag day^{-1}. The maximum-likelihood fit model is shown as the solid curve; it is the convolution of the dotted curves shown (at arbitrary scale). SN 2000cx, a clear outlier, was not included in the fit; see text for details.

overplotted on the histogram and the components inset. The maximum-likelihood model parameters are $(B-V)_{+35} = 1.055 \pm 0.024$, $\sigma_{B-V} = 0.055 \pm 0.017$, and $\tau_{E(B-V)} = 0.113 \pm 0.027$, where the uncertainties were determined by bootstrap resampling of the data set.

There are a couple of cautionary points about this result. First, we have excluded from the fit the very peculiar SN 2000cx (Li et al. 2001), which is a clear outlier in the histogram and whose light curve (but not peak luminosity) is significantly unlike other SNe Ia. The wealth of data on this SN Ia (Li et al. 2001; Jha et al. 2002, Chapter 3), makes its peculiarity very easy to detect, but it is unclear whether a sparsely sampled data set (such as is usually obtained at high-redshift) would have raised any concern. For now we assume that SN 2000cx is unique. Second, because our sample of SNe Ia is not complete nor well-defined based on external criteria, it may be biased with respect to the true distribution of SN Ia late-time color. In particular, there may be a significant population of heavily obscured SN Ia which are not present in our sample, leading to an underestimate of $\tau_{E(B-V)}$ (assuming an exponential distribution is valid at all).

Fortunately, we are chiefly interested in $(B-V)_{+35}$ and σ_{B-V}, and it is difficult to imagine our estimates of these are significantly biased. Furthermore, our measurement is based on the same sample which we will use to measure distances, so the effects of a possible bias are less relevant. It is reassuring, then, that our results with this maximum likelihood method are in good accord with the Lira relation (which predicts $(B-V)_{+35} \simeq 1.044$) and its estimated dispersion. We use this maximum-likelihood zeropoint to make a first guess of the host-galaxy extinctions in our training set sample (using $R_V^{\rm obs}$ and $\vec{\zeta}_V$ to transform the late-time color to our

desired A_V^0), with an uncertainty that is dominated by the intrinsic color dispersion σ_{B-V}.

4.3 Model

We are now in a position to define our model. For each passband, X, we fit the observed light curves (corrected for Galactic extinction, K-correction, and time dilation), $\vec{m_X}$, with

$$\vec{m_X}(t - t_0) = \vec{M_X^0} + \mu_0 + \vec{\zeta_X}\,(\alpha_X + \beta_X/R_V)\,A_V^0 + \vec{P_X}\Delta + \vec{Q_X}\Delta^2, \qquad (4.3)$$

where t_0 is the epoch of maximum light in B, $\vec{M_X^0}$ are the absolute magnitudes of the fiducial SN Ia, μ_0 is the true distance modulus, Δ is the luminosity correction, and $\vec{P_X}$ and $\vec{Q_X}$ are vectors describing the change in light curve shape as a (quadratic) function of the luminosity correction. There are five "free" parameters in the model: t_0, μ_0, Δ, A_V^0, and R_V. As in previous versions of MLCS, we solve for the optimal vectors $\vec{M_X^0}$, $\vec{P_X}$, and $\vec{Q_X}$ using a training set for which we estimate initial values of the free parameters.

Given a training set and solution for the optimal vectors, we construct an empirical model covariance matrix S that incorporates the variance and covariance in the residuals of the training set data from the model (minus the variance and covariance in the training set data itself). Following Riess et al. (1998a), the diagonal elements of the S matrix are derived from the variance about the model, while the off-diagonal elements are estimated from two-point correlations (in the same passband at different epochs, in different passbands at the same epoch and in

different passbands at different epochs).

Armed with the template vectors and the model covariance matrix, we can apply the model. Along with the light curve observations $\vec{m_X}$, conscientious observers provide a covariance matrix of "noise", N, albeit typically only a diagonal one consisting of the variance of each data point (even though SN light curve data can be highly correlated, for instance in the fact that all the light curve points are usually referenced to the same few field comparison stars). We correct these data for Galactic extinction, and incorporate the uncertainty estimate of Schlegel et al. (1998), whereby $\sigma\left(E\left(B-V\right)_{\rm true}\right) \simeq 0.16E(B-V)_{\rm true}$, updating both the diagonal and off-diagonal elements of N (the uncertainties in the Galactic extinction correction are highly correlated, but generally small). We also apply the K-correction, and incorporate the K-correction uncertainty in the diagonal elements of N (unfortunately we do not have enough data to estimate the K-correction correlations) and correct for time-dilation.

We find the best-fit model parameters via χ^2 minimization, with

$$\chi^2 = \vec{r}^{\,T} C^{-1} \vec{r}, \tag{4.4}$$

where $\vec{r}$ is the vector of residuals (in all bands) for a given set of model parameters, and $C = S + N$. We use a downhill simplex method (amoeba; Press et al. 1992) to perform the minimization (though linear algebra suffices in solving for μ_0 and A_V^0, if the other model parameters are fixed) and determine their best-fit parameters. Because the S matrix is empirically determined from the training set, application of the model to objects in the training set will necessarily have a minimum reduced χ^2_ν ($\equiv \chi^2$ per degree of freedom) close to unity, but in applying the model to other

objects, the minimum χ^2_ν still yields useful goodness-of-fit information (indicating how similar the light curves of the new object are to those in the training set, given the nature of the model).

We have also incorporated the ability to add priors on any of the model parameters directly into the fit. The previous versions of MLCS, for instance, used a Bayesian filter requiring the extinction to be non-negative, but this was enforced after the best fits were determined. The advantage of that approach is convenience and expediency, but at the expense of ignoring correlations among the parameters. Previous versions of MLCS used μ_V, the distance modulus uncorrected for extinction, as the basic distance model parameter rather than $\mu_0 = \mu_V - A_V$, thus minimizing the correlation among the model parameters and making the Bayesian filter simple and effective. However, there are situations in which one might like to include other prior information into the fit. For example, a sparsely-sampled light curve may not allow for a good determination of the time of maximum light, but we may have other information about the time of maximum from spectroscopy (Riess et al. 1997). In the extreme limit of the "snapshot" method, (Riess et al. 1998b), spectroscopy could be used to determine prior constraints on both t_0 and Δ. Alternately, we may have observations in additional, non-modeled passbands (such as in the near-infrared), which impose prior constraints on A^0_V or R_V. Incorporating priors, $\hat{p}$, into the fit is straightforward, we simply adjust the χ^2 to

$$\chi^2 = \vec{r}^T C^{-1} \vec{r} - 2 \ln \hat{p}(t_0, \mu_0, \Delta, A^0_V, R_V), \tag{4.5}$$

taking care to reinterpret this "χ^2" in the proper way when estimating goodness-of-fit and parameter uncertainties.

4.4 Training

The training set is the most critical part of the analysis; it requires objects with accurate (and hopefully, precise) estimates of the model parameters, in order to construct the template vectors and covariance matrix. As in Riess et al. (1998a), we use the Hubble law to determine precise relative distances, thus useful objects in the training set need to have recession velocities that are dominated by the cosmological expansion as opposed to peculiar motions. The objects also need to have well-measured light curves at maximum light so that t_0 and $V_{\max}$ (to be used in determining Δ, as below) can be reliably determined. Finally, we require accurate host-galaxy extinction estimates for the training-set objects, meaning well-sampled late-time B and V light curves, as described in §4.2.3. Ideally, we would also like estimates of the host-galaxy extinction law R_V for each SN, but this is hard to come by *a priori*, and estimates based on the SN light curves require knowledge of the intrinsic colors we are trying to determine! To avoid this conundrum, then, we restrict the sample to objects not very significantly reddened (as determined from the tail $B-V$ color), so that variation in R_V does not have a large effect (and we adopt $R_V = 3.1$ for the training set; see below).

Our final training set consists of 30 SNe Ia, with $cz \geq 2500$ km s^{-1} (measured in the CMB frame) and well-sampled light curves beginning earlier than 10 days past maximum light: SNe 1990O, 1991ag, 1992P, 1992al, 1992bc, 1992bg, 1992bl, 1992bo, 1993O, 1993ag, 1994M, 1995ac, 1995ak, 1996C, 1997E, 1997Y, 1997bq, 1998V, 1998ab, 1998bp, 1998de, 1998es, 1999aa, 1999ac, 1999dq, 1999gp, 2000cn, 2000dk, 2000fa, and 2001V. For each SN, we calculate Δ as the difference between

V magnitude at maximum light (corrected for host-galaxy extinction) and the Hubble line given the host-galaxy redshift. We assign an uncertainty in Δ from the quadrature sum of the uncertainty in the direct fit of $V_{\rm max}$, the extinction uncertainty and a distance uncertainty based on a peculiar velocity dispersion[6] of $\sigma = 300$ km s^{-1}. These initial guesses of Δ span a range of over two magnitudes, and the sample includes a wide range of over- and under-luminous objects.

From the initial guesses of the model parameters and uncertainties, we derive the best fit vectors, $\vec{M_X^0}$, $\vec{P_X}$, and $\vec{Q_X}$, as well as the model covariance matrix S. We then apply the model to the training set to produce a new set of parameters for each object and iterate the procedure, until the training converges to a consistent set of parameters and vectors.[7]. In Figure 4.7, we present the unreddened template light curves in *UBVRI* over a wide range of luminosity, based on the final template vectors derived in the training process. The characteristic result that intrinsically brighter SN Ia (low Δ) have broader light curves is clearly established in all passbands.

The MLCS2k2 relations allow us to determine the intrinsic colors of SN Ia with varying luminosity at any epoch. In Figure 4.8, we show a sample of the color relations in $U-B$, $B-V$, and $V-I$, at maximum light and 35 days after maximum. The maximum light color variation in $U-B$ and $B-V$ can be compared directly to Figure 3.10 (where a smaller stretch corresponds to a larger Δ), and it is reassuring that the results are very similar in the two approaches. Similarly, the late-time

[6]We use the conservative estimate $\sigma = 300$ km s^{-1} for consistency with previous versions of MLCS (cf. discussion in Riess et al. 1996).

[7]During this procedure, we employ priors as described in §4.3 to constrain the model parameters to their original values within the appropriate uncertainties. This prevents the model parameters from "seeping", for instance, by globally shifting all of the colors and extinctions in one direction.

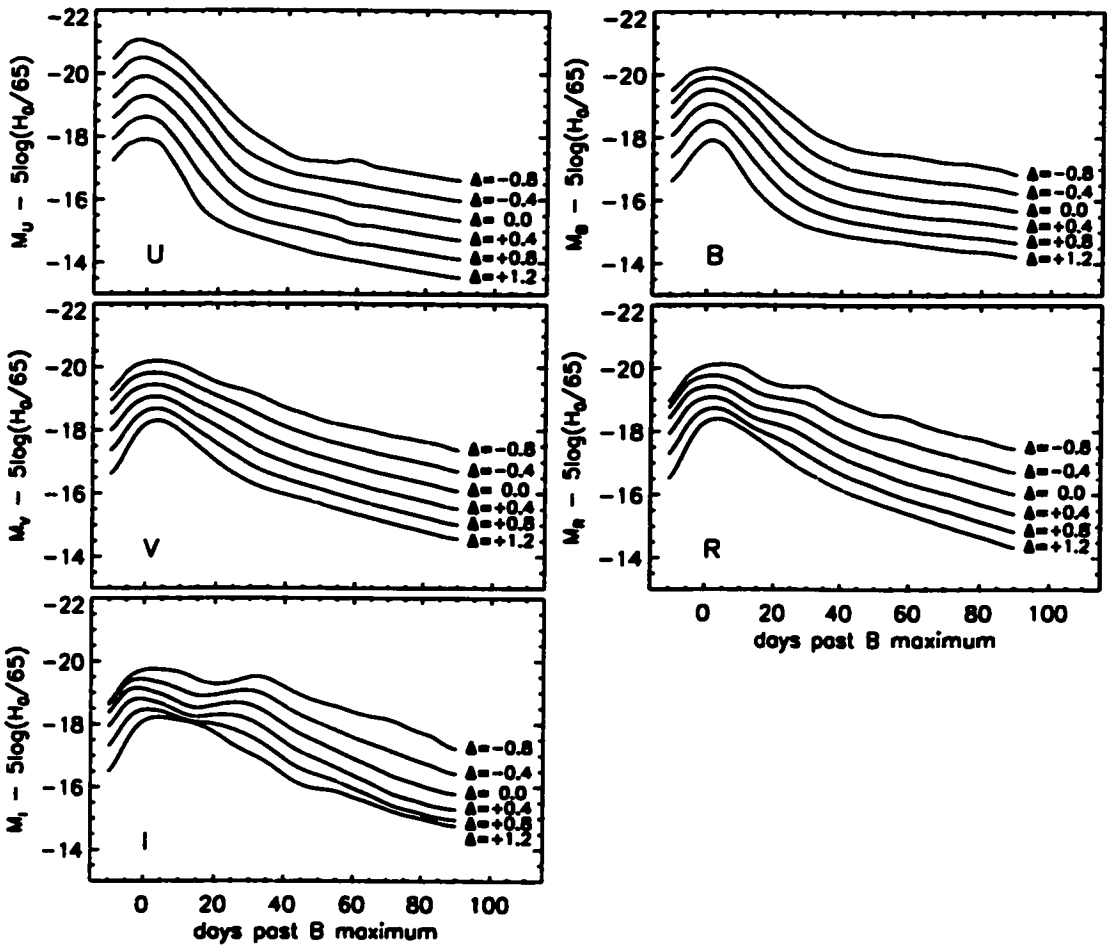

Figure 4.7.— MLCS2k2 intrinsic *UBVRI* light curve templates, $\vec{M}_X = \vec{M}_X^0 + \vec{P}_X\Delta + \vec{Q}_X\Delta^2$, shown over a range luminosity from $\Delta = -0.8$ (brighter) to $\Delta = +1.2$ (fainter).

colors show little variation with luminosity, in harmony with our use of the late-time $B-V$ color to provide initial guesses of the extinction.

4.5 Application

We have applied the model to our full sample of 114 SNe Ia. We have employed two prior constraints; the first is that the host-galaxy extinction is forced to be non-negative. As discussed above, we do not use the direct implementation of the Bayesian filter introduced by Riess et al. (1996a). Rather, we incorporate the prior directly into the fitting procedure, and thus the resultant extinction (and its uncertainty) are "naturally" filtered during the fit. Secondly, for the time being we have constrained the host galaxy extinction-law to $R_V = 3.1$.

Our original motivation for introducing R_V as a model parameter was threefold: first, extragalactic extinction laws are known to vary (e.g., see Falco et al. 1999); second, there is one heavily-reddened supernova, SN 1999cl, for which near-infrared data strongly suggest an extinction law $R_V \simeq 1.8$ (Krisciunas et al. 2002; Jha et al. 2002, Chapter 3); and finally, there were early indications that the U-band showed increased dispersion, and because variations in the extinction law are more significant in U, allowing for a variable R_V seemed like a good candidate to explain this dispersion. However, in doing the fits it turned out that for most of the objects (with low reddening) the data constrain R_V only very weakly. If we incorporate even a weak prior, e.g., a Gaussian with $\hat{p}(R_V) = 3.1 \pm 0.5$, the best fits for R_V cluster at the peak of the prior distribution (i.e., the fits in R_V are prior dominated even for weak priors). Furthermore, for the objects with U data it became clear

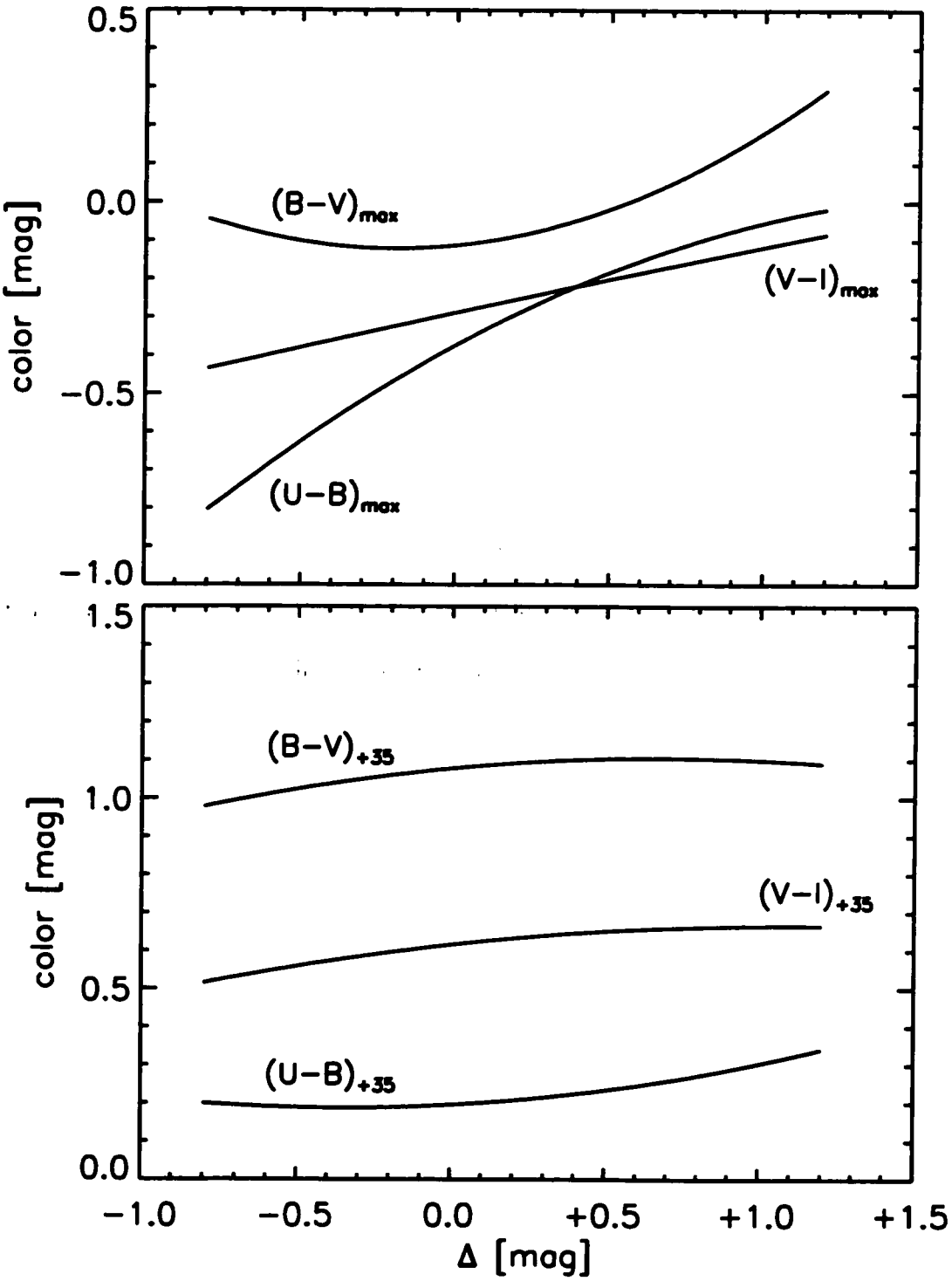

Figure 4.8.— MLCS2k2 maximum light (top panel) and late time (+35 days, bottom panel) intrinsic $U-B$, $B-V$, and $V-I$ colors as a function of decreasing intrinsic luminosity (increasing Δ).

that the excess dispersion was intrinsic, not a result of varying R_V (cf. discussion in §3.4 and Figure 3.9). Thus we have fixed $R_V = 3.1$ to simplify the analysis; only one object, the aforementioned heavily extinguished SN 1999cl is badly fit with this constraint, and we have excluded it from the sample. We will explore the variation in R_V for heavily reddened SN Ia in a future paper (cf. Riess, Press, & Kirshner 1996b; Phillips et al. 1999), and we encourage near-infrared observations of SN Ia to provide greater leverage on constraining R_V.

We show an example light curve fit for SN 2000fa (Jha et al. 2002, Chapter 3) in Figure 4.9. To determine the distance modulus uncertainty in the fit, we explicitly calculate the posterior probability density function over a grid of μ_0 and A_V^0, where we allow t_0 and Δ to float to their best fit values at each grid point (the likelihood distributions of these latter two parameters are well-described by Gaussians). The prior constraint on A_V^0 makes this two-dimensional distribution significantly non-Gaussian in the cases where the best-fit host-galaxy extinction is near zero. Thus we determine the posterior probability distribution of μ_0 by marginalizing over A_V^0. Our best estimate of the distance is given by the mean of this distribution (not the mode), and uses the second moment to estimate the uncertainty. Because these distributions can be slightly asymmetric, we should formally perform derivative calculations using the distributions directly (for example, measuring the intercept of the Hubble line). However, after combination of just a few objects, the formally correct (but computationally intensive) method yields results indistinguishable from those based on the means.

Our final Hubble flow sample, with $cz \geq 2500$ kms^{-1} in the CMB frame, consists of 80 SNe Ia, including 34 out of 44 of the objects presented in Chapter 3. This

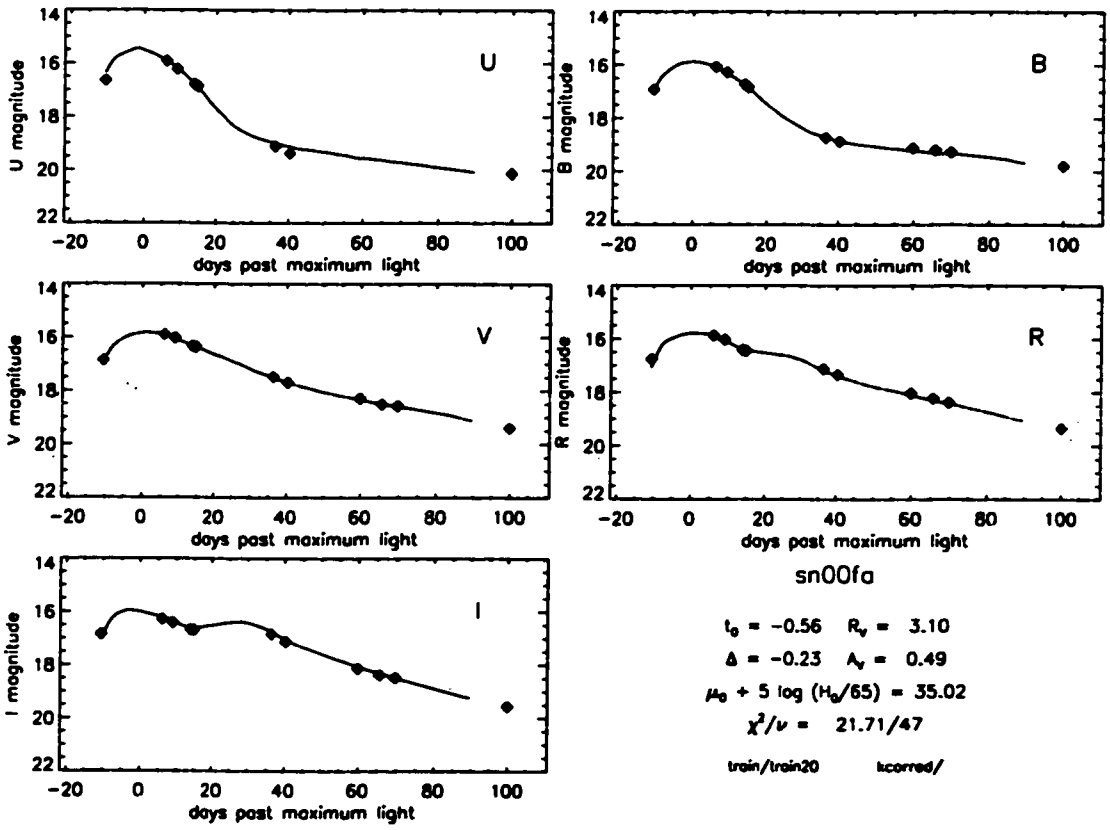

Figure 4.9.— Example MLCS2k2 fit of SN 2000fa. The best-fit *UBVRI* light curves are plotted with the photometry, and the best fit parameters are presented in the lower right. The supernova is well-fit, even with gaps in the light curve.

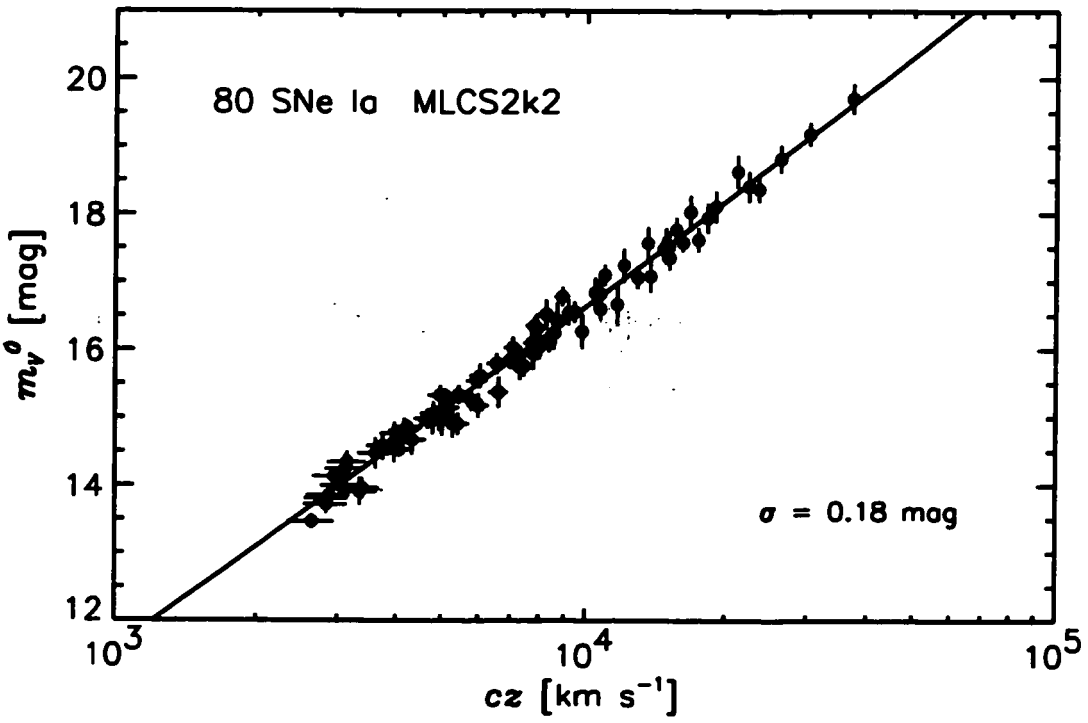

Figure 4.10.— Apparent magnitude-redshift relation for our Hubble flow sample of 80 SNe Ia, using MLCS2k2 to correct for host-galaxy extinction and intrinsic luminosity differences.

nearly doubles the Hubble flow sample as compared to the one presented by Jha et al. (1999, Chapter 2). The Hubble diagram for this sample is shown in Figure 4.10, where, as in Figure 2.10, we have fit for only one free parameter, the intercept of the ridge line a_V, defined in equation 2.8.[8] As discussed in detail by Jha et al. (1999, Chapter 2), the ridge line intercept is measured from the Hubble Flow SNe Ia alone, with a best-fit value and formal uncertainty, $a_V = 0.6838 \pm 0.0045$. Unfortunately we cannot compare this result directly with that presented in Jha et al. (1999, Chapter 2, because we have used a new training set sample, and consequently new template vectors with new magnitude and Δ zeropoints. Of course, these differences apply equally to our Cepheid-calibrated sample, and the resultant estimates of H_0 are directly comparable. We adopt a systematic uncertainty of $\sim$ 3% in distance (and H_0) from the Hubble flow sample, as discussed by Jha et al. (1999, Chapter 2), including the effects of sample differences and peculiar velocities, yielding $a_V = 0.6838 \pm 0.0045$ (random) ± 0.0120 (systematic).

The scatter about the Hubble line in Figure 4.10, $\sigma = 0.18$ mag is a cause of some concern, as it is slightly higher than other methods (including prior versions of MLCS) which typically yield ($\sigma \simeq 0.12$ to 0.16 mag). One component in this increased dispersion is certainly the fact that the new objects presented by Jha et al. (2002, Chapter 3) have a significantly lower mean redshift, meaning that peculiar motions are more important. We are in the process of refining the method, with particular attention to the very fast-declining objects, where it seems that the model is ascribing more extinction to the SN Ia than one would expect. This may be from

[8]We have adopted an $\Omega_M = 0.3$, $\Omega_\Lambda = 0.7$ cosmology, which is significant for the more distant objects, and assumed a peculiar velocity uncertainty of ± 300 km s^{-1}, important for the nearby objects.

a lack of sufficient very fast decliners in the training set, and might be rectified by expanding the training set to include more of the 114 objects. For now, we present the results using the current distances, bearing in mind that these distances may be subject to (small) adjustment.

In addition to nearly doubling the Hubble flow sample, we also have a doubled sample of well-observed SN Ia with Cepheid distances. Eight objects are now available to form our Cepheid-calibrated sample; the four SNe 1972E, 1981B, 1990N, and 1998bu were described in Chapter 2. New Cepheid distances have been obtained for the host galaxies of SN 1989B (NGC 3627; Saha et al. 1999), SN 1991T (NGC 4527; Saha et al. 2001a), SN 1998aq (NGC 3982; Saha et al. 2001b), and SN 1999by (NGC 2841; Macri et al. 2001). Unfortunately, these Cepheid distances are controversial, with two groups presenting discrepant values from the same data: the HST SN Ia Project (Saha et al. 2001b) and the HST H_0 Key Project (Freedman et al. 2001). The reasons for the discrepancies are often subtle (see, e.g., Gibson et al. 2000), though some divergent choices are straightforward (for instance, in the Cepheid PL relation that is fit).

Insofar as possible, we remain neutral between these two groups, and here present the results using both sets of distances. The SN Ia Project adopted distances to 6 of the 8 supernovae are given most recently by Saha et al. (2001b) in their Table 6, and the SN Ia Project distance to the host of SN 1991T is given by Saha et al. (2001a). To date, the SN Ia Project have not applied their analysis procedure to HST observations of Cepheids in NGC 2841, the host of SN 1999by. We use the Key Project distances to 5 of the 8 supernova host galaxies as given by Freedman et al. (2001) in their Table 4, and distances to the three remaining hosts are presented

by Gibson & Stetson (2001; NGC 4527/SN 1991T), Stetson & Gibson (2001; NGC 3982/SN 1998aq) and Macri et al. (2001; NGC 2841/SN 1999by).[9] The Cepheid distances to the SN Ia host galaxies from both teams are presented in Table 4.2. The mean difference between the 7 Cepheid distances in common is 0.33 mag, more than 15% in distance. This discrepancy translates directly into a $\gtrsim$15% discrepancy in the inferred Hubble constant, irrespective of the SNe Ia themselves or inherent systematic uncertainties.

Table 4.2. MLCS2k2 and Cepheid Calibrated SNe Ia

SN Ia	Galaxy (NGC)	m_V^0	$\mu_{\rm Cepheid}$		M_V^0	
			SN Ia Project	Key Project	SN Ia Project	Key Project
1972E	5253	8.73 ± 0.18	27.93 ± 0.08	27.49 ± 0.15	-19.20 ± 0.20	-18.76 ± 0.23
1981B	4536	11.78 ± 0.18	31.17 ± 0.13	30.87 ± 0.06	-19.39 ± 0.22	-19.09 ± 0.18
1989B	3627	10.62 ± 0.14	30.37 ± 0.13	30.01 ± 0.09	-19.75 ± 0.19	-19.39 ± 0.16
1990N	4639	12.84 ± 0.13	32.13 ± 0.22	31.71 ± 0.09	-19.29 ± 0.26	-18.87 ± 0.16
1991T	4527	11.71 ± 0.12	30.82 ± 0.13	30.61 ± 0.09	-19.11 ± 0.17	-18.90 ± 0.15
1998aq	3982	12.78 ± 0.09	31.80 ± 0.15	31.64 ± 0.09	-19.02 ± 0.17	-18.86 ± 0.13
1998bu	3368	11.00 ± 0.12	30.51 ± 0.16	30.11 ± 0.07	-19.51 ± 0.20	-19.11 ± 0.14
1999by	2841	11.71 ± 0.12	...	30.74 ± 0.15	...	-19.03 ± 0.19
Mean	...	...	...	...	-19.31 ± 0.10	-19.00 ± 0.07

In Table 4.2, we also present the calibrator sample SN Ia peak magnitudes, m_V^0, corrected for host-galaxy extinction and to the fiducial luminosity (we use the same notation as in Jha et al. 1999, Chapter 2, and follow that presentation), and derived exactly the same way as the Hubble flow sample displayed in Figure 4.10. From these and the Cepheid distances, we calculate directly the fiducial SN

[9]Strictly speaking, these papers are not part of the Key Project, but they follow the Key Project methodology. We have adjusted the NGC 4527 distance presented by Gibson & Stetson (2001) to an assumed LMC distance modulus of 18.50, for consistency with all the other Cepheid distances.

Ia maximum light absolute magnitude, $M_V^0 = m_V^0 - \mu_{\rm Cepheid}$, which is a constant in our calibrated-candle framework. In Figure 4.11, we show the individual estimates of M_V^0 presented in the table, clearly indicating the discrepancy between the two groups. The scatter in M_V^0 is $\sigma = 0.25$ mag using the SN Ia Project distances, and $\sigma = 0.20$ mag for the Key Project distances. Both of these are reasonable given the uncertainties in the SN Ia and Cepheid distances.

The uncertainties associated with the weighted mean SN Ia Project and Key Project M_V^0 values presented in Table 4.2 are statistical (including covariance in the Cepheid distances). Jha et al. (1999, Chapter 2) provide a discussion of the systematic uncertainties that (still) plague Cepheid distances in general. Here we adopt the Key Project systematic error budget presented in Table 14 of Freedman et al. (2001), including uncertainties in the LMC distance, HST zeropoints, metallicity, and crowding, which yield a total systematic error of $\pm 10\%$ in distance. Assuming the systematic uncertainties in the MLCS2k2 fits to the calibrator SNe Ia are smaller than this, our final estimates of the fiducial absolute peak magnitude are

$$M_V^0 = -19.31 \pm 0.10\ \text{(random)}\ \pm 0.20\ \text{(systematic)} \qquad \text{SN Ia Project,} \tag{4.6}$$

$$M_V^0 = -19.00 \pm 0.07\ \text{(random)}\ \pm 0.20\ \text{(systematic)} \qquad \text{Key Project.} \tag{4.7}$$

Using these values with the previously measured intercept, $a_V = 0.6838 \pm 0.0035 \pm 0.0120$, and the relation $\log H_0 = 0.2 M_V^0 + a_V + 5$, we arrive at our best estimates of the Hubble Constant from SNe Ia,

$$H_0 = 66 \pm 3 \pm 7\ \text{km s}^{-1}\ \text{Mpc}^{-1} \qquad \text{SN Ia Project,} \tag{4.8}$$

$$H_0 = 76 \pm 3 \pm 8\ \text{km s}^{-1}\ \text{Mpc}^{-1} \qquad \text{Key Project.} \tag{4.9}$$

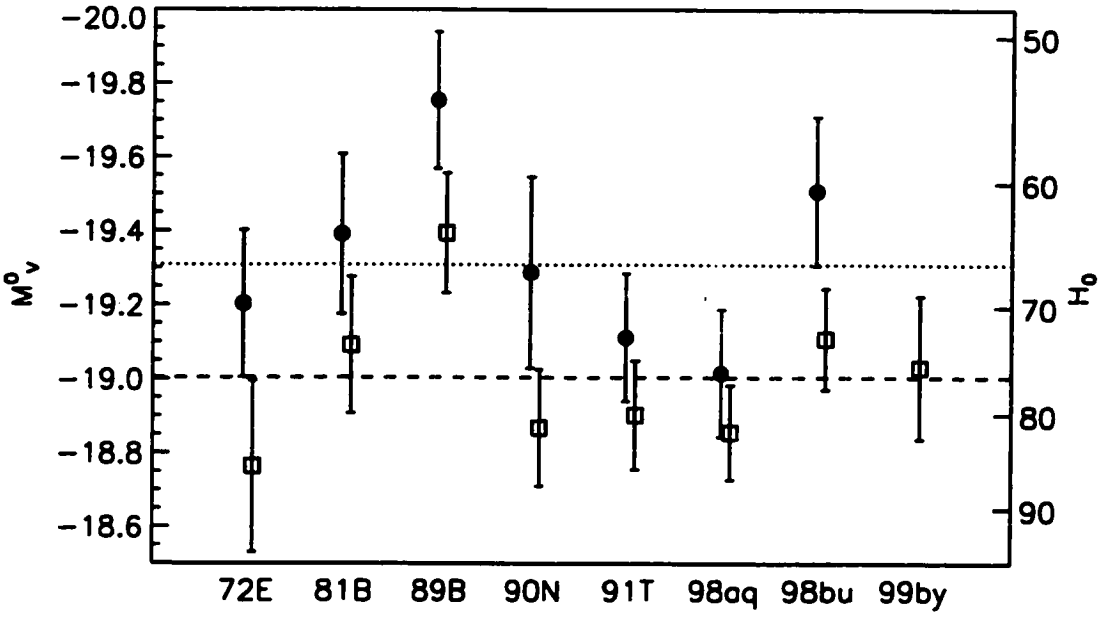

Figure 4.11.— Individual estimates of M_V^0 from each of the calibrator SNe Ia, using the Cepheid distances of the SN Ia Project (filled circles) and the Key Project (open squares). The dotted and dashed lines respectively indicate the weighted means for the two groups.

We note that in Table 4.2, we used metallicity corrected distance moduli (with identical corrections to both groups' distances, using the Key Project value of $\gamma_{VI} = -0.2 \pm 0.2$ mag dex^{-1}. If we use distance moduli uncorrected for metallicity (i.e., $\gamma_{VI} = 0$), our estimates of H_0 increase by 4% for the SN Ia project, and 5% for the Key Project.

Finally, we show in Figure 4.12 a clear detection of the Local Group motion relative to the frame defined by the SNe Ia. The figure shows the peculiar velocities for the 66 of 114 SNe Ia in our sample which have $cz \leq 6000$ km s^{-1} in the Local Group frame (excepting the peculiar SN 1999cl and SN 2000cx). The mean redshift of the sample presented by Jha et al. (2002, Chapter 3) is significantly smaller than the previous large samples of Hamuy et al. (1996b) and Riess et al. (1999) making it especially well-suited for constraining peculiar motions and flows.

We thank Alex Filippenko and Weidong Li for providing access to unpublished spectroscopy and photometry. We also thank Peter Nugent for helpful discussions.

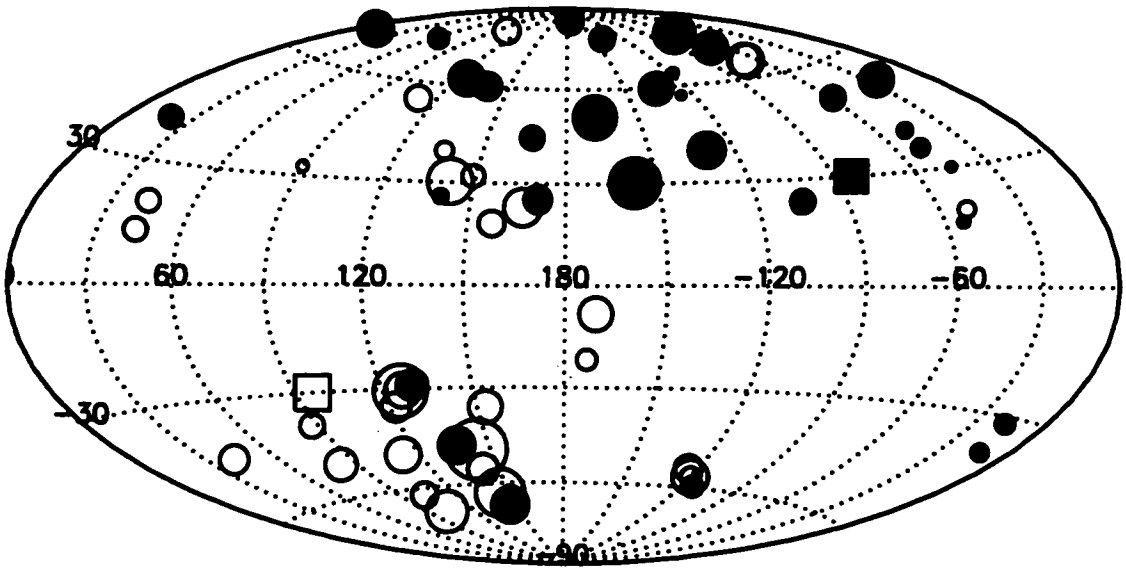

Figure 4.12.— Peculiar velocities of 66 SNe Ia with $cz \leq 6000$ km s^{-1} in the rest-frame of the Local Group, plotted in Galactic coordinates (with central meridian $\ell = 180°$). The solid circles indicate SNe Ia in galaxies with negative peculiar velocities (i.e., approaching us relative to the cosmic expansion). The empty circles indicate positive peculiar velocities, objects from which we are moving away. The area of the symbols is proportional to the amplitude of the peculiar velocity. The squares mark the location of the CMB dipole and are drawn to scale relative to the circles, with the Local Group moving towards (276°, +30°) at 627 km s^{-1} (Cox 2000).

4.6 References

Bessell, M.S. 1990, PASP, 102, 1181

Buta, R.J., & Turner, A. 1983, PASP, 95, 72

Cardelli, J.A., Clayton, G.C., & Mathis, J.S. 1989, ApJ, 345, 245 (CCM89)

Cox, A.N., ed. 2000, Allen's Astrophysical Quantities, 4th ed., New York: AIP

Falco, E.E., Impey, C.D., Kochanek, C.S., Lehár, J., McLeod, B.A., Rix, H.-W., Keeton, C.R., Muñoz, J.A., & Peng, C.Y., ApJ, 523, 617

Filippenko, A.V., Richmond, M.W., Branch, D., Gaskell, C.M., Herbst, W., Ford, C.H., Treffers, R.R., Matheson, T., Ho, L.C., Dey, A., Sargent, W.L.W., Small, T.A., & van Breugel, W.J.M. 1992, AJ, 104, 1543

Filippenko, A.V. 1997, ARA&A, 35, 309

Fitzpatrick, E.L. 1999, PASP, 111, 63

Freedman, W.L., et al. 2001, ApJ, 553, 47

Garnavich, P.M., Bonanos, A.Z., Jha, S., Kirshner, R.P., Schlegel, E.M., Challis, P., Macri, L.M., Hatano, K., Branch, D., Bothun, G.D., & Freedman, W.L. 2002, in press (astro-ph/0105490)

Gibson, B.K., et al. 2000, ApJ, 529, 723

Gibson, B.K., & Stetson, P.B. 2001, ApJ, 547, L103

Hamuy, M., Phillips, M.M., Maza, J., Wischnjewsky, M., Uomoto, A., Landolt, A.U., & Khatwani, R. 1991, AJ, 102, 208

Hamuy, M., Phillips, M.M., Wells, L., & Maza, J. 1993, PASP, 105, 787

Hamuy, M., Phillips, M.M., Maza, J., Suntzeff, N.B., Schommer, R.A., & Avilés, R. 1995, AJ, 109, 1

Hamuy, M., Phillips, M.M., Suntzeff, N.B., Schommer, R.A., Maza, J., Smith, R.C., Lira, P., & Avilés, R. 1996a, 112, 2438

Hamuy, M., et al. 1996b, AJ, 112, 2408

Jha, S., et al. 1999, ApJS, 125, 73

Kim, A., Goobar, A., & Perlmutter, S. 1996, PASP, 108, 190

Krisciunas, K., Hastings, N.C., Loomis, K., McMillan, R., Rest, A., Riess, A.G., & Stubbs, C. 2000, ApJ, 539, 658

Krisciunas, K., Phillips, M.M., Stubs, C., Rest, A., Miknaitis, G., Riess, A.G., Suntzeff, N.B., Roth, M., Persson, S.E., & Freedman, W.L. 2001, AJ, 122, 1616

Leibundgut, B., Tammann, G.A., Cadonau, R., & Cerrito, D. 1991, A&AS, 89, 537

Leibundgut, B., et al. 1993, AJ, 105, 301

Li, W.D., Qiu, Y.L., Qiao, Q.Y., Zhu, X.H., Hu, J.Y., Richmond, M.W., Filippenko, A.V., Treffers, R.R., Peng, C.Y., & Leonard, D.C. 1999, AJ, 117, 2709

Li, W.D., Filippenko, A.V., Gates, E., Chornock, R., Gal-Yam, A., Ofek, E.O., Leonard, D.C., Modjaz, M., Rich, R.M., Riess, A.G., & Treffers, R.R. 2001, PASP, 113, 1178

Lira, P. 1995, Master's Thesis, University of Chile

Lira, P., et al. 1998, AJ, 115, 234

Macri, L.M., Stetson, P.B., Bothun, G.D., Freedman, W.L., Garnavich, P.M., Jha, S., Madore, B.F., & Richmond, M.W. 2001, ApJ, 559, 243

Meikle, W.P.S., et al. 1996, MNRAS, 281, 263

Modjaz, M., Li, W.D., Filippenko, A.V., King, J.Y., Leonard, D.C., Matheson, T., & Treffers, R.R. 2001, PASP, 113, 308

Nugent, P., Kim, A., & Perlmutter, S. 2002, in press

O'Donnell, J.E. 1994, ApJ, 422, 158

Parodi, B.R., Saha, A., Sandage, A., Tammann, G.A. 2000, ApJ, 540, 634

Patat, F., Benetti, S., Cappellaro, E., Danziger, I.J., Della Valle, M., Mazzali, P.A., Turatto, M. 1996, MNRAS, 278, 111

Perlmutter, S., et al. 1997, ApJ, 483, 565

Phillips, M.M., et al. 1987, PASP, 99, 592

Phillips, M.M. 1993, ApJ, 413, L105

Phillips, M.M., Lira, P., Suntzeff, N.B., Schommer, R.A., Hamuy, M., & Maza, J. 1999, AJ, 118, 1766

Press, W.H., Teukolsky, S.A., Vetterling, W.T., & Flannery, B.P. 1992, Numerical Recipes in C, 2nd ed., New York: Cambridge University Press

Richmond, M.W., Treffers, R.R., Filippenko, A.V., van Dyk, S.D., Paik, Y., Peng, C., Marschall, L.A., Laaksonen, B.D., Macintosh, B., & McLean, I.S. 1995, AJ, 109, 2121

Riess, A.G., Press, W.H., & Kirshner, R.P., 1995, ApJ, 438, L17

Riess, A.G., Press, W.H., & Kirshner, R.P. 1996a, ApJ, 473, 88

Riess, A.G., Press, W.H., & Kirshner, R.P. 1996b, ApJ, 473, 588

Riess, A.G., et al. 1997, AJ, 114, 722

Riess, A.G., et al. 1998a, AJ, 116, 1009

Riess, A.G., Nugent, P., Filippenko, A.V., Kirshner, R.P., & Perlmutter, S. 1998b, ApJ, 504, 935

Riess, A.G., et al. 1999, AJ, 117, 707

Saha, A., Sandage, A., Tammann, G.A., Labhardt, L., Macchetto, F.D., & Panagia, N. 1999, ApJ, 522, 802

Saha, A., Sandage, A., Thim, F., Labhardt, L., Tammann, G.A., Christensen, J., Panagia, N., & Macchetto, F.D. 2001a, ApJ, 551, 973

Saha, A., Sandage, A., Tammann, G.A., Dolphin, A.E., Christensen, J., Panagia, N., & Macchetto, F.D. 2001b, ApJ, 562, 314

Schlegel, D. J., Finkbeiner, D. P., & Davis, M. 1998, ApJ, 500, 525

Stetson, P.B., & Gibson, B.K. 2001, MNRAS, 328, L1

Suntzeff, N.B., et al. 1999, AJ, 117, 1175

Tripp, R., & Branch, D. 1999, ApJ, 525, 209

Tsvetkov, D.Yu. 1982, Sov. Astron. Lett. 8, 115

Turatto, M., Benetti, S., Cappellaro, E., Danziger, I.J., Della Valle, M., Gouiffes, C., Mazzali, P.A., & Patat, F. 1996, MNRAS, 283, 1

Turatto, M., Piemonte, A., Benetti, S., Cappellaro, E., Mazzali, P.A., Danziger, I.J., & Patat, F. 1998, AJ, 116, 2431

Wells, L. A., et al. 1994, AJ, 108, 2233

Chapter 5

Cosmological Parameters from High-Redshift Supernovae and the Cosmic Microwave Background

adapted from:

"Supernova Limits on the Cosmic Equation of State," Peter M. Garnavich, Saurabh Jha, Peter Challis, Alejandro Clocchiatti, Alan Diercks, Alexei V. Filippenko, Ron L. Gilliland, Craig J. Hogan, Robert P. Kirshner, Bruno Leibundgut, M. M. Phillips, David Reiss, Adam G. Riess, Brian P. Schmidt, Robert A. Schommer, R. Chris Smith, Jason Spyromilio, Chris Stubbs, Nicholas B. Suntzeff, John Tonry, and Sean M. Carroll 1998, *The Astrophysical Journal*, **509**, 74 and

"Testing Cosmic Acceleration with Type Ia Supernovae," Saurabh Jha and the High-Z Supernova Search Team 2001, proceedings of IAU Symposium 201, *New*

Cosmological Data and the Values of the Fundamental Parameters, eds. A. Lasenby and A. Wilkinson, in press (astro-ph/0101521)

Abstract

We use Type Ia supernovae studied by the High-Z Supernova Search Team to constrain the properties of an energy component which may have contributed to accelerating the cosmic expansion. We find that for a flat geometry the equation of state parameter for the unknown component, $\alpha_x = P_x/\rho_x$, must be less than -0.55 (95% confidence) for any value of Ω_m and is further limited to $\alpha_x < -0.60$ (95%) if Ω_m is assumed to be greater than 0.1 . These values are inconsistent with the unknown component being topological defects such as domain walls, strings, or textures. The supernova data are consistent with a cosmological constant ($\alpha_x = -1$) or a scalar field which has had, on average, an equation of state parameter similar to the cosmological constant value of -1 over the redshift range of $z \approx 1$ to the present. Supernova and cosmic microwave background observations give complementary constraints on the densities of matter and the unknown component. If only matter and vacuum energy are considered, then the combined data sets provide direct evidence for a spatially flat Universe with $\Omega_{tot} = \Omega_m + \Omega_\Lambda = 0.94 \pm 0.26$ (1σ). Updating these constraints with independent SN Ia data and new CMB results strengthens these results.

5.1 Introduction

Matter that clusters on the scale of galaxies or galaxy clusters is insufficient to close the Universe, with conventional values near $\Omega_m = 0.2 \pm 0.1$ (Gott et al. 1974; Carlberg et al. 1996; Lin et al. 1996; Bahcall, Fan, & Cen 1997). Observations of distant supernovae provide credible evidence that the deceleration rate of the Universal expansion is small, implying that the total matter density, clustered or smooth, is insufficient to create a flat geometry (Garnavich et al. 1998; Perlmutter et al. 1998). Either the Universe has an open geometry or, if flat, other forms of energy are more important than matter.

Large samples of supernovae analyzed by the High-Z Supernova Search collaboration (Riess et al. 1998a, hereinafter [Riess98]) and the Supernova Cosmology Project (Kim 1998) now suggest that the Universe may well be accelerating. Matter alone cannot accelerate the expansion; so if taken at face value, the observations demand an additional energy component for the Universe. While the vigorous pursuit of possible systematic effects (e.g. Höflich, Wheeler, & Thielemann 1998) will be important in understanding these observations, it is instructive to see what they imply about the energy content of the Universe.

The cosmological constant was revived to fill the gap between the observed mass density and the theoretical preference for a flat Universe (Turner, Steigman, & Krauss 1984; Peebles 1984) and also to alleviate the embarrassment of a young Universe with older stars (Carroll, Press, & Turner 1992). The cosmological constant is a negative pressure component arising from non-zero vacuum energy (Weinberg 1989). It would be extraordinarily difficult to detect on a small scale,

but $\Omega_\Lambda = 1 - \Omega_m$ could make up the difference between the matter density Ω_m and a flat geometry and might be detected by measurements on a cosmological scale. There are few independent observational constraints on the cosmological constant, but Falco, Kochanek, & Muñoz (1998) estimated that $\Omega_\Lambda < 0.7$ (95% confidence) from the current statistics of strong gravitational lenses. If the matter density is less than $\Omega_m \sim 0.3$, this limit is close to preventing the cosmological constant from making a flat geometry. Further, a cosmological constant which just happens to be of the same order as the matter content at the present epoch raises the issue of "fine tuning" (Coles & Ellis 1997). A number of exotic forms of matter which might contribute to cosmic acceleration are physically possible and viable alternatives to the cosmological constant (Frieman & Waga 1998; Caldwell, Dave, & Steinhardt 1998). The range of possibilities can be narrowed using supernovae because the luminosity distance not only depends on the present densities of the various energy components but also on their equations of state while the photons we see were in flight. Here, with some simplifying assumptions, we consider the constraints that recent supernova observations place on the properties of an energy component accelerating the cosmic expansion.

5.2 Observations

The type Ia supernovae (SN Ia) have been analyzed by the High-Z Supernova Search Team and described by Riess98, Garnavich et al. (1998), Schmidt et al. (1998), and Riess et al. (1998b). The full sample from Riess98 consists of 50 SN Ia. Of these, 34 are at $z < 0.2$ while the remaining 16 cover a range in redshift of $0.3 < z < 1.0$. Six

of the high-redshift events were analyzed using the "snapshot" method developed by Riess et al. (1998b). This innovative technique uses high-quality spectra to deduce information unavailable due to a poorly sampled light curve. While the errors estimated from the snapshot method are larger than those from direct light curve fitting, the snapshot sample provides a significant, independent set of SN Ia distances.

As shown by Phillips (1993), the light curve decline rate of SN Ia is correlated with the luminosity at maximum brightness of these exploding white dwarfs. This correlation has been calibrated by Hamuy et al. (1996, the $\Delta m_{15}(B)$ method) and by Riess, Press, & Kirshner (1995, 1996, the Multi-Color Light Curve Shape or MLCS method which includes a correction for extinction), and both show that applying this correction to the SN Ia Hubble diagram significantly reduces the scatter. Phillips et al. (1999) extended the $\Delta m_{15}(B)$ approach to include an estimate of the extinction. In Riess98, an improved version of the MLCS method is presented. Here, as in Riess98, we apply both MLCS and $\Delta m_{15}(B)$ (with extinction correction) techniques to the analysis to gauge the systematic errors introduced by different light curve fitting methods.

5.3 Analysis

The apparent brightness of a SN Ia corrected for light curve decline rate and extinction provides an estimate of the luminosity distance, D_L, from the K-corrected observed magnitude, $m = M + 5\log D_L + 25$, and the absolute magnitude, M, of SN Ia. As described by Schmidt et al. (1998) and Carroll, Press, & Turner (1992),

the luminosity distance depends on the content and geometry of the Universe in a Friedmann-Robertson-Walker cosmology

$$D_L = \frac{c(1+z)}{H_0\sqrt{|\Omega_k|}} sinn\left\{\sqrt{|\Omega_k|}\int_0^z [\sum_i \Omega_i(1+z')^{3(1+\alpha_i)} + \Omega_k(1+z')^2]^{-1/2} dz'\right\} \quad (5.1)$$

$$sinn(x) = \begin{cases} sinh(x), & \text{if } \Omega_k > 0; \\ x, & \text{if } \Omega_k = 0; \\ sin(x), & \text{if } \Omega_k < 0, \end{cases} \quad (5.2)$$

where Ω_i are the normalized densities of the various energy components of the Universe and $\Omega_k = 1 - \sum_i \Omega_i$ describes the effects of curvature. The exponent $n = 3(1+\alpha)$ defines the way each component density varies as the Universe expands, $\rho \propto a^{-n}$, where a is the cosmic scale factor. For example, n has the value 3 for normal matter since the mass density declines proportionally to the volume. Alternatively, α_i is the equation of state parameter for component i defined as the ratio of the pressure to the energy density, $\alpha_i = P_i/\rho_i$ (sometimes denoted in the literature as w). The relation $n = 3(1+\alpha)$ is derived from the conservation of energy equation in comoving coordinates (e.g. Weinberg (1972) equation 15.1.21). In the most general case, the equation of state can vary with time in ways other than assumed here (as the sum of power laws in $1+z$), but we are limited by the quality and range of the supernova observations to consider only its average effect between the present and $z < 1$. The present-day value of the Hubble constant (H_0) and the absolute magnitude of SN Ia (M) are primarily set by the low-redshift sample, which allows the high-redshift events to constrain the cosmological effects. This means that conclusions derived from SN Ia are independent of the absolute distance scale.

Gravitational lensing by matter distributed between the observer and supernovae

at high redshift can affect the observed brightness of SN Ia and induce errors in the estimate of their luminosity distances (Kantowski, Vaughan, & Branch 1995). For realistic models of the matter distribution and $\Omega_m < 0.5$, the most likely effect of the lensing is to make the supernovae at $z = 0.5$ about 2% fainter than they would appear if the matter were distributed uniformly (filled-beam) as shown by Wambsganss et al. (1997). Holz & Wald (1997) have shown that the magnitude of the effect also depends on whether the matter is distributed smoothly on galaxy scales or is clumped in MACHOS, but the error induced remains small when $\Omega_m < 0.5$. For simplicity, our calculations consider only the filled-beam case, however, the effect of assuming the extreme case of an empty-beam is shown by Holz (1998).

There are a few known, and possibly some unknown, energy components that affect D_L. Ordinary gravitating matter, Ω_m, certainly has had some effect on the Universal expansion between $z \approx 1$ and now. Since the matter density scales inversely with the volume, $\alpha_m = 0$, and matter (baryons, neutrinos, and dark matter; formerly Earth, Air, and Water) contributes no pressure. Radiation (Fire in an earlier lexicon) ($\alpha_r = +1/3$) dominated during a period in the early Universe but is negligible for $z < 1$. Equation 1 shows that for non-flat models the curvature term, Ω_k, contributes to the luminosity distance like a component with $\alpha_k = -1/3$, but additional geometrical effects as prescribed by equation 2 are also important.

Other more speculative components have been proposed. A non-zero vacuum energy, Ω_Λ, is a popular possibility explored by Riess98 for this data set. Because the vacuum energy density remains constant as the Universe expands (that is, $\rho_\Lambda \propto a^0$), we have $\alpha_\Lambda = -1$. Topological defects created in the early Universe could also leave remnants that might contribute to the energy now. Networks of cosmic strings may

be a natural consequence of phase transitions in the young Universe and if they did not intercommute would have an average effective $\alpha_s = -1/3$ (Vilenkin 1984; Spergel & Pen 1997). A network of comoving domain walls would have an average equation of state parameter of $-2/3$ (Vilenkin 1985) while a globally wound texture would produce an $\alpha_t = -1/3$ (Davis 1987; Kamionkowski & Toumbas 1996).

Evolving cosmic scalar fields with suitable potentials could produce a variety of exotic equations of state with significant densities at the present epoch (Peebles & Ratra 1988; Frieman et al. 1995; Frieman & Waga 1998). Scalar fields could also produce variable mass particles (VAMPS) which would redshift more slowly than ordinary matter creating an effective $\alpha_{\rm VAMP} < 0$ (Anderson & Carroll 1997). These fields may evolve over time and would produce an interesting variety of cosmic histories. Our goal is modest: we only hope to constrain the average α over the range where SN Ia are presently observed.

To simplify the analysis, we assume that only one component affects the cosmic expansion in addition to gravitating matter. Because the origin of the acceleration is unknown, we will refer to this as the "X" component with a density of Ω_x and equation of state of $P_x = \alpha_x \rho_x$. Caldwell, Dave, & Steinhardt (1998) have dubbed the unknown component "quintessence" as the other four essences have already been employed above. We assume that the Universe on very large scales is accurately described by general relativity and that the "X" component obeys the null energy condition (NEC). The NEC states that, for any null vector v^μ, the energy-momentum tensor satisfies $T_{\mu\nu} v^\mu v^\nu \geq 0$ (see, e.g., Wald 1984). This is the weakest of all conventional energy conditions, and should be satisfied by any classical source of energy and momentum including those discussed above. In a

Robertson-Walker metric, the NEC is equivalent to requiring $\rho_x + P_x \geq 0$. The NEC therefore restricts the energy density of the unknown component to be positive for $\alpha_x > -1$ and negative when $\alpha_x < -1$ while the energy density of the cosmological constant ($\alpha_x = -1$) is unconstrained.

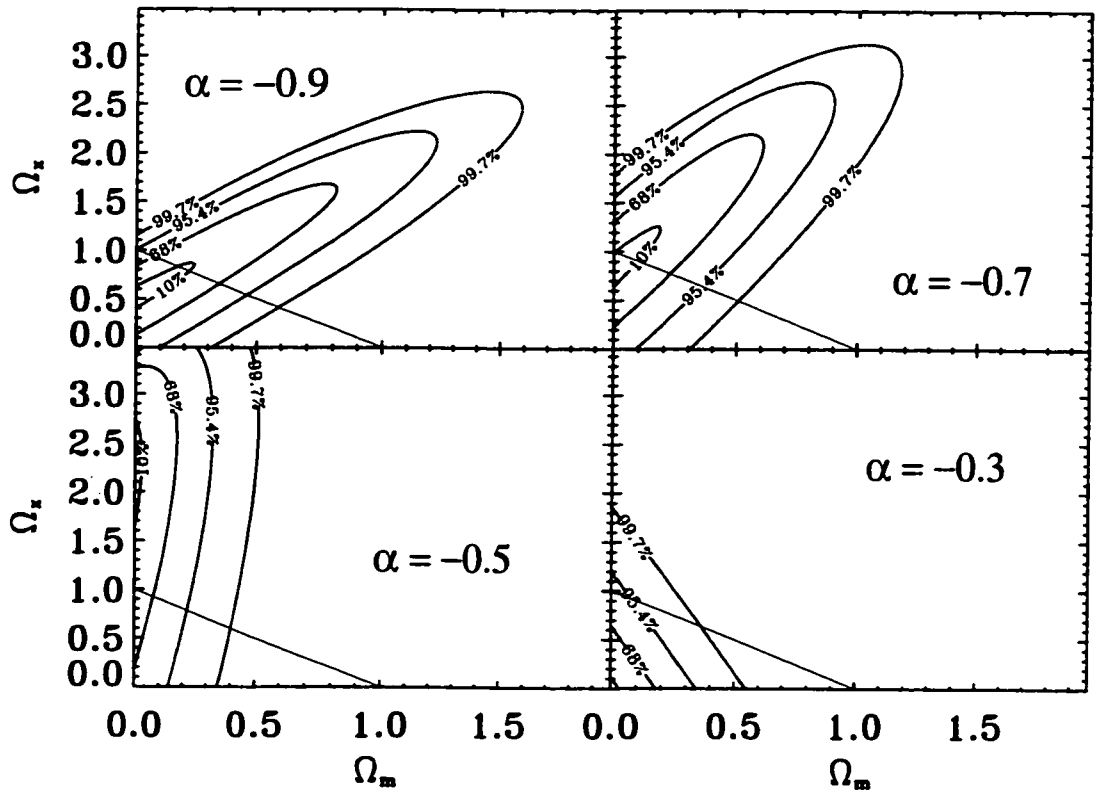

Figure 5.1.— The joint probability distributions for Ω_m and the density of the unknown component, Ω_x, based on the SN Ia magnitudes reduced with the MLCS method. Four representative values of the equation of state parameter, α_x, are shown. See Riess98 for the distribution when $\alpha_x = -1$.

5.4 Results

First, we fix the equation of state of the unknown component and estimate the probability density function for the parameters Ω_x, Ω_m, and H_0 given the observed SN Ia distance moduli. The joint likelihood distributions are then calculated in the same way as by Riess98 and shown for representative values of α_x in Figure 5.1. Here we integrate over all possible H_0 with the prior assumption that all values are equally likely. For $\alpha_x < -0.7$, the derived constraints are similar to those found by Riess98 for a cosmological constant ($\alpha_x = -1$). However, as the equation of state parameter increases, the major axis of the uncertainty ellipses rotates about a point on the $\Omega_x = 0$ line. For an accelerating Universe, the pivot point is on the negative Ω_m side. When $\alpha_x > -0.4$, the "X" component could not reproduce the observed acceleration and all of these models give a poor fit to the observed SN Ia data: the best fit occurs for a completely empty Universe.

Next, we allow the equation of state to vary freely but restrict the densities to $\Omega_m + \Omega_x < 1$, or open models. We then integrate over all possible values of Ω_x assuming a uniform prior distribution to provide the joint probability for α_x and the matter density. From the NEC we must include regions where $\alpha_x < -1$ and Ω_x is negative, but these are unable to produce an accelerating Universe so they have a very low probability. For open models, highest joint probabilities are confined to a region bounded by $-1.0 < \alpha_x < -0.4$ and $\Omega_m < 0.2$. If we consider any value of Ω_m equally likely, then $\alpha_x < -0.47$ for the MLCS method and $\alpha_x < -0.64$ for the $\Delta m_{15}(B)$ results with 95% confidence.

Finally, we consider flat models for the Universe. The joint probability between

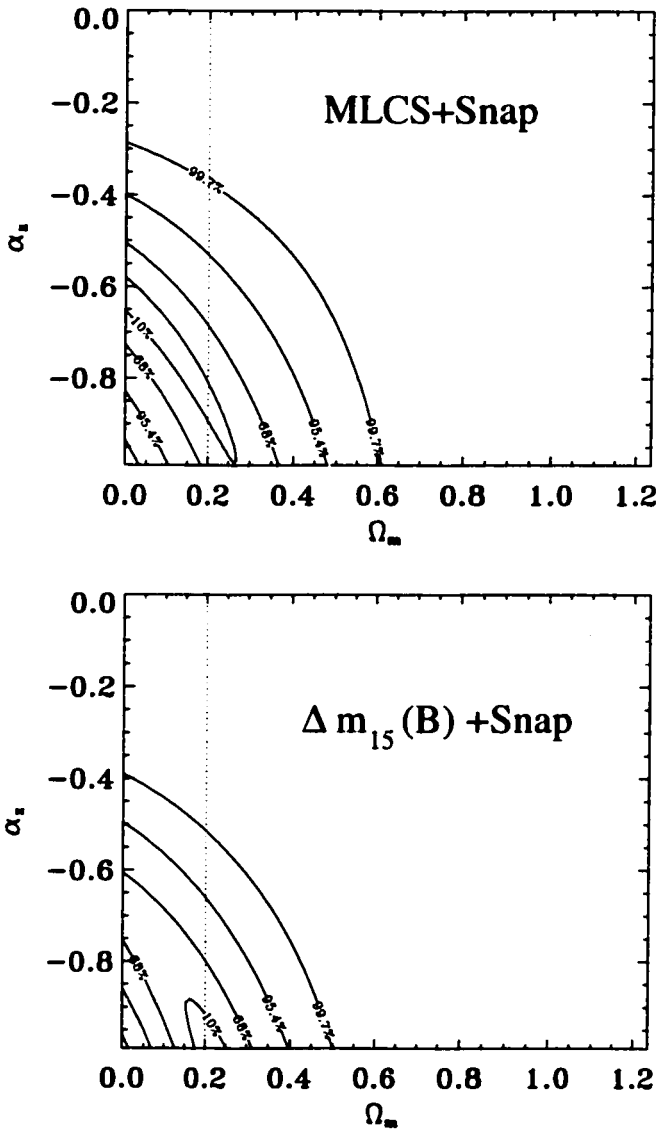

Figure 5.2.— The joint probability distributions from SN Ia for Ω_m and the equation of state parameter, α_x, assuming a flat spatial geometry ($\Omega_m + \Omega_x = 1$). The top panel uses supernova distances from the MLCS method combined with supernovae reduced using the snapshot method, while the bottom panel is from the $\Delta m_{15}(B)$ technique plus snapshot results. The vertical broken line marks the matter density estimated from galaxy cluster dynamics.

the equation of state parameter and the matter density for $\Omega_m + \Omega_x = 1$ is shown in Figure 5.2. The two cases are for the MLCS and the $\Delta m_{15}(B)$ light curve fits and demonstrate that the two methods for deriving luminosity from light curves provide consistent constraints. Note that in the flat case, the NEC allows $\alpha_x < -1$ only when $\Omega_m > 1$ which has an insignificant probability and is not plotted. These plots can be compared to pioneering calculations by Turner & White (1997) and White (1998) which used smaller supernova samples. The improved SN Ia data favor acceleration and support both a low Ω_m and a small value of α_x. Integrating the probability over all values of Ω_m assuming a uniform prior shows that $\alpha_x < -0.55$ for MLCS and $\alpha_x < -0.63$ for $\Delta m_{15}(B)$ (95% confidence). If we assume $\Omega_m > 0.1$ then the limits tighten to $\alpha_x < -0.60$ (MLCS) and $\alpha_x < -0.69$ ($\Delta m_{15}(B)$). For matter densities near ~ 0.2 favored by galaxy cluster dispersions, the most probable equation of state parameters are between -0.7 and -1.0. These results disfavor topological defect models such as domain walls (90% confidence) and eliminate strings and textures (99% level) as the principal component of the unknown energy. The cosmological constant, or a form of quintessence that resembles it for $z < 1$, is supported by the data. Constraints that refer to higher redshift are needed to narrow the range of possible models.

5.5 Other Constraints

High-Z SN Ia observations combined with the cosmic microwave background (CMB) anisotropy angular power spectrum provide complementary constraints on the densities of matter and the "X" component (White 1998; Tegmark et al. 1998).

Details of the CMB power spectrum depend on a large number of variables, but the angular scale of the first acoustic peak depends primarily on the physics of recombination and the angular diameter distance to the surface of last scattering (White & Scott 1996; White 1998). Rather than fit the power spectrum in detail, we have restricted our attention to the location of the first acoustic peak as estimated from current CMB experiments (Hancock et al. 1998). This is a rapidly moving experimental field, and new results will surely supersede these, but they illustrate the power of combining the supernova data with the CMB. We employ the analytic approximations of White (1998) to determine the wavenumber of the acoustic peak at recombination, and those of Hu & Sugiyama (1996) to determine the recombination redshift; thus we assume adiabatic fluctuations generate the anisotropy. In addition, we have ignored reionization and fixed the number of neutrino species at three, as well as assuming only scalar modes, with a spectral index $n = 1$. A thorough treatment of this problem would allow all of these parameters to vary and integrate the probability over all possible values (that is, marginalize over them); however, this would be very time-consuming, even with the fast CMB code of Seljak & Zaldarriaga (1996), and disproportionate to the precision of the current data. A large exploration of the parameter space involved (though lacking a full variation of Ω_Λ) can be found in Bartlett et al. (1998) and Lineweaver (1998).

Our calculation determines the angular scale multipole of the first acoustic peak for a grid in a three-dimensional parameter space of $(\Omega_M, \Omega_\Lambda, H_0)$, where we explicitly allow for open, flat, and closed universes with and without a cosmological constant. We also employ the additional constraint on the baryon density $\Omega_b h^2 = 0.024$ ($h = H_0/100\ \mathrm{km\,s^{-1}\,Mpc^{-1}}$) derived from the primordial deuterium abundance

and nucleosynthesis (Tytler, Fan, & Burles 1996). Other estimates of the baryon fraction (see Fugikita, Hogan, & Peebles 1998) could be used, but the location of the peak depends only weakly on this parameter. Where possible, we checked these calculations with numerical integrations (Seljak & Zaldarriaga 1996) and confirmed that the peak locations agree to $\lesssim 10\%$, which is adequate for this exploration.

Following White (1998), we combine the predicted peak location with the observations using a phenomenological model for the peak (Scott, Silk, & White 1995). Recent CMB measurements analyzed by Hancock et al. (1998) give the conditional likelihood of the first acoustic peak position as $l_{\rm peak} = 263^{+139}_{-94}$, based on best-fit values of the peak amplitude and low multipole normalization. Rocha et al. (1998) have provided us with a probability distribution function for the first peak position based on marginalizations over the amplitude and normalization which is a more general approach than by Hancock et al.. The Rocha et al. function gives $l_{\rm peak} = 284^{+191}_{-84}$ which is only a small shift from the value derived using the conditional likelihood method. We then marginalize the likelihood in our three-dimensional parameter space over H_0 with a Gaussian prior based on our own SN Ia result including our estimate of the systematic error from the Cepheid distance scale, $H_0 = 65 \pm 7\ {\rm km\,s^{-1}\,Mpc^{-1}}$ (Riess98). It is important to note that the SN Ia constraints on $(\Omega_{\rm m}, \Omega_\Lambda)$ are independent of the distance scale, but the CMB constraints are not. We then combine marginalized likelihood functions of the CMB and SNe Ia data. The result is shown in Figure 5.3. Again, we must caution that systematic errors in either the SN Ia data (Riess98) or the CMB could affect this result.

Nevertheless, it is heartening to see that the combined constraint favors a

location in this parameter space which has not been ruled out by other observations, though there may be mild conflict with constraints on Ω_Λ from gravitational lensing (Falco, Kochanek, & Muñoz 1998). In fact, the region selected by the SN Ia and CMB observations is in concordance with inflation, large-scale structure measurements, and the ages of stars (Ostriker & Steinhardt 1995; Krauss & Turner 1995). The combined constraint removes much of the high Ω_m, high Ω_Λ region which was not ruled out by the SN Ia data alone, as well as much of the high Ω_m, low Ω_Λ region allowed by the CMB data alone. The combined constraint is consistent with a flat universe, as $\Omega_{tot} = \Omega_m + \Omega_\Lambda = 0.94 \pm 0.26$ for MLCS and 1.00 ± 0.22 for $\Delta m_{15}(B)$ (1σ errors). The enormous redshift difference between the CMB and the SN Ia makes it dangerous to generalize this result beyond a cosmological constant model because of the possible time-dependence on α_x. But for an equation of state fixed after recombination, the combined constraints continue to be consistent with a flat geometry as long as $\alpha_x \lesssim -0.6$. With better estimates of the systematic errors in the SN Ia data and new measurements of the CMB anisotropy, these preliminary indications should quickly turn into very strong constraints (Tegmark et al. 1998).

5.6 Updated Constraints

With further results from both observations of high-redshift SN Ia and observations of the CMB anisotropy, we are in a position to update the combined constraints on cosmological parameters shown in Figure 5.3. We have combined the supernova results of Riess98 with those of Perlmutter et al. (1999) to produce a probability distribution function in the $(\Omega_m, \Omega_\Lambda)$ plane incorporating the data of both the

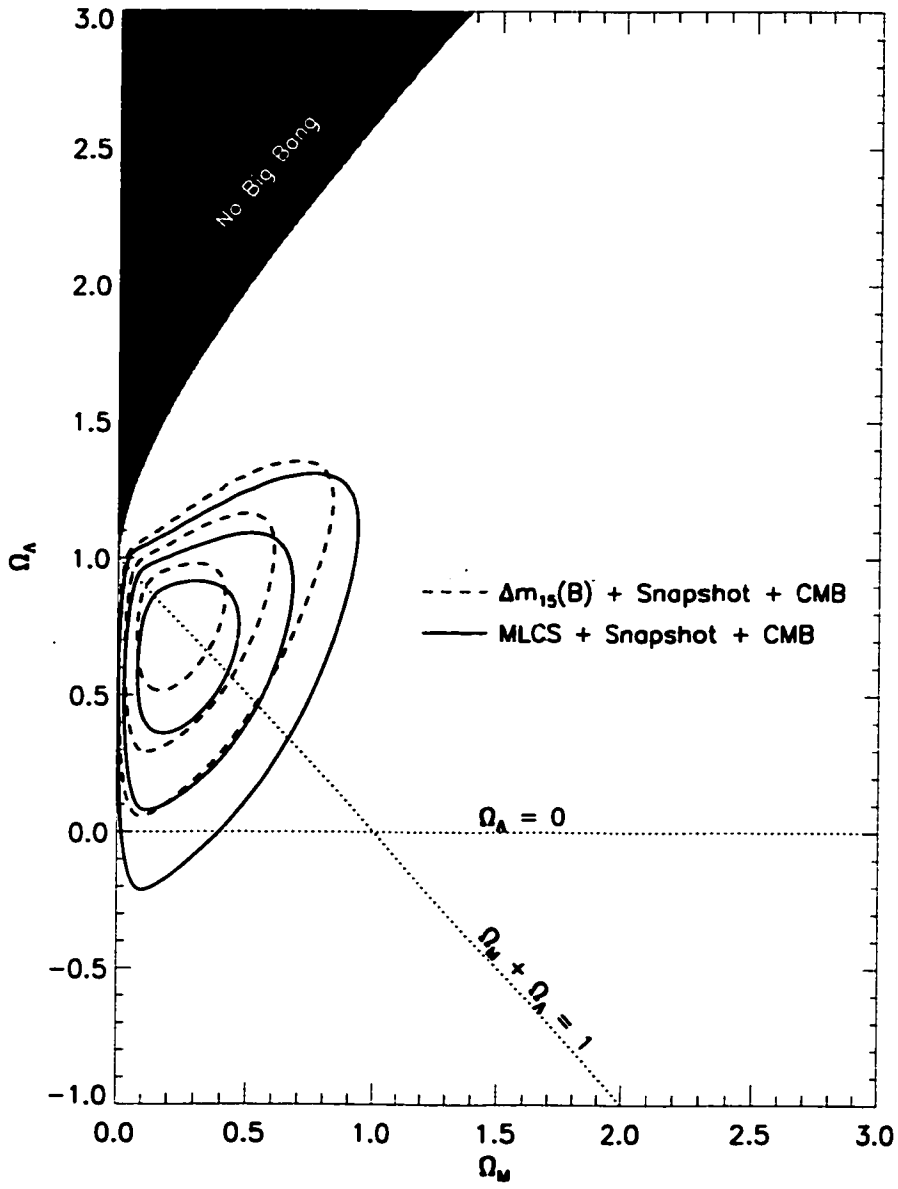

Figure 5.3.— The combined constraints from SN Ia and the position of the first Doppler peak of the CMB angular power spectrum. The equation of state parameter for the unknown component is $\alpha_x = -1$, like that for a cosmological constant. The contours mark the 68%, 95.4%, and 99.7% enclosed probability regions.

High-Z Supernova Search Team and the Supernova Cosmology Project. We have taken care to perform this combination using independent data; in particular, the low-redshift sample used by both groups have many objects in common, from the Calán/Tololo survey (Hamuy et al. 1996). Perlmutter et al. (1999) rely on a subset of the Calán/Tololo survey exclusively for their low-redshift sample, while Riess98 use additional objects from that survey as well as more recent SN Ia observed as part of the CfA monitoring campaign (Riess et al. 1999), making it possible to separate the low-redshift SN Ia into independent sets for comparison with the two groups' independent high-redshift SN Ia[1]. In addition to ensuring the SN Ia samples are independent, we integrate the probability density function from each sample individually over H_0, to allow for different normalizations in the light curve fitting techniques and combine the results in the two-dimensional $(\Omega_m, \Omega_\Lambda)$ plane. The constraints from the independent combination of the two groups' data are shown as the SN Ia contours in Figure 5.4, and represent the best constraints on cosmological parameters from high-redshift supernovae to date, based on published data. The combined likelihood function has been made available to other researchers and is used, e.g., by Balbi et al. (2000) and Lange et al. (2001).

Recent measurements of the CMB anisotropy have also improved considerably since the results presented in section 5.5. We have incorporated an updated likelihood distribution based on the results from the BOOMERANG-98 and MAXIMA-1 data sets (Jaffe et al. 2001). The 99.7% confidence region from the

[1]A few of the "snapshot" high-redshift SN Ia described in the Riess98 paper are part of the Perlmutter et al. 1999 high-redshift sample. These objects were excluded from the Riess98 sample in determining the combined constraints to ensure independence of the data sets.

CMB anisotropy measurements (employing "weak" priors on the Hubble constant, $45 \leq H_0 \leq 90\ \mathrm{km\,s^{-1}\,Mpc^{-1}}$, matter density, $\Omega_m \geq 0.1$, and age of the Universe, $t_0 \geq 10\mathrm{Gyr}$) is shown as the darker shaded region in Figure 5.4.

As before the constraints on Ω_m and Ω_Λ from the CMB and SN Ia measurements are nearly orthogonal, allowing us to zero in on the best-fit cosmology with significantly improved precision than either set of observations could provide alone. The dark solid contours in Figure 5.4 show the combined constraints, ruling out a flat, matter-dominated Universe ($\Omega_m = 1$, $\Omega_\Lambda = 0$) as well as an open, low matter-density Universe (e.g., $\Omega_m = 0.2$, $\Omega_\Lambda = 0$) at high statistical significance. The improved data precision also allows us to display the confidence contours "zoomed-in" compared to Figure 5.3; it is heartening that parameter space that we would have considered unreasonable a priori truly is excluded by the data. In the context of a Λ model, the data clearly favor a significant, and likely dominant, fraction of the energy density of the Universe in the cosmological constant. The results from measurements of high-redshift SN Ia and the CMB anisotropy also continue to be in good concordance with other estimates of the matter density, for instance, $\Omega_m \simeq 0.3$ measured via large-scale structure in the 2dF Galaxy Redshift Survey (Peacock et al. 2001), as well as the theoretical prediction of a flat Universe from inflation.

5.7 Conclusions

The current results from the High-Z Supernova Search Team suggest that there is an additional energy component sharing the Universe with gravitating matter. For

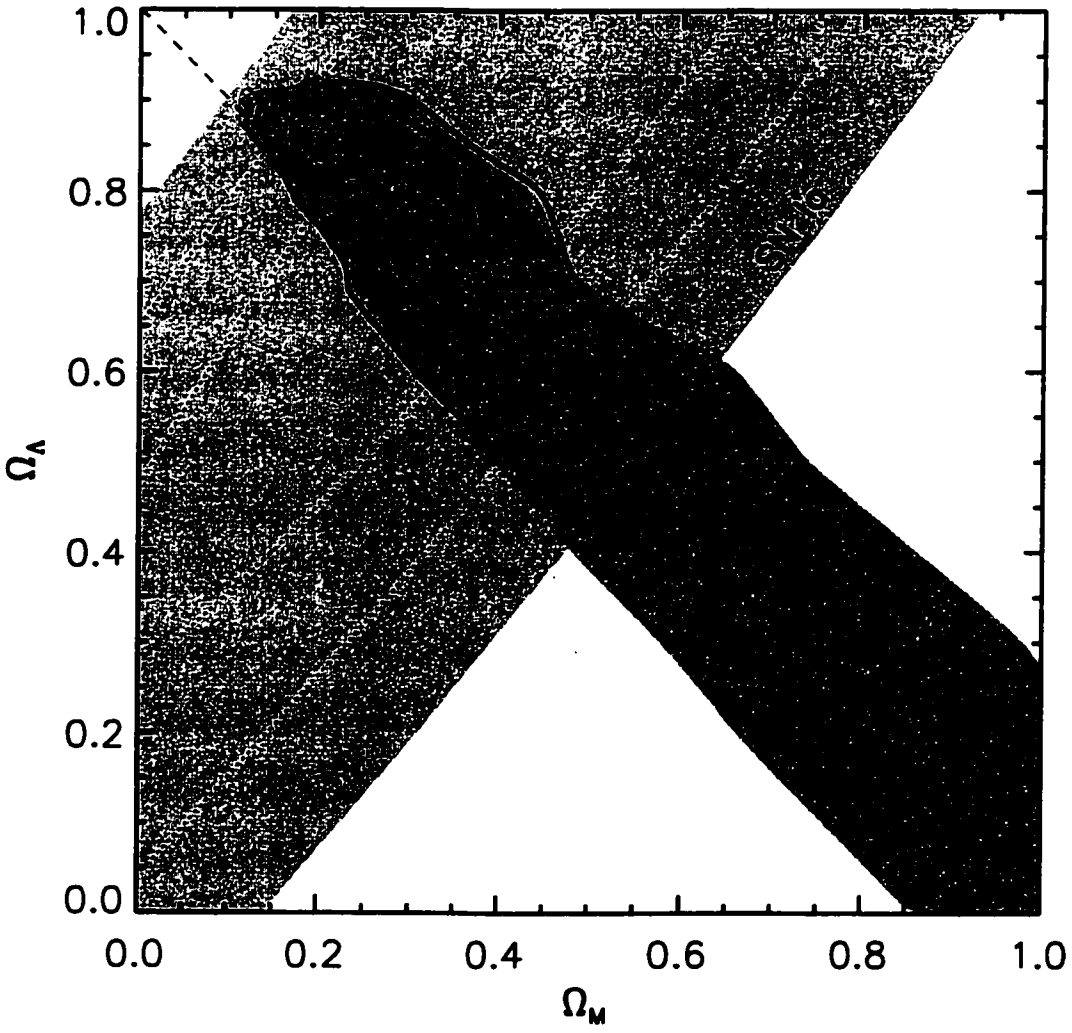

Figure 5.4.— Updated cosmological constraints from SN Ia and CMB data. The SN Ia shaded region marks the 99.7% confidence region from an independent combination of SN Ia data from the High-Z SN Search Team (Riess et al. 1998) and the Supernova Cosmology Project (Perlmutter et al. 1999). The 68.3% and 95.4% SN Ia confidence regions are also shown, with dotted lines. The shaded CMB region indicates the 99.7% confidence region from the latest CMB results (Jaffe et al. 2001). Combing the constraints results in the 68.3, 95.4 and 99.7% dark solid contours displayed.

a flat geometry, the ratio of the pressure of the unknown energy to its density is probably more negative than -0.6. This effectively rules out topological defects such as strings and textures as the additional component and disfavors domain walls as that component. Open models are less constrained, but favor $\alpha_x < -0.5$. Although there are many intriguing candidates for the "X" component, the current SN Ia observations imply that a vacuum energy or a scalar field that resembles the cosmological constant is the most likely culprit.

Combining the SN Ia probability distribution with constraints from the position of the first acoustic peak in the CMB power spectrum provides a simultaneous observational measurement of the densities of matter and of the unknown component. Using CMB data from Hancock et al. (1998) and following the analysis by White (1998) the result favors a flat Universe, with $\Omega_{tot} = 0.94 \pm 0.26$, dominated by the "X" component for $\alpha_x \approx -1$. Incorporation of independent SN Ia results from Perlmutter et al. (1999) and new CMB results from Jaffe et al. (2001) sharpens these constraints and bolsters the emerging new "standard" cosmological model, with dark energy dominating the Universe today.

We thank U. Seljak and M. Tegmark for some informative discussions and G. Rocha for making the CMB likelihood function available before publication. We also thank A. Jaffe for providing the updated CMB likelihood used in Figure 5.4. This work was supported by grant GO-7505 from the Space Telescope Science Institute, which is operated by the Association of Universities for Research in Astronomy, Inc., under NASA contract NAS5-26555, and at Harvard University through NSF grants AST 92-21648 and AST 95-28899 and an NSF Graduate Research Fellowship. Work

at the University of Washington was supported through NSF grant AST-9617036. A.V.F acknowledges the support of NSF grant AST-9417213. S.M.C. was supported by NSF grant PHY/94-07194.

5.8 References

Anderson, G.W., & Carroll, S.M. 1997, astro-ph/9711288

Bahcall, N.A., Fan, X., & Cen, R. 1997, ApJ, 485, 53

Balbi, A., et al. 2000, ApJ, 545, L1

Bartlett, J. G., Blanchard, A., Le Dour, M., Douspis, M., & Barbosa, D. 1998, to appear in "Fundamental Parameters in Cosmology", proceedings of the Rencontres de Moriond 1998, astro-ph/9804158

Caldwell, R.R., Dave, R., & Steinhardt, P.J. 1998, Phys. Rev. Lett., 80, 1582

Carlberg, R.G., Yee, K.C., Ellingson, E., Abraham, R., Gravel, P., Morris, S., & Pritchet, C.J., 1996, ApJ, 462, 32

Carroll, S.M., Press, W.H., & Turner, E.L. 1992, ARAA, 30, 499

Coles, P., & Ellis, G. 1997, "Is the Universe Open or Closed", Cambridge: Cambridge Univ. Press

Davis, R.L. 1987, Phys. Rev. D, 35, 3705

Falco, E.E., Kochanek, C.S., & Muñoz, J.A. 1998, ApJ, 494, 47

Frieman, J.A., & Waga, I. 1998, Phys. Rev. D, 57, 4642

Frieman, J.A., Hill, C.T., Stebbins, A., & Waga, I. 1995, Phys. Rev. Lett., 75, 2077

Fukugita, M., Hogan, C.J., & Peebles, P.J.E. 1998, ApJ, 503, 518

Garnavich, P.M., et al. 1998, ApJ, 493, L53

Gott, J.R., Gunn, J.E., Schramm, D.N., & Tinsley, B.M. 1974, ApJ, 194, 543

Hamuy, M., Phillips, M.M., Maza, J., Suntzeff, N.B., Schommer, R.A., Maza, J., Smith, R.C., Lira, P., & Avilés, R. 1996, AJ, 112, 2438

Hancock, S., Rocha, G., Lasenby, A. N., & Gutiérrez, C. M. 1998, MNRAS, 294, L1

Höflich, P., Wheeler, J.C., & Thielemann, F.K. 1998, ApJ, 495, 617

Holz, D.E., & Wald, R. 1998, Phys. Rev. D, 58, 063501

Holz, D.E. 1998, ApJ, 506, L1

Hu, W., & Sugiyama, N. 1996, ApJ, 471, 542

Jaffe, A. H., et al. 2001, Phys. Rev. Lett., 86, 3475

Kamionkowski, M., & Toumbas, N. 1996, Phys Rev Lett, 77, 587

Kim, A. 1998, in "Fundamental Parameters in Cosmology," proceedings of the XXXIIIrd Rencontres de Moriond (astro-ph/9805196)

Kantowski, R., Vaughan, T., & Branch, D. 1995, ApJ, 447, 35

Krauss, L.M., & Turner, M.S. 1995, Gen. Rel. Grav., 27, 1137

Lange, A. E., et al. 2001, Phys. Rev. D., 63, 042001

Lin, H., et al. 1996, ApJ, 471, 617

Lineweaver, C.H. 1998, ApJ, 505, L69

Ostriker, J.P., & Steinhardt, P.J. 1995, Nature, 377, 600

Peacock, J. A., et al. 2001, Nature, 410, 169

Peebles, P.J.E. 1984, ApJ, 284, 439

Peebles, P.J.E., & Ratra, B. 1988, ApJ, 325, L17

Perlmutter, S., et al. 1998, Nature, 391, 51

Perlmutter, S., et al. 1999, ApJ, 517, 565

Phillips, M.M. 1993, ApJ, 413, L105

Phillips, M.M., Lira, P., Suntzeff, N.B., Schommer, R.A., Hamuy, M., & Maza, J. 1999, AJ, 118, 1766

Riess, A.G., et al. 1998a, AJ, 116, 1009 [Riess98]

Riess, A.G., Nugent, P.E., Filippenko, A.V., Kirshner, R.P., & Perlmutter, S. 1998b, ApJ, 504, 935

Riess, A.G., et al. 1999, AJ, 117, 707

Riess, A.G., Press, W.H., & Kirshner, R.P. 1995, ApJ, 438, L17

Riess, A.G., Press, W.H., & Kirshner, R.P. 1996, ApJ, 473, 88

Rocha, G., Hancock, S., Lasenby, A. N., & Gutiérrez, C. M. 1998, in preparation

Schmidt, B.P., et al. 1998, ApJ, 507, 46

Scott, D., Silk, J., & White, M. 1995, Science, 268, 829

Seljak, U., & Zaldarriaga, M. 1996, ApJ, 469, 437

Spergel, D., & Pen U. 1997, ApJ, 491, L67

Tegmark, M., Eisenstein, D. J., Hu, W., & Kron, R.G. 1998, ApJ, submitted (astro-ph/9805117)

Turner, M.S., Steigman, G., & Krauss, L.M. 1984, Phys. Rev. Lett., 84, 2090

Turner, M.S., & White, M. 1997, Phys Rev D, 56, 4439

Tytler, D., Fan, X.-M., & Burles, S. 1996, Nature, 381, 207

Vilenkin, A. 1984, Phys. Rev. Lett., 53, 1016

Vilenkin, A. 1985, Phys. Rep., 121, 263

Wald, R.M. 1984, "General Relativity", Chicago: University of Chicago Press

Wambsganss, J., Cen, R., Guohong, X., & Ostriker, J. 1997, ApJ, 475, L81

Weinberg, S. 1972, "Gravitation and Cosmology", New York: John Wiley & Sons

Weinberg, S. 1989, Rev. Mod. Phys, 61, 1

White, M. 1998, ApJ, 506, 495

White, M., & Scott, D. 1996, ApJ, 459, 415

Chapter 6

The Redshift of the Optical Transient Associated with GRB 010222

Saurabh Jha, Michael A. Pahre, Peter M. Garnavich, Michael L. Calkins, Roy E. Kilgard, Thomas Matheson, Jonathan C. McDowell, John B. Roll, and Krzysztof Z. Stanek 2001, *The Astrophysical Journal*, **554**, L155

Abstract

The gamma-ray burst (GRB) 010222 is the brightest GRB detected to date by the BeppoSAX satellite. Prompt identification of the associated optical transient (OT) allowed for spectroscopy with the Tillinghast 1.5 m telescope at F. L. Whipple Observatory while the source was still relatively bright ($R \simeq 18.6$ mag), within

five hours of the burst. The OT shows a blue continuum with many superimposed absorption features corresponding to metal lines at $z = 1.477$, 1.157, and possibly also at 0.928. The redshift of GRB 010222 is therefore unambiguously placed at $z \geq 1.477$. The high number of Mg II absorbers and especially the large equivalent widths of the Mg II, Mg I, and Fe II absorption lines in the $z = 1.477$ system further argue either for a very small impact parameter or that the $z = 1.477$ system is the GRB host galaxy itself. The spectral index of the OT is relatively steep, $F_\nu \propto \nu^{-0.89\pm0.03}$, and this cannot be caused by dust with a standard Galactic extinction law in the $z = 1.477$ absorption system. This spectroscopic identification of the redshift of GRB 010222 shows that prompt and well-coordinated followup of bright GRBs can be successful even with telescopes of modest aperture.

6.1 Introduction

Since the discovery of gamma-ray bursts (GRBs; Klebesadel, Strong, & Olson 1973), their nature has proved enigmatic. The CGRO and BATSE observations demonstrated they were isotropically distributed on the sky (Meegan et al. 1992), which could either have been explained by Galactic (Lamb 1995) or cosmological (Paczyński 1995) spatial distributions. The BeppoSAX satellite (Boella et al. 1997) contributed the breakthrough in this field by providing rapid localizations of the X-ray afterglow of a GRB to a precision of several arcminutes. Such precision allowed for rapid optical (van Paradijs et al. 1997) and radio (Frail et al. 1997) identifications of transients associated with individual GRBs. The identification of the optical transient (OT) associated with GRB 970508 (Bond 1997; Djorgovski et

al. 1997) led to the first optical spectroscopic redshift determination for a GRB, placing it at $z \geq 0.835$ (Metzger et al. 1997), and thus firmly at a cosmological distance.

Despite such rapid progress and intensive followup campaigns at many wavelengths, only some GRBs have had associated X-ray, optical or radio afterglows, and all of these events have been among the "long-duration" GRB population (Kulkarni et al. 2000). Of these, only $\sim$15 have had unambiguous spectroscopic redshift identification (see those to date tabulated by Bloom, Kulkarni & Djorgovski 2002). The primary difficulty is the combined delays imposed by the time necessary to improve the X-ray localizations, interruption of a telescope observing program to obtain optical imaging data, reduction and analysis of those data relative to POSS images to identify the OT, and interruption of another telescope observing program to obtain a spectrum (usually on a different telescope, since there are very few combined imaging and spectrograph instruments). By the time a spectrum is taken, the OT has usually faded significantly, generally limiting such followup observations to only the largest available ground-based optical telescopes or the Hubble Space Telescope. Furthermore, observational conditions may not be optimal immediately after a GRB event, such that only approximately half of the known GRB redshifts were obtained with spectroscopy of the OT itself—the others were obtained at later times from the presumptive host galaxy, after the OT had faded.

Here we report the rapid identification of an OT associated with GRB 010222, and the spectroscopy of the source within five hours after the GRB occured. The quick localization of the X-ray and optical transients allowed for spectroscopic observations on a modest 1.5 m telescope, the smallest aperture telescope to measure

the redshift of a GRB to date.

6.2 Data

GRB 010222 was detected by the Gamma-Ray Burst Monitor and Wide Field Camera 1 instruments on board BeppoSAX at 07:23:30 UT on 2001 February 22 (Piro 2001). An optical transient (OT) associated with GRB 010222 was reported within several hours by Henden (2001a). McDowell et al. (2001) provided independent confirmation of the OT from images taken with the F. L. Whipple Observatory (FLWO) 1.2 m telescope and 4Shooter CCD mosaic camera (Szentgyorgyi et al. 2002). The identification of the OT ($\alpha = 14^{h}52^{m}12\overset{s}{.}54$, $\delta = +43°01'06\overset{''}{.}2$, J2000.0) on these latter discovery images is shown in Figure 6.1.

A spectrum of the OT was obtained with the FLWO 1.5 m Tillinghast telescope beginning at UT 2001 February 22 12:18, 4.92 hours after the burst. The OT apparent magnitude was $R \simeq 18.6$ mag around the time of the spectroscopy (McDowell et al. 2001; Henden 2001b). Despite the faintness of the OT, it was visible on the telescope acquisition camera, such that it could unambiguously identified and placed on the spectrograph slit. The observations were made with the FAST spectrograph (Fabricant et al. 1998) using a 3 arcsec wide slit and 300 l/mm grating, yielding 6 Å FWHM resolution over the range $3720 < \lambda < 7540$ Å. Two 1200s exposures were taken with the slit rotated to the parallactic angle (and moreover the airmass was $\leq$1.04), reduced in the standard manner with an optimal extraction (Horne 1986), and combined. Wavelength calibration was provided via HeNeAr lamp spectra taken immediately after the OT exposures, with minor adjustment based

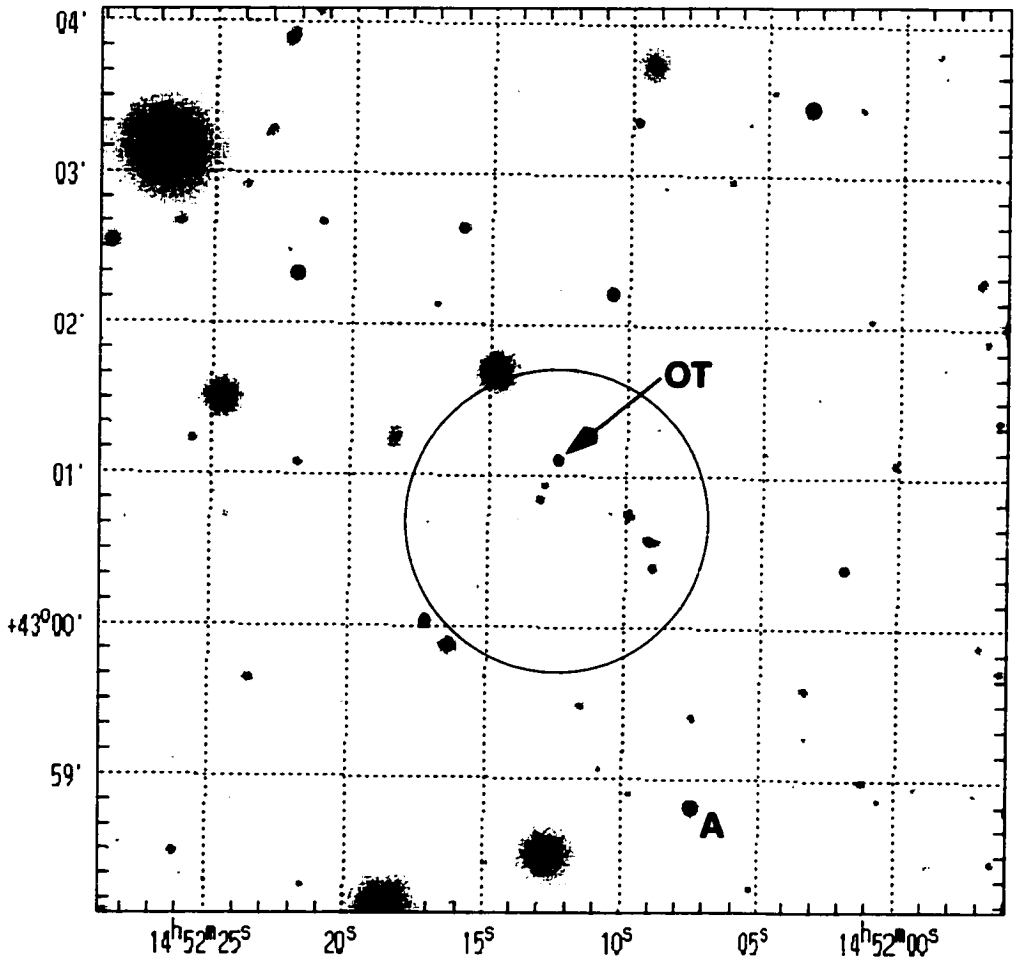

Figure 6.1.— Identification of the optical transient associated with GRB 010222. This 600s R_C-band image, taken with the F. L. Whipple Observatory 1.2-m telescope (+ 4Shooter) beginning at UT 2001 February 22 12:12, shows the optical transient (OT) and comparison star A of McDowell et al. (2001). The image covers 6 arcmin on a side, with north up and east to the left. The position error circle from the BeppoSAX followup of the X-ray afterglow (Gandolfi 2001) is also shown.

on night sky lines in the OT frames. We corrected for telluric lines (Wade & Horne 1988) and flux-calibrated the spectra with exposures of the spectrophotometric standard star Hiltner 600 (Stone 1977), also taken at the parallactic angle, yielding relative fluxes in our OT spectrum accurate to ~5% over the observed wavelength range. The discovery spectrum is shown in Figure 6.2, and preliminary results from it have been reported previously (Garnavich et al. 2001; Jha et al. 2001). Four additional spectra of 1800 s each were obtained the following night (UT 2001 February 23) when the OT had faded by ~1.5 to 2 mag (Stanek et al. 2001). The dispersed spectrum was at the detection threshold of the spectrograph, hence no reliable results could be obtained from these data.

6.3 Results

The optical spectrum of GRB 010222 in Figure 6.2 shows a blue continuum that is typical for GRBs. Superimposed upon this continuum are a number of strong and weak absorption line systems at $z = 1.157$ and 1.477, which are identified by the metallic lines of Mg I, Mg II, Fe II, Mn II, Si II, Al II, Zn II, Cr II, and C IV. Two additional lines are tentatively identified with Mg II at $z = 0.928$ because these lines are weaker and no other lines are found at a similar redshift (although the S/N is worse at these shorter wavelengths). All three systems were independently detected by Bloom et al. (2001) and confirmed by Castro et al. (2001) from spectroscopy at the Keck Observatory. Our line identifications are summarized in Table 6.1; as is typical for metal-line absorption systems, the Mg II lines are the strongest in the spectrum, nearly reaching zero flux for the highest redshift system even at this

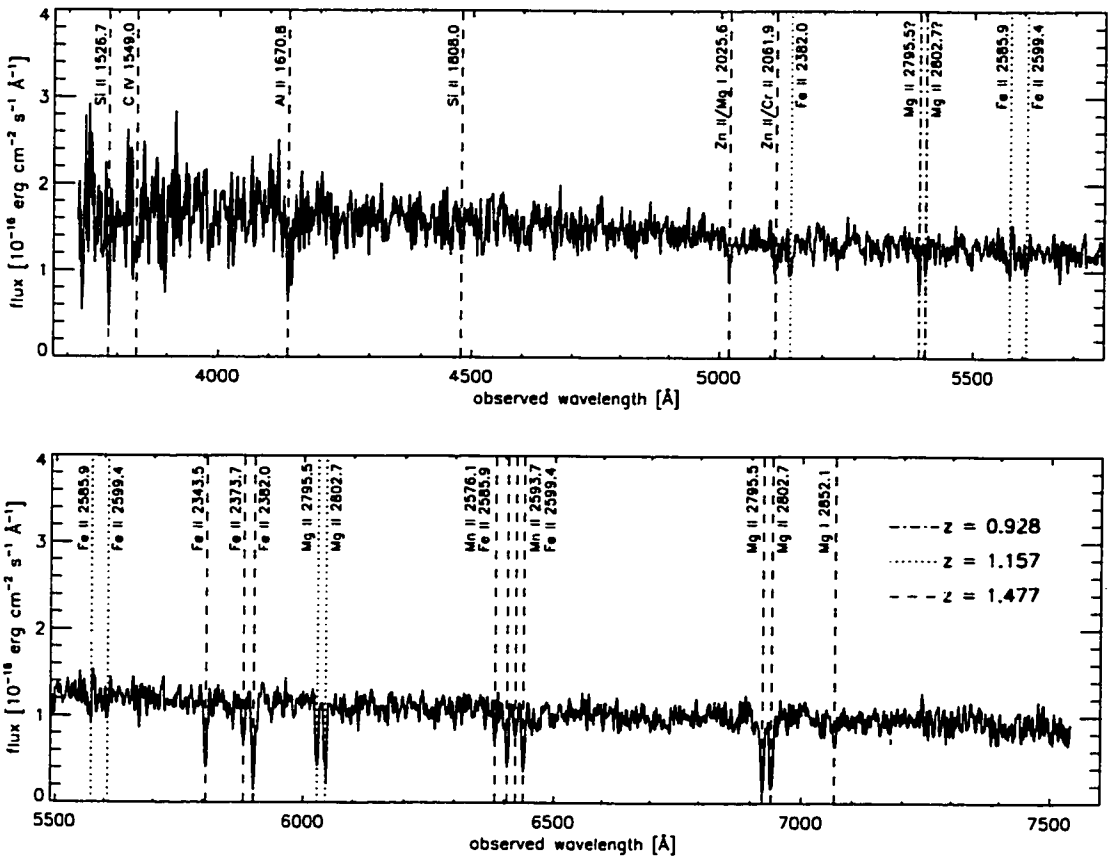

Figure 6.2.— Discovery spectrum of the optical transient associated with GRB 010222 taken with the F. L. Whipple Observatory 1.5-m telescope (+ FAST spectrograph) on UT 2001 February 22, approximately 5 hours after the GRB. The OT has a blue continuum spectrum with two absorption systems at $z = 1.157$ (dotted vertical lines) and 1.477 (dashed vertical lines). Various redshifted metal absorption features are labelled. Two absorption lines at $\lambda = 5389.1$ and 5402.2 Å (dash/dotted vertical lines) may be due to an additional Mg II system at $z = 0.928$. The redshift of GRB 010222 is therefore constrained to lie at $z \geq 1.477$. If the highest-redshift absorption lines correspond to the host galaxy of the OT, then the redshift of GRB 010222 is $z = 1.477$.

relatively low spectral resolution.

The redshift of GRB 010222 is therefore unambiguously $z \geq 1.477$, corresponding to the most distant absorber. Furthermore, the non-detection of Lyα forest absorption or continuum decrement at $\lambda > 4000$ Å would suggest the GRB host is at $z < 2.3$, though this is not a firm constraint given the S/N ratio of the data. If the highest-redshift lines are from the GRB host itself, then the GRB is at $z = 1.477$. Several other GRB OTs have shown absorption line systems which have been argued to arise from the ISM of the GRB host galaxy: GRB 090508 (Metzger et al. 1997), GRB 980703 (Djorgovski et al. 1998), GRB 990123 (Kulkarni et al. 1999), GRB 990510 and GRB 990712 (Vreeswijk et al. 2001), and GRB 991216 (Vreeswijk et al. 1999).

While Mg II absorption systems are commonly found along the line-of-sight to distant QSOs, the three detected at $3800 < \lambda < 7500$ Å—corresponding to a redshift interval of $0.36 < z < 1.68$, or $\Delta z = 1.32$—is significantly larger than the mean of $\langle N/z \rangle = 0.97$ (Steidel & Sargent 1992). Moreover, that value was derived based on systems with a Mg II λ2796 Å rest-frame equivalent width $W_0(\lambda 2796) \geq 0.3$ Å, measured with generally similar spectral resolution as the observations presented here. Though our detection threshhold for this line is difficult to determine a priori, it is likely at least 0.6 Å, and Steidel & Sargent (1992) find an average of $\langle N/z \rangle = 0.52$ for systems with such strong absorption ($W_0(\lambda 2796) \geq 0.6$ Å). Thus, there is quite a discrepancy between the expectation of $\sim$0.7 systems over the observed wavelength region compared to the 3 systems actually detected. This discrepancy would be mitigated if the $z = 1.477$ system were the host galaxy of the GRB.

Table 6.1. Absorption Line Identifications in the Spectrum of GRB 010222.

Observed Wavelength [Å]	Line Identification	Rest Wavelength [Å]	Rest-frame Equivalent Width [Å]	Redshift
7065.4	Mg I	2852.1	0.9 ± 0.2	1.477
6941.7	Mg II	2802.7	2.7 ± 0.2	1.477
6924.0	Mg II	2795.5	3.0 ± 0.2	1.477
6438.5	Fe II	2599.4	1.9 ± 0.2	1.477
6422.4	Mn II	2593.7	0.7 ± 0.2	1.476
6405.4	Fe II	2585.9	1.5 ± 0.2	1.477
6381.2	Mn II	2576.1	0.7 ± 0.2	1.477
5900.1	Fe II	2382.0	2.4 ± 0.2	1.477
5879.6	Fe II	2373.7	1.2 ± 0.2	1.477
5805.4	Fe II	2343.5	1.8 ± 0.2	1.477
5108.5	Zn II/Cr II blend	2061.9	0.7 ± 0.3	1.478
5018.5	Zn II/Mg I blend	2025.6	1.0 ± 0.3	1.478
4478.9	Si II	1808.0	0.5 ± 0.3	1.477
4137.8	Al II	1670.8	1.1 ± 0.3	1.477
3838.0	C IV blend	1549.0	1.9 ± 0.4	1.478
3781.8	Si II	1526.7	1.4 ± 0.4	1.477
6045.0	Mg II	2802.7	2.1 ± 0.2	1.157
6028.2	Mg II	2795.5	1.9 ± 0.2	1.156
5606.7	Fe II	2599.4	0.5 ± 0.3	1.157
5574.1	Fe II	2585.9	0.6 ± 0.3	1.156
5137.2	Fe II	2382.0	1.2 ± 0.3	1.157
5402.2	Mg II?	2802.7	0.6 ± 0.3	0.927
5389.1	Mg II?	2795.5	0.9 ± 0.3	0.928

In addition, $z = 1.477$ system has an unusually large rest-frame equivalent width of the Mg II λ 2796 Å line of $W_0(\lambda 2796) = 3.0 \pm 0.2$ Å, which is larger than all 111 systems found by Steidel & Sargent (1992). The $z = 1.157$ system equivalent width places it in the top 10%, while the $z = 0.928$ system is more typical. The Mg II doublet ratios $W_0(\lambda 2796)/W_0(\lambda 2803)$ are 1.1 ± 0.3, 0.9 ± 0.3, and 1.5 ± 0.4) for systems with redshifts of 1.477, 1.157, and 0.928, respectively; these values are typical of the anticorrelation between $W(\lambda 2796)$ and the doublet ratio, indicating the lines are strongly saturated (Steidel & Sargent 1992). The Fe II and Mg I equivalent widths for the $z = 1.477$ system are likewise unusually strong (Churchill et al. 2000). Since these absorption line strengths for the $z = 1.477$ are so large, either the impact parameter is extremely small or this system represents the OT host galaxy. Nearly all of the absorption line systems in GRB OTs show substantially weaker lines than the $z = 1.477$ system (the host of GRB 990712 is the lone exception, with an equivalent width of $W_0(\lambda 2796) + W_0(\lambda 2803) = 9$ Å; Vreeswijk et al. 2001) further strengthening the case that the high-redshift system is the OT host.

To make these arguments more quantitative, we calculate the Bayesian odds ratio for the following two hypotheses (assumed to be equally likely a priori): H_1, that the OT is at redshift $z > 1.477$ with three foreground absorption systems, and H_2, that the OT is at redshift $z = 1.477$ with two foreground absorption systems. For H_1, the redshift path-length for detection of absorption systems is our full spectral window,[1] $\Delta z = 1.32$, implying, as above, an expectation of $\bar{N} = 0.52 \times 1.32 = 0.69$

[1]Actually, this leads to a very slight overestimate of the likelihood of H_1, because the spectral window for detecting foreground Mg II is less than our observed wavelength range if the OT redshift is $z \leq 1.7$. This only strengthens the argument presented.

absorption systems, assuming a detection threshold of $W_0 \geq 0.6$ Å (Steidel & Sargent 1992). For H_2, the redshift path has an upper bound at $z = 1.477$, yielding $\Delta z = 1.12$ and $\bar{N} = 0.52 \times 1.12 = 0.58$. The observed number of systems follows a simple Poisson distribution, and so the Bayesian odds $p(H_2)/p(H_1)$ are given by $[P(N = 2; \bar{N} = 0.58)/P(N = 3; \bar{N} = 0.69)] = 3.4$, indicating that H_2 is more than three times as likely as H_1 under the given assumptions. In addition to the *number* of observed absorption systems, we can also take into account their *strength*, by adopting the Mg II λ2796 equivalent width distribution function of Steidel & Sargent (1992), $n(W_0)dW_0 \propto \exp(-W_0/W_0^*)dW_0$ with $W_0^* = 0.66$ Å (a good fit to the data for $W_0 \geq 0.6$ Å, our detection threshhold[2]). Because of the rarity of absorption systems as strong as the one detected at $z = 1.477$, incorporating the line strengths into the calculation increases the Bayesian odds favoring H_2 over H_1 to 28:1. Thus, there is strong support for the identification of the $z = 1.477$ system as the host of GRB 010222.

Beyond the absorption systems along the line of sight, we also use the observed spectrum to measure the spectral power-law index of the OT. The continuum flux is overwhelmingly dominated by the OT, so contamination from an underlying host or other objects on the slit is negligible. After correcting for Galactic extinction, $E(B-V) = 0.023$ mag (Schlegel, Finkbeiner, & Davis 1998), adopting a standard $R_V = 3.1$ extinction law (Cardelli, Clayton, & Mathis 1989), we bin the spectrum

[2]Steidel & Sargent (1992) note that for the strongest absorbers, $n(W_0)$ seems to change with redshift, whereas we have assumed it to be fixed over the redshift range $0.35 \leq z \leq 1.7$. However, we do not expect significant changes in the results taking this evolution into account, because the mean redshift of the absorber population that Steidel & Sargent (1992) used to derive $n(W_0)$, $\langle z_{\rm abs} \rangle = 1.17$, well matches our observable redshift range.

into ten segments (excluding the absorption lines), using the rms deviation in each bin as an estimate of the uncertainty, as shown in Figure 6.3. We have adjusted the normalization to match the concurrent photometry (Stanek et al. 2001). A least squares minimization yields a power law index $\beta = 0.89 \pm 0.03$ (where $F_\nu \propto \nu^{-\beta}$). As mentioned above, additional uncertainty due to the relative flux calibration is likely to be small. The spectral slope is rather steep in comparison to early observations of other bright GRB afterglows. For example GRB 990510 had a $\beta \simeq 0.5$ less than one day after the burst (Stanek et al. 1999) and GRB 991216 had $\beta \simeq 0.6$ after a correction for large Galactic extinction (Garnavich et al. 2000). On the other hand, GRB 000926 exhibited a very steep spectral slope with an index of 1.5 which was attributed to significant dust extinction along the line of sight (Price et al. 2001).

The steep spectral slope for GRB 010222 may also indicate significant extinction from dust in the host galaxy. Furthermore, jet models by Sari, Piran, & Halpern (1999) predict a shallower spectral index than we observe given the reported light curve decline rates (for details, see Stanek et al. 2001), also suggesting significant extinction. However, as shown in Figure 6.3, the spectrum exhibits no clear evidence for the $\lambda 2175$ Å "bump", typical of Galactic interstellar dust (Cardelli et al. 1989), which falls in the observed spectral region for $z = 1.477$. Such a feature would be easily detectable even at levels $A_V \simeq 0.1$ mag. Thus we conclude that there is no significant extinction from Galactic-type dust in the $z = 1.477$ absorption system. However, substantial extinction from dust with an extinction law like that found in the SMC could still account for the steep spectral slope, as such dust does not show a significant $\lambda 2175$ Å feature (Prévot et al. 1984). An SMC-like extinction curve may be a more natural choice if GRBs come from young stellar environments,

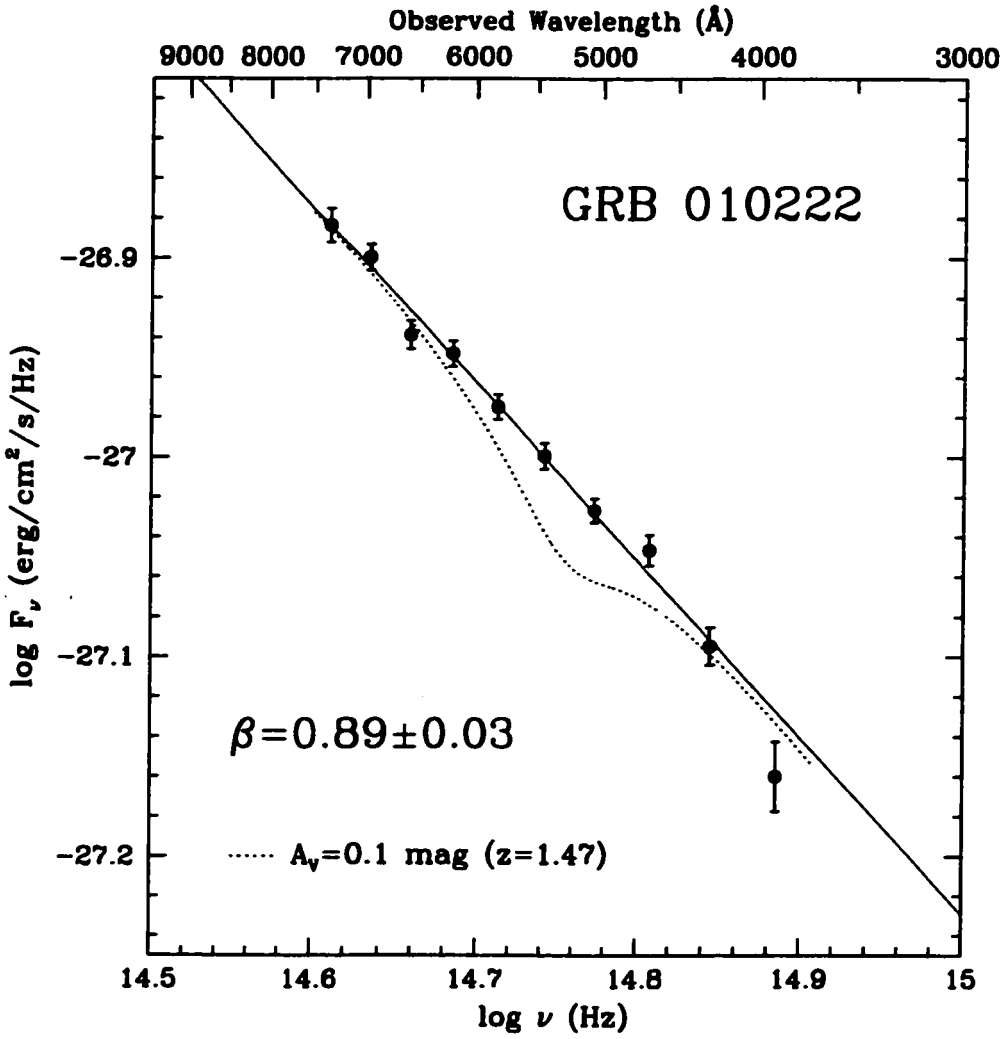

Figure 6.3.— Continuum flux of the OT associated with GRB 010222 based on the FLWO 1.5 m spectrum. The observed flux has been corrected to match the FLWO 1.2 m photometry from the same epoch (Stanek et al. 2001). The solid line shows the best-fit continuum slope, $F_\nu \propto \nu^{-\beta}$, with $\beta = 0.89 \pm 0.03$. The dotted line shows the effect of 0.1 mag of visual extinction from the host galaxy, assuming an $R_V = 3.1$ extinction law and $z = 1.477$ for GRB 010222. The lack of a dust feature like the $\lambda 2175$ Å bump suggests that either there is very little extinction from the $z = 1.477$ system or that the extinction law differs from the standard Galactic extinction law.

since dust in starburst galaxies tends to lack the λ2175 Å bump (Gordon, Calzetti, & Witt 1997).

We are grateful to the entire BeppoSAX team for the quick turnaround in providing precise GRB positions to the astronomical community, as well as to Scott Barthelmy and the GRB Coordinates Network (GCN). That these results could be obtained with small aperture telescopes is entirely due to the speed in which positions are reported and disseminated.

6.4 References

Bloom, J. S., Djorgovski, S. G., Halpern, J. P., Kulkarni, S. R., Galama, T. J., Price, P. A., & Castro, S. M. 2001, GCN Circular 989

Bloom, J. S., Kulkarni, S. R., & Djorgovski, S. G. 2002, AJ, 123, 1111

Boella, G., Butler, R. C., Perola, G. C., Piro, L., Scarsi, L., & Bleeker, J. A. M. 1997, A&AS, 122, 299

Bond, H. E. 1997, IAU Circ.6654

Cardelli, J. A., Clayton, G. C., & Mathis, J. S. 1989, ApJ, 345, 245

Castro, S., et al. 2001, GCN Circular 999

Churchill, C. W., Mellon, R. R., Charlton, J. C., Jannuzi, B. T., Kirhakos, S., Steidel, C. C., & Schneider, D. P. 2000, ApJS, 130, 91

Djorgovski, S. G., et al. 1997, Nature, 387, 876

Djorgovski, S. G., Kulkarni, S. R., Bloom, J. S., Goodrich, R., Frail, D. A., Piro, L., & Palazzi, E. 1998, ApJ, 508, L17

Fabricant, D., Cheimets, P., Caldwell, N., & Geary, J. 1998, PASP, 110, 79

Frail, D. A., Kulkarni, S. R., Nicastro, S. R., Feroci, M., & Taylor, G. B. 1997, Nature, 389, 261

Gandolfi, G. 2001, GCN Circular 966

Garnavich, P. M., Jha, S., Pahre, M. A., Stanek, K. Z., Kirshner, R. P., Garcia, M. R., Szentgyorgyi, A. H., & Tonry, J. L. 2000, ApJ, 543, 61

Garnavich, P. M., Pahre, M. A., Jha, S., Calkins, M., Stanek, K. Z., McDowell, J., & Kilgard, R. 2001, GCN Circular 965

Gordon, K. D., Calzetti, D., & Witt, A.N. 1997, ApJ, 487, 625

Henden, A. A. 2001a, GCN Circulars 961 and 962

Henden, A. A. 2001b, GCN Circular 987

Horne, K. 1986, PASP, 98, 609

Jha, S., Matheson, T., Calkins, M., Pahre, M. A., Stanek, K. Z., McDowell, J., Kilgard, R., & Garnavich, P. M. 2001, GCN Circular 974

Klebesadel, R. W., Strong, I. B., & Olson, R. A. 1973, ApJ, 182, L85

Kulkarni, S. R., et al. 1999, Nature, 398, 389

Kulkarni, S. R., et al. 2000, in Gamma-Ray Bursts: 5th Huntsville Symposium, eds. R. M. Kippen, R. S. Mallozzi, & G. J. Fishman (New York: AIP), 277

Lamb, D. Q. 1995, PASP, 107, 1152

McDowell, J., Kilgard, R., Garnavich, P. M., Stanek, K. Z., & Jha, S. 2001, GCN Circular 963

Meegan, C. A., Fishman, G. J., Wilson, R. B., Horack, J. M., Brock, M. N., Paciesas, W. S., Pendleton, G. N., & Kouveliotou, C. 1992, Nature, 355, 143

Metzger, M. R., Djorgovski, S. G., Kulkarni, S. R., Steidel, C. C., Adelberger, K. L., Frail, D. A., Costa, E., & Frontera, F. 1997, Nature, 387, 878

Paczyński, B. 1995, PASP, 107, 1167

Piro, L. 2001, GCN Circular 959

Prévot, M. L., Lequeux, J., Maurice, E., Prévot, L., & Rocca-Volmerange, B. 1984, A&A, 132, 389

Price, P. A., et al. 2001, ApJ, 549, L7

Sari, R., Piran, T., & Halpern, J. P. 1999, ApJ, 519, L17

Schlegel, D. J., Finkbeiner, D. P., & Davis, M. 1998, ApJ, 500, 525

Stanek, K. Z., Garnavich, P. M., Kaluzny, J., Pych, W., & Thompson, I. 1999, ApJ, 522, 39

Stanek, K. Z., Garnavich, P.M., Jha, S., Kilgard, R.E., McDowell, J.C., Bersier, D., Challis, P.M., Falco, E., & Quinn, J.L. 2001, ApJ, 563, 592

Steidel, C. C. & Sargent, W. L. W. 1992, ApJS, 80, 1

Stone, R. P. S. 1977, ApJ, 218, 767

Szentgyorgyi, A. H., et al. 2002, in preparation

van Paradijs, J., et al. 1997, Nature, 386, 686

Vreeswijk, P. M., Rol, E., Hjorth, J., Kouveliotou, C., Pian, E., Palazzi, E., Pedersen, H., Gorosabel, J., Castro-Tirado, A., & Greinder, J. 1999, GCN Circular 496

Vreeswijk, P. M., et al. 2001, ApJ, 546, 672

Wade, R. A., & Horne, K. D. 1988, ApJ, 324, 411

Chapter 7

Conclusions and Future Prospects

The exciting era of "precision cosmology" that we are perhaps now entering is buoyed substantially by work on SNe Ia and their cosmological applications. The data presented in this thesis should have a significant impact on upcoming (and ongoing) projects using SNe Ia to test and better characterize the new cosmological paradigm of an accelerating Universe filled with dark energy. Here we describe three projects that build upon this work.

7.1 Dustbusting

Currently, only SNe Ia provide *direct* evidence for an accelerating Universe and dark energy. For that reason, it is important to test this lynchpin in our cosmological model against other alternatives. We in the High-Z SN Search Team have undertaken a systematic effort to look for systematic errors that may plague the distant objects, making SNe Ia at $z \simeq 0.5$ appear faint (by as little as 0.25 mag, to reconcile the SN

Ia data with an open Universe). There are two main non-cosmological suspects that could lead to the apparent dimming of high-redshift SNe Ia — dust and evolution — and we are currently working on observations to test these possibilities.

Extinction by dust is one of the most natural explanations for the observed dimming of high-redshift SN Ia; many nearby SNe Ia are found to be extinguished (Jha et al. 1999, Chapter 2; Phillips et al. 1999). The $B-V$ colors of high-redshift SNe Ia show little evidence for reddening (Riess et al. 1998; Perlmutter et al. 1999). However, this does not rule out the possibility of so-called "grey" dust, i.e. dust which extinguishes but does not significantly redden. Though detecting the effects of completely grey dust may not be possible, fortunately for us, we can test *realistic* models for such dust. For instance, the model proposed by Aguirre et al. (1999), in which the smallest dust grains are preferentially destroyed by sputtering, is consistent with current constraints, but can be tested by observing high-redshift SN Ia over a wider wavelength range (beyond just rest-frame B and V). During the fall of 2000, we in the High-Z SN Search Team undertook a project to extensively observe a sample of 7 $z \simeq 0.5$ SN Ia, from the ground and with HST over a very wide wavelength range: rest-frame UBVRI (corresponding to observed-frame VRIZJ; Figure 7.1). As shown in Figure 7.2, the expected uncertainties in the color measurements from this set of SN Ia should definitively test realistic models of grey dust (Jha et al. 2001). These UBVRI observations of high-redshift SN Ia are a natural extension and application of the data and methods presented in Chapters 3 and 4.

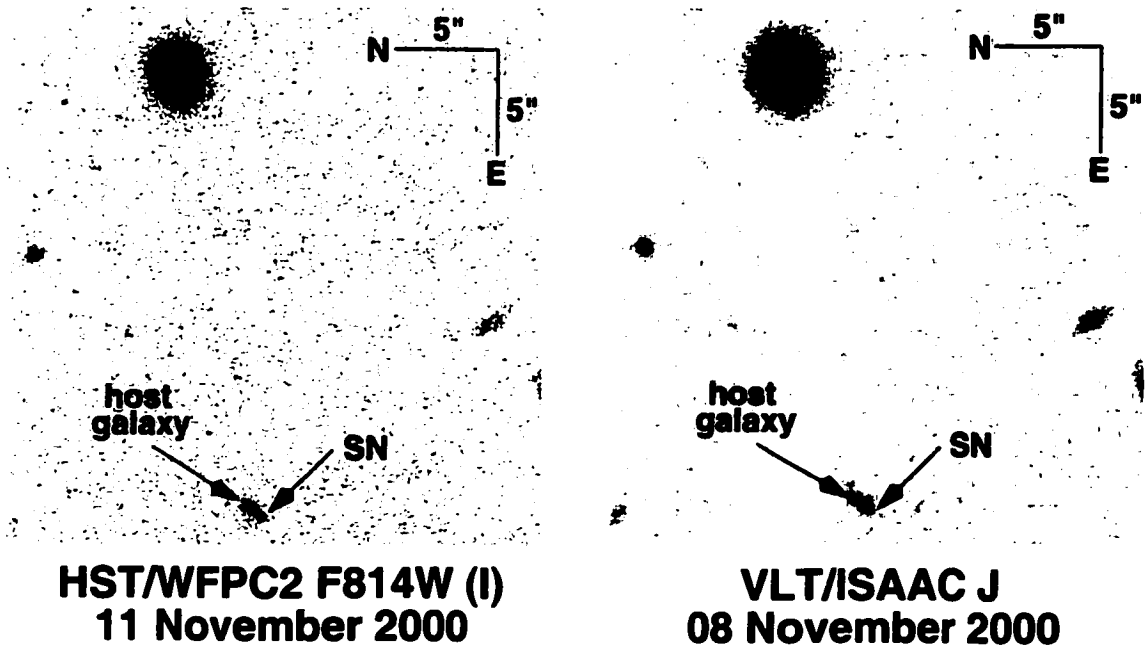

Figure 7.1.— Images of SN 2000ee at $z = 0.47$, one of 7 SNe Ia intensively observed by the High-Z SN Search Team in late 2000. The left panel is an HST image (I-band, corresponding to rest-frame V), and the image on the right is from the ground (VLT J-band, corresponding to rest-frame I).

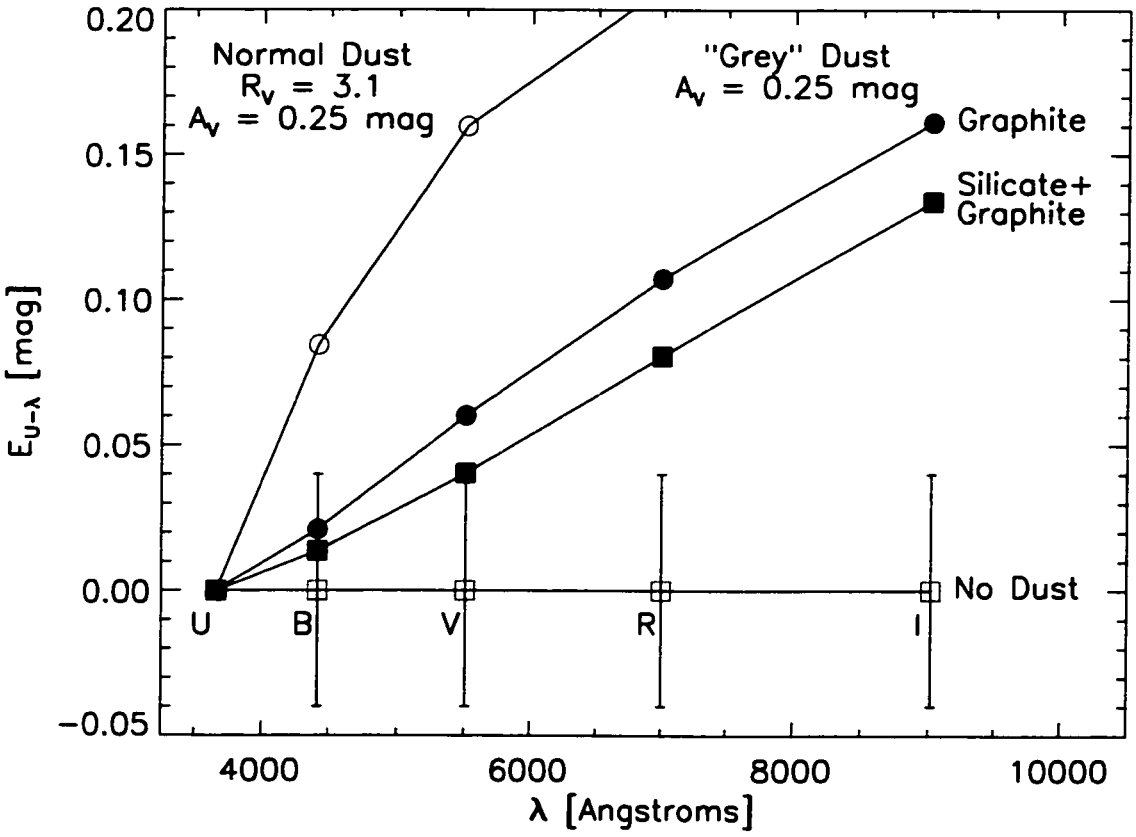

Figure 7.2.— Expected color excesses, $E(U-B)$, $E(U-V)$, $E(U-R)$ and $E(U-I)$, and uncertainties per object from the 2000 campaign. With 7 objects, we can rule out models of grey dust.

7.2 Reaching the Epoch of Deceleration

A strong test for evolution in SN Ia, and sources of systematic error in general, comes from observing SN Ia at higher redshift. Because the energy density of the cosmological constant does not change with the scale factor, while the matter density is increasing as $(1+z)^3$, at high enough redshifts, we should observe an epoch of matter-domination and consequently, deceleration. For an Ω_M=0.3, Ω_Λ=0.7 Universe, the transition from deceleration to acceleration occurred at $z \simeq 0.7$. If the results of SN Ia at $z \simeq 0.5$ are due to cosmology, we expect the Hubble diagram of SN Ia at higher redshift to "turn over," showing decreasing deviation from the empty-Universe line. Our first results from a few $z \simeq 1$ SN Ia with ground-based observations show hints of this turnover (Tonry et al. 2001, in preparation), but the results are not yet conclusive.

Precise distance measurements of SN Ia at very high redshift ($z \gtrsim 1.2$) require observations from space, as the desired rest-frame optical bands redshift into the near-infrared. An excellent example of the potential of such SN Ia came by pure luck, with the discovery of SN 1997ff at $z \simeq 1.7$, in followup observations the Hubble Deep Field and completely fortuitous NICMOS followup of a small portion of the Deep Field which happened to contain SN 1997ff at one edge (Riess et al. 2001). The results from SN 1997ff also seem to indicate we are observing the epoch of deceleration, but there are a number of potential uncertainties (e.g., gravitational lensing) that could muddle the interpretation of one object.

Ideally we would like observations of a number of very high redshift SN Ia to solidify the measurement of the epoch of deceleration. However, the cost in terms

of telescope time (necessarily meaning HST time) seems prohibitive because of the large number of orbits required to both discover SN Ia at these redshifts as well as follow them up with high-quality rest-frame B and V light curves (corresponding to NICMOS observations in J and H). Fortunately, though, the availability of ACS on HST for Cycle 11 (to begin in mid-2002) makes such an effort possible. We plan to piggyback on the GOODS high-galactic-latitude ACS survey. Observations for this survey will be undertaken in a manner conducive to the discovery of very high redshift SN, by splitting long integrations of fields over a few epochs separated by several weeks. Of course, beyond discovery, follow-up observations of the SN light curves are essential. Here, the results presented in Chapter 3 of this thesis on the rest-frame U-band properties of SN Ia are critical. We have shown that the U-band and B-band light curves of nearby SN Ia are closely correlated. At high redshift, then, our strategy will be to observe light curves in z-band with ACS (corresponding to rest-frame U-band for $z \simeq 1.4$). We will also observe two epochs each in J and H with NICMOS (rest-frame B and V) to determine precise zeropoint and reddening information, yielding a much more reasonable usage of limited telescope time compared to full light-curves in J and H. Our approved HST observations of 6 SNe Ia at $z \simeq 1.4$ should lead to a precise measurement of the very high-redshift Hubble diagram and a clear detection of a past epoch of deceleration.

7.3 What is the Dark Energy?

Finally, if observations of high-redshift SN Ia pass these stringent tests, and the existence of dark energy is more firmly established, the next, longer-term goal will

be to understand its nature. One clear path is to try to better measure the equation of state of the dark energy, parameterized by $w = P/\rho$ (called α in Chapter 5; Garnavich, Jha, et al. 1998). The results already presented here constrain $w \lesssim -0.5$, in the assumption of a flat, $\Omega_M \simeq 0.3$ Universe. SN Ia at redshifts $z \simeq 0.5$ are ideal probes of the dark energy and measuring w, compared to results from higher redshift (or the CMB at extremely high redshift $z \simeq 1000$), because the dark energy has only begun to dominate the expansion recently. However, because the luminosity-distance differences arising from small differences in w are extremely small (at the level of hundredths of magnitudes), measuring them requires a very large number of objects for good statistics and excellent control of systematic errors.

It is feasible, however, that we can constrain w with moderate precision, $\sigma_w \simeq 0.1$, on a relatively short timescale. Such precision will be good enough to rule out many quintessence models, and perhaps we will find that the cosmological constant is excluded as well. Our High-Z SN Search Team has proposed a major effort to find about 200 SN Ia with $0.3 \lesssim z \lesssim 0.8$ over the next few years using shared nights on the NOAO 4m Blanco Telescope at CTIO. If approved, this project would provide an excellent first step towards understanding what the mysterious dark energy really is, and further solidify the role of SNe Ia as excellent tools for observational cosmology.

7.4 References

Aguirre, A. 1999, ApJ, 535, 583

Garnavich, P. M., Jha, S., et al. 1998, ApJ, 509, 74

Jha, S., et al. 1999, ApJS, 125, 73

Jha, S., & the High-Z SN Search Team 2001, in proceedings of IAU Symposium 201, "New Cosmological Data and the Values of the Fundamental Parameters," eds: A. Lasenby & A. Wilkinson (astro-ph/0101521)

Perlmutter, S., et al. 1999, ApJ, 517, 565

Phillips, M.M., Lira, P., Suntzeff, N.B., Schommer, R.A., Hamuy, M., & Maza, J. 1999, AJ, 118, 1766

Riess, A. G., et al. 1998, AJ, 116, 1009

Riess, A.G., et al. 2001, ApJ, 560, 49